



Terms and Conditions of Use of Digitised Theses from Trinity College Library Dublin

Copyright statement

All material supplied by Trinity College Library is protected by copyright (under the Copyright and Related Rights Act, 2000 as amended) and other relevant Intellectual Property Rights. By accessing and using a Digitised Thesis from Trinity College Library you acknowledge that all Intellectual Property Rights in any Works supplied are the sole and exclusive property of the copyright and/or other IPR holder. Specific copyright holders may not be explicitly identified. Use of materials from other sources within a thesis should not be construed as a claim over them.

A non-exclusive, non-transferable licence is hereby granted to those using or reproducing, in whole or in part, the material for valid purposes, providing the copyright owners are acknowledged using the normal conventions. Where specific permission to use material is required, this is identified and such permission must be sought from the copyright holder or agency cited.

Liability statement

By using a Digitised Thesis, I accept that Trinity College Dublin bears no legal responsibility for the accuracy, legality or comprehensiveness of materials contained within the thesis, and that Trinity College Dublin accepts no liability for indirect, consequential, or incidental, damages or losses arising from use of the thesis for whatever reason. Information located in a thesis may be subject to specific use constraints, details of which may not be explicitly described. It is the responsibility of potential and actual users to be aware of such constraints and to abide by them. By making use of material from a digitised thesis, you accept these copyright and disclaimer provisions. Where it is brought to the attention of Trinity College Library that there may be a breach of copyright or other restraint, it is the policy to withdraw or take down access to a thesis while the issue is being resolved.

Access Agreement

By using a Digitised Thesis from Trinity College Library you are bound by the following Terms & Conditions. Please read them carefully.

I have read and I understand the following statement: All material supplied via a Digitised Thesis from Trinity College Library is protected by copyright and other intellectual property rights, and duplication or sale of all or part of any of a thesis is not permitted, except that material may be duplicated by you for your research use or for educational purposes in electronic or print form providing the copyright owners are acknowledged using the normal conventions. You must obtain permission for any other use. Electronic or print copies may not be offered, whether for sale or otherwise to anyone. This copy has been supplied on the understanding that it is copyright material and that no quotation from the thesis may be published without proper acknowledgement.

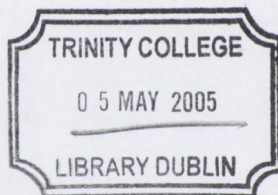
**AN EXPERIMENTAL AND 3D FINITE ELEMENT
ANALYSIS
OF A
FORM ROLLING PROCESS**

George Eyres

SUBMITTED IN FULFILLMENT OF THE REQUIREMENTS FOR THE
DEGREE OF DOCTOR OF PHILOSOPHY AT UNIVERSITY OF DUBLIN,
TRINITY COLLEGE DUBLIN, IRELAND, OCTOBER 2004.

Supervisor: Professor John Monaghan

The work presented in this thesis was conducted at the Department of Mechanical
and Manufacturing Engineering, University of Dublin, Trinity College, Ireland.



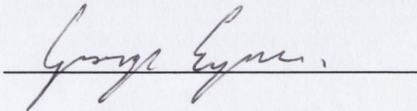
THESIS
7577

DECLARATION

Date: October 2004
Author: George Eyres
Title: Finite Element and Experimental Analysis of a Form Rolling Process
Department: Mechanical & Manufacturing Engineering
Degree: Ph.D.
Year: 2004

This thesis has not been submitted as an exercise for a degree at any other university. Except where stated, the work described therein was carried out by me alone.

I give permission for the Library to lend or copy this thesis upon request.


Signature of Author

ACKNOWLEDGMENTS

I am deeply indebted to my supervisor Prof. John Monaghan who provided me with the opportunity to do postgraduate study in Trinity and without his support, guidance and patience I would not be in the position to submit this thesis.

A special acknowledgment must go to Toman, Ray, Conor and Michael from Materials Ireland who were always available and willing to provide technical and financial support throughout the last three years.

I would also like to thank Jim Ryall and Ali Pasalar at Hi-Life Tools in Shannon for providing time and resources for testing.

To all my friends and the postgraduates who've kept me sane during the final stretch, I owe special thanks. In particular I'd like to thank Oran, Karol, Simmons, Richie, the three John's, Brian, Damo and Paul. I wish them every success and good fortune in the future. I would also like to offer my best wishes to Alan and Kevin, my office mates for the past three years and Emmet who has been with us for the last year.

I would like to thank my family Dad, Mom, Aideen, Evelyn and Lorcan for their constant support, even though it seemed I'd never finish, and for putting up with me over the years.

Finally, to Laura for her eternal optimism, humour and belief (so she said at the time!!!) that I would eventually complete this thesis.

AN EXPERIMENTAL AND 3D FINITE ELEMENT ANALYSIS OF A FORM ROLLING PROCESS

GEORGE EYRES

ABSTRACT

This thesis investigates a cold forming process called Form Rolling. Form Rolling is an innovative method of producing near-net shape parts, which is being implemented in particular by fastener manufacturers. In this study, a 3D finite element analysis of a flat die Form Rolling process that formed two different depth grooves on a rolling workpiece was simulated and compared to experimental tests. The FEA package used for this study was DEFORM3D which is an implicit Lagrangian adaptive remeshing finite element code that has the ability to characterise the workpiece material stresses and deformation behaviour.

The objective of this study is to attempt to explain the underlying mechanisms responsible for various defects and failures associated with Form Rolled components. In particular, the generation of lapping and twisting which are failure mechanisms influenced by material flow behaviour. The stress distributions that are generated in the workpiece during the process are also investigated to describe the conditions that led to the generation of a crack on the surface of the workpiece.

The complex material behaviour of the workpiece material was successfully modelled to reveal the mechanisms by which lapping and twisting occur. It was also found that a crack on the surface of the workpiece was generated by large tensile axial stresses combining with large shear stresses, at 90° to the die/workpiece interface.

TABLE OF CONTENTS

Declaration.....	I
Acknowledgments.....	II
Abstract.....	III
Table of Contents.....	IV
List of Figures.....	VII
List of Tables.....	XVI
Nomenclature.....	XVII
1 Introduction.....	2
1.1 Research Objectives.....	4
1.2 Form Rolling.....	5
1.2.1 Product Range.....	5
1.2.2 Machine Configurations.....	7
1.2.3 Developments in Form Rolling Machines.....	10
1.2.4 Form Roll Machine and Tool Design.....	14
2 Literature Review.....	19
2.1 Workpiece Deformation.....	19
2.1.1 Analysis of Contact Width and Pressure.....	19
2.1.2 Workpiece Defect Mechanisms.....	22
2.2 Fracture.....	35
2.2.1 Ductile Failure.....	35
2.2.2 Brittle Fracture.....	37
2.2.3 Fatigue.....	38
2.3 FEA of Form Rolling Processes.....	39
3 Metal Forming and the Finite Element Method.....	41
3.1 Principles of FEA.....	41
3.1.1 Basic Concept of FEA.....	42
3.1.2 Modelling the Form Rolling Process using DEFORM	42
3.1.3 The Yield Criterion.....	43
3.1.4 Prandtl-Reuss Flow Rule.....	45

	3.1.5 Hardening Rule.....	46
	3.1.6 Contact Modelling.....	47
4	Work Program.....	50
	4.1 Experimental Procedures.....	50
	4.1.1 Mechanical Testing.....	50
	4.1.2 Form Roll Testing.....	53
	4.2 Finite Element Analysis.....	60
	4.2.1 2D Finite Element Modelling Method.....	60
	4.2.2 Boundary Conditions Applied in 2D Modelling.....	62
	4.2.3 Advantages of 2D FEA.....	64
	4.2.4 Disadvantages of 2D FEA.....	65
	4.2.5 3D Finite Element Analysis Assumptions.....	68
	4.2.6 3D Die Stress Analysis.....	73
5	Results and Discussion.....	77
	5.1 Workpiece Deformation.....	77
	5.1.1 Validation of the Finite Element Model.....	78
	5.1.2 Workpiece Material Flow.....	85
	5.2 Surface Workpiece Defect Mechanisms.....	87
	5.2.1 Lap Generation.....	87
	5.2.1.1 Lapping at the Angled Sides of the Groove..	88
	5.2.1.2 Lapping at the Base of the Groove.....	95
	5.2.1.3 Validation that Laps are Generated at the Base of the Groove.....	103
	5.2.2 Surface Fracture.....	108
	5.2.2.1 Analysis of Surface Fracture.....	108
	5.2.2.2 Stress State Analysis of a Fastener During Form Rolling.....	116
	5.2.2.2.1 Knifing Stage.....	120
	5.2.2.2.2 Stretching Stage.....	127
	5.2.2.3 Combination of Tensile and Shear Stress in Crack Formation and Propagation.....	135

5.2.2.4	The Normalised Cockcroft-Latham Fracture Law Applied to Predict the Location of Surface Fracture.....	141
5.2.3	Development of Shear Induced Twist.....	143
5.2.3.1	Twist During the Knifing Stage.....	144
5.2.3.2	Twist During the Stretching Stage.....	150
5.3	Internal Workpiece Defects.....	155
5.3.1	Central Stresses Developed During the Knifing and Stretching Stages.....	158
5.3.2	The Normalised Cockcroft-Latham Fracture Law Applied to Predict the Location of Central Fracture...	164
5.3.3	Prediction of Internal Fracture Location using Hydrostatic Stress.....	166
5.4	Die Stress Analysis.....	168
5.4.1	Stress Analysis of the Die Feature that Formed the Second Groove.....	168
6	Conclusions.....	176
6.1	Material Flow Behaviour.....	176
6.1.1	Lapping.....	176
6.1.2	Twisting Effect.....	177
6.2	Stress Distributions.....	177
6.2.1	Surface Stress Distributions.....	177
6.2.1.1	Surface Fracture.....	178
6.2.2	Internal Stresses.....	178
6.2.3	Die Stress Analysis.....	179
7	Future Work.....	182
	References.....	184
	Appendix A.....	190

LIST OF FIGURES

- 1.1 Assortment of Form Rolled products.
- 1.2 Lever arm produced from a pre-form.
- 1.3 Form Rolling die configurations.
- 1.4 Two-roll die setups (a) reduction of the centre distance of the rolls, (b) increase of the rolling radius of the rolls and (c) feed of the blank perpendicular to its axis in the direction of decreasing distance between the rolls.
- 1.5 Three-roll tapered dies.
- 1.6 Position of dies on a 10 Waterbury machine.
- 1.7 CWR tool design and workpiece deformation process.
- 1.8 Radiused die.
- 1.9 Conical pointed die.
- 1.10 (a) Radiused point, (b) conical point and a (c) conical point fastener with a cavity at the tip.
- 1.11 Fastener with excess material.
- 1.12 Cavity pointed fastener.
- 1.13 EDM die surface.
- 2.1 Contact width for a flat die Form Rolling process.
- 2.2 Contact surface on a workpiece for a CWR process.
- 2.3 Modes of failure.
- 2.4 Central cavity in a three-roll process.
- 2.5 Slip line field for a (a) flat die and (b) three-roll process.
- 2.6 Void mechanism induced by tensile stress.
- 2.7 Void mechanism induced by shear stress.
- 2.8 Cruciform shape in a cross-section of an Aluminium CWR billet.
- 2.9 Illustration of crack generation.
- 2.10 Torsional deformation of a squeeze-rolled shaft.
- 2.11 Rolling force components on a workpiece.
- 2.12 Free-body diagram of a CWR process.
- 2.13 Shear deformation of radial insert in plasticine clay on (a) two-roll and (b) three-roll Mannesmann mills.

- 2.14 Ductile fracture due to void growth which is initiated at second phase particles which grow and generate localised strain between the voids causing excessive necking of the ligaments between the voids which eventually fracture.
- 2.15 Illustration of changing crack path due to the orientation of grains and grain boundaries.
- 2.16 Fracture surface attributed to fatigue failure.
- 4.1 Flow stress of SPS 8.8.
- 4.2 Flow stress of M2.
- 4.3 (a) Starting workpiece which is used to produce (b) a Double Groove fastener.
- 4.4 Double Groove Form Rolling dies.
- 4.5 Fastener cross-sections during Form Rolling in increments of 360° rotation.
- 4.6 Starting machine setup.
- 4.7 Leica L2 optical microscope.
- 4.8 Mounted longitudinal sections of a complete Double Groove workpiece.
- 4.9 Flow line orientation at the corner of the second groove.
- 4.10 Cross sections taken from double groove Form Rolling die.
- 4.11 Outline of the cross-sections imported into DEFORM2D as iges files.
- 4.12 Highlighted nodes restricting movement in the y direction.
- 4.13 Vector plot of 2D workpiece material flow.
- 4.14 Workpiece boundary conditions imposed in the x direction.
- 4.15 Vector plot of 2D workpiece material flow for the corrected model.
- 4.16 Boundary conditions were imposed on the highlighted nodes in the x direction.
- 4.17 2D representation of Form Rolled workpiece material.
- 4.18 Cross-section of the first groove of an experimental specimen.
- 4.19 Vector plot of the workpiece material using 2D FEA while forming a groove corresponding to 720° rotation of the workpiece.
- 4.20 3D FEA setup.
- 4.21 Axis of rotation.
- 4.22 Die movement setup.
- 4.23 3D boundary conditions.
- 4.24 Mesh density windows.

- 4.25 Reduced section of the die from which die stress results are obtained.
- 4.26 Illustration of the mesh density of the die while using die stress analysis.
- 5.1 Experimental Form Rolled Double Groove fasteners shown for every 360° rotation.
- 5.2 FEA representation of the progression of Form Rolling a Double Groove feature onto a workpiece shown for every 360° rotation.
- 5.3 Labels for the locations at which dimensions were taken from experimental fasteners and the FE model.
- 5.4 Average of the experimental and FEA measured lengths (mm), L , of the fastener taken for every 360° rotation of the workpiece.
- 5.5 Finite element representation of the first groove Form Rolled onto a workpiece which indicates the rounded edges at the corners of the groove.
- 5.6 Picture of a cross-section of the first groove from a finished Form Rolled workpiece.
- 5.7 Roughened surface on the workpiece due to the EDM finish on the tooling.
- 5.8 (a) Surface of the workpiece after 360° rotation and (b) the associated vector plot.
- 5.9 (a) Surface of the workpiece during the last 360° rotation and (b) the associated vector plot.
- 5.10 Form Rolled groove features through 180° rotation of the workpiece.
- 5.11 (a) Illustration of the first groove form and (b) area of contact between the workpiece and the bottom die, after 180° workpiece rotation.
- 5.12 (a) Illustration of the first groove form and (b) area of contact between the workpiece and both dies, after 270° workpiece rotation.
- 5.13 (a) Illustration of the first groove form and (b) area of contact between the workpiece and the top die, after 360° workpiece rotation.
- 5.14 Illustration of the V form shape produced by a die after 180° workpiece rotation.
- 5.15 Illustration, taken through Section AA from Figure 5.14, of the generation of a material step after 180° fastener rotation.

- 5.16 Vector plot of material flow for a cross-section taken through the first groove after 180° fastener rotation.
- 5.17 Illustration of the generation of a material fold after 200° rotation of the fastener.
- 5.18 Image of cross-section of the workpiece taken after approximately 360° rotation.
- 5.19 Lap located at the same position where folding material was observed during the Form Rolling of the side of the groove.
- 5.20 Picture of a *wave form* of deformed material on the second groove after 5 rotations of the fastener.
- 5.21 Generation of a *wave form* in the fastener material as the first groove is Form Rolled through (a) 180° (b) 720° (c) 900° and (d) 1260° rotation.
- 5.22 (a) Plan view of the material flow vector plot and (b) die/workpiece contact area, of the first groove after 540° rotation.
- 5.23 (a) Angled view and (b) side view of the velocity vectors in a cross-section of the workpiece after 540° rotation, located at the first groove.
- 5.24 Translucent radial view through first groove after 540° rotation.
- 5.25 Radial cross-section through the smallest diameter of the workpiece at 540° rotation.
- 5.26 Cross-section of the first groove of a finished fastener.
- 5.27 Cross-section of the fastener showing that there is no evidence of cracking at the corner of the first groove after 720° rotation.
- 5.28 Illustration of the appearance of defects due to lapping in the first groove of the workpiece over 3.5 rotations.
- 5.29 Origin of numbered cracks on the base of the groove.
- 5.30 Photograph of the second groove surface of a fully Form Rolled fastener.
- 5.31 Photograph of a cross-section of the second groove showing a crack and illustrating missing fastener material.

- 5.32 Material folds along the periphery of the second groove after 5 rotations of the fastener.
- 5.33 Photograph showing the length of a crack in the second groove which first appeared after 6 rotations of the fastener.
- 5.34 Location of necking in the second groove of the workpiece as observed in experimental testing.
- 5.35 (a) Photograph of a macroetched axial cross-section of a finished fastener using 2% Nital etchant for 30 seconds. (b) Photograph of the circled section in (a) showing the direction of material flow lines.
- 5.36 Photograph of a crack in the second groove after 6 rotations of the workpiece.
- 5.37 Orientation of voids at the crack tip.
- 5.38 Macroetch revealing the direction of the crack tip.
- 5.39 Selection of 13 selected points along the surface of the workpiece at regular intervals of 0.25mm during the Form Rolling of the second groove after (a) 3 (b) 5 and (c) 7 rotations.
- 5.40 Surface effective stress distribution while forming the second groove.
- 5.41 Effective stress distribution after 5.5 rotations of the workpiece where the *point tracking* points are in contact with the die.
- 5.42 Effective stress distribution after 5.75 rotations of the workpiece where the *point tracking* points are not in contact with the die.
- 5.43 Illustration of the displacement of point 4 as it moved from one side of the groove profile after (a) 4 rotations, to other after (b) 4.4 and (c) 4.5 rotations.
- 5.44 Effective stress distribution of point 4 during the *knifing* stage of the forming process.
- 5.45 Comparison of the surface axial, hoop and radial stresses for point 4 during the *knifing* stage while forming the second groove.
- 5.46 Comparison of the maximum axial, hoop and radial stresses during the *knifing* stage while forming the second groove.

- 5.47 Axial tensile stress distribution after 5.2 rotations at 90° to the die/workpiece interface.
- 5.48 Radial compressive stress distribution after 5.2 rotations generated at the die/workpiece interface.
- 5.49 Comparison of the axial and effective stresses for point 4 during the *knifing* stage.
- 5.50 Comparison of maximum axial and effective stresses during the *knifing* stage.
- 5.51 Axial tensile stress distribution taken after 4.25 rotations.
- 5.52 Illustration of the displacement of point 5 during the stretching stage of the die after (a) 5, (b) 6 and (c) 7 rotations, respectively.
- 5.53 Surface effective stress distribution of point 5 while forming the second groove.
- 5.54 Comparison of the surface axial, hoop and radial stresses at point 5 while forming the second groove.
- 5.55 Comparison of the maximum axial and radial stresses during the forming of the second groove.
- 5.56 (a) Isometric and (b) isometric cross-section view of the axial tensile stress distribution on the workpiece after 5.75 rotations.
- 5.57 (a) Isometric and (b) isometric cross-section view of the radial tensile stress distribution on the workpiece after 5.75 rotations.
- 5.58 Comparison of the maximum surface axial stress to the maximum surface effective stress while forming the second groove.
- 5.59 Vector plot of the maximum principal stress where the profile of the workpiece is highlighted in green.
- 5.60 Illustration of the positions of the point tracking point after 5.75 rotations with an (a) isometric and (b) axial cross-section view of the tensile stress distribution.
- 5.61 Side view of the (a) axial tensile stress and (b) shear stress, τ_{zr} , surface distribution on a fastener after 5 rotations.
- 5.62 Side view of the (a) axial tensile stress and (b) shear stress, τ_{zr} , surface distribution on a fastener after 5.25 rotations.
- 5.63 Side view of the (a) axial tensile stress and (b) shear stress, τ_{zr} , surface distribution on a fastener after 5.5 rotations.

- 5.64 Side view of the (a) axial tensile stress and (b) shear stress, τ_{zr} , surface distribution in a fastener after 5.75 rotations.
- 5.65 Side view of the (a) axial tensile stress and (b) shear stress, τ_{zr} , surface distribution on a fastener after 6 rotations.
- 5.66 Axial cross-section of the shear stress, τ_{zr} , distribution after 5 rotations.
- 5.67 Axial cross-section of the shear stress, τ_{zr} , distribution after 5.25 rotations.
- 5.68 Axial cross-section of the shear stress, τ_{zr} , distribution after 5.5 rotations.
- 5.69 Axial cross-section of the shear stress, τ_{zr} , distribution after 5.75 rotations.
- 5.70 Axial cross-section of the shear stress, τ_{zr} , distribution after 6 rotations.
- 5.71 Macroetch revealing the direction of the crack tip with an illustration of the maximum principal stress direction.
- 5.72 Damage distribution of point 5 while forming the second groove.
- 5.73 Surface damage distribution in the workpiece after 5.75 rotations.
- 5.74 Schematic of the angle of twist, ϕ .
- 5.75 Plan view of the point tracking points plotted (a) before indentation of the second groove occurred i.e. after 3 rotations, (b) after 4 rotations and (c) a side view taken after 4 rotations.
- 5.76 Plan view of the surface strains in the (a) radial, (b) axial, (c) hoop directions and the (d) corresponding shear stress τ_{zr} with the contact area shaded, taken after 4 rotations.
- 5.77 (a) Plan and (b) side view of the fastener after 5 rotations.
- 5.78 Plan view of the (a) radial, (b) axial, (c) hoop strains and the (d) corresponding shear stress τ_{zr} with the contact area shaded.
- 5.79 (a) Plan and (b) side view of the fastener after 6 rotations.
- 5.80 Plan view of the (a) radial, (b) axial, (c) hoop strains and the (d) corresponding shear stress τ_{zr} with the contact area shaded.
- 5.81 (a) Plan and (b) side view of the workpiece surface after 7 rotations.
- 5.82 Selection of 13 selected points at the centre of the workpiece, at regular intervals of 0.25mm, during the Form Rolling the second groove after (a) 3 (b) 5 and (c) 7 rotations.
- 5.83 Effective stress distribution at the centre of the workpiece at the selected point tracking points while forming the second groove.

- 5.84 Effective stress distribution at the centre of the groove at point 6 while forming the second groove.
- 5.85 Effective stress distribution after 4.1 rotations of the workpiece.
- 5.86 Comparison of central axial and radial stress distribution for point 6 while forming the second groove.
- 5.87 (a) Radial and (b) axial tensile stress distribution after 4 rotations.
- 5.88 (a) Radial and (b) axial tensile stress distribution after 5 rotations.
- 5.89 (a) Radial and (b) axial tensile stress distribution after 6 rotations.
- 5.90 (a) Radial and (b) axial tensile stress distribution after 7 rotations.
- 5.91 Shear stress distribution in a radial cross-section after 5 rotations.
- 5.92 Shear stress distribution in a radial cross-section after 6 rotations.
- 5.93 Magnitude of the shear stress distribution at the centre of the workpiece.
- 5.94 Damage distribution for point 6 while forming the second groove.
- 5.95 Damage distribution related to the Normalised Cockcroft-Latham fracture law after (a) 4, (b) 5 and (c) 6 rotations.
- 5.96 Hydrostatic stress distribution attributed to point 6 while forming the second groove.
- 5.97 Tensile hydrostatic stress distribution in radial cross-sections of the workpiece taken after (a) 4, (b) 5 and (c) 6 rotations.
- 5.98 Die effective stress of the feature that formed the second groove taken after 4 rotations of the workpiece.
- 5.99 Die effective stress of the feature that formed the second groove taken after 5 rotations of the workpiece.
- 5.100 Die effective stress of the feature that formed the second groove taken after 6 rotations of the workpiece.
- 5.101 Die effective stress of the feature that formed the second groove taken after 7 rotations of the workpiece.
- 5.102 Maximum die effective stress distribution while forming the workpiece.
- 5.103 Effective stress distribution in the die form that Form Rolled the second groove taken after 4 rotations of the workpiece.
- 5.104 Die effective stress distribution in the die form that Form Rolled the second groove after 6 rotations of the workpiece.

- 5.105 Cross-section view of the die effective stress distribution in the die form that Form Rolled the second groove after 6 rotations of the workpiece.
- 5.106 Maximum principal stress distribution in the die form that Form Rolled the second groove after 5 rotations of the workpiece.

NOMENCLATURE

Symbol	Definition
α	Forming angle
β	Stretching angle
δ	Relative area reduction
δ	Displacement
ϵ	Strain
ϵ^e	Elastic strain
ϵ^p	Plastic strain
$\bar{\epsilon}^p$	Effective plastic strain
γ	Inclined angle
μ	Friction coefficient
μ_0	Specified mean
π	Pi
σ	Stress
$\bar{\sigma}$	Effective stress
σ_y	Yield stress
σ_h	Hydrostatic stress
σ_M	Mean stress
σ_N	Normal force
σ_1	Maximum principal stress
σ_2	Secondary principal stress
σ_3	Minimum principal stress
τ_F	Friction shear stress
τ_{\max}	Shear strength of the material
μ_b	Friction of the side of the tool
μ_k	Friction on the stretching surface of the tool
ϕ	Angle of twist
ν	Poisson's ratio
ω	Angular velocity
Δ_A	Area reduction

Δr	Total radial reduction
θ	Angular rotation
d	Billet diameter
d_o	Original billet diameter
$d\lambda$	Plastic proportionality constant
$f(\sigma_{ij})$	Yield function
k	Shear yield stress
l_o	Length in contact
m_k	Sizing surface shear friction factor
m	Hardening index
m	Sensitivity to hardening index
m	Friction factor
n	Sample number
q_μ	Mean unit pressure
r	Radius
s	Standard deviation
s_x	Estimate of the variance
u_t	Linear tool displacement
u_w	Linear workpiece displacement
v	Feed speed
2D	Two dimensional
3D	Three dimensional
A	Area
A_o	Original area
C	Strength coefficient
B	Contact width in CWR process
C	Constant
C	Critical damage
CWR	Cross wedge rolling
E	Young's modulus
EDM	Electro-discharge machining

F	Slipping friction
F	Force
FE	Finite element
FEA	Finite element analysis
FEM	Finite element modelling
G	Shear modulus
H _A	Alternate hypothesis
H ₀	Null hypothesis
I ₁	First stress invariant
I ₂	Second stress invariant
I ₃	Third stress invariant
K	Stiffness
N	Normal force
S	Interfacial slip
W _p	Plastic work
\bar{X}	Sample average

CHAPTER 1
INTRODUCTION

CHAPTER 1

INTRODUCTION

Form Rolling is a manufacturing process that has gained much popularity in recent years due to high productivity, material savings, increased product strength and consistent quality when compared to machining [1]. Parts often include a combination of threads, grooves, chamfering and radiusing on axisymmetric parts which are rolled on a standard thread rolling machine.

Orlomoski [1] states that Form Rolling is a viable endeavour when the part quantity exceeds 50,000 pieces and the right size machine is available. However, if no machine is available an initial investment can be justified by spreading the cost over millions of pieces that can be produced annually.

The mechanical properties of the material are improved through controlled deformation resulting in improved strength, ductility and resistance to impact and fatigue as a result of the manipulation of the grain flow in the worked material. In most cases, forming stock has been pre-worked to remove porosity arising from the solidification process. This produces directional alignment or grain flow which can induce anisotropy and influence properties such as strength, ductility, and resistance to impact and fatigue. These properties are deliberately orientated in directions requiring maximum strength. Because of this improvement in mechanical properties it is sometimes possible to use lower cost and lower strength raw material than if the parts were to be produced by machining. For example, by substituting less costly low or medium carbon steels for high carbon alloy steels.

In many cases, parts produced by cold forming are net-shaped which have an excellent surface finish and require no subsequent machining. Therefore, when a part is made from expensive alloys, the financial saving resulting from using less material can be substantial. Furthermore, reduced inspection costs can be achieved due to consistent product quality.

Form Rolling has the added advantage of being able to produce pieces that are either too long or too small to hold properly for a turning operation. Shapes that are difficult or economically impractical to machine can frequently be produced by a cold forming process. In terms of high production rates, reduced material handling and no preheating, cold Form Rolling can be compared

favourably with other processes such as hot forging, casting, sintering and conventional machining.

Form Rolling is performed by placing a cylindrical billet between two flat reciprocating dies which are moved relative to each other in the same fashion as a thread rolling process. However, the manufacturing industry has been slow to utilise this technology even though manufacturers who already have thread rolling machines can easily fit them with Form Rolling dies, minimising setup costs and enabling them to manufacture an entirely new range of products quickly. The reason for this is that the deformation and failure mechanisms of the process are, for the most part, unpredictable thereby making it difficult to design Form Roll tooling. Consulting companies that specialise in Form Rolling generally undertake designs on a product-to-product basis. This is expensive for the customer because accurate knowledge on how the material will flow to produce a given geometry is difficult to obtain. Determining this can still require considerable prototyping of the tooling involving a lot of trial and error rolling tests depending on the complexity of the shape required. Another problem of the Form Rolling process is the generation of very high forces on the tooling that in turn leads to high tool stresses. These can result in short tool life due failure from cyclic loading or excessive tensile stress leading to rapid fracture in the form of chipping.

Finite element modelling can be used to predict material flow and stresses in the workpiece and tooling. This can then be used to determine the stress distributions during the forming process which can then be used to determine optimum tool design in order to decrease excessive tool and workpiece stresses.

1.1 Research Objectives

The present research is a combination of experimental testing and finite element modelling, performed with the intention of studying a Form Rolling process. Experimental work was required in order to validate the adopted finite element model setup which could then be applied to describe workpiece defects that occurred during testing.

This research was undertaken to remove the “black art” uncertainty associated with the Form Rolling process and to attempt to explain the underlying mechanisms responsible for various defects and failures associated with Form Rolled components. It is the author’s intention to analyse the generation of lapping and twisting which are surface failure mechanisms that are influenced by the material flow behaviour during the Form Rolling process. A secondary objective was to analyse the stress distributions within the workpiece in order to describe the conditions that led to the generation of a crack on the surface of the workpiece.

1.2 Form Rolling

This chapter introduces the Form Rolling process and the range of products that have been manufactured to date using this process. This will then be followed by a description of the different tool configurations used in industry for Form Rolling and individual features of the tooling will be explained. The chapter will conclude with a description of the development of Form Rolling machines from the origins of the process to the present day.

1.2.1 Product Range

Form Rolling has been used to manufacture net or near net shaped axisymmetric components since 1960 [2]. In general, net-shaped products that require no trimming or finishing operations can have relatively short lengths, small diameters and consist of complex geometries. Typically these geometries can include grooves, threads, radiused points, conical points or as is the case in many examples, a combination of two or more of these features. Examples of these geometries/features are illustrated in Figure 1.1. These parts were manufactured at Rol-Flo Engineering Inc. in the U.S [1]. Other examples of complex Form Rolled parts can be found in the following literature [3-5]



Figure 1.1 Assortment of Form Rolled products.

The manufacture of near net shaped components consists of pre-forming or intermediate shape production stages from which the billet material is subsequently die forged to produce parts having less flash than would normally be present in a die forging process without the pre-form stage. Having less flash has the benefit of greatly reducing tool stresses and tool wear thereby prolonging tool life. On the left of Figure 1.2 a typical pre-form geometry has been purposely Form Rolled with excess billet material [5]. This excess material formed the flash, shown on the right of Figure 1.2, when the pre-form was compressed in the forging press. This ensured there was enough pressure on the material to properly form the end product which in this case was a lever arm shown in the centre. Other examples of products manufactured using pre-forms such as bicycle cranks, double-handed wrenches, steering arms and others can be found in the following literature [5-10].

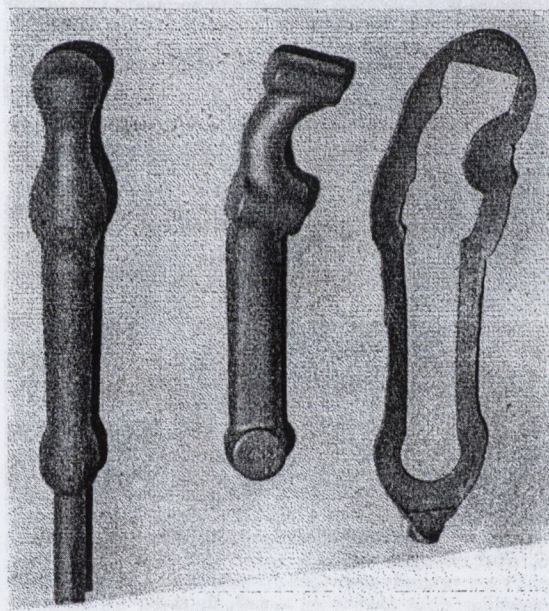


Figure 1.2 Lever arm produced from a pre-form [5].

1.2.2 Machine Configurations

Form Rolling machines are classified according to any one of five types of die configuration commonly used in industry: one-roll; two-roll; three-roll; concave; and flat (Figure 1.3).

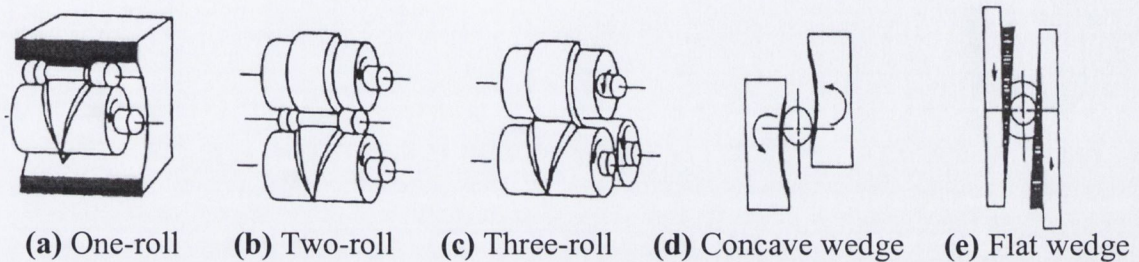


Figure 1.3 Form Rolling die configurations [11].

One-roll: In this configuration the workpiece is deformed between the rotating roll and the stationary concave base. The roll and the base have matching geometries that form the desired shape onto the workpiece. However, this type of tooling is difficult to make and adjust and is not commonly used in industry today.

Two-roll: As described by Tselikov [12] there are three methods used to Form Roll a part using two-roll dies:

- As the dies and workpiece rotate the distance between the centres of the dies is gradually reduced causing the billet to elongate and reduce in diameter (Figure 1.4 (a)).
- The dies rotate about their centre axes. Diameter reduction and elongation is achieved by the increasing rolling radius of the dies (Figure 1.4 (b)).
- A billet is fed between dies with uniform diameter as they rotate about their axes. The extent of diameter reduction is set by the distance between the rolls (Figure 1.4 (c)).

For each respective setup the rolls have identical geometries and rotate in the same direction on parallel axes causing the workpiece to rotate in a direction counter to the rolls. A feature that is not shown in Figure 1.4 is a stopper mechanism which holds the billet in the correct position between the dies.

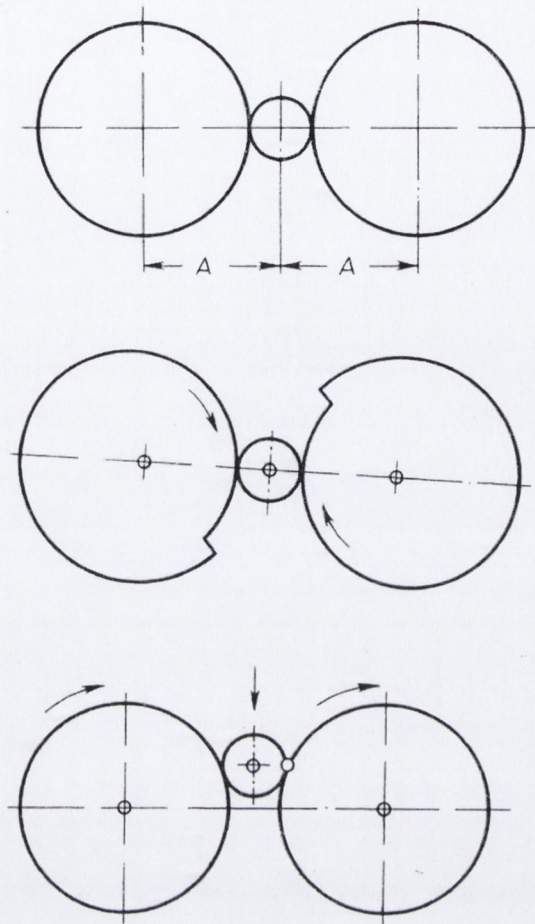


Figure 1.4 Two-roll die setups (a) reduction of the centre distance of the rolls, (b) increase of the rolling radius of the rolls and (c) feed of the blank perpendicular to its axis in the direction of decreasing distance between the rolls [12].

Three-roll: A three-roll configuration (Figure 1.3 (c)) can have the same Form Rolling mechanism as the first two examples given for the two-roll machines as described above. However, on a three-roll machine the smallest diameter of a product is limited compared to two-roll tooling. For example, if the same diameter dies were used a two-roll machine could roll very small pieces whereas the minimum diameter of a billet rolled using a three-roll machine is limited to the space between the three rolls as shown in Figure 1.5.

In most cases the billet is dropped in the middle of the rolls which has led it to being described as a drop forging process [5].

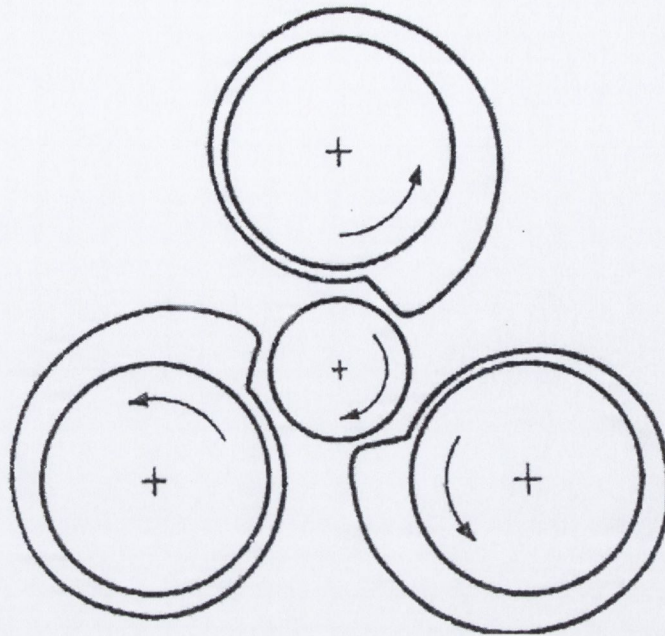


Figure 1.5 Three-roll tapered dies [6].

Concave: For the concave die configuration (Figure 1.3 (d)) the workpiece remains stationary while the dies rotate eccentrically in the same direction. This ensures that the dies progress into the workpiece during rolling. Similar to the one-roll configuration, tool manufacture and die setup is difficult which has made it an unpopular configuration for industrial applications.

Flat: The flat die configuration (Figure 1.3 (e)) investigated in this study forms a cylindrical billet by rolling it between two flat dies, one of which is stationary while the other moves with a reciprocating motion to form the desired geometry in the same fashion as that of a thread rolling process [13]. The geometry on the die faces is impressed onto the periphery of a plain cylindrical billet to form the desired end product. The flat die configuration is described in detail on the following pages with particular emphasis on the tool design and machine setup. Andreev *et al* [14] recommends using flat dies as they are more accurate and easier to manufacture compared to cylindrical dies consequently leading to an improvement in product accuracy and quality.

All of the die configurations listed above can be orientated either vertically or horizontally depending on the machine design.

1.2.3 Developments in Form Rolling Machines

The first patent for a Form Rolling machine was filed by Lebek [15] in 1879 and used two moving flat dies. In 1885, as reported by Fu and Dean [16], Simonds [17] patented the first two-roll machine used to produce shafts for the vehicle industry. Eight years later, Erkenzweig [18] patented a flat die Form Rolling machine in which the bottom die was stationary. It then took until 1961 for a fully developed commercial machine to be available for industry. This was a two-roll CWR machine developed by Holub [2] at the Letnany automobile works in Czechoslovakia. Consequently, the most significant development in Form Rolling machines was undertaken in Czechoslovakia, and the former Soviet Union in particular, where most of the research into metal flow behaviour and stress development has been undertaken. With the fall of the Soviet Union other countries such as China, Japan, Germany and the United States realised the potential financial and mechanical advantages of the process and endeavoured to augment their understanding of the range of potential applications for the process in modern industry.

Many of the patents and references in the following section have been taken from Fu and Dean's paper titled "*Past developments, current applications and trends in the cross wedge rolling process*" [16] which contains references only obtainable in German, Russian, Japanese and Chinese. However it is important to include them in order to provide a full background of the development of the Form Rolling process.

The following section has been categorised geographically.

Czechoslovakia (the former)

In 1971, ten years after Holub's first patent [19], three machines designated UL-35, UL-60 and UL-100 were developed. These were vertically supported two-roll machines with workpiece diameter capacities of 35mm, 60mm and 100mm respectively which could handle components of 300mm, 450mm and 600mm in length. The rolls were machined with T-slots so that the dies could be inserted into them and then secured with T-bolts. This saved on the cost of the tool steel as only the outer periphery with a certain depth of the die had to be machined instead of a whole new roll every time a die was changed or replaced.

The machine was also supplied with an induction heater which heated the billets before rolling. This reduced the stresses on the tooling by reducing the flow stress of the billet material thereby making it easier to flow plastically.

Soviet Union (the former)

The first two-roll machine was developed by Balin [20] in 1961 at the Technology Design Institute of Gorikij. It rolled billets which were preheated by an induction heater and then fed into the machine via a bar feeder. The dies were driven by a motor, belt and gearbox which allowed for variable speed Form Rolling. Universal couplings allowed for die adjustment.

In 1971, Tselikov *et al* [21] at the Soviet Metallurgical Machinery Institute in Moscow built their first two-roll machine designated P-140000. Three years later, Tselikov *et al* [22] patented a horizontal two-roll machine and produced five machines designated 40-400, 50-520, 110-300, 100-500 and 130-600. The first of the two numbers indicates the maximum rollable workpiece diameter and the second the maximum rollable workpiece length. These machines Form Rolled warm or hot billets. In 1972, Dulov and Astafiev [23] made a significant contribution to Form Rolling by patenting the first cold Form Rolling machine. It was a horizontal two-roll machine with a billet support between the dies which made parts with diameters from 1.8mm to 10mm.

In 1973, Deordiev *et al* [24] at the Institute of Machinery and Design in Voronezh, built one-roll machines, the configuration of which is illustrated in Figure 1.3(a). Due to the difficulty in die manufacture and adjustment very few machines were produced.

At the Physics and Technology Institute of The Academy of Science in what is now Belarus, a horizontal flat wedge rolling machine design was patented by Andreev *et al* [25, 26] in 1975. This was a cold rolling machine where the bottom die remained stationary and was later constructed in various sizes which could roll diameters from 5mm to 45mm with lengths of between 10mm to 400mm. In 1984, based on a transmission designed by Prokolov *et al* [27], Urazov [28] built a horizontal cold rolling machine where both dies moved in a reciprocating motion.

No research into three-roll processes was performed in the Soviet Union.

Great Britain

In 1969, Henry Wiggin & Co. Ltd. produced the first three-roll CWR machine in the world [6]. In the same year based on this design Redman Engineering Ltd. produced two three-roll machines for the Drop Forging Research Association which could make

components with maximum diameters between 12mm and 50mm and lengths between 150mm and 300mm [5].

Poland

Marciniak [29] patented a machine designated WPM-120 in 1972 to roll spline shafts. The machine was fitted with concave tooling as shown in Figure 1.3 (d) which was eccentrically rotated in the same direction around the component. However this tool configuration was not widely utilised due to the manufacturing complexity of the tooling.

United States

In 1972, Belmont [30] started to investigate a two-roll CWR process based on the UL-35 Czech model at Wedgeroll Tool & Machine Incorporated. The roll diameters were 610mm with lengths of 406mm. Two years later this machine was redesigned to take rolls of diameter up to 1219mm and length 1067mm.

At the end of the 1980s Rol-Flo Inc. started to mass produce fasteners which contained radiused and conical points combined with threading and grooving. These were produced using two machines designated #30 and #60 using flat tooling designed by Orloski [1] and stock heated between 430°C and 650°C. Ever since the 1980s to the present day Rol-Flo Inc. under Orloski has become the world leader in Form Rolling design. The fasteners produced can contain multiple grooves, points and threaded sections which can be rolled in a single operation with excellent surface finish and size tolerance.

Japan

Japanese Form Rolling machine development has been exclusively concerned with either two-roll or three-roll machines. In 1955 Motomura [31] and in 1960 Shirai [32] were awarded patents for horizontal two-roll machines.

People's Republic of China

In China most of the research into Form Rolling machines has concentrated on two-roll and three-roll die configurations, except in 1972 at the Third Forging Machinery Works of Shanghai where a one-roll machine was used to make spanner preforms [33].

In 1970, at Chongqing University a two-roll CWR machine was developed for ball stud rolling [34]. Four years later, the Hua Shan Machinery Factory and the University of Beijing Science and Technology designed and built a vertical two-roll machine with a roll diameter of 750mm designated H750. The "H" type series consisted of a non-compact machine arrangement within cast steel frames. Cross plate coupling was used to provide simultaneous drive to the dies [35]. In 1987, Li *et al* [36, 37] designed two machines designated H680 and H800 which were put into production at the Jiangshu Bike Industrial Co. and Shanxi Heavy Forging Works. Meanwhile, a new "D" type two-roll series was designed at the Jinan Forging and Foundry Institute [38]. This series has a compact design where universal couplings are used instead of the cross plate coupling used in the "H" series.

In 1985, Luan *et al* [39] patented the first Chinese three-roll machine which was the result of 10 years research and development at the Northeast University of Technology. This design was for a CWR process that incorporated induction heating and a feed and discharge system for the billets.

Current Status

Since the end of the 1980s most machine development has centred on three of the die configurations being: flat, two-roll and three-roll. The one-roll and concave dies have, to a large extent, been ignored due to the difficulty in tool manufacture and adjustment within the machine. The design of the machines has not greatly changed to the present day except for the introduction of accurate control systems which gives the user more control of the feed speed and the accurate alignment of the dies.

An interesting trend is the design of machines to Form Roll increasingly smaller parts to cater for the medical and electronic industries an example of which is the use of small screws for mobile phones. EWM [40] from Germany produce machines that will roll 3mm maximum pieces.

1.2.4 Form Roll Machine and Tool Design

An industrial horizontal thread rolling machine was used for this study, with flat Form Roll tooling replacing the flat thread rolling dies. For a thread rolling process the size of the machine used depends on the stroke required to form the screw. Generally, the length of a thread rolling die is approximately 5-6 times the circumference of the billet. However, compared to thread rolling, Form Rolling dies are longer because more material is displaced than in a normal thread rolling operation. Consequently, during Form Rolling a longer stroke is required to produce a feature on a given diameter workpiece compared to that required to roll a thread on a workpiece of equivalent diameter. Orlomski [1] recommended moving up one size when choosing a machine for a Form Rolling process. This is necessary because unlike thread rolling, where the material deforms radially into the grooves, most Form Rolling processes require that the material be displaced and elongated axially while maintaining the original billet diameter. Therefore the machine must be rigid enough to resist the high radial loads caused by the displaced material and have sufficient stroke to produce the required geometrical feature.

Flat Form Rolling dies always come in pairs consisting of a moving (reciprocating) and a stationary die, as shown in Figure 1.6. These are secured into the machine using clamps and shims to ensure that both die surfaces are parallel and aligned correctly. The reciprocating (moving) die which is secured into the ram, drives the workpiece whereby the desired geometry is progressively formed onto the rolling workpiece. For a typical flat Form Rolling machine 40% of the operation time is required for the return stroke.

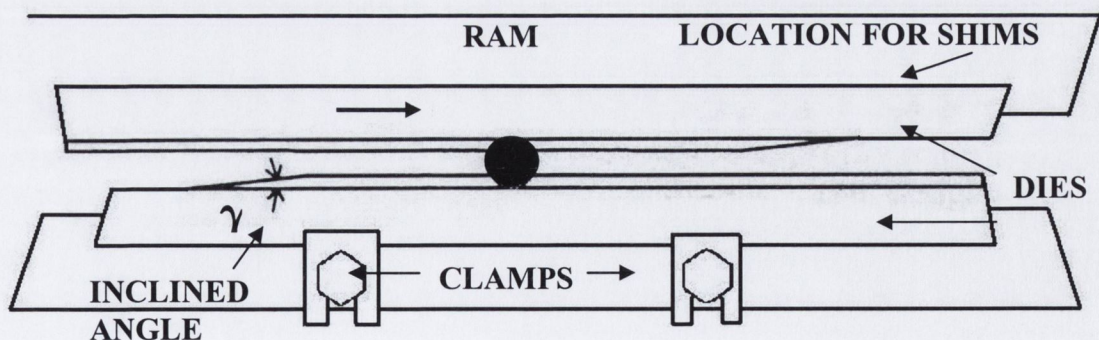


Figure 1.6 Position of dies on a 10 Waterbury machine.

In Form Rolling there are three distinct stages of workpiece deformation corresponding to three zones of the tool geometry. These stages are described below and illustrated in Figure 1.7 which shows a typical Cross Wedge Roll (CWR) die used to form a groove on a workpiece.

Stage 1: Knifing stage: The *knifing* zone consists of a wedge shape whose height starts at zero and increases until the total radial reduction Δr is achieved. The angle from the start to the end of the *knifing* zone is the *inclined angle* γ and is shown in Figure 1.6. It should be noted that with this tool geometry, material is displaced simultaneously in both directions along the axis of the part.

Stage 2: Stretching stage: When the full depth of penetration has been achieved the *stretching* zone increases the width of the wedge being formed. The angle of the wedge is commonly known as the *stretching angle* β . The shoulder angle of the wedge is the *forming angle* α . Stages 1 and 2 when combined make up the ramp of the die.

Stage 3: Sizing stage: The sizing zone is also known as the *dwell* of the die. Imperfections on the surface of the workpiece are “ironed out” in this section by the geometry of the die which is uniform. Typically, the length of the dwell region is equal to twice the circumference of the fastener.

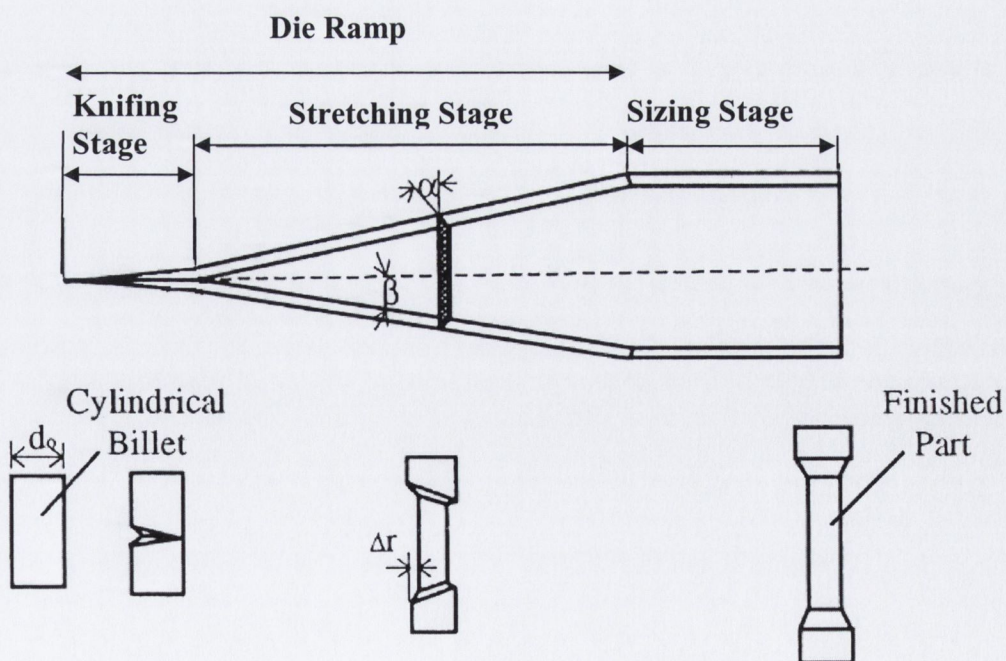


Figure 1.7 CWR tool design and workpiece deformation process [16].

Figures 1.8 and 1.9 show a representation of dies used to form a radiused and a conical pointed fastener, respectively which are illustrated in Figures 1.10 (a), (b) and (c). These dies consist of a ramp and dwell similar to the CWR die the difference being the inclusion of a slug cut-off feature in the dwell sections of the tooling to remove excess material.

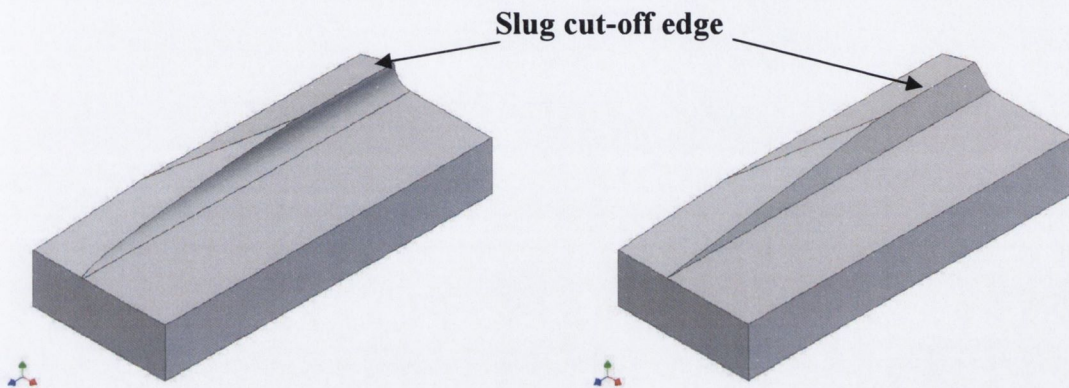


Figure 1.8 Radiused die.

Figure 1.9 Conical pointed die.

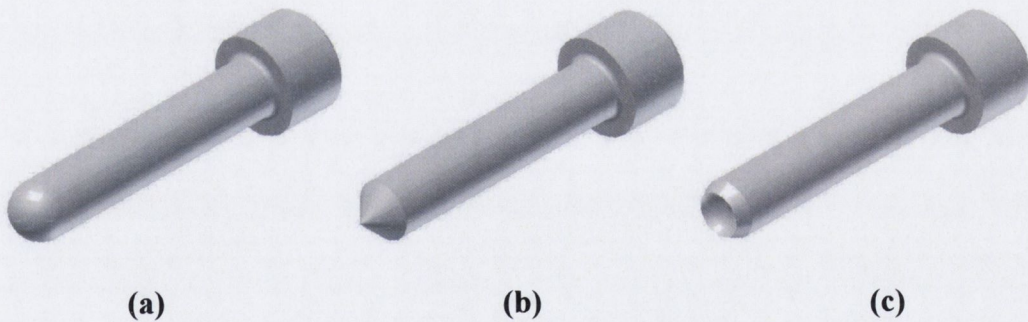


Figure 1.10 (a) Radiused point, (b) conical point and a (c) conical point fastener with a cavity at the tip.

Excess material must be used to completely fill the area between the dies in order to form a point without a cavity at the tip. To ensure this occurs a billet that is initially longer than the final product is used. Once the tip is formed the excess material is cut-off by the sharp edges of the slug cut-off feature in the dwell section which is illustrated in Figure 1.11. Alternatively, to form a tip with a cavity

requires no excess material as shown in Figure 1.12. However, a die that includes the slug cut-off feature can be used to produce both cavity and non-cavity points.

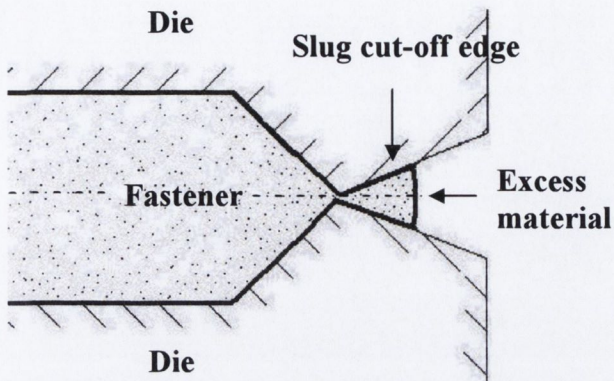


Figure 1.11 Fastener with excess material.

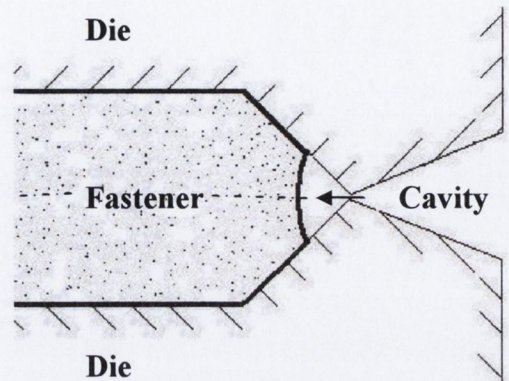


Figure 1.12 Cavity pointed fastener.

To enable the dies to grip and roll the fastener, a *rough* or *friction* surface, such as that produced by EDM (electro discharge machining), is required on the flat part of the die to provide enough grip in order to prevent interfacial slip, see Figure 1.13. Typically, this feature is machined from the start of the die to the end of the ramp section. Any imperfections i.e. rough surface indents can be ironed out in the dwell section.

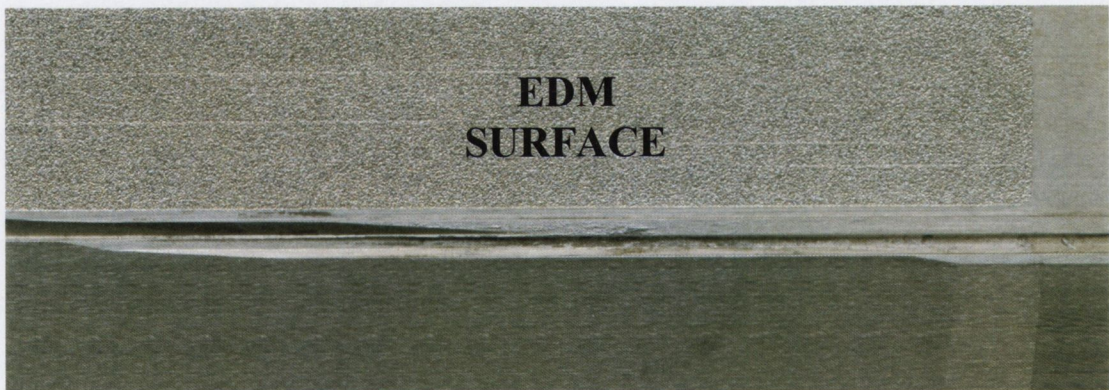


Figure 1.13 EDM die surface.

CHAPTER 2

LITERATURE REVIEW

CHAPTER 2

LITERATURE REVIEW

This chapter consists of an investigation into the literature available on the various modes of failure associated with the Form Rolling process. To date, literature on workpiece deformation is only available for the thread rolling and cross wedge rolling (CWR) processes. A review of these investigations will be given and then followed by a description of the modes of failure that are relevant to this study and the associated literature.

2.1 Workpiece Deformation

The following sections consist of a review of literature which is relevant to a flat die Form Rolling process. In particular, a detailed analysis of the various modes of failure found in rolled fasteners will be given.

2.1.1 Analysis of Contact Width and Pressure

To date, theoretical investigations to calculate the contact width and pressure have exclusively dealt with the CWR process. These parameters are important because they can be used to determine the forces and stresses exerted during the process. The determination of the contact pressure was then used to describe interfacial slip at the tool/workpiece contact zone. This will be discussed in the next section on defect mechanisms.

Smirnov [41], using a plane strain deformation model of a billet under compression, proposed that the contact width B , in a CWR process could be defined as:

$$B = \sqrt{2\Delta r(\Delta r + r)} \quad (2.1)$$

The contact width is dependent on the magnitude of the radial reduction Δr , as well as on the radius r of the blank (Figure 2.1).

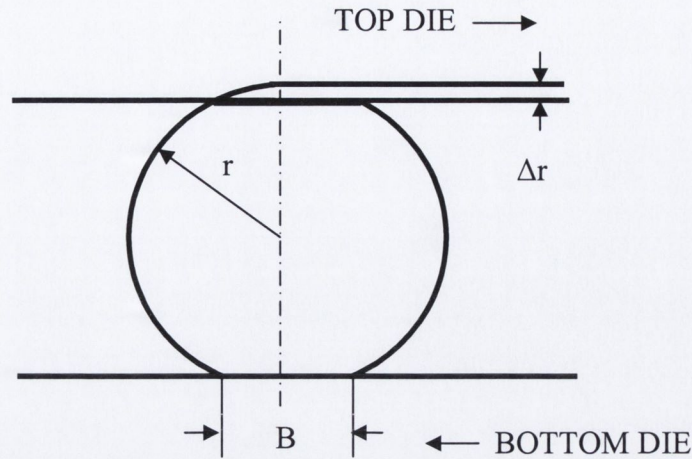


Figure 2.1 Contact width for a flat die Form Rolling process.

Pater and Weronki [42] referenced work carried out in Russia to determine the contact area (only available in Russian). They experimentally verified that their method was more accurate than previous investigations [43, 44, 45] over a certain range of parameters. From their investigation they deduced that the contact area was made up of contact on two planes (Figure 2.2). The parallel plane ABC corresponds to the *stretching* zone and the inclined plane BCDE corresponds to deformation in the *forming* zone of a typical CWR workpiece.

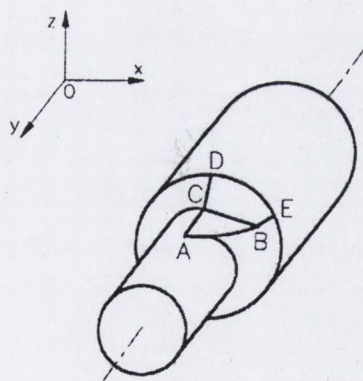


Figure 2.2 Contact surface on a workpiece for a CWR process [42].

Pater [46] assumed that the mean pressure in a CWR process is equal to the pressure in the reduction process of a round bar. The mean unit pressure was expressed as:

$$\frac{q_m}{\sigma_y} = \frac{2}{\sin \alpha (\delta_0 - 1)} \left(\ln \delta_0 + \frac{2}{\sqrt{3}} m_k \frac{l_0}{d} \right) + \frac{m}{\sqrt{3} \cos \alpha \sin 2\alpha} \frac{\delta_0^2 + 1}{\delta_0^2} \quad (2.2)$$

where q_m is the mean unit pressure, σ_y the yield stress of the workpiece material, α the forming angle, δ_0 the original billet diameter d_0 divided by the final product diameter d , m_k the shear friction factor on the sizing surface, m the shear friction factor on the conical surface and l_0 the length of contact between the tool and the workpiece on the finishing surface. Based on this assumption, he compared the Energy Method to the solutions predicted by the Upper Bound Method for the mean pressure between a tool and workpiece in a CWR process. He found that the Upper Bound solutions overestimated the mean pressure whereas the Energy Method underestimated the mean pressure for a forming angle, α , ranging from 20° to 50°.

Dong *et al* [47], using the finite element package ANSYS/LS-DYNA, compared finite element results to those obtained by Pater [46] using equation 2.2 above. Their FE results showed that the percentage area reduction increases as the contact pressure increases. However, Pater's expression contradicted this and showed that the contact pressure reduced as the area reduction increased. Dong *et al* [47] attribute this discrepancy to the strain hardening effect on the workpiece material in their FE model.

2.1.2 Workpiece Defect Mechanisms

Form Rolling is such a difficult manufacturing process because of the number of different variables that can cause failure of the finished product. These can be divided into two categories: failure due to internal defects and failure due to surface defects (Figure 2.3).

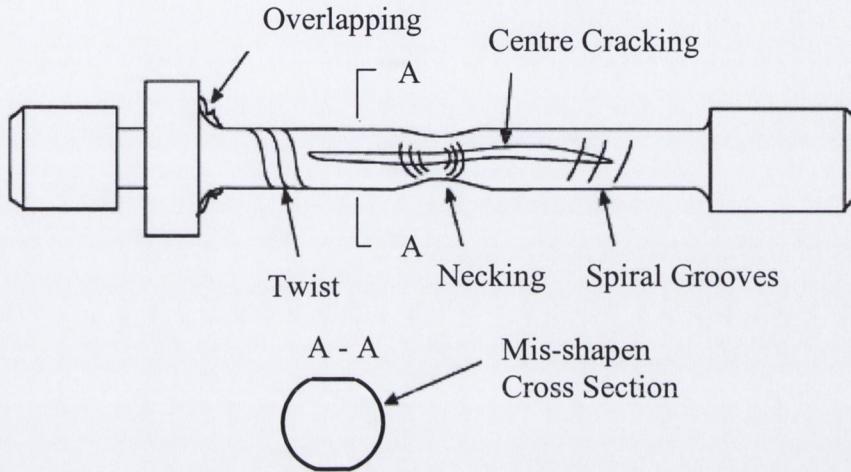


Figure 2.3 Modes of failure [48].

Internal Defects

Thompson and Hawkyard [49] surmised that internal defects included voids, cavities and cracks within the workpiece. These failures can appear in a rolled fastener as either an axial [50] or annular fissure [51]. The particular mode of failure that occurs depends on the manufacturing process. Central voids appear along axis of fasteners rolled using two-roll or flat die machines while an annular fissure is generated in a three-roll machine process [49] [52] (Figure 2.4).

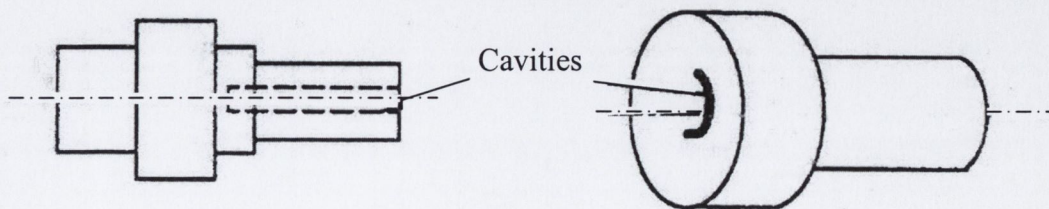


Figure 2.4 Central cavity in a three-roll process [16].

In Figure 2.5 (a) Tselikov [12] shows a typical slip line field for a workpiece rolled in a flat die machine under plane-strain conditions which shows the lines of maximum shear stress within the billet. The central portion is subjected to compression in the direction normal to the tool surface and to tension in the lateral direction. Internal failures occur in the central zone where from Figure 2.5 (b) the tensile stress is highest.

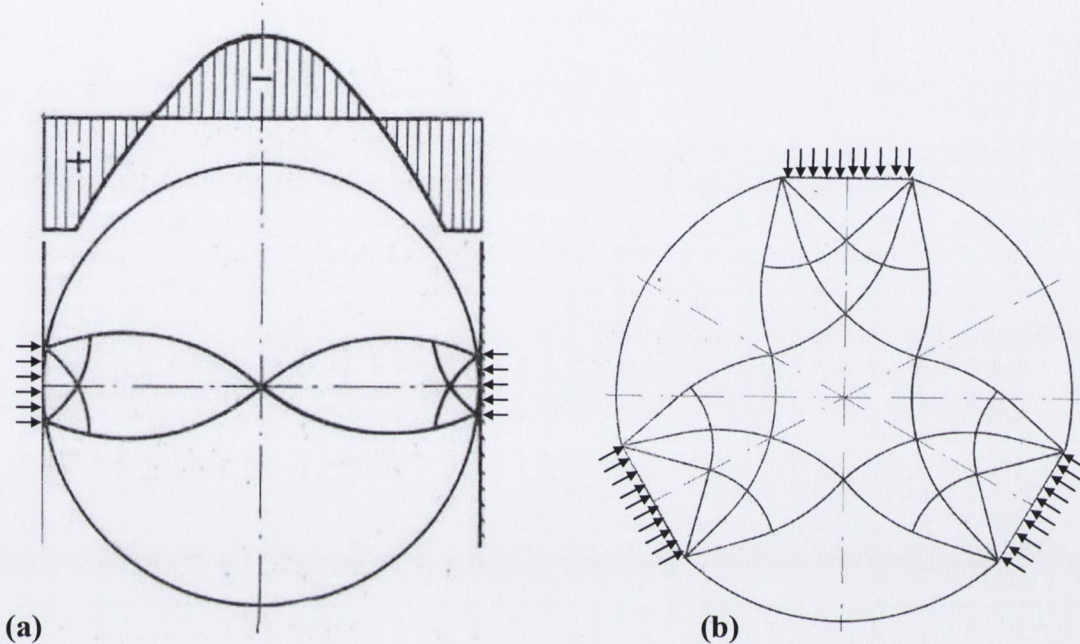


Figure 2.5 Slip line field for a (a) flat die and (b) three-roll process [12].

Similarly, Figure 2.5 (b) illustrates the slip line field for a three-roll process. A rigid core exists at the centre of the workpiece. Failure occurs outside the rigid core which subsequently propagates to form an annular fissure as illustrated in Figure 2.4.

Four theories have been put forward in an attempted to describe the cause of central cavities:

- Failure attributed to tensile stress
- Failure attributed to shear stress
- Failure caused by low cycle fatigue that develops during rolling
- Failure generated due to torsional effects on the billet

In 1960, Teterin and Luzin [50] describe Smirnov's [41] theory on the mechanism of failure in 2-roll cross rolling as being the most developed at that time. Teterin and Luzin summarised Smirnov's theory, where he attributed central cavitation to a combination of shear stress and tensile stress on the workpiece. This theory stated that the central portion of the workpiece is in a state of constant tension during diameter reduction. In the region where the diameter is reducing, the principal stresses, i.e. axial, radial and tangential stresses increase, however the differences between them decrease as hydrostatic conditions are approached. Consequently, plastic deformation is inhibited at the centre of the workpiece which develops a resilient core along its axis. Failure of the workpiece occurs when one of the principal stresses exceeds the brittle strength of the workpiece material. This theory was also supported by I.I. Kazanskaya *et al* [53] and Tselikov *et al* [51] who claimed, independently from each other, that brittle failure in the centre of a billet occurred because the maximum tensile stresses in the centre of the billet exceeded the yield strength of the material.

Smirnov [54] later altered his theory and proposed another definition which was based on experimental testing. He found that the critical reduction of the billet diameter at which axial rupture is initiated increases as the initial billet length is decreased. Therefore, in short billets failure occurs through shear because the influence of the axial stresses diminishes and promotes the development of shearing stresses.

Teterin and Luzin [50] showed that the occurrence of axial tension in the centre of a solid billet as its diameter is being reduced indicates the development of shear stresses in the axial zone. Teterin and Luzin [50] then examined an axial etched section of a solid billet with equal diameter to length ratio and observed that directly before failure a fine grain structure existed at the periphery and in the centre of the billet which indicated plastic deformation. They attributed the plastic deformation at the centre of the billet to large shear stresses which generate microcracks. These microcracks propagate during deformation and generate internal voids.

According to Danno and Tanaka [55, 56], Li *et al* [48], Fang *et al* [57] and Pater *et al* [58] central voids are caused by the radial or secondary tensile stress and the shear stress induced repeatedly at the central region of the billet during rolling, in a similar way to the Mannesmann rotary piercing method. This is a

manufacturing process whereby a billet of material is placed between rollers that compress the billet as it rotates. This has the effect of inducing large tensile and shear stresses in the centre of the billet which make it easier for a piercing tool to form a hollow seamless pipe. Consequently, all of the aforementioned authors describe the formation of central voids as the “*Mannesmann Effect*”. The stress state in the centre of the billet is the key factor of the *Mannesmann Effect*.

Fang *et al* [57] using the results of both FE and experimental analysis suggested that during rotation the billet undergoes changing states of stress i.e. alternating from compressive to tensile stress. With increasing rotations residual stress accumulates giving rise to a high stress concentration in the centre of the billet in particular. Fang *et al* found that the stress at the centre of the billet is tensile and is a large contributive factor to crack propagation and extension. They also state that hydrostatic stress is a key factor in metal failure. From their FEA results they noted that tensile hydrostatic stress occurs in the centre of the billet which would make it more susceptible to microcrack evolution.

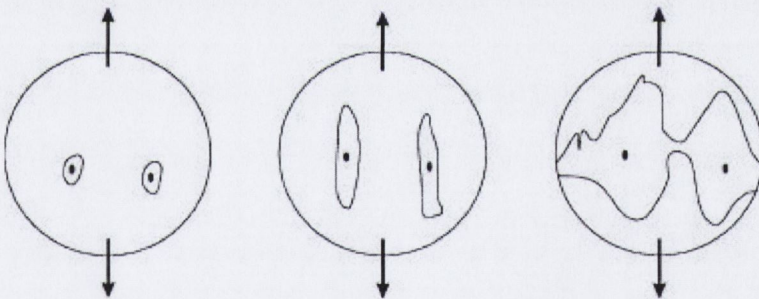


Figure 2.6 Void mechanism induced by tensile stress [48].

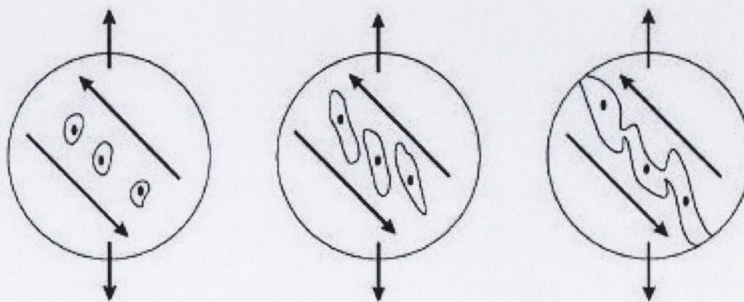


Figure 2.7 Void mechanism induced by shear stress [48].

Li *et al* [48], in a paper investigating the morphology of internal defects in a CWR process using cold aluminium billets attribute the *Mannesmann Effect* to both shear and tensile stresses. They found that by the end of the *knifing* stage a large void surrounded by small inclusions was found. However, by the end of the process a substantial large void was found which would indicate that void growth and bridging had occurred. Therefore, under radial deformation the small inclusions generate cracks. These cracks merge with cracks from other inclusions and create a macroscopic fracture. A large enough tensile stress can not only initiate void formation but can also accelerate void growth by opening matrix material in the direction of the highest principal stress. Micro-scale necking merges two inclusions when the distance between them is comparable to their lengths, as shown in Figure 2.6.

Using microscopic examination Li *et al* [48] claim that large tensile stresses are responsible for initiating void opening while shear stress determines the density and the size of voids within the workpiece. Under tensile stress, slip dislocation occurs between metal crystals [59]. The optimum angle for slip dislocation corresponds to the maximum shear flow angle of 45° to the maximum principal stress direction. Hence voids are generated in a direction 45° to the maximum principal stress direction and elongated by the shear stresses. As the slip deformation becomes more extensive, voids merge into a macroscopic fracture as illustrated in Figure 2.7.



Figure 2.8 Cruciform shape in a cross-section of an Aluminium CWR billet [48].

Li *et al* [48] observed from cross-sections which were through the portion of the billet with the least diameter, that a distinct cruciform shape occurred as illustrated in Figure 2.8. This characteristic cruciform shape is also shown by Danno and Awano [60] in a paper written in Japanese. Li *et al* [48] proposed that as the workpiece rotates the direction of plastic flow changes the shape of the crack as the workpiece rotates. As illustrated in Figure 2.9 the larger crack is generated in the direction of the maximum principal stress (σ_1) and elongates in the direction normal to the maximum principal stress due to tensile force in the principal direction. The smaller crack is generated by the second principal stress (σ_2).

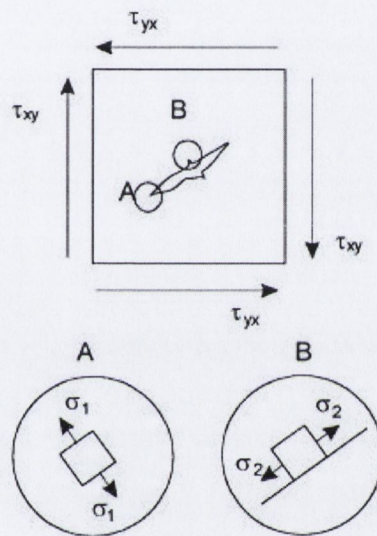


Figure 2.9 Illustration of crack generation [48].

Andreev [61] suggested that central cracking was attributed to low cycle fatigue due to the accumulation of tensile stresses induced by several rotations of the billet while rolling. He also proposed an equation to predict the number of load cycles till failure in a hot CWR process. This equation is dependant on the billet material, the tool geometry, the amount of diameter reduction and the starting rolling radius.

Fu and Dean [16] refer to a patent awarded to Guzavichus *et al* [62] where they maintain that torsion is associated with shear stress which can result in the generation of internal voids. In the case where a groove is impressed into a billet thereby reducing the diameter in that section, the relative velocities differ along the deformation zone which would lead to torsion of the billet. The difference between the velocities in the deformation zone increases, as does the relative

torsion and the associated shear stresses, with every rotation as the groove eventually reaches the required depth. Failure is initiated when the magnitude of the shear stresses exceeds the yield strength of the workpiece.

Surface Defects

In the following section it can be assumed that α and β are the forming and stretching angles, respectively, as described in the previous chapter.

According to Pater *et al* [58] the instability of a CWR process is revealed by the occurrence of certain surface defects which are illustrated in Figure 2.3, namely:

- Lapping
- Spiralling
- Necking
- Twisting
- Squaring
- Surface cracking

Nefedov *et al* [63] attributed lapping to tangential deformation which occurs when too much material per rotation is moved in the radial direction creating a large *wave form* of billet material which folds over itself as rolling progresses. Hayama [64] suggested limiting the relative area reduction, $\delta = d_0/d$, in order to prevent this defect:

$$\delta \geq 1 + \pi \tan \alpha \tan \beta \quad (2.3)$$

where the stability of the process is dependent on the forming and stretching angles.

Spiral grooves are a helical shaped indentation caused by the contact of a die edge as a desired geometry is Form Rolled. This defect is caused by the pressure of the dies on the workpiece and occurs in every Form Rolling process. Spiral grooves however can be ironed out in the dwell section of a die.

Necking is a failure mechanism predominantly experienced when forming grooves. The diameter of the billet thins due to the presence of an axial force [52].

Hu *et al* [34] stated that when the axial force exceeds the tensile strength of the billet material, necking will commence at the location of the smallest diameter. When a large stretching angle β is employed, the axial force increases as the groove widens causing large tensile stresses. Subsequently, necking occurs in a way similar to a standard tensile test specimen. Tsukamoto [65], as referred by Pater *et al* [58], determined that necking could be prevented by adhering to the following equation:

$$\frac{\sqrt{2 \tan \alpha \tan \beta}}{\pi} \left(1 + \sqrt{\frac{1}{\delta}} \right) (\delta - 1) \leq 0.2 \quad (2.4)$$

Based on force distributions occurring in a CWR process Pater *et al* [58] defined a limit condition for the occurrence of necking:

$$\frac{4\delta^2 q_m \cos \beta}{3\pi\sigma_y} \frac{\delta-1}{\delta} \sqrt{3c \frac{\delta-1}{\delta}} \times \left\{ \left(1 + \frac{\mu_b \sin \beta}{\tan \alpha} \right) \left[1 - \sqrt{\left(\frac{1+c\delta-c}{\delta} \right)^3} + c \frac{\delta-1}{\delta} \right] + \frac{\mu_k \sin \beta}{\tan \alpha} \left[\frac{3}{2}(c-1) + \sqrt{\frac{\delta+1}{2\delta}} \right] \right\} < 1 \quad (2.5)$$

where c is a shape parameter, σ_y is the yield stress, μ_b is the friction of the side of the tool and μ_k is the friction on the stretching surface of the tool.

In the case of any section of a fastener where the diameter is being reduced, the tooling imparts the same tangential velocity to the surface of all sections of the fastener. Twisting may occur because the diameters in the deformation zone vary, resulting in differing angular velocities throughout the deformation zone. Therefore, fasteners that require a large diameter reduction will experience greater torsion effects. Thompson and Hawkyard [49] stated that torsional effects combined with the axial force makes the fastener susceptible to torsion failure. Danno and Tanaka [56] performed squeeze-rolled tests using hot steel shafts and measured the angle of torsional deformation. They found that with a reduction in area of 80% the angle of twist, ϕ , can be as large as 100°. The typical torsional deformation they described is shown in Figure 2.10 below.

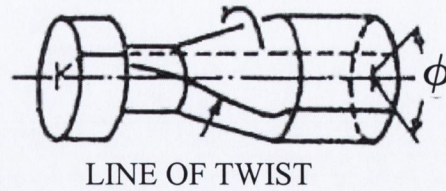


Figure 2.10 Torsional deformation of a squeeze-rolled shaft [56].

Another failure mechanism in the Form Rolling process is squaring. Squaring is a direct consequence of slipping between the interface of the workpiece and the dies. Figure 2.3 illustrates the undesirable cross-section shape of a “squared” workpiece where the opposite sides have been flattened to produce a truncated square shape. When a billet rotates between two dies the tangential force, P_x , is less than the friction force (Figure 2.11). However, when slipping occurs the tangential force acting on the workpiece is larger than the friction force. The workpiece stops rotating and is continuously compressed between the dies until the stroke of the machine is complete.

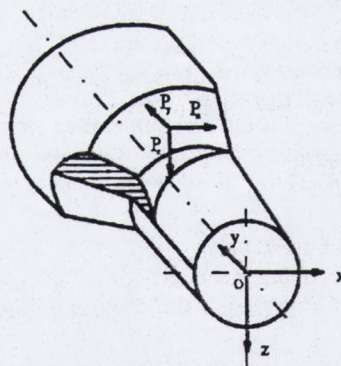


Figure 2.11 Rolling force components on a workpiece [16].

Hayama [64] defined a slip-free process using the following empirical equation:

$$(0.15 + 0.0038\alpha)\beta^{0.925} \leq 1.93 \quad (2.6)$$

where the friction coefficient is assumed to be constant, $\mu=0.35$.

Pater *et al* [58] defined two equations to determine process stability in view of slipping depending on a parameter labelled *rolling itch* which is defined by the following expression:

$$c = \frac{\pi\delta \tan \alpha \tan \beta}{\delta - 1} \quad (2.7)$$

So, for a CWR process where $c \leq 1$ the process stability can be defined as:

$$\begin{aligned} & \frac{1}{\delta^3} \sqrt{1+c} \frac{\delta-1}{2} \left[\frac{2}{3} \mu_k (c\delta - c)^{3/2} - \frac{\sqrt{3}}{4} \sqrt{1+c} \frac{\delta-1}{2} \left(c \frac{\delta-1}{\delta} \right)^2 \right] \\ & + \left(\frac{\tan \alpha \tan \beta}{\cos \beta} + \mu_b \right) \sqrt{c \frac{\delta-1}{\delta}} \left\{ \frac{2}{5} \left[1 - \left(\frac{c\delta - c + 1}{\delta} \right)^{5/2} \right] - \frac{2}{3} \left(\frac{c\delta - c}{\delta} \right)^{3/2} - \frac{2}{5} \left(\frac{c\delta - c}{\delta} \right)^{5/2} \right\} \\ & - \frac{\sqrt{3}}{4} (1 - \mu_b \sin \beta \tan \alpha) \left(\frac{\delta-1}{\delta} \right)^2 \frac{c}{\delta} \left\{ \left[\delta(1-c^2) - c(2+c) + 1 \right] + c^2 \right\} \geq 0 \end{aligned} \quad (2.8)$$

And if $c > 1$ then:

$$\begin{aligned} & \frac{\mu_k}{\delta} \left(\frac{\sqrt{2}}{3} \sqrt{\frac{\delta+1}{\delta}} + c - 1 \right) - \frac{\sqrt{3}}{2} \sqrt{\frac{\delta-1}{\delta}} \left[\frac{\delta+1}{4\delta} + c - \frac{1}{2} (1 + \mu_b \sin \beta \tan \alpha) \right] \\ & + \left(\frac{\tan \alpha \tan \beta}{\cos \beta} + \mu_b \right) \frac{8\delta + 2}{15\delta} \geq 0 \end{aligned} \quad (2.9)$$

where $\mu_k = 0.2$ and $\mu_b = 0.4$.

Dong *et al* [66] compared experimental results to a 3D finite element model generated using the ANSYS/LS-DYNA program. Interfacial slip, S , was defined as the difference between the tool translation and the workpiece rotation:

$$S = \frac{u_t - u_w}{\pi d_0} \quad (2.10)$$

where d_0 is the original billet diameter, u_t is the linear tool displacement and u_w is the linear displacement of the workpiece defined as:

$$u_w = \frac{\pi d_0 \theta}{360} \quad (2.11)$$

where θ is the angular rotation of the workpiece in degrees. Results illustrated that interfacial slip reduced for decreasing area reduction i.e. as the contact area increased the propensity for slipping to occur decreased.

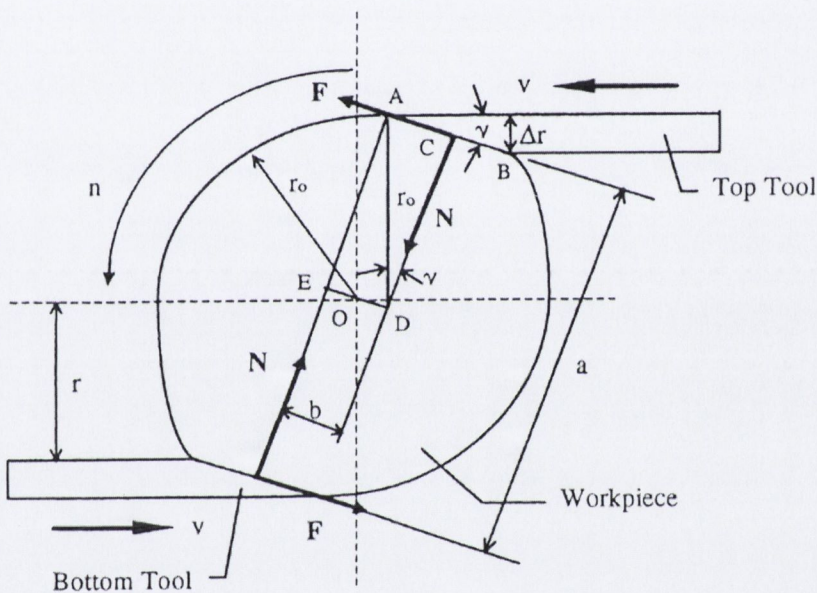


Figure 2.12 Free-body diagram of a CWR process [67].

Dong *et al* [67] compared FE results, from their paper mentioned previously [66], to a theoretical expression they derived to predict the onset of interfacial slip. This expression was derived using a 2D force analysis model illustrated in Figure 2.12. It is assumed there is a constant coefficient of friction, μ , over the entire contact area and that there is slipping friction, F , over this surface. Hence:

$$F = \mu N \quad (2.12)$$

From the free-body diagram Dong *et al* [67], derived the critical friction coefficient, i.e. the friction coefficient required to induce rotation, as:

$$\mu \geq \frac{1}{2} \left(\frac{2}{\Delta r/r_0} - 1 \right)^{\frac{1}{2}} \quad (2.13)$$

Eq. (2.10) can be rewritten to get:

$$\frac{\Delta r}{r_0} \leq \frac{8\mu^2}{1 + 4\mu^2} \quad (2.14)$$

The area reduction is expressed as:

$$\Delta_A = (A_0 - A)/A_0 = 1 - (r/r_0)^2 \quad (2.15)$$

Therefore, the maximum area reduction rate can be related to the friction coefficient with the following expression:

$$(\Delta_A)_{\max} = \frac{16\mu^2}{(1 + 4\mu^2)^2} \quad (2.16)$$

It should also be noted from the free body diagram above, that the direction of the two normal forces, N , and the two frictional forces, F , are dependent on the inclined angle, γ .

From Eq. (2.14), a relationship between a maximum area reduction for a given friction coefficient can be obtained where the greater the area reduction, the greater the friction coefficient required to prevent slipping occurring.

Thompson and Hawkyard [49] performed experiments using plasticine clay billets with radial inserts on a two-roll and three-roll Mannesmann piercing mills without the piercer. They observed that there was significant shear deformation through the whole section of the billet. Figures 2.13 (a) and (b) show the deformation of the radial inserts of the two-roll and three-roll mills respectively.

Danno *et al* [56, 60] performed similar tests to Thompson and Hawkyard [49] using plasticine billets for a three-roll process with similar findings.

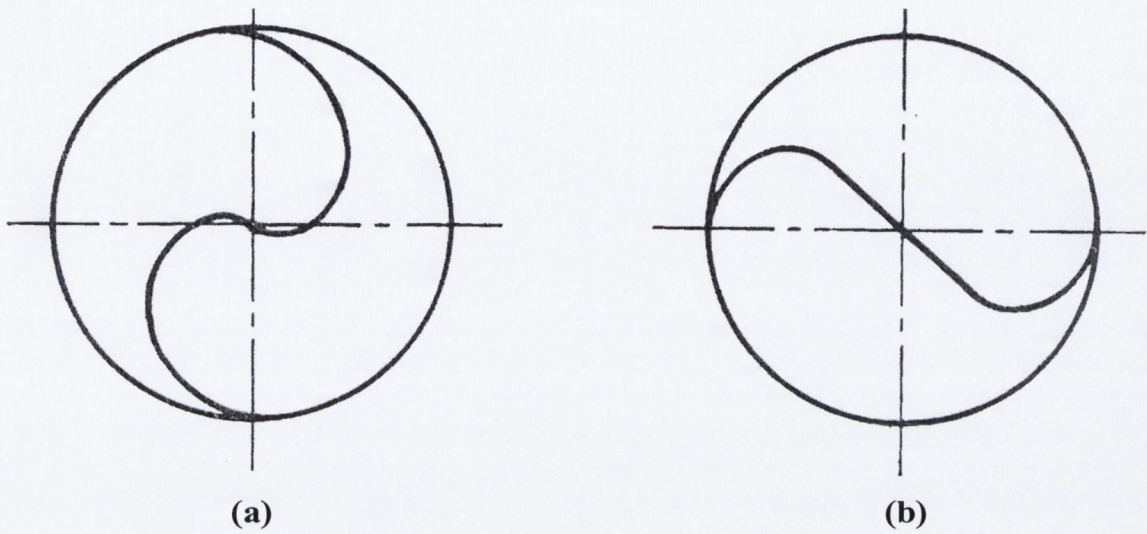


Figure 2.13 Shear deformation of radial insert in plasticine clay on (a) two-roll and (b) three-roll Mannesmann mills [49].

CHAPTER 2

LITERATURE REVIEW

This chapter consists of an investigation into the literature available on the various modes of failure associated with the Form Rolling process. To date, literature on workpiece deformation is only available for the thread rolling and cross wedge rolling (CWR) processes. A review of these investigations will be given and then followed by a description of the modes of failure that are relevant to this study and the associated literature.

2.1 Workpiece Deformation

The following sections consist of a review of literature which is relevant to a flat die Form Rolling process. In particular, a detailed analysis of the various modes of failure found in rolled fasteners will be given.

2.1.1 Analysis of Contact Width and Pressure

To date, theoretical investigations to calculate the contact width and pressure have exclusively dealt with the CWR process. These parameters are important because they can be used to determine the forces and stresses exerted during the process. The determination of the contact pressure was then used to describe interfacial slip at the tool/workpiece contact zone. This will be discussed in the next section on defect mechanisms.

Smirnov [41], using a plane strain deformation model of a billet under compression, proposed that the contact width B , in a CWR process could be defined as:

$$B = \sqrt{2\Delta r(\Delta r + r)} \quad (2.1)$$

The contact width is dependent on the magnitude of the radial reduction Δr , as well as on the radius r of the blank (Figure 2.1).

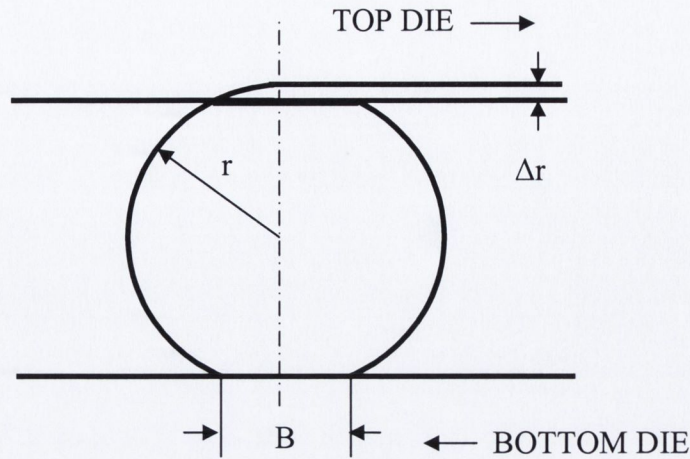


Figure 2.1 Contact width for a flat die Form Rolling process.

Pater and Weronki [42] referenced work carried out in Russia to determine the contact area (only available in Russian). They experimentally verified that their method was more accurate than previous investigations [43, 44, 45] over a certain range of parameters. From their investigation they deduced that the contact area was made up of contact on two planes (Figure 2.2). The parallel plane ABC corresponds to the *stretching* zone and the inclined plane BCDE corresponds to deformation in the *forming* zone of a typical CWR workpiece.

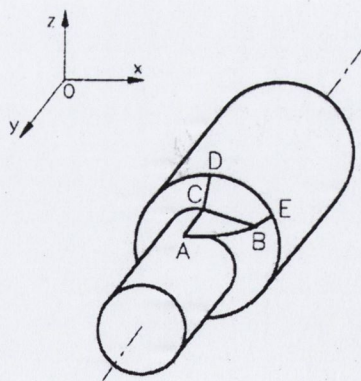


Figure 2.2 Contact surface on a workpiece for a CWR process [42].

Pater [46] assumed that the mean pressure in a CWR process is equal to the pressure in the reduction process of a round bar. The mean unit pressure was expressed as:

$$\frac{q_m}{\sigma_y} = \frac{2}{\sin \alpha (\delta_0 - 1)} \left(\ln \delta_0 + \frac{2}{\sqrt{3}} m_k \frac{l_0}{d} \right) + \frac{m}{\sqrt{3} \cos \alpha \sin 2\alpha} \frac{\delta_0^2 + 1}{\delta_0^2} \quad (2.2)$$

where q_m is the mean unit pressure, σ_y the yield stress of the workpiece material, α the forming angle, δ_0 the original billet diameter d_0 divided by the final product diameter d , m_k the shear friction factor on the sizing surface, m the shear friction factor on the conical surface and l_0 the length of contact between the tool and the workpiece on the finishing surface. Based on this assumption, he compared the Energy Method to the solutions predicted by the Upper Bound Method for the mean pressure between a tool and workpiece in a CWR process. He found that the Upper Bound solutions overestimated the mean pressure whereas the Energy Method underestimated the mean pressure for a forming angle, α , ranging from 20° to 50°.

Dong *et al* [47], using the finite element package ANSYS/LS-DYNA, compared finite element results to those obtained by Pater [46] using equation 2.2 above. Their FE results showed that the percentage area reduction increases as the contact pressure increases. However, Pater's expression contradicted this and showed that the contact pressure reduced as the area reduction increased. Dong *et al* [47] attribute this discrepancy to the strain hardening effect on the workpiece material in their FE model.

2.1.2 Workpiece Defect Mechanisms

Form Rolling is such a difficult manufacturing process because of the number of different variables that can cause failure of the finished product. These can be divided into two categories: failure due to internal defects and failure due to surface defects (Figure 2.3).

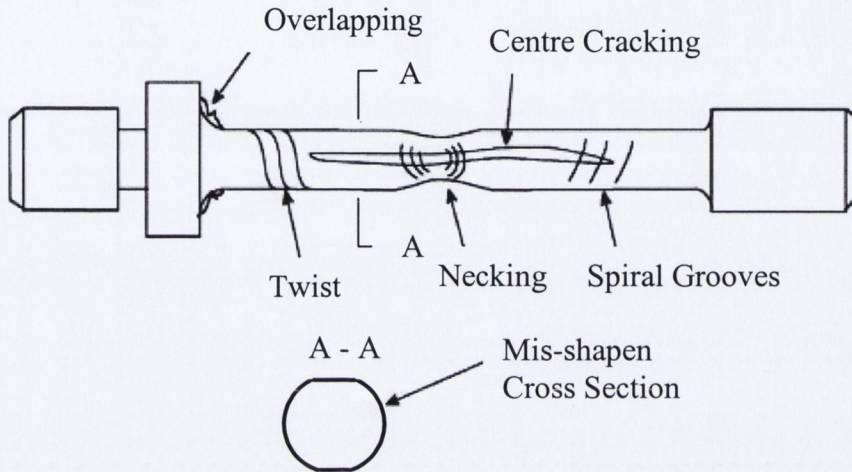


Figure 2.3 Modes of failure [48].

Internal Defects

Thompson and Hawkyard [49] surmised that internal defects included voids, cavities and cracks within the workpiece. These failures can appear in a rolled fastener as either an axial [50] or annular fissure [51]. The particular mode of failure that occurs depends on the manufacturing process. Central voids appear along axis of fasteners rolled using two-roll or flat die machines while an annular fissure is generated in a three-roll machine process [49] [52] (Figure 2.4).

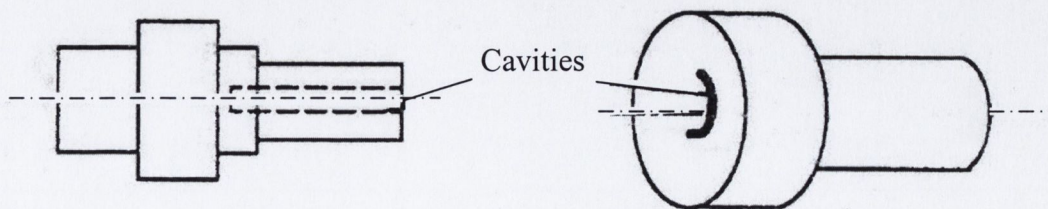


Figure 2.4 Central cavity in a three-roll process [16].

In Figure 2.5 (a) Tselikov [12] shows a typical slip line field for a workpiece rolled in a flat die machine under plane-strain conditions which shows the lines of maximum shear stress within the billet. The central portion is subjected to compression in the direction normal to the tool surface and to tension in the lateral direction. Internal failures occur in the central zone where from Figure 2.5 (b) the tensile stress is highest.

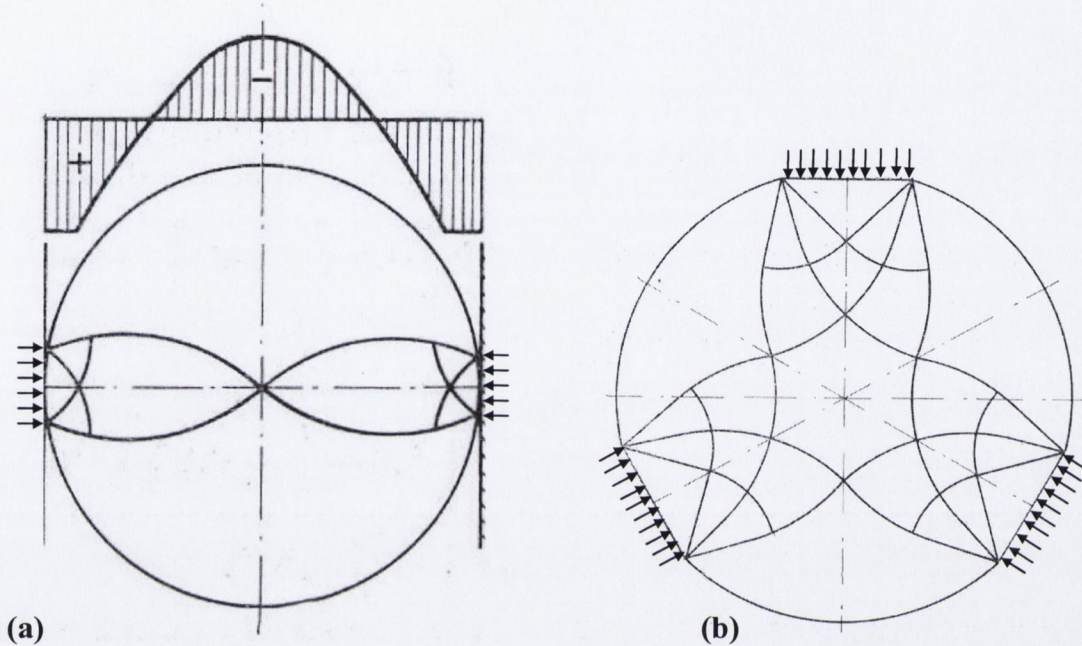


Figure 2.5 Slip line field for a (a) flat die and (b) three-roll process [12].

Similarly, Figure 2.5 (b) illustrates the slip line field for a three-roll process. A rigid core exists at the centre of the workpiece. Failure occurs outside the rigid core which subsequently propagates to form an annular fissure as illustrated in Figure 2.4.

Four theories have been put forward in an attempted to describe the cause of central cavities:

- Failure attributed to tensile stress
- Failure attributed to shear stress
- Failure caused by low cycle fatigue that develops during rolling
- Failure generated due to torsional effects on the billet

In 1960, Teterin and Luzin [50] describe Smirnov's [41] theory on the mechanism of failure in 2-roll cross rolling as being the most developed at that time. Teterin and Luzin summarised Smirnov's theory, where he attributed central cavitation to a combination of shear stress and tensile stress on the workpiece. This theory stated that the central portion of the workpiece is in a state of constant tension during diameter reduction. In the region where the diameter is reducing, the principal stresses, i.e. axial, radial and tangential stresses increase, however the differences between them decrease as hydrostatic conditions are approached. Consequently, plastic deformation is inhibited at the centre of the workpiece which develops a resilient core along its axis. Failure of the workpiece occurs when one of the principal stresses exceeds the brittle strength of the workpiece material. This theory was also supported by I.I. Kazanskaya *et al* [53] and Tselikov *et al* [51] who claimed, independently from each other, that brittle failure in the centre of a billet occurred because the maximum tensile stresses in the centre of the billet exceeded the yield strength of the material.

Smirnov [54] later altered his theory and proposed another definition which was based on experimental testing. He found that the critical reduction of the billet diameter at which axial rupture is initiated increases as the initial billet length is decreased. Therefore, in short billets failure occurs through shear because the influence of the axial stresses diminishes and promotes the development of shearing stresses.

Teterin and Luzin [50] showed that the occurrence of axial tension in the centre of a solid billet as its diameter is being reduced indicates the development of shear stresses in the axial zone. Teterin and Luzin [50] then examined an axial etched section of a solid billet with equal diameter to length ratio and observed that directly before failure a fine grain structure existed at the periphery and in the centre of the billet which indicated plastic deformation. They attributed the plastic deformation at the centre of the billet to large shear stresses which generate microcracks. These microcracks propagate during deformation and generate internal voids.

According to Danno and Tanaka [55, 56], Li *et al* [48], Fang *et al* [57] and Pater *et al* [58] central voids are caused by the radial or secondary tensile stress and the shear stress induced repeatedly at the central region of the billet during rolling, in a similar way to the Mannesmann rotary piercing method. This is a

manufacturing process whereby a billet of material is placed between rollers that compress the billet as it rotates. This has the effect of inducing large tensile and shear stresses in the centre of the billet which make it easier for a piercing tool to form a hollow seamless pipe. Consequently, all of the aforementioned authors describe the formation of central voids as the “*Mannesmann Effect*”. The stress state in the centre of the billet is the key factor of the *Mannesmann Effect*.

Fang *et al* [57] using the results of both FE and experimental analysis suggested that during rotation the billet undergoes changing states of stress i.e. alternating from compressive to tensile stress. With increasing rotations residual stress accumulates giving rise to a high stress concentration in the centre of the billet in particular. Fang *et al* found that the stress at the centre of the billet is tensile and is a large contributive factor to crack propagation and extension. They also state that hydrostatic stress is a key factor in metal failure. From their FEA results they noted that tensile hydrostatic stress occurs in the centre of the billet which would make it more susceptible to microcrack evolution.

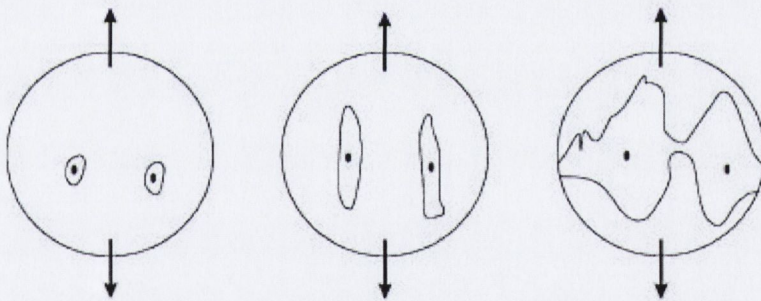


Figure 2.6 Void mechanism induced by tensile stress [48].

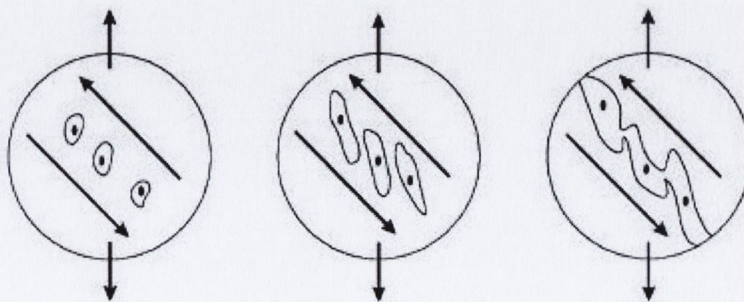


Figure 2.7 Void mechanism induced by shear stress [48].

Li *et al* [48], in a paper investigating the morphology of internal defects in a CWR process using cold aluminium billets attribute the *Mannesmann Effect* to both shear and tensile stresses. They found that by the end of the *knifing* stage a large void surrounded by small inclusions was found. However, by the end of the process a substantial large void was found which would indicate that void growth and bridging had occurred. Therefore, under radial deformation the small inclusions generate cracks. These cracks merge with cracks from other inclusions and create a macroscopic fracture. A large enough tensile stress can not only initiate void formation but can also accelerate void growth by opening matrix material in the direction of the highest principal stress. Micro-scale necking merges two inclusions when the distance between them is comparable to their lengths, as shown in Figure 2.6.

Using microscopic examination Li *et al* [48] claim that large tensile stresses are responsible for initiating void opening while shear stress determines the density and the size of voids within the workpiece. Under tensile stress, slip dislocation occurs between metal crystals [59]. The optimum angle for slip dislocation corresponds to the maximum shear flow angle of 45° to the maximum principal stress direction. Hence voids are generated in a direction 45° to the maximum principal stress direction and elongated by the shear stresses. As the slip deformation becomes more extensive, voids merge into a macroscopic fracture as illustrated in Figure 2.7.



Figure 2.8 Cruciform shape in a cross-section of an Aluminium CWR billet [48].

Li *et al* [48] observed from cross-sections which were through the portion of the billet with the least diameter, that a distinct cruciform shape occurred as illustrated in Figure 2.8. This characteristic cruciform shape is also shown by Danno and Awano [60] in a paper written in Japanese. Li *et al* [48] proposed that as the workpiece rotates the direction of plastic flow changes the shape of the crack as the workpiece rotates. As illustrated in Figure 2.9 the larger crack is generated in the direction of the maximum principal stress (σ_1) and elongates in the direction normal to the maximum principal stress due to tensile force in the principal direction. The smaller crack is generated by the second principal stress (σ_2).

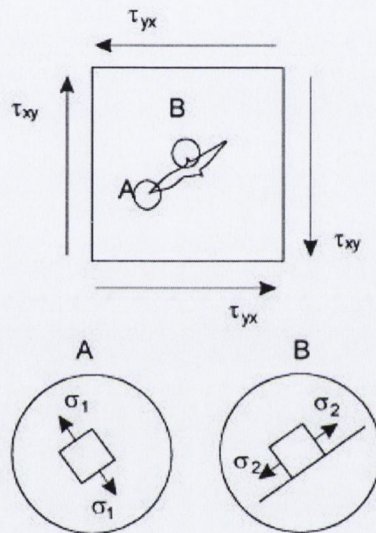


Figure 2.9 Illustration of crack generation [48].

Andreev [61] suggested that central cracking was attributed to low cycle fatigue due to the accumulation of tensile stresses induced by several rotations of the billet while rolling. He also proposed an equation to predict the number of load cycles till failure in a hot CWR process. This equation is dependant on the billet material, the tool geometry, the amount of diameter reduction and the starting rolling radius.

Fu and Dean [16] refer to a patent awarded to Guzavichus *et al* [62] where they maintain that torsion is associated with shear stress which can result in the generation of internal voids. In the case where a groove is impressed into a billet thereby reducing the diameter in that section, the relative velocities differ along the deformation zone which would lead to torsion of the billet. The difference between the velocities in the deformation zone increases, as does the relative

torsion and the associated shear stresses, with every rotation as the groove eventually reaches the required depth. Failure is initiated when the magnitude of the shear stresses exceeds the yield strength of the workpiece.

Surface Defects

In the following section it can be assumed that α and β are the forming and stretching angles, respectively, as described in the previous chapter.

According to Pater *et al* [58] the instability of a CWR process is revealed by the occurrence of certain surface defects which are illustrated in Figure 2.3, namely:

- Lapping
- Spiralling
- Necking
- Twisting
- Squaring
- Surface cracking

Nefedov *et al* [63] attributed lapping to tangential deformation which occurs when too much material per rotation is moved in the radial direction creating a large *wave form* of billet material which folds over itself as rolling progresses. Hayama [64] suggested limiting the relative area reduction, $\delta = d_0/d$, in order to prevent this defect:

$$\delta \geq 1 + \pi \tan \alpha \tan \beta \quad (2.3)$$

where the stability of the process is dependent on the forming and stretching angles.

Spiral grooves are a helical shaped indentation caused by the contact of a die edge as a desired geometry is Form Rolled. This defect is caused by the pressure of the dies on the workpiece and occurs in every Form Rolling process. Spiral grooves however can be ironed out in the dwell section of a die.

Necking is a failure mechanism predominantly experienced when forming grooves. The diameter of the billet thins due to the presence of an axial force [52].

Hu *et al* [34] stated that when the axial force exceeds the tensile strength of the billet material, necking will commence at the location of the smallest diameter. When a large stretching angle β is employed, the axial force increases as the groove widens causing large tensile stresses. Subsequently, necking occurs in a way similar to a standard tensile test specimen. Tsukamoto [65], as referred by Pater *et al* [58], determined that necking could be prevented by adhering to the following equation:

$$\frac{\sqrt{2 \tan \alpha \tan \beta}}{\pi} \left(1 + \sqrt{\frac{1}{\delta}} \right) (\delta - 1) \leq 0.2 \quad (2.4)$$

Based on force distributions occurring in a CWR process Pater *et al* [58] defined a limit condition for the occurrence of necking:

$$\frac{4\delta^2 q_m}{3\pi\sigma_y} \cos \beta \frac{\delta-1}{\delta} \sqrt{3c \frac{\delta-1}{\delta}} \times \left\{ \left(1 + \frac{\mu_b \sin \beta}{\tan \alpha} \right) \left[1 - \sqrt{\left(\frac{1+c\delta-c}{\delta} \right)^3} + c \frac{\delta-1}{\delta} \right] + \frac{\mu_k \sin \beta}{\tan \alpha} \left[\frac{3}{2}(c-1) + \sqrt{\frac{\delta+1}{2\delta}} \right] \right\} < 1 \quad (2.5)$$

where c is a shape parameter, σ_y is the yield stress, μ_b is the friction of the side of the tool and μ_k is the friction on the stretching surface of the tool.

In the case of any section of a fastener where the diameter is being reduced, the tooling imparts the same tangential velocity to the surface of all sections of the fastener. Twisting may occur because the diameters in the deformation zone vary, resulting in differing angular velocities throughout the deformation zone. Therefore, fasteners that require a large diameter reduction will experience greater torsion effects. Thompson and Hawkyard [49] stated that torsional effects combined with the axial force makes the fastener susceptible to torsion failure. Danno and Tanaka [56] performed squeeze-rolled tests using hot steel shafts and measured the angle of torsional deformation. They found that with a reduction in area of 80% the angle of twist, ϕ , can be as large as 100°. The typical torsional deformation they described is shown in Figure 2.10 below.

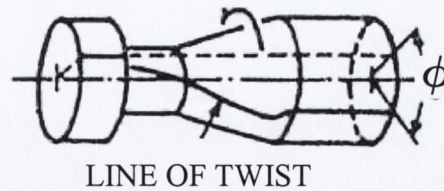


Figure 2.10 Torsional deformation of a squeeze-rolled shaft [56].

Another failure mechanism in the Form Rolling process is squaring. Squaring is a direct consequence of slipping between the interface of the workpiece and the dies. Figure 2.3 illustrates the undesirable cross-section shape of a “squared” workpiece where the opposite sides have been flattened to produce a truncated square shape. When a billet rotates between two dies the tangential force, P_x , is less than the friction force (Figure 2.11). However, when slipping occurs the tangential force acting on the workpiece is larger than the friction force. The workpiece stops rotating and is continuously compressed between the dies until the stroke of the machine is complete.

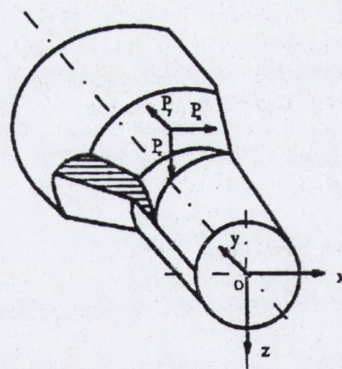


Figure 2.11 Rolling force components on a workpiece [16].

Hayama [64] defined a slip-free process using the following empirical equation:

$$(0.15 + 0.0038\alpha)\beta^{0.925} \leq 1.93 \quad (2.6)$$

where the friction coefficient is assumed to be constant, $\mu=0.35$.

Pater *et al* [58] defined two equations to determine process stability in view of slipping depending on a parameter labelled *rolling itch* which is defined by the following expression:

$$c = \frac{\pi\delta \tan \alpha \tan \beta}{\delta - 1} \quad (2.7)$$

So, for a CWR process where $c \leq 1$ the process stability can be defined as:

$$\begin{aligned} & \frac{1}{\delta^3} \sqrt{1+c} \frac{\delta-1}{2} \left[\frac{2}{3} \mu_k (c\delta - c)^{3/2} - \frac{\sqrt{3}}{4} \sqrt{1+c} \frac{\delta-1}{2} \left(c \frac{\delta-1}{\delta} \right)^2 \right] \\ & + \left(\frac{\tan \alpha \tan \beta}{\cos \beta} + \mu_b \right) \sqrt{c \frac{\delta-1}{\delta}} \left\{ \frac{2}{5} \left[1 - \left(\frac{c\delta - c + 1}{\delta} \right)^{5/2} \right] - \frac{2}{3} \left(\frac{c\delta - c}{\delta} \right)^{3/2} - \frac{2}{5} \left(\frac{c\delta - c}{\delta} \right)^{5/2} \right\} \\ & - \frac{\sqrt{3}}{4} (1 - \mu_b \sin \beta \tan \alpha) \left(\frac{\delta-1}{\delta} \right)^2 \frac{c}{\delta} \left\{ \delta(1-c^2) - c(2+c) + 1 \right\} + c^2 \geq 0 \end{aligned} \quad (2.8)$$

And if $c > 1$ then:

$$\begin{aligned} & \frac{\mu_k}{\delta} \left(\frac{\sqrt{2}}{3} \sqrt{\frac{\delta+1}{\delta}} + c - 1 \right) - \frac{\sqrt{3}}{2} \sqrt{\frac{\delta-1}{\delta}} \left[\frac{\delta+1}{4\delta} + c - \frac{1}{2} (1 + \mu_b \sin \beta \tan \alpha) \right] \\ & + \left(\frac{\tan \alpha \tan \beta}{\cos \beta} + \mu_b \right) \frac{8\delta + 2}{15\delta} \geq 0 \end{aligned} \quad (2.9)$$

where $\mu_k = 0.2$ and $\mu_b = 0.4$.

Dong *et al* [66] compared experimental results to a 3D finite element model generated using the ANSYS/LS-DYNA program. Interfacial slip, S , was defined as the difference between the tool translation and the workpiece rotation:

$$S = \frac{u_t - u_w}{\pi d_0} \quad (2.10)$$

where d_0 is the original billet diameter, u_t is the linear tool displacement and u_w is the linear displacement of the workpiece defined as:

$$u_w = \frac{\pi d_0 \theta}{360} \quad (2.11)$$

where θ is the angular rotation of the workpiece in degrees. Results illustrated that interfacial slip reduced for decreasing area reduction i.e. as the contact area increased the propensity for slipping to occur decreased.

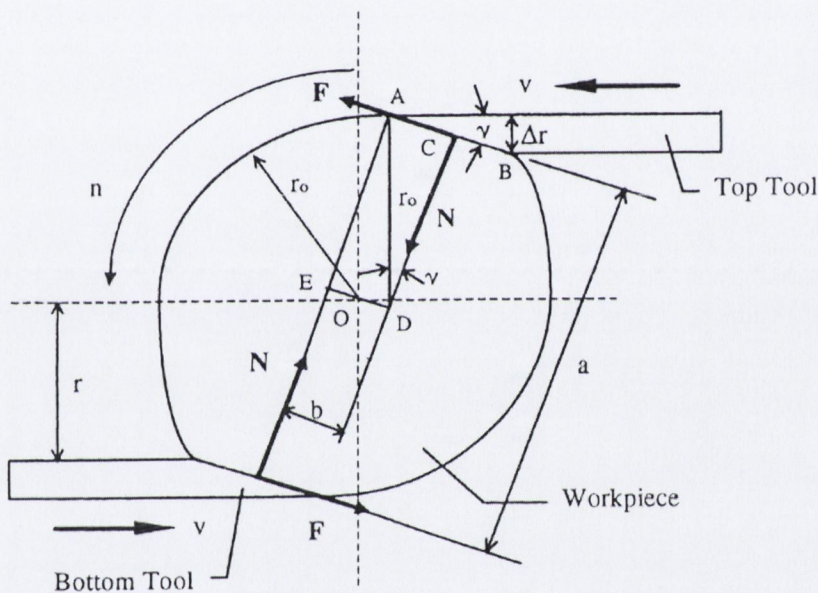


Figure 2.12 Free-body diagram of a CWR process [67].

Dong *et al* [67] compared FE results, from their paper mention previously [66], to a theoretical expression they derived to predict the onset of interfacial slip. This expression was derived using a 2D force analysis model illustrated in Figure 2.12. It is assumed there is a constant coefficient of friction, μ , over the entire contact area and that there is slipping friction, F , over this surface. Hence:

$$F = \mu N \quad (2.12)$$

From the free-body diagram Dong *et al* [67], derived the critical friction coefficient, i.e. the friction coefficient required to induce rotation, as:

$$\mu \geq \frac{1}{2} \left(\frac{2}{\Delta r/r_0} - 1 \right)^{-\frac{1}{2}} \quad (2.13)$$

Eq. (2.10) can be rewritten to get:

$$\frac{\Delta r}{r_0} \leq \frac{8\mu^2}{1+4\mu^2} \quad (2.14)$$

The area reduction is expressed as:

$$\Delta_A = (A_0 - A)/A_0 = 1 - (r/r_0)^2 \quad (2.15)$$

Therefore, the maximum area reduction rate can be related to the friction coefficient with the following expression:

$$(\Delta_A)_{\max} = \frac{16\mu^2}{(1+4\mu^2)^2} \quad (2.16)$$

It should also be noted from the free body diagram above, that the direction of the two normal forces, N , and the two frictional forces, F , are dependent on the inclined angle, γ .

From Eq. (2.14), a relationship between a maximum area reduction for a given friction coefficient can be obtained where the greater the area reduction, the greater the friction coefficient required to prevent slipping occurring.

Thompson and Hawkyard [49] performed experiments using plasticine clay billets with radial inserts on a two-roll and three-roll Mannesmann piercing mills without the piercer. They observed that there was significant shear deformation through the whole section of the billet. Figures 2.13 (a) and (b) show the deformation of the radial inserts of the two-roll and three-roll mills respectively.

Danno *et al* [56, 60] performed similar tests to Thompson and Hawkyard [49] using plasticine billets for a three-roll process with similar findings.

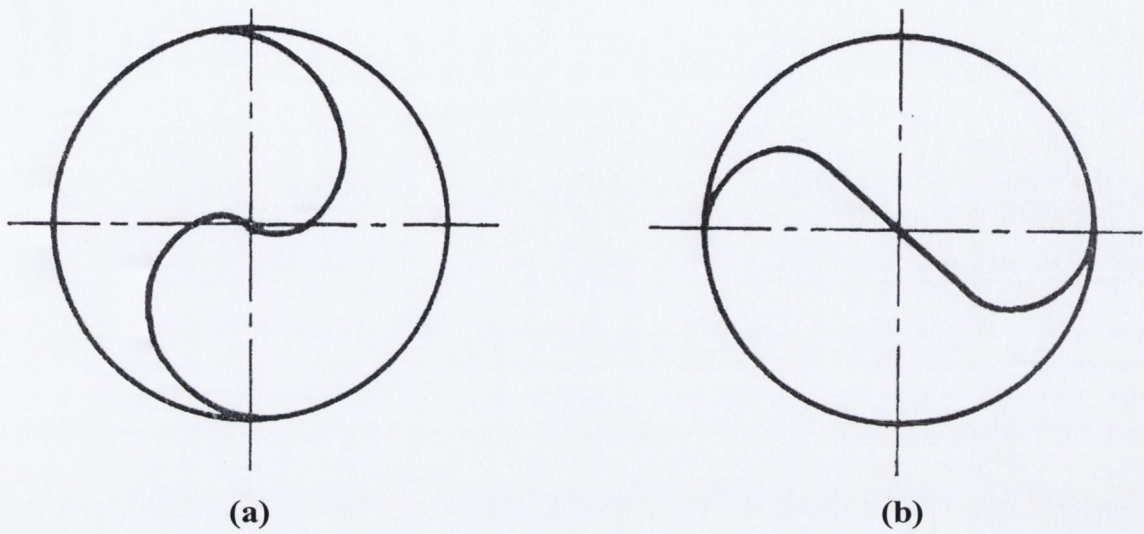


Figure 2.13 Shear deformation of radial insert in plasticine clay on (a) two-roll and (b) three-roll Mannesmann mills [49].

2.2 Fracture

When a crack reaches a critical size it reduces the strength of the material to carry a given load. This causes the material to completely separate resulting in fracture. Based on the appearance of the fractured surface, fracture modes can be considered as either:

- Ductile
- Brittle
- Fatigue

2.2.1 Ductile Fracture

The fracture surface of a metal due to ductile failure is extremely rough or dimpled, indicating that a lot of plastic deformation has taken place [68]. Ductile fracture occurs in the presence of significant plastic deformation. Internal voids are initiated and join together resulting in total separation which forms a crack.

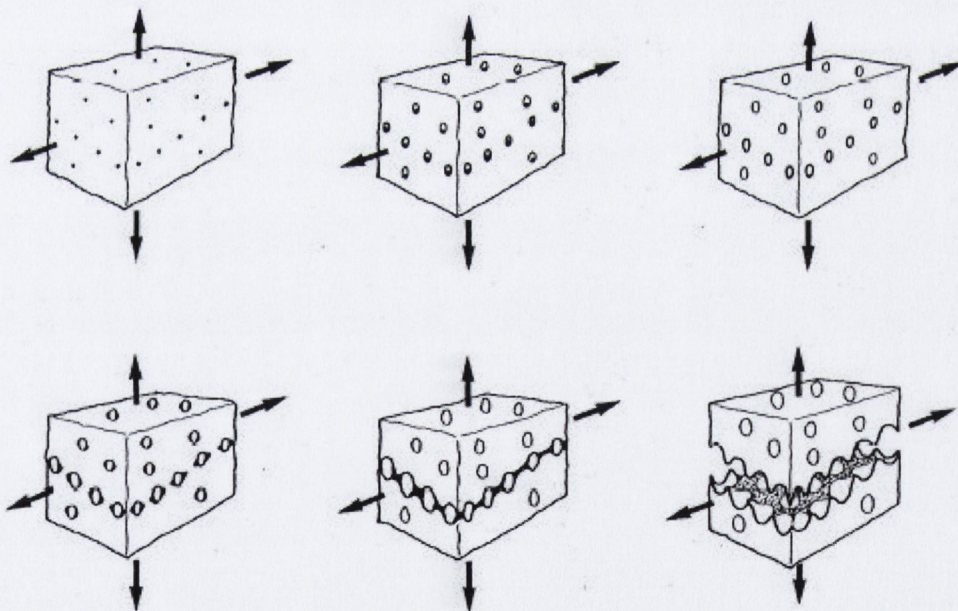


Figure 2.14 Ductile fracture due to void growth which is initiated at second phase particles which grow and generate localised strain between the voids causing excessive necking of the ligaments between the voids which eventually fracture [69].

There are two mechanisms of ductile failure which are generated by either tensile or shear stresses. In an elastoplastic material ductile failure occurs by nucleation of voids from inclusions, void growth and void coalescence [69]. The voids nucleate [70] at second

phase particles or inclusions by either particle failure or separation from the softer matrix material surrounding them and then grow due to the plastic straining and the hydrostatic stress state of the surrounding material. Void nucleation at a particle is dependant on the bonding of the particle to the matrix material. In the case of strong bonds, as for carbon steels, nucleation will take place after large plastic straining and fracture will occur when the ligaments of the matrix material between the voids becomes thin. The final stage, void coalescence, occurs due to the separation of the ligaments.

However, accurately predicting the location of ductile fracture has been the focus of a lot of research [71-73]. Altan *et al* [71] performed a series of tests using the FE program DEFORM2D in order to predict ductile failure of workpiece material using a range of ductile fracture laws. The various fracture models were applied to a simulated compression test and compared to experimental tests to determine whether they predicted the location and level of deformation of the billet that coincided with the first appearance of fracture on the surface of the experimental test piece. Using this technique Altan *et al* [71] concluded that the Normalised Cockcroft-Latham fracture law was the best suited for predicting the location of ductile shear fracture. Therefore, the maximum damage value that coincided with the location of the crack in the experimental test was termed the critical damage value, C . They then suggested that the critical damage value can be therefore used as a material parameter to predict the location of cracking in other metal forming processes.

The Normalised Cockcroft-Latham fracture criteria can be described by the following equation which postulates that fracture will occur when the accumulated plastic strain reaches a critical level [73]:

$$C = \int \frac{\sigma_1}{\sigma_{eq}} d\varepsilon_{eq} \quad (2.17)$$

where

C = Critical damage

σ_1 is the maximum tensile principal stress

σ_{eq} is the equivalent stress

ε_{eq} is the equivalent strain

Due to the severe level of shear stress induced material flow during Form Rolling, the critical damage value obtained from a compression test cannot be applied. However, as will be discussed in the results section, the Normalised Cockcroft-Latham fracture law accurately predicts the location of a crack on the surface of the workpiece during the Form Rolling process. It was also used to successfully predict the stage in the process that the fracture occurred.

The hydrostatic σ_h or mean σ_m stress, is a state of stress in which the normal stresses on any one plane are equal and where shear stresses do not exist in the material. Therefore, regions of highest tensile hydrostatic stress are the most likely to fracture and alternatively regions of high compressive hydrostatic stress can prevent material from fracture. This criteria was used by Fang *et al* [57] to predict the likelihood of internal fracture generation during a CWR process. The hydrostatic stress, as will be shown, can be used to predict the most likely location and the stage of a crack appearing in a Form Rolled workpiece. The hydrostatic stress is described by the following equation:

$$\sigma_h = \sigma_m = \frac{\sigma_1 + \sigma_2 + \sigma_3}{3} \quad (2.18)$$

where

$\sigma_1, \sigma_2, \sigma_3$ are the three principal stresses

2.2.2 Brittle Fracture

Brittle fracture generally occurs with little evidence of plastic deformation. Crack propagation is by cleavage where the atomic bonds along crystal planes become separated resulting in rapid fracture. The crack spreads through grains and grain boundaries which affect the crack path because the grains are orientated in different directions, as illustrated in Figure 2.15 below. Cleavage fracture surfaces are characterised by large smooth shiny surfaces separated by cleavage steps that form river markings and chevron markings which point back to the point of fracture initiation. These are directly attributed to crack path disturbances [59].

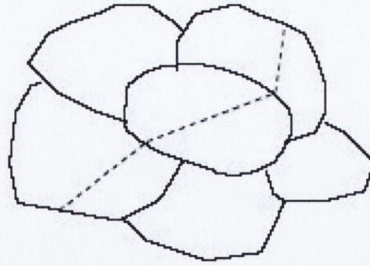


Figure 2.15 Illustration of changing crack path due to the orientation of grains and grain boundaries [74].

2.2.3 Fatigue

Fatigue is a mode of fracture where relatively small static loads that generate cyclic magnitudes of stress can cause failure. The smaller the load the longer it takes for fracture to occur, but all materials eventually, if they don't fail by another mechanism, fail due to fatigue.

Fatigue fracture is characterised by the changing appearance of the fracture surface. As shown in Figure 2.16, the origin of a crack can be easily determined by the surrounding fatigue striations emanating from the crack. The fracture surface is dimpled typical of plastic fracture. Then the rest of the fracture surface is smooth showing the rapid and final failure of the product which resulted in cleavage of the material.

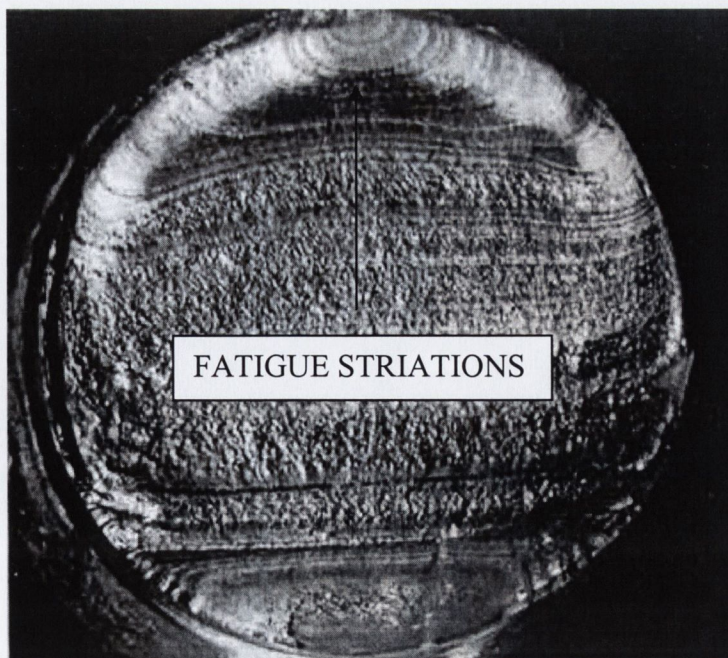


Figure 2.16 Fracture surface attributed to fatigue failure [75].

2.2 Fracture

When a crack reaches a critical size it reduces the strength of the material to carry a given load. This causes the material to completely separate resulting in fracture. Based on the appearance of the fractured surface, fracture modes can be considered as either:

- Ductile
- Brittle
- Fatigue

2.2.1 Ductile Fracture

The fracture surface of a metal due to ductile failure is extremely rough or dimpled, indicating that a lot of plastic deformation has taken place [68]. Ductile fracture occurs in the presence of significant plastic deformation. Internal voids are initiated and join together resulting in total separation which forms a crack.

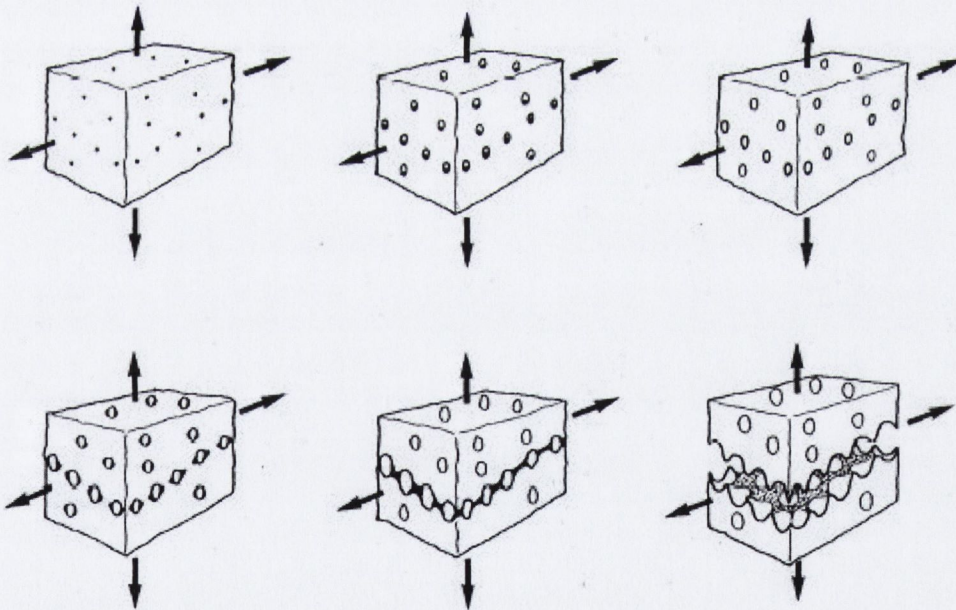


Figure 2.14 Ductile fracture due to void growth which is initiated at second phase particles which grow and generate localised strain between the voids causing excessive necking of the ligaments between the voids which eventually fracture [69].

There are two mechanisms of ductile failure which are generated by either tensile or shear stresses. In an elastoplastic material ductile failure occurs by nucleation of voids from inclusions, void growth and void coalescence [69]. The voids nucleate [70] at second

phase particles or inclusions by either particle failure or separation from the softer matrix material surrounding them and then grow due to the plastic straining and the hydrostatic stress state of the surrounding material. Void nucleation at a particle is dependant on the bonding of the particle to the matrix material. In the case of strong bonds, as for carbon steels, nucleation will take place after large plastic straining and fracture will occur when the ligaments of the matrix material between the voids becomes thin. The final stage, void coalescence, occurs due to the separation of the ligaments.

However, accurately predicting the location of ductile fracture has been the focus of a lot of research [71-73]. Altan *et al* [71] performed a series of tests using the FE program DEFORM2D in order to predict ductile failure of workpiece material using a range of ductile fracture laws. The various fracture models were applied to a simulated compression test and compared to experimental tests to determine whether they predicted the location and level of deformation of the billet that coincided with the first appearance of fracture on the surface of the experimental test piece. Using this technique Altan *et al* [71] concluded that the Normalised Cockcroft-Latham fracture law was the best suited for predicting the location of ductile shear fracture. Therefore, the maximum damage value that coincided with the location of the crack in the experimental test was termed the critical damage value, C . They then suggested that the critical damage value can be therefore used as a material parameter to predict the location of cracking in other metal forming processes.

The Normalised Cockcroft-Latham fracture criteria can be described by the following equation which postulates that fracture will occur when the accumulated plastic strain reaches a critical level [73]:

$$C = \int \frac{\sigma_1}{\sigma_{eq}} d\varepsilon_{eq} \quad (2.17)$$

where

C = Critical damage

σ_1 is the maximum tensile principal stress

σ_{eq} is the equivalent stress

ε_{eq} is the equivalent strain

Due to the severe level of shear stress induced material flow during Form Rolling, the critical damage value obtained from a compression test cannot be applied. However, as will be discussed in the results section, the Normalised Cockcroft-Latham fracture law accurately predicts the location of a crack on the surface of the workpiece during the Form Rolling process. It was also used to successfully predict the stage in the process that the fracture occurred.

The hydrostatic σ_h or mean σ_m stress, is a state of stress in which the normal stresses on any one plane are equal and where shear stresses do not exist in the material. Therefore, regions of highest tensile hydrostatic stress are the most likely to fracture and alternatively regions of high compressive hydrostatic stress can prevent material from fracture. This criteria was used by Fang *et al* [57] to predict the likelihood of internal fracture generation during a CWR process. The hydrostatic stress, as will be shown, can be used to predict the most likely location and the stage of a crack appearing in a Form Rolled workpiece. The hydrostatic stress is described by the following equation:

$$\sigma_h = \sigma_m = \frac{\sigma_1 + \sigma_2 + \sigma_3}{3} \quad (2.18)$$

where

$\sigma_1, \sigma_2, \sigma_3$ are the three principal stresses

2.2.2 Brittle Fracture

Brittle fracture generally occurs with little evidence of plastic deformation. Crack propagation is by cleavage where the atomic bonds along crystal planes become separated resulting in rapid fracture. The crack spreads through grains and grain boundaries which affect the crack path because the grains are orientated in different directions, as illustrated in Figure 2.15 below. Cleavage fracture surfaces are characterised by large smooth shiny surfaces separated by cleavage steps that form river markings and chevron markings which point back to the point of fracture initiation. These are directly attributed to crack path disturbances [59].

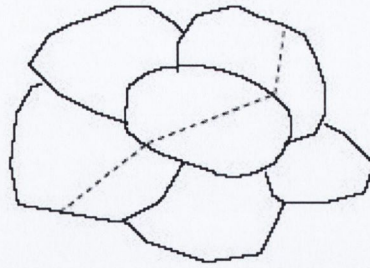


Figure 2.15 Illustration of changing crack path due to the orientation of grains and grain boundaries [74].

2.2.3 Fatigue

Fatigue is a mode of fracture where relatively small static loads that generate cyclic magnitudes of stress can cause failure. The smaller the load the longer it takes for fracture to occur, but all materials eventually, if they don't fail by another mechanism, fail due to fatigue.

Fatigue fracture is characterised by the changing appearance of the fracture surface. As shown in Figure 2.16, the origin of a crack can be easily determined by the surrounding fatigue striations emanating from the crack. The fracture surface is dimpled typical of plastic fracture. Then the rest of the fracture surface is smooth showing the rapid and final failure of the product which resulted in cleavage of the material.

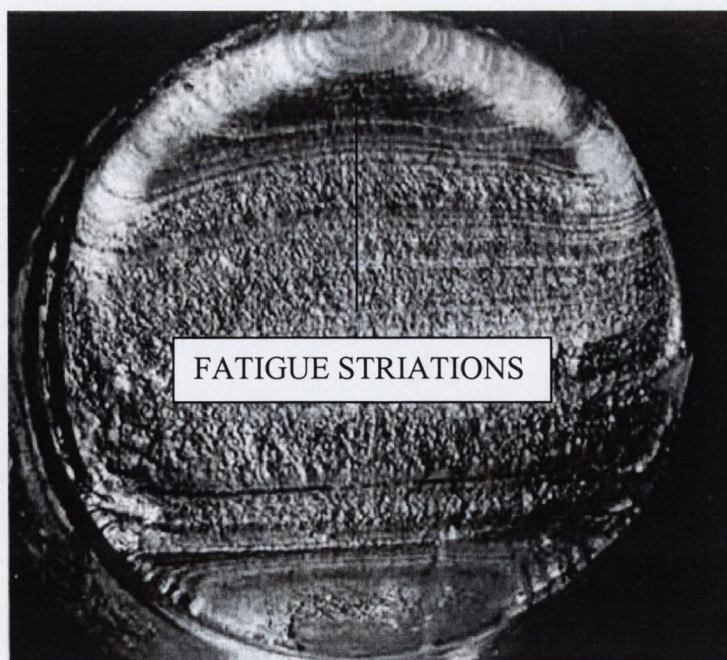


Figure 2.16 Fracture surface attributed to fatigue failure [75].

2.3 FEA of Form Rolling Processes

At the onset of this research 2D finite element analysis had been applied to a flat die thread rolling process by Domblesky and Feng [13]. They investigated the influence of the thread form on stress and strain levels at the thread root. They used DEFORM2D for their analysis and compared the results to a 3D model they simulated using DEFORM3D. In the case of the 3D model the analysis was incomplete, as the model crashed after one rotation of the workpiece. As such, Domblesky and Feng recommended 2D analysis for predicting stress and strain in the workpiece material. However, both 2D and 3D simulations obtained no stress or strain results for the tooling because it was modelled as a rigid object. The workpiece was modelled as a plastic object therefore there was no possibility of predicting the residual stresses that would normally be generated in the workpiece.

In 1998 at the University of Kentucky, Lexington, USA, Lovell *et al* [47, 48, 76-79] started a series of investigations into a flat die CWR process using a combination of experimental and 3D finite element analysis. The FE package they used was ANSYS LS-DYNA and similar to Domblesky and Feng [13] the dies were modelled as rigid and the workpiece as plastic objects. Results equating to the *guiding* stage of the die, which is a lead-in to the *knifing* stage that is rarely used in industry, were presented. The primary aim of these papers is the investigation of slip between the die/workpiece interface and the morphology of internal defects.

In 2002, Fang *et al* [57] using DEFORM3D were the first to present a 3D model of a CWR process in its entirety. The model consisted of 2 rigid rolls and a plastic workpiece.

However, despite the literature available the question still remained as to whether 2D or 3D FE analysis was the proper method to proceed with in the current investigation of the Form Rolling process. During the course of the research performed by the present author a new modelling technique was developed to represent the process. This will be discussed later in section 4.2.

2.3 FEA of Form Rolling Processes

At the onset of this research 2D finite element analysis had been applied to a flat die thread rolling process by Domblesky and Feng [13]. They investigated the influence of the thread form on stress and strain levels at the thread root. They used DEFORM2D for their analysis and compared the results to a 3D model they simulated using DEFORM3D. In the case of the 3D model the analysis was incomplete, as the model crashed after one rotation of the workpiece. As such, Domblesky and Feng recommended 2D analysis for predicting stress and strain in the workpiece material. However, both 2D and 3D simulations obtained no stress or strain results for the tooling because it was modelled as a rigid object. The workpiece was modelled as a plastic object therefore there was no possibility of predicting the residual stresses that would normally be generated in the workpiece.

In 1998 at the University of Kentucky, Lexington, USA, Lovell *et al* [47, 48, 76-79] started a series of investigations into a flat die CWR process using a combination of experimental and 3D finite element analysis. The FE package they used was ANSYS LS-DYNA and similar to Domblesky and Feng [13] the dies were modelled as rigid and the workpiece as plastic objects. Results equating to the *guiding* stage of the die, which is a lead-in to the *knifing* stage that is rarely used in industry, were presented. The primary aim of these papers is the investigation of slip between the die/workpiece interface and the morphology of internal defects.

In 2002, Fang *et al* [57] using DEFORM3D were the first to present a 3D model of a CWR process in its entirety. The model consisted of 2 rigid rolls and a plastic workpiece.

However, despite the literature available the question still remained as to whether 2D or 3D FE analysis was the proper method to proceed with in the current investigation of the Form Rolling process. During the course of the research performed by the present author a new modelling technique was developed to represent the process. This will be discussed later in section 4.2.

CHAPTER 3

METAL FORMING AND THE FINITE ELEMENT METHOD

CHAPTER 3

METAL FORMING AND THE FINITE ELEMENT METHOD

DEFORM, which stands for Design Environment for FORMing, was the finite element package used for this study. DEFORM2D and DEFORM3D have automatic remeshing capabilities. This capability allowed for adaptive remeshing where elements were remeshed automatically when the mesh of one object overlapped with the mesh of another object. When creating a new mesh, temperature and strain data is interpolated from the old mesh to the new one. This ability enabled a simulation that would normally require several manual remeshes, to be performed automatically thereby retaining a high level of accuracy while saving on simulation time.

Finite element analysis involves the simultaneous solution of hundreds to thousands of equations in order to formulate equilibrium conditions. With the advancement of computer technology simulation times have been greatly reduced since the inception of FEA in the 1940's. Consequently with the improvement in mathematical techniques finite element analysis has gained popularity due to its ability to successfully simulate many different processes and applications.

3.1 Principles of FEA

The finite element technique can be used to solve complex engineering problems in stress analysis by computational means. The component being investigated is divided into smaller regions called elements that are connected together at boundary points called nodes. An approximate mathematical representation of the component being modelled is formed by the elements when they are assembled. The mathematical or computational model must first be supplied with information before it can be solved, this information includes the:

- Coordinates of each node
- Material properties of the body
- Loading conditions

- Boundary conditions
- Type of analysis to be performed

Equilibrium conditions are formulated for the whole body resulting in nodal displacements. These are then used to obtain strain and stress distributions. The displacement of each node is calculated using a vector matrix notation. This matrix incorporates the displacement of a node, caused by an applied force, to find the displacements of other nodes that are simultaneously affected by this force.

3.1.1 Basic Concept of FEA

Finite element analysis uses the relationship between the force exerted on a spring and the displacement caused by that force. For metalforming processes the stiffness equation (3.1) is used to represent the problem.

$$F = K\delta \quad (3.1)$$

where F is the force exerted, K the stiffness of the spring and δ its displacement. The stiffness corresponds to the slope of the force versus displacement curve. By knowing the force applied and the stiffness, the displacement of a node can be obtained. Having obtained the displacement the strain at that node can be calculated and also the stress by using the constitutive equations. However, an applied force is not considered to influence a solitary node but all the nodes in an element.

3.1.2 Modelling the Form Rolling Process using DEFORM

In simulating the Form Rolling process it was necessary to model the dies and workpiece as either elastic or elastoplastic materials. In the DEFORM code elastoplastic behaviour is modelled using the von Mises yield criteria, the Prandtl-Reuss flow rule and an isotropic hardening rule.

3.1.3 The Yield Criterion

In general, the law that determines when a material starts to yield can be written in the form [80]

$$f(\sigma_{ij}) = C \text{ (constant)} \quad (3.2)$$

$f(\sigma_{ij})$ is called a yield function and C is a experimentally determined material parameter. For isotropic materials, plastic yielding can depend only on the magnitude of the three principal stresses and not their directions. This implies that a yield criterion should be a function of the three stress invariants only

$$f(I_1, I_2, I_3) = C \quad (3.3)$$

Experimental observations indicate plastic deformation of metals is essentially independent of hydrostatic pressure. Consequently yielding depends only on the principal components $(\sigma_1, \sigma_2, \sigma_3)$ of the deviatoric stress tensor

$$\sigma'_{ij} = \sigma_{ij} - \sigma_m \quad (3.4)$$

where $\sigma_m = \frac{1}{3}(\sigma_1 + \sigma_2 + \sigma_3)$ is the hydrostatic component of the stress. The principal components of the deviatoric stress tensor are not independent, since $I_1 = \sigma_1 + \sigma_2 + \sigma_3$ is identically zero, hence the yield criterion can be reduced to the form:

$$f(I_2, I_3) = C \quad (3.5)$$

where I_2 and I_3 are the second and third invariants of the deviatoric stresses, and are equal to

$$I_2 = -(\sigma_1\sigma_2 + \sigma_2\sigma_3 + \sigma_3\sigma_1) \quad (3.6)$$

$$I_3 = \sigma_1 \sigma_2 \sigma_3 \quad (3.7)$$

The criterion used by DEFORM for metal deformation analysis is the von Mises yield criterion. Von Mises suggested that yielding occurs when I_2 reaches a critical value and does not involve I_3 from equation (3.5). The second deviatoric stress invariant, I_2 , can be written explicitly as

$$I_2 = \frac{1}{2} \sigma_{ij} \sigma_{ij} = \frac{1}{2} (\sigma_1^2 + \sigma_2^2 + \sigma_3^2) = k^2 \quad (3.9)$$

or

$$I_2 = (\sigma_1 - \sigma_2)^2 + (\sigma_2 - \sigma_3)^2 + (\sigma_3 - \sigma_1)^2 = 6k^2 \quad (3.10)$$

or

$$I_2 = \sqrt{(\sigma_x - \sigma_y)^2 + (\sigma_y - \sigma_z)^2 + (\sigma_z - \sigma_x)^2 + 6(\tau_{xy}^2 + \tau_{yz}^2 + \tau_{zx}^2)} = 6k^2 \quad (3.11)$$

where k is the shear yield stress obtainable from a uniaxial tension or compression test and is defined as:

$$k = \frac{\sigma_y}{\sqrt{3}} \quad (3.12)$$

Yielding is initiated when the stress in the object reaches the yield stress of the material which is obtained from a tensile test. Therefore, by substituting equation (3.12) into equation (3.11) gives:

$$\sigma_y = \sqrt{(\sigma_x - \sigma_y)^2 + (\sigma_y - \sigma_z)^2 + (\sigma_z - \sigma_x)^2 + 6(\tau_{xy}^2 + \tau_{yz}^2 + \tau_{zx}^2)} \quad (3.13)$$

3.1.4 Prandtl-Reuss Flow Rule

The flow rule used with the von Mises criteria is called the Prandtl-Reuss flow rule. It assumes that the plastic strain increment, denoted by the superfix p , is proportional to the instantaneous deviatoric stress and the shear stress components and can be expressed in rate form as:

$$\frac{d\varepsilon_x^p}{\sigma'_x} = \frac{d\varepsilon_y^p}{\sigma'_y} = \frac{d\varepsilon_z^p}{\sigma'_z} = \frac{d\gamma_{yz}^p}{\tau_{yz}} = \frac{d\gamma_{zx}^p}{\tau_{zx}} = \frac{d\gamma_{xy}^p}{\tau_{xy}} = d\lambda \quad (3.14)$$

or

$$d\varepsilon_{ij}^p = \sigma'_{ij} d\lambda \quad (3.15)$$

where $d\lambda$ is a positive proportionality constant. Therefore, equation 3.15 describes the direction of the plastic strain increments in the x , y , z directions when yielding occurs.

The total strain increment which gives the Prandtl-Reuss equation for elastoplastic materials is the sum of the elastic strain increment and the plastic strain increment. Thus,

$$d\varepsilon_{ij} = d\varepsilon_{ij}^p + d\varepsilon_{ij}^e \quad (3.16)$$

or

$$d\varepsilon_{ij} = \sigma'_{ij} d\lambda + \frac{d\sigma'_{ij}}{2G} + \delta_{ij} \frac{(1-2\nu)}{E} d\sigma_m \quad (3.17)$$

where G , E and ν are the shear modulus, Young's Modulus and Poisson's ratio, respectively. The delta symbol, δ_{ij} , is equal to one when $i=j$ and zero when $i \neq j$ [80].

3.1.5 Hardening Rule

Work hardening occurs in cold formed metals when subjected to plastic deformation. As the plastic deformation increases, the level of stress needed to generate further deformation increases. The work hardening rule hypothesises that the degree of hardening is only a function of the total plastic work. The resistance to further distortion depends on the amount of work done on the material since it was in its initial annealed state. According to the von Mises yield criterion the final yield locus expands uniformly in all directions. This is known as isotropic hardening and can be expressed in terms of principal stresses as:

$$\bar{\sigma} = \sqrt{\frac{1}{2} \{ (\sigma_1 - \sigma_2)^2 + (\sigma_2 - \sigma_3)^2 + (\sigma_3 - \sigma_1)^2 \}} \quad (3.18)$$

or

$$= \sqrt{\frac{3}{2} (\sigma_1'^2 + \sigma_2'^2 + \sigma_3'^2)} \quad (3.19)$$

where $\bar{\sigma} = Y$ and is known as either the effective, equivalent or flow stress. According to the hypothesis stated above, the effective stress, $\bar{\sigma}$, is a function of the total plastic work, W_p .

$$\bar{\sigma} = F(W_p) \quad (3.20)$$

An alternative hypothesis exists where the strain hardening is related to the effective stress, $\bar{\sigma}$, and to the effective plastic strain, $d\bar{\epsilon}^p$ which can be expressed as:

$$dW_p = \sigma_{ij} d\epsilon_{ij} = \bar{\sigma} d\bar{\epsilon}^p \quad (3.21)$$

where

$$d\bar{\varepsilon}^p = \sqrt{\frac{2}{3} \left\{ (d\varepsilon_1^p - d\varepsilon_2^p)^2 + (d\varepsilon_2^p - d\varepsilon_3^p)^2 + (d\varepsilon_3^p - d\varepsilon_1^p)^2 \right\}} \quad (3.22)$$

Thus equation (3.20) can be written as:

$$\bar{\sigma} = F\left(\int \bar{\sigma} d\bar{\varepsilon}^p\right) \quad (3.23)$$

where $\bar{\sigma}$ is a function of $\int d\bar{\varepsilon}^p$ which is integrated over the strain path. Therefore:

$$\bar{\sigma} = H\left(\int d\bar{\varepsilon}^p\right) \quad (3.24)$$

It should be noted that equations (3.20) and (3.24) will derive different results for a real material because of anisotropy and the Bauschinger effect which describes that the elastic limit of a tensile test specimen is increased in tension but is decreased in compression. Similarly, the elastic limit of a compression test specimen is increased in compression and decreased in tension.

3.1.6 Contact Modelling

Typically only two friction formulations are used [81]. Coulomb's friction law states that the friction shear stress, τ_F , resisting relative motion is proportional to the normal force, σ_N ,

$$\tau_F = \mu |\sigma_N| \quad (3.25)$$

where μ is the friction coefficient. Whenever the unbalanced force at a node is less than the friction force, the node does not move, or is considered sticking. Whenever the internal force equals or exceeds the friction force, the friction force impedes relative motion.

The second friction formulation is known as Tresca friction which can be written as,

$$\tau_F = -m \tau_{\max} \quad (3.26)$$

where m is the friction factor, and τ_{\max} is the shear strength of the material.

For a Tresca yield function,

$$\tau_{\max} = \frac{\bar{\sigma}}{2} \quad (3.27)$$

and for a von Mises yield criterion it is,

$$\tau_{\max} = \frac{\bar{\sigma}}{\sqrt{3}} \quad (3.28)$$

The Tresca friction law is recommended for bulk forming processes by DEFORM which as previously stated utilises the von Mises yield criterion to predict the onset of yielding. The friction factor, m , can be used to represent various metal forming conditions such as:

- $m = 0.05-0.15$ for cold forming of steels, aluminium alloys and copper using phosphate lubricants
- $m = 0.2-0.4$ for hot forming of steels, aluminium alloys and copper using graphite based lubricants
- $m = 0.7-1.0$ for processes involving no lubricant

CHAPTER 4

WORK PROGRAM

CHAPTER 4

WORK PROGRAM

4.1 Experimental Procedures

The objectives of the experimental procedures were to:

- Obtain material stress/strain data that could be inputted into the finite element model (FEM)
- Form Roll Double Groove test fasteners which would be subsequently measured and compared to the FEM results
- Section and etch the test fasteners for macroscopic analysis in order to:
 - Reveal the flow lines
 - Investigate for any evidence of surface or internal cracking

4.1.1 Mechanical Testing

The purpose of the mechanical testing programme was to obtain full elastoplastic stress/strain curves for the materials being simulated in the finite element model. These stress/strain curves enable the FE program to calculate the stress/strain state of the test material in question during Form Rolling. Most rolling, forging and extrusion processes are inherently compressive and so the behaviour of a test material under compressive conditions is of particular interest.

Compression test specimens were machined to produce cylindrical billets 12mm in diameter and 12mm in height. This aspect ratio of 1:1 was used for all the samples which were then compressed using an Instron 1196 250kN hydraulic press. The compression test procedure was as follows:

- The test billet was placed between two tungsten carbide plates so that die deformation did not occur during the test.
- PTFE tape was placed between the interfaces of the sample and the carbide plates. The PTFE acts as a lubricant to counteract the effects of barrelling thereby promoting homogeneous deformation.

- The billets were compressed by the hydraulic press in increasing load increments of 25kN.
- Measurements of the height and diameter of the sample were taken after each load increment so that the stress and strain could be calculated

To ensure accuracy, three samples were tested for each material and the average of each test was used to obtain the compressive stress/strain curve. The compressive stress/strain curves were obtained for the workpiece material SPS 8.8 which is a low alloy steel and for the tools which were manufactured from M2 tool steel. Due to the fact that the stress/strain behaviour of a material is dependent on the strain rate, it was necessary to account for the effects of changing strain rate to ensure accuracy of the FE model. Therefore, the compression test procedure described above was carried out for strain rates of 0.1mm/sec/sec and 10mm/sec/sec. The power law:

$$\sigma = C\dot{\epsilon}^m \quad (4.1)$$

was fitted to the test data to obtain the sensitivity to hardening index, m . This was found by a linear regression of the strain/strain log curve. The slope of the line is m while the y axis intercept is the constant C , the strength coefficient. Stress and strain values for SPS 8.8 and M2 are shown below for both strain rates in Tables 4.1-2, respectively. The corresponding flow stress curves are shown in Figure 4.1 and Figure 4.2.

STRAIN	STRESS [MPa] for STRAIN RATE = 0.1	STRESS [MPa] for STRAIN RATE = 10
0.05	372	382
0.10	520	530
0.20	638	648
0.30	690	700
0.40	721	731
0.50	744	754
0.60	759	769
0.70	768	778

Table 4.1 Flow stress (MPa) for SPS 8.8 corresponding to a given strain and strain rate.

STRAIN	STRESS [MPa] for STRAIN RATE = 0.1	STRESS [MPa] for STRAIN RATE = 10
0.00	1	1
0.01	2500	2520
0.02	3050	3070
0.30	3450	3470
0.10	3750	3770
0.20	4000	4020
0.30	4150	4170
1.00	4200	4220

Table 4.2 Flow stress (MPa) for M2 tool steel corresponding to a given strain and strain rate.

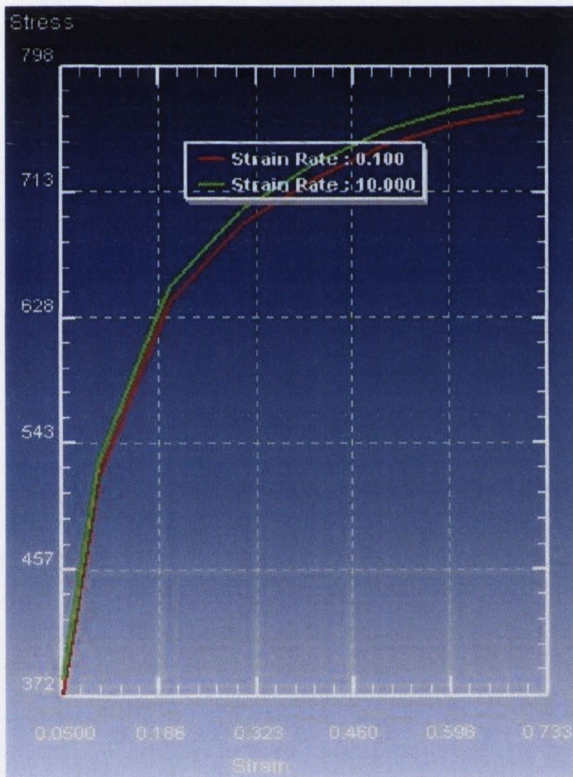


Figure 4.1 Flow stress of SPS 8.8.

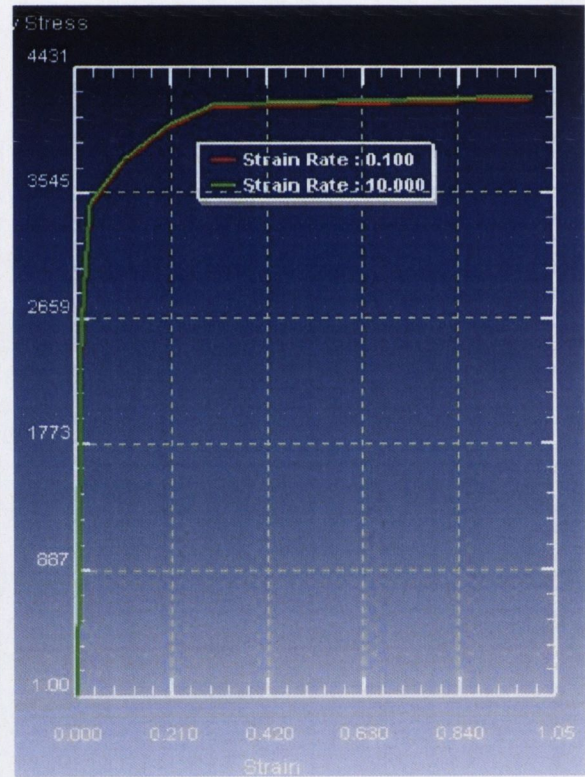


Figure 4.2 Flow stress of M2.

Ideally more stress values should have been obtained for more strain rates however the two chosen strain rates bracket the deformation range of the material for this process.

4.1.2 Form Roll Testing

The product manufactured by the Form Rolling process in this study was a fastener incorporating a Double Groove, as illustrated in Figure 4.3 (b). Die designs were drawn up by the author (see Appendix A) and the tools were manufactured by Hi-Life Tools in Shannon Co. Clare.

The feature that formed the first groove was designed, within parameters specified by Pater *et al* [58], so as to minimise the risk of fracture. However, the second groove was purposely designed to fracture so that the failure mechanisms could be analysed.

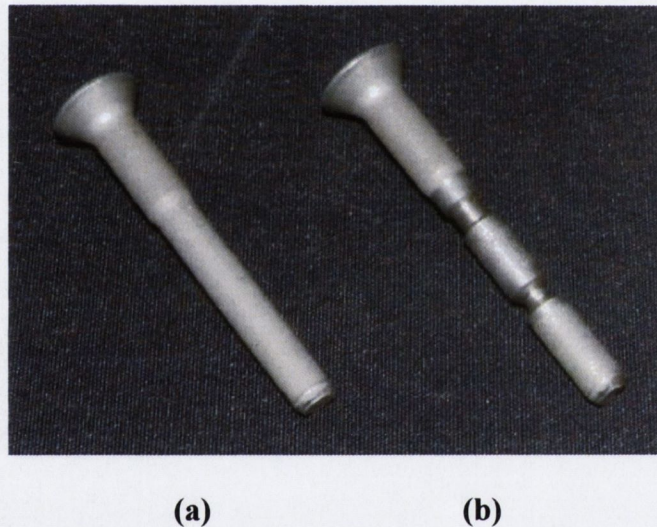


Figure 4.3 (a) Starting workpiece which is used to produce **(b)** a Double Groove fastener.

Figure 4.4 shows the finished dies. The top die is longer than the bottom die because it contains a lead in so that the fastener can be gripped between the dies and moved towards the start of the first groove. In order to ensure that there is enough friction at the workpiece/die interfaces an EDM surface was included on the dies, as shown in Figure 4.4 below.

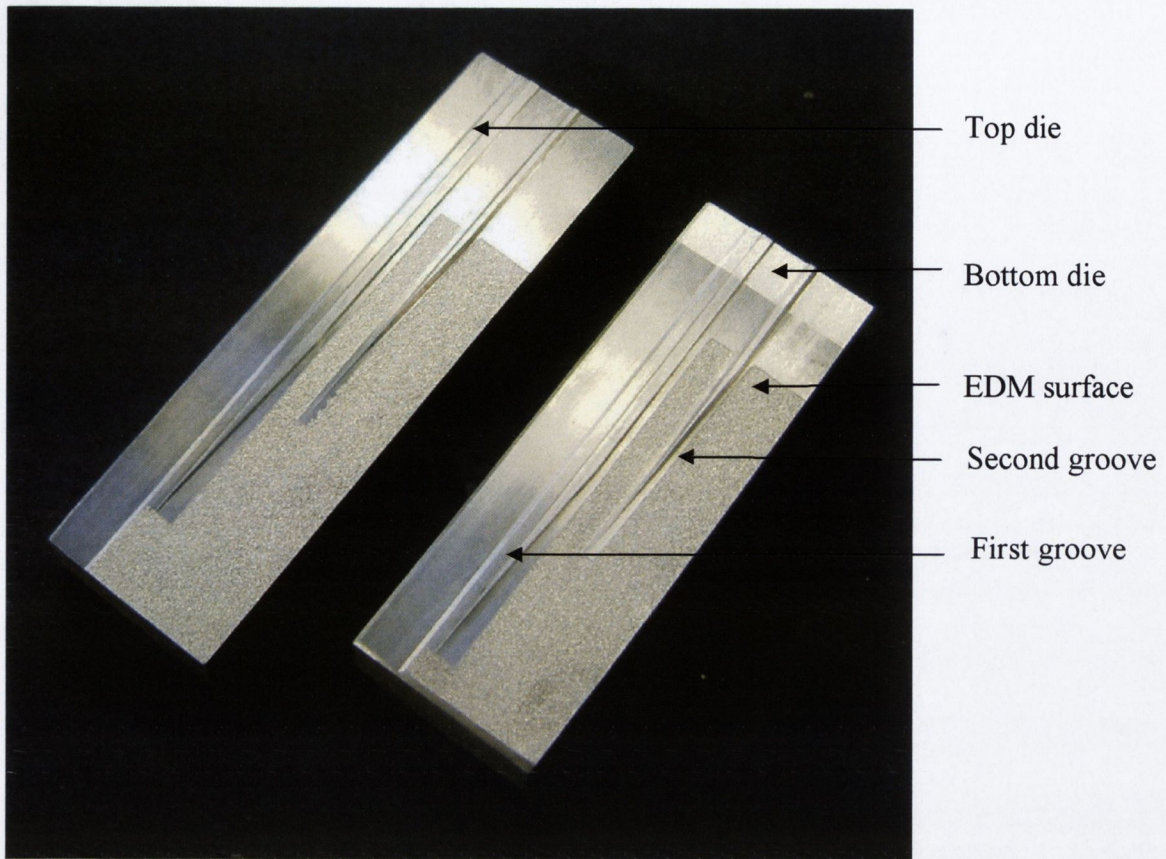


Figure 4.4 Double Groove Form Rolling dies.

A feature of the die design is that the form used to produce the groove on the fastener is designed to induce material flow towards the front end of the fastener. This is illustrated in Figure 4.5 below which shows cross-sections after every 360° rotation of the fastener. As can be seen, both grooves are developed from left to right from the head towards the tip of the fastener. The second groove was started before the first was completed so that back pressure could be provided to the material in the deformed zone of the first groove would remain in contact with the die. However, the starting point of the second groove was calculated so that material build-up between the two grooves did not occur. If this happened it would have had the effect of increasing the fastener diameter in this region thereby generating very high tool forces which could have lead to premature tool failure. The dies were fitted to a 10 Waterbury thread rolling machine at the SPS Unbrako Plant in Shannon.



Figure 4.5 Fastener cross-sections during Form Rolling in increments of 360° rotation.

To ensure precise Form Rolling of the desired geometry, correct and accurate machine setup was essential. Test fasteners were first rolled to ensure the dies were correctly aligned. This procedure consisted of rolling a fastener, stopping it after a half rotation and inspecting it to ensure that the straight edges of the groove matched up. When the alignment was corrected, test fasteners were again rolled to see if the fasteners rolled the full length of the die. Generally, slipping would occur, caused by the application of either too little or too much side pressure on the dies. This was rectified by adjusting pressure bolts to alter the pressure on the dies. Sometimes, if the dies were not parallel to each other, slipping would also occur. To correct this, shims were placed beneath the dies until the test fasteners rolled successfully down the entire length of the die. This setup process is common for any fastener rolling operation, including thread rolling.

Stationary Die Workpiece Reciprocating Die

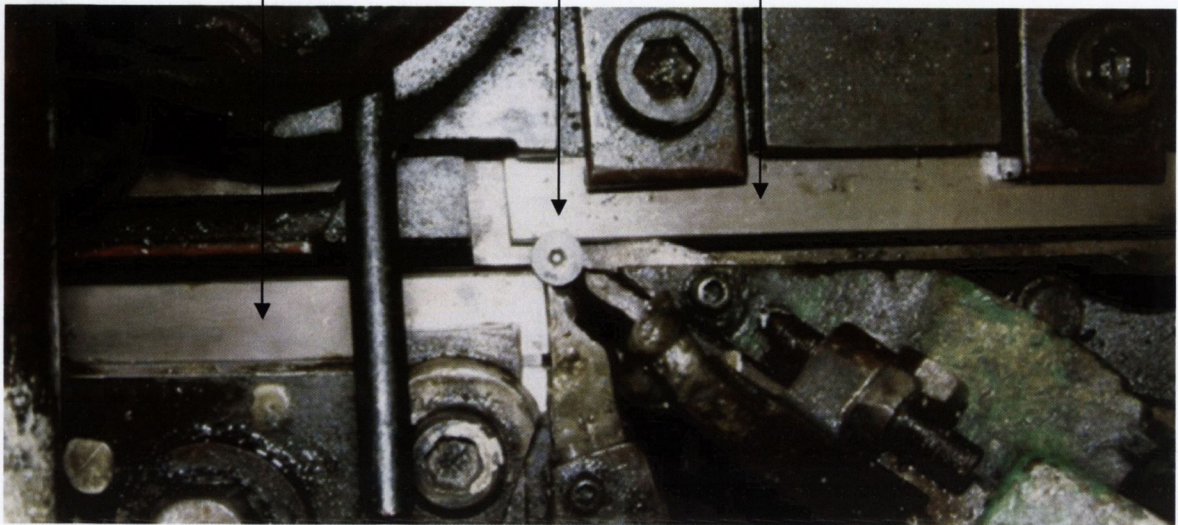


Figure 4.6 Starting machine setup.

Having perfected the machine setup which is shown in Figure 4.6, the following procedure was followed:

- A billet was placed between the Form Rolling dies.
- The machine was jogged until the workpiece was positioned at the start of the first groove.
- The machine was again jogged to move the die until the workpiece had rotated 360°.
- The die motion was then reversed to the starting position and the workpiece was extracted from the machine.
- The steps outlined above were repeated for every 360° rotation of the workpiece required to complete the entire process, the exception being the completed fasteners which passed between the entire lengths of the dies.

When the machine testing was concluded, measurements of the test fastener geometries were obtained. This was achieved by inserting digital photographs, taken through an optical microscope (Figure 4.7), into a data image programme called Scion Image. In Scion Image the ruler used to measure dimensions was calibrated by drawing the ruler to measure the workpiece diameter and setting that

distance equal to the experimentally measured diameter. Once the ruler is calibrated other dimensions can be easily and accurately measured.



Figure 4.7 Leica L2 optical microscope.

Having completed the Form Rolling tests, the billets were then prepared for macroscopic analysis. As illustrated in Figure 4.8, samples were sectioned and mounted in a thermoset polymer to provide a longitudinal cross-section of the workpiece. The samples were then etched in order to reveal the effects of work hardening, which can be determined by the material flow lines, as shown in Figure 4.9. The sectioning and etching procedure is described below:

- The head of the workpiece was removed using a diamond coated cutting disc.
- The shank of the workpiece containing the most severely deformed region was mounted in a thermoset polymer.

- The cylindrical mounting was placed into a milling machine and the sample cross-section was machined down to just off the centre line of the fastener.
- The sample was ground and polished using a 6 micron diamond spray (Figure 4.8).
- The sample was etched to reveal material flow lines (Figure 4.9) using 2% Nital which is a mixture of 2% Nitric acid and 98% methanol.
- The etched samples were viewed using a Leica L2 microscope and digital images were taken of the etched surfaces.

As with the machine testing procedure, macroscopic samples were prepared for each 360° rotation of the workpiece throughout the process. For each rotation 10 samples were prepared.



Figure 4.8 Mounted longitudinal sections of a complete Double Groove workpiece.

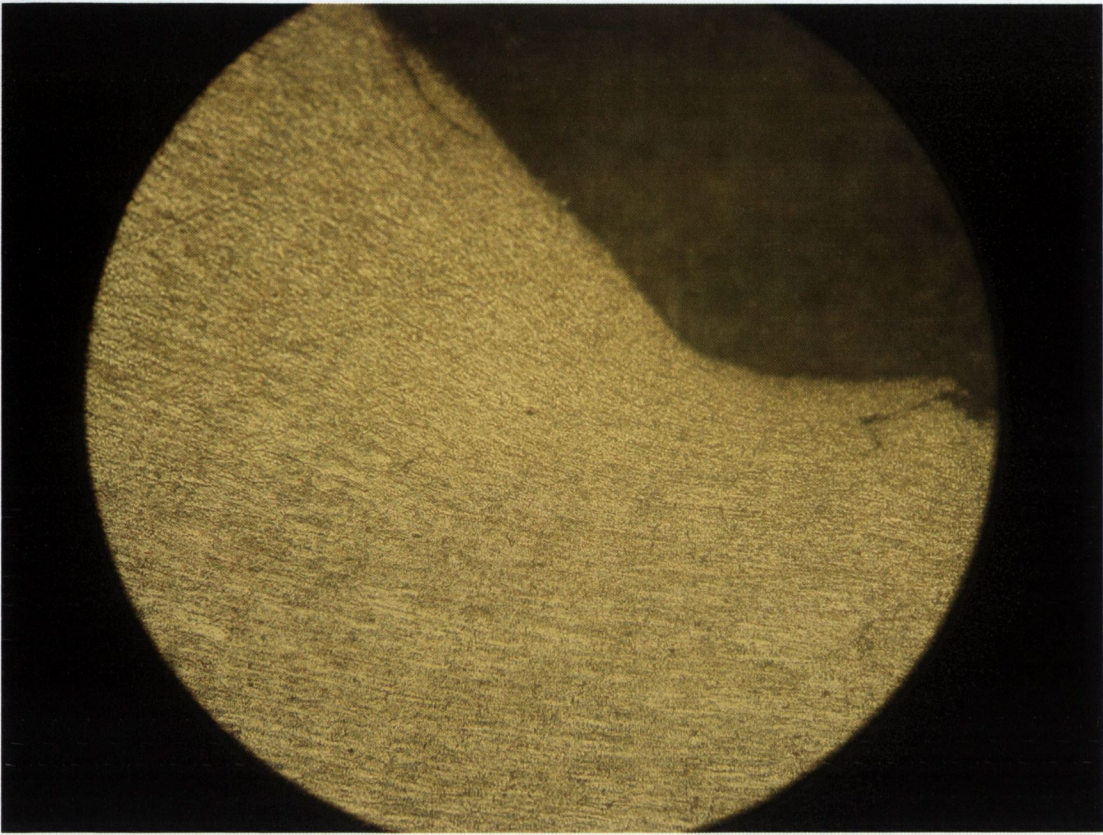


Figure 4.9 Flow line orientation at the corner of the second groove.

4.2 Finite Element Analysis

As discussed in Section 2.3 Domblesky and Feng [13] used 2D finite element analysis to successfully model a thread rolling process under plain-strain conditions. The following section will describe the method employed by Domblesky and Feng and show why it cannot be successfully applied to model a Form Rolling process by comparing experimentally rolled Double Groove samples to the geometry predicted by a 2D FE model of the same process. The FE package used was DEFORM2Dv8.0.

Having established that the 2D model was not sufficiently accurate, the reader will be brought through the various approaches employed in order to successfully simulate the Form Rolling process using a 3D model. The 3D investigation was carried out using the DEFORM3Dv5.0 finite element package.

4.2.1 2D Finite Element Modelling Method

The hypothesis and method of simulating the thread rolling process by 2D finite element analysis as a plane-strain model is as follows [13]:

- By taking a point on the workpiece and following it as it is rolled, it is clear that this point comes into contact with the top and bottom dies after every 180° rotation of the workpiece. Therefore, at any given moment in time, the same profile is being produced on opposite sides of the fastener.
- Cross-sections of the die were taken at precise intervals equal to every 180° rotations of the workpiece along the length of the die (Figure 4.10).
- These die cross-sections, Figure 4.11, were imported into DEFORM2D as iges files and were then incrementally indented into, and retracted from, the workpiece in the finite element model.
- The models consisted of an elastoplastic workpiece and die thereby allowing for stress-relieve between each indentation to occur, as happens in the actual process. This enabled the residual stresses in the tool and workpiece to be determined throughout the process for each incremental step.

- Effectively a point on the fastener is tracked throughout the process and modelled every time it comes into contact with the top and bottom die.

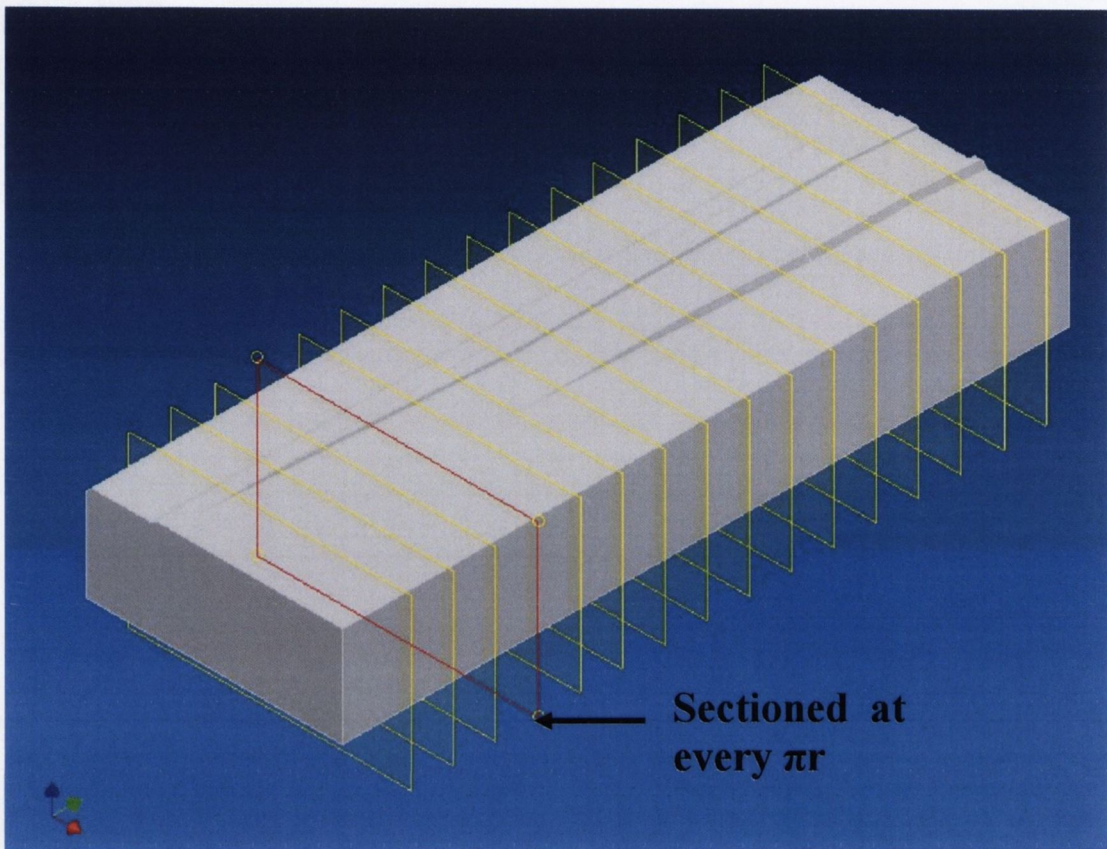


Figure 4.10 Cross sections taken from Double Groove Form Rolling die.

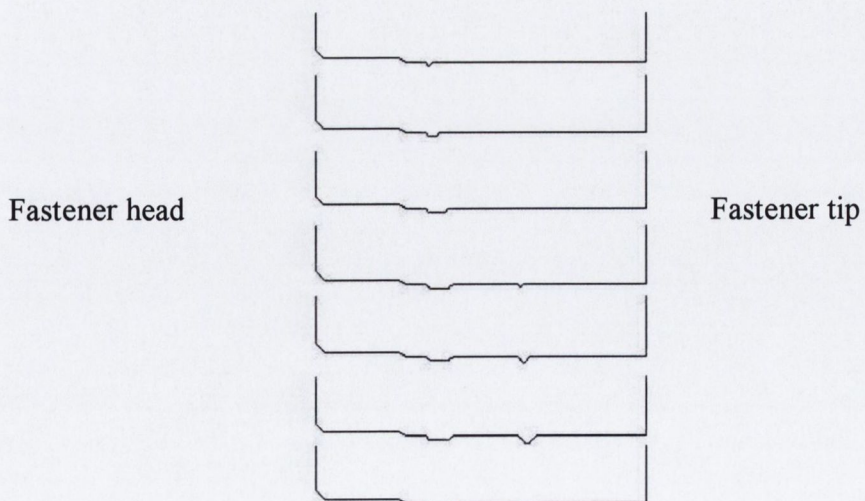


Figure 4.11 Outline of the cross-sections imported into DEFORM2D as iges files.

4.2.2 Boundary Conditions Applied in 2D Modelling

All the 2D models discussed in this section contained 4000 elements within each object. At the start of the FE programme, a model was run with workpiece boundary conditions imposed only along its central axis, which restricted movement in the y direction (Figure 4.12). However, it was soon realised that the model was under-constrained and allowed a large volume of workpiece material to move in the x direction towards the head of the workpiece which does not occur in reality. Figure 4.13 illustrates the direction and magnitude of the workpiece material during the second indentation of the die into the workpiece i.e. after 360° rotation, given the above mentioned boundary conditions. The direction of the arrows indicates the direction of the material flow and the lighter the colour illustrates increasing material velocity. It is clearly evident that the workpiece material moves predominantly towards the head of the fastener which was found to be in contrast to the material flow direction during an actual Form Rolling process.

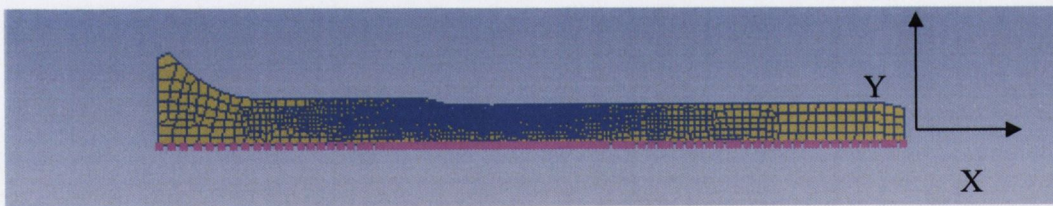


Figure 4.12 Highlighted nodes restricting movement in the y direction.

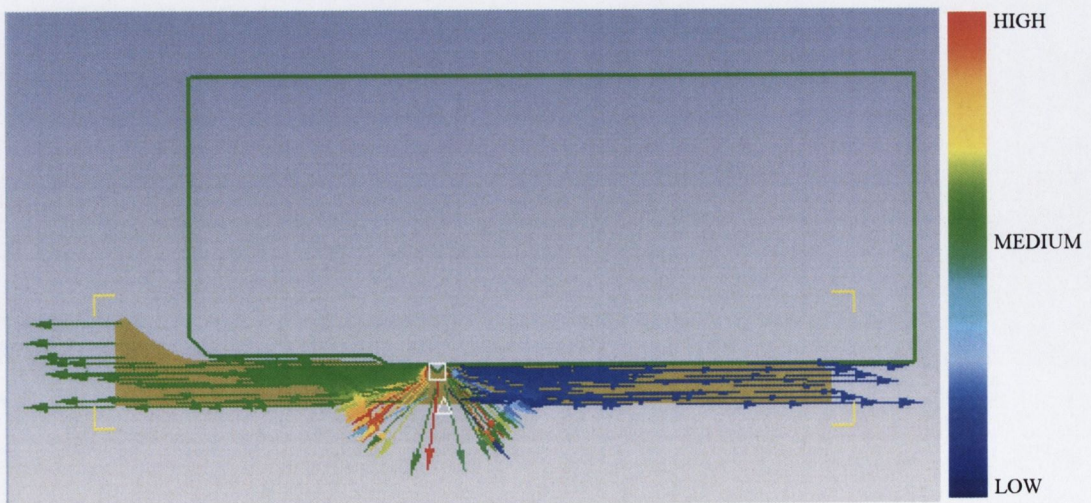


Figure 4.13 Vector plot of 2D workpiece material flow.

After this initial investigation it was decided to impose boundary conditions in both the x and y directions. The same y direction boundary conditions were applied as in the previous model, however, as illustrated in Figure 4.14 the highlighted selected nodes at the top of the fastener head were restricted from moving in the x direction.

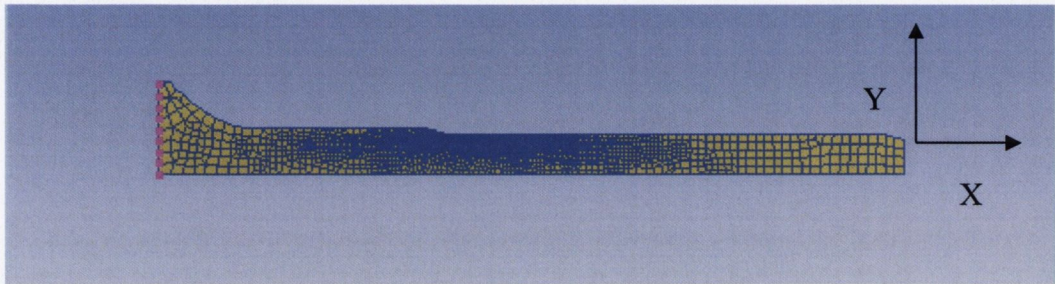


Figure 4.14 Workpiece boundary conditions imposed in the x direction.

Figure 4.15 shows a vector plot of the workpiece material under the new boundary conditions outlined above. As intended, the material now flows in the desired direction, that is, axially towards the tip of the workpiece.

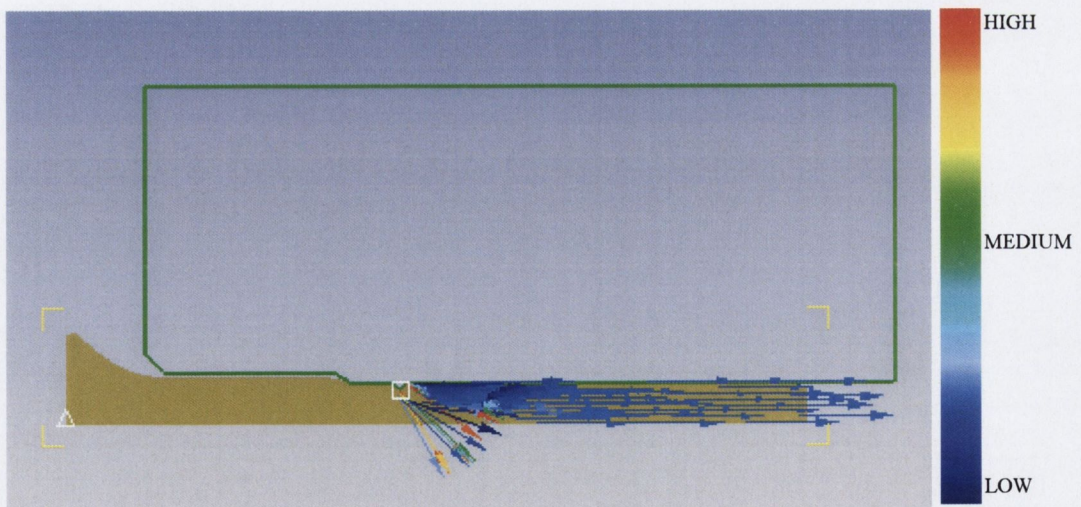


Figure 4.15 Vector plot of 2D workpiece material flow for the corrected model.

By imposing the boundary conditions shown in Figure 4.16 it was possible to model die stresses that are generated during the process. The boundary conditions applied at the highlighted nodes restricted the die from moving in the x

direction on all boundaries except for those facing the workpiece which replicates the restraints on the die while in the Form Rolling machine. The die was free to move in the y direction because this was the direction in which the die moved as it indented the workpiece to form the desired geometry.

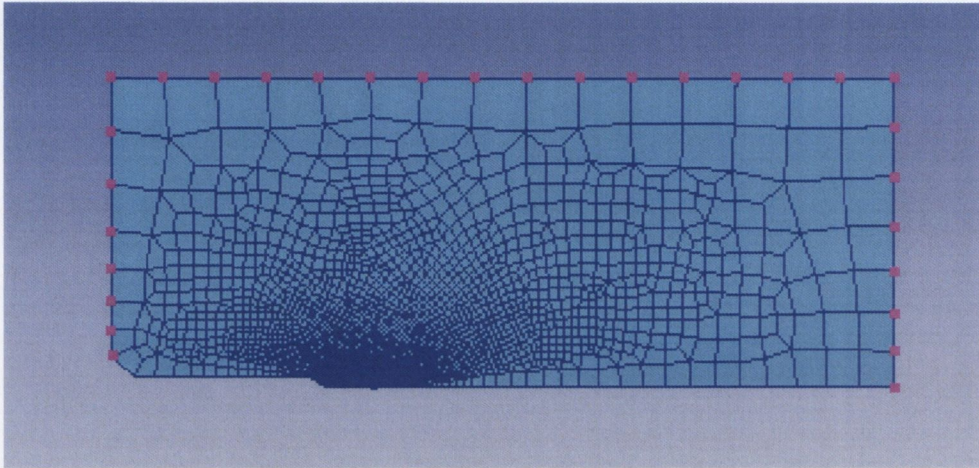


Figure 4.16 Boundary conditions were imposed on the highlighted nodes in the x direction.

4.2.3 Advantages of 2D FEA

The main advantage of this modelling method is that it was possible to perform elastoplastic analysis of both the workpiece and the dies thereby obtaining information on any work hardening effects that might occur during forming of the workpiece material, and also obtaining information on the residual stresses remaining in the die following each indentation.

Typically, simulations were run to completion in about 24 hours when modelling a plastic workpiece with a rigid die. When running with an elastoplastic workpiece with a rigid die, computational time increased to about 72 hours.

To obtain die stresses the computational time was increased even further whereby a model of an elastoplastic workpiece with an elastic die took about 120 hours to run and to model both the workpiece and die as elastoplastic took approximately 144 hours.

4.2.4 Disadvantages of 2D FEA

It was discovered that 2D FE analysis has limitations when it comes to simulating the Form Rolling process. Despite the fact that 2D models provide a good correlation with the thread rolling process [13], this was not found to be the case for Form Rolling. In actual thread rolling the material flows predominantly in a radial direction to fill the thread forms. The 2D method described above accurately models this process because as the thread forms are incrementally indented and retracted from the workpiece, the workpiece material will flow radially into the thread forms. However, for the Form Rolling process analysed in this project, the material is prevented from flowing radially because the diameter of the workpiece remains constant throughout; instead the material flows predominantly in an axial direction towards the tip of the workpiece.

Figure 4.17 shows the finished form of the first groove in the workpiece which was obtained through 2D FE analysis. As with Figures 4.17-19, the head of the workpiece is towards the left and the tip is towards the right of the figures. When Figure 4.17 is compared to the experimentally rolled workpiece, illustrated in Figure 4.18, the contrast between them is clearly apparent. In the FE model depressions on either side of the groove can be seen, however, they are not apparent in the experimental workpieces. The green line in Figure 4.17 is the outline of the die at full indentation of the workpiece material. At this stage the workpiece material should be flat and in contact with the die, however as can be seen, it has become separated from the die. How this occurs is illustrated in Figure 4.19. This figure shows the workpiece material flow as the first groove is being Form Rolled corresponding to 720° rotation of the workpiece. The workpiece material is seen to be forged by the die as it is indented which causes the material to flow in a predominantly downwards direction thus tending to create the depression of material in the centre of the groove.

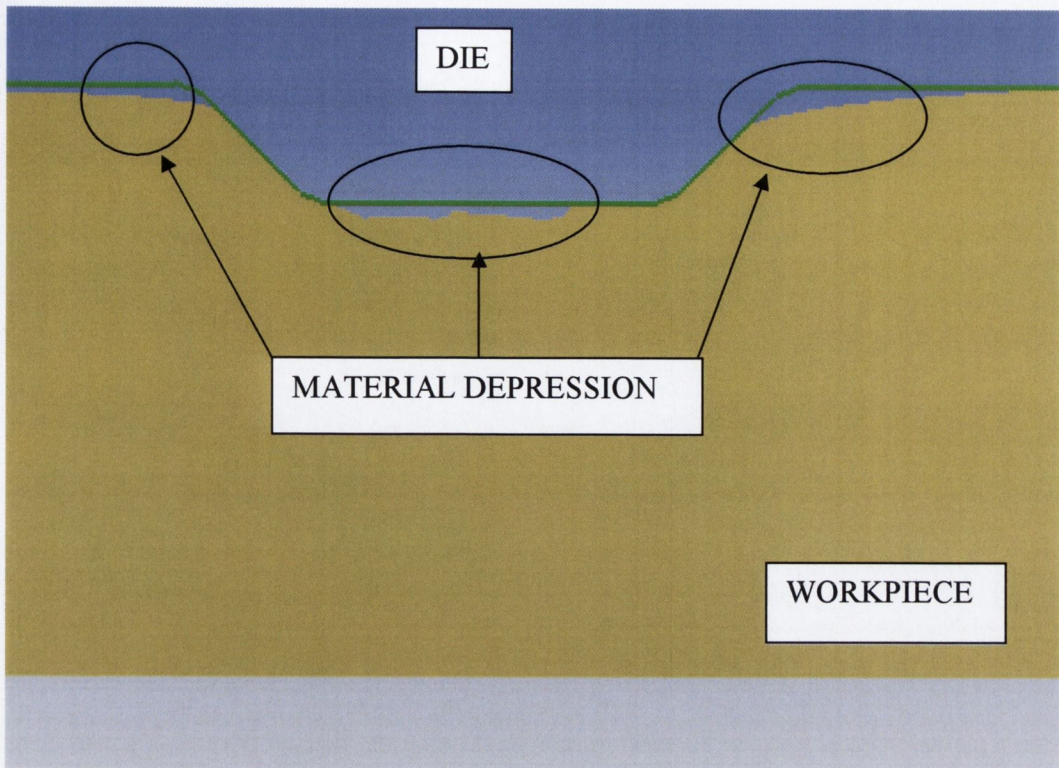


Figure 4.17 2D representation of Form Rolled workpiece material.

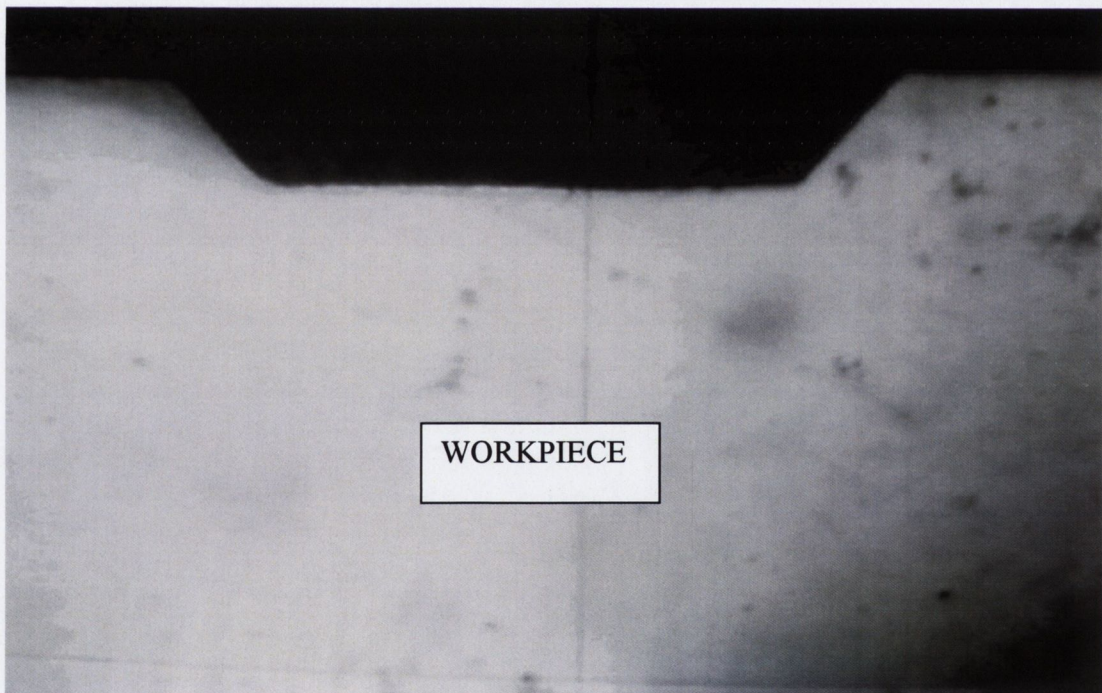


Figure 4.18 Cross-section of the first groove of an experimental specimen. (x10)

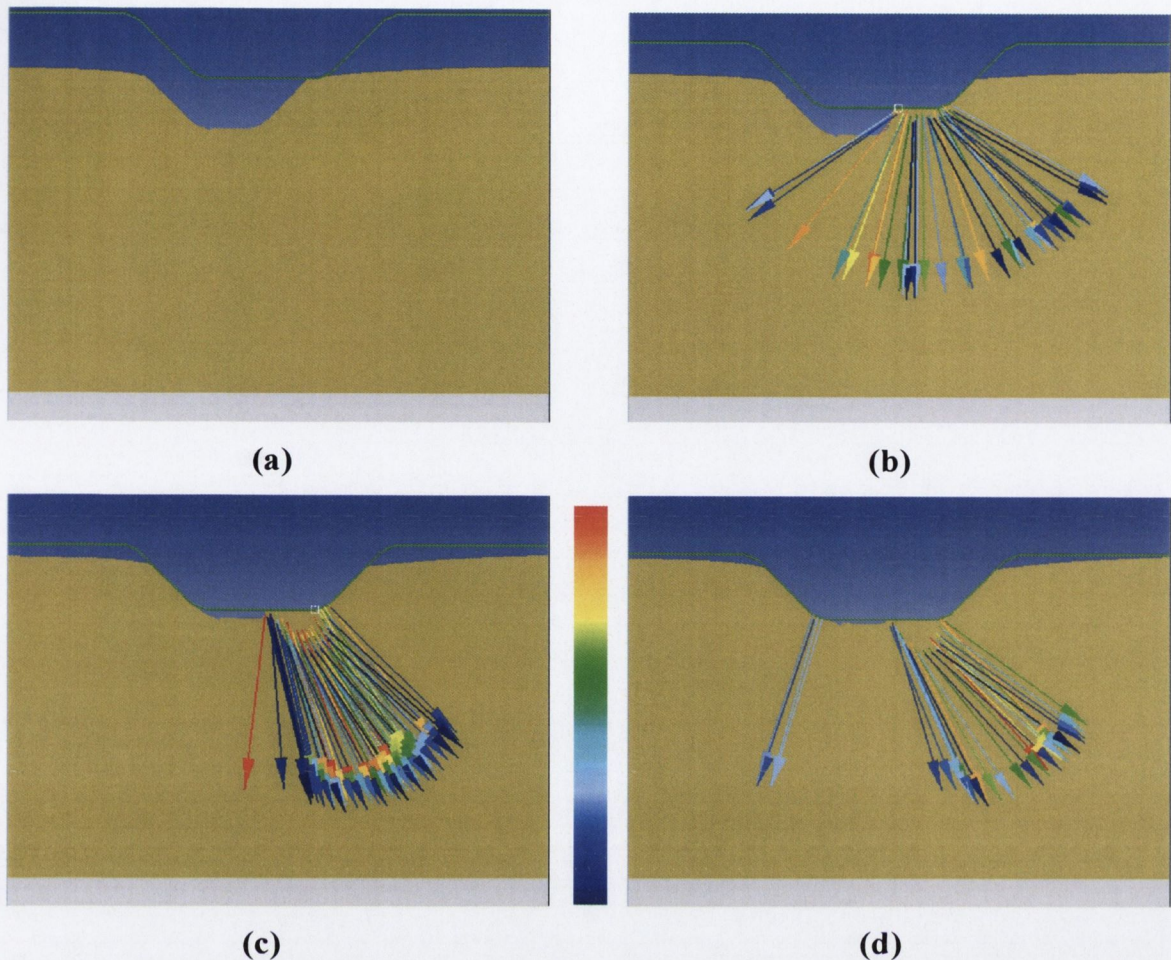


Figure 4.19 Vector plot of the workpiece material using 2D FEA while forming the first groove corresponding to 720° rotation of the workpiece.

This appears to be a 2D modelling problem, and so the only way to model the actual material flow during the process is to introduce artificial boundary constraints at the tip of the fastener to prevent it from moving. This would lead to over constraining of the model and therefore it was concluded that 2D FEA was not suitable for modelling the Form Rolling process.

Another disadvantage of 2D modelling is that when the workpiece material is not in contact with the die, it experiences large tensile stresses which can lead to void formation. These tensile regions cannot be simulated using 2D techniques.

4.2.5 3D Finite Element Analysis Assumptions

There are only two reports of successful 3D modelling of a Form Rolling process, both of which are concerned with the CWR process. Lovell *et al* [47, 48 76-79] used ANSYS LS-DYNA and Fang *et al* [57] used DEFORM3D. Lovell *et al* were able to model the initial *knifing* stage of the process comprising of flat dies whereas Fang *et al* modelled a complete two roll process. Both simulations were run using rigid dies and a plastic workpiece, hence the continuous build-up of residual stresses in the workpiece or plastic deformation of the tooling could not be modelled.

3D models require a solid mesh that contains a lot more elements than a 2D model. In the case of the FE models shown in this section the workpiece contains approximately 60,000 tetrahedral solids elements comprising of approximately 13,500 nodes.

Initially, in the investigation carried out in this study, 3D modelling of the Form Rolling process proved difficult. Three different approaches to the modelling of the process were considered and tested with varying degrees of success. All of these approaches used rigid dies and a plastic workpiece and are listed below in chronological order:

1. The bottom die was modelled as stationary with the workpiece being rolled by the movement of the top die. (This is what occurs on the actual Form Rolling process)
2. Both dies were modelled as moving laterally in opposite directions, causing the workpiece to rotate about its central axis.
3. The workpiece was modelled as a stationary object and the dies were rotated about the workpiece.

The first approach, where it was attempted to roll the workpiece as it is done in reality, proved very problematic. This was due to the fact that even when modelling with a high friction factor of 1 slipping occurred between the rotating workpiece and the dies. It was found that changing the friction factor had no effect on the occurrence of slipping. Therefore, it was decided to adopt an approach developed by Fang *et al* [57] with the intention of reducing the occurrence of

slipping by having the workpiece rotating about its own axis. The method of performing this approach is as follows:

- The top and bottom dies were modelled as rigid objects and the workpiece was modelled as plastic SPS 8.8
- This model setup is illustrated in Figure 4.20 where the top die was moved in the $+y$ direction and the bottom die was moved in the $-y$ direction. Both dies were given the same velocity.
- As the dies moved they caused the workpiece to rotate
- In order to stop the workpiece from slipping the nodes through the axis of the workpiece were restricted from moving in the y direction, as shown in Figure 4.21.

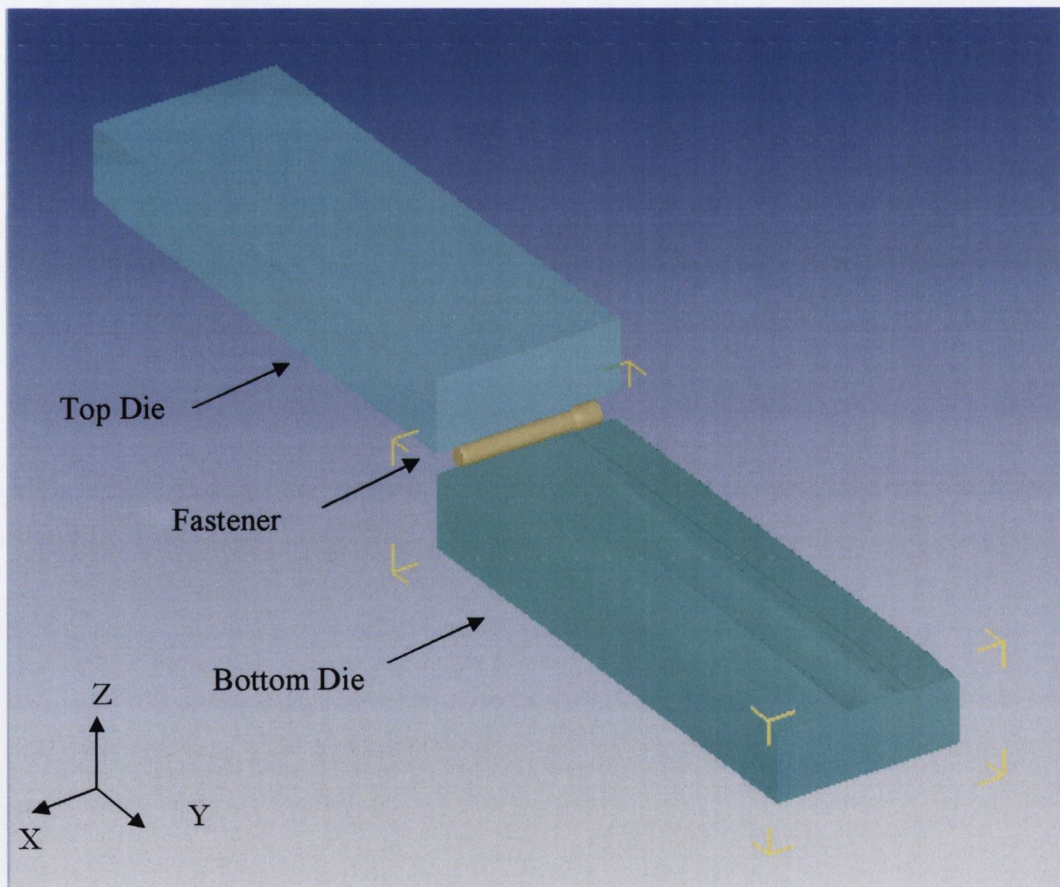


Figure 4.20 3D FEA setup.

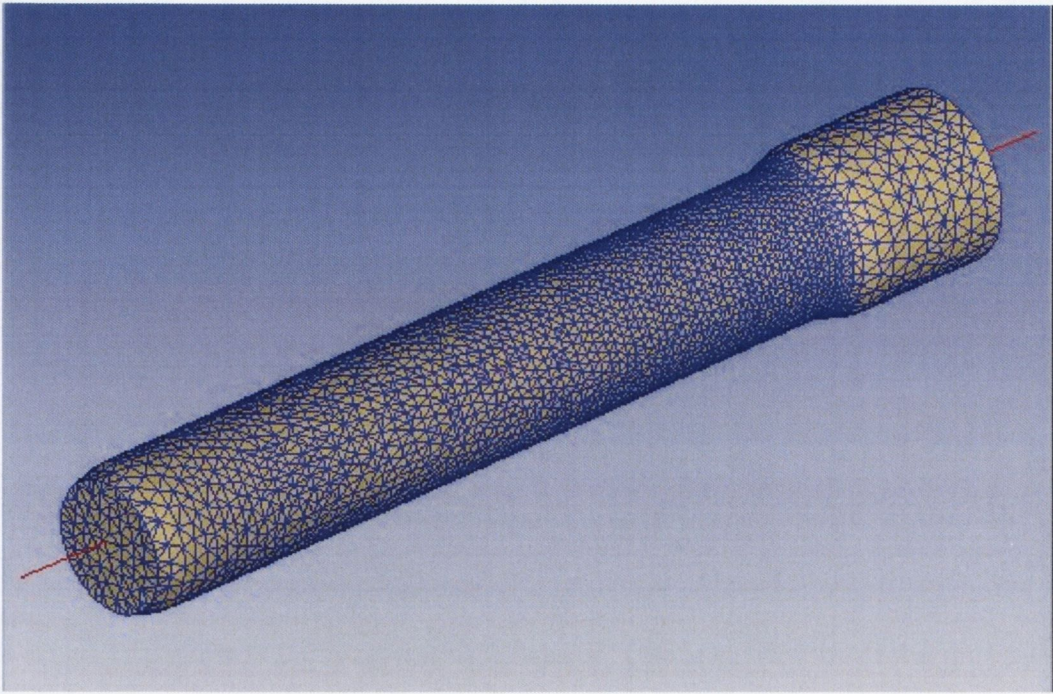


Figure 4.21 Axis of rotation.

Despite these efforts and modifications however, slipping was still evident in the model. Therefore, an alternative method had to be developed where the problem of slipping occurring in the model could be nullified. This was achieved by rotating the dies about a stationary workpiece. The method adopted is as follows:

- The dies were rotated about the fastener to gradually form the desired shape onto the fastener (Figure 4.22). The angular rotation of the dies was governed by the following equation

$$\omega = vr \quad (4.1)$$

where

ω is the angular velocity (rad/sec)

v is the die feed speed (mm/sec)

r is the fastener radius (mm)

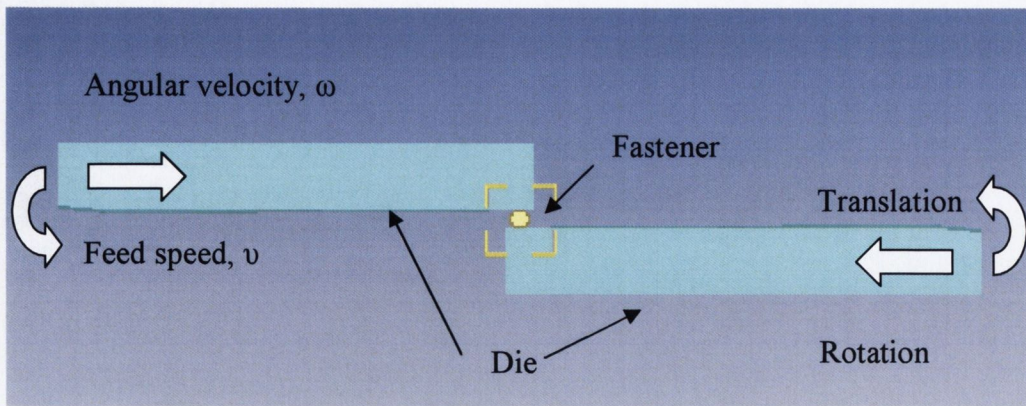


Figure 4.22 Die movement setup.

- The fastener remained stationary under the boundary conditions imposed on it. Figure 4.23 shows the meshed fastener at the start of the simulation and the boundary conditions used in the model. The highlighted nodes shown on either end of the fastener are restricted from moving in the x and z directions. This closely replicates what happens in practice whereby the fastener material is able to flow axially thus allowing the fastener to increase in length.
- In order to maximise the computational accuracy of the model, cylindrical mesh density windows were added in regions of large plastic deformation thereby increasing the number of elements in these regions, as shown in Figure 4.24.

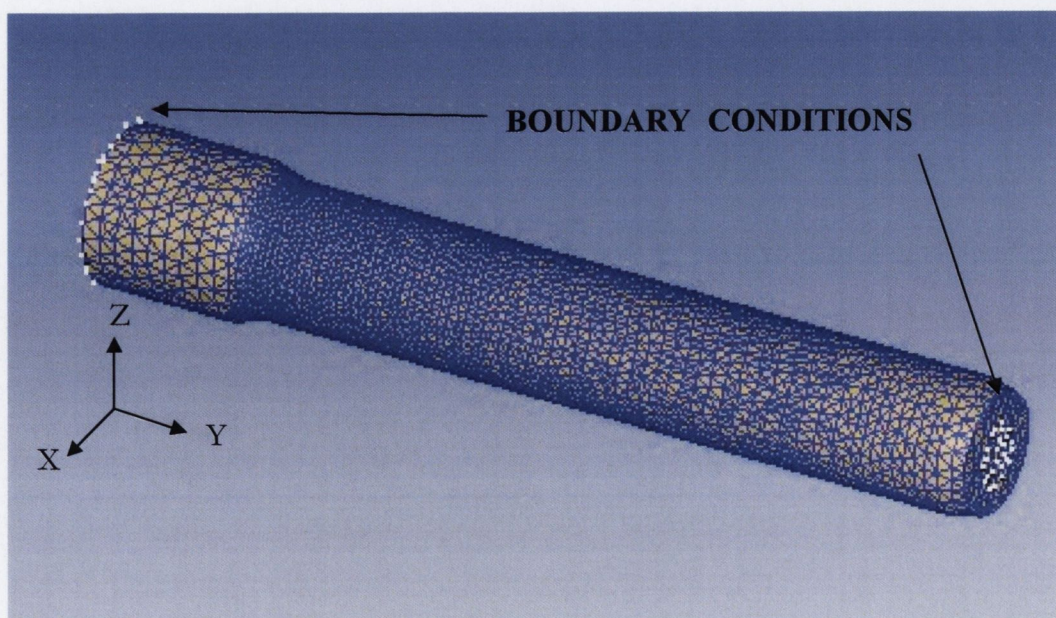


Figure 4.23 3D boundary conditions.

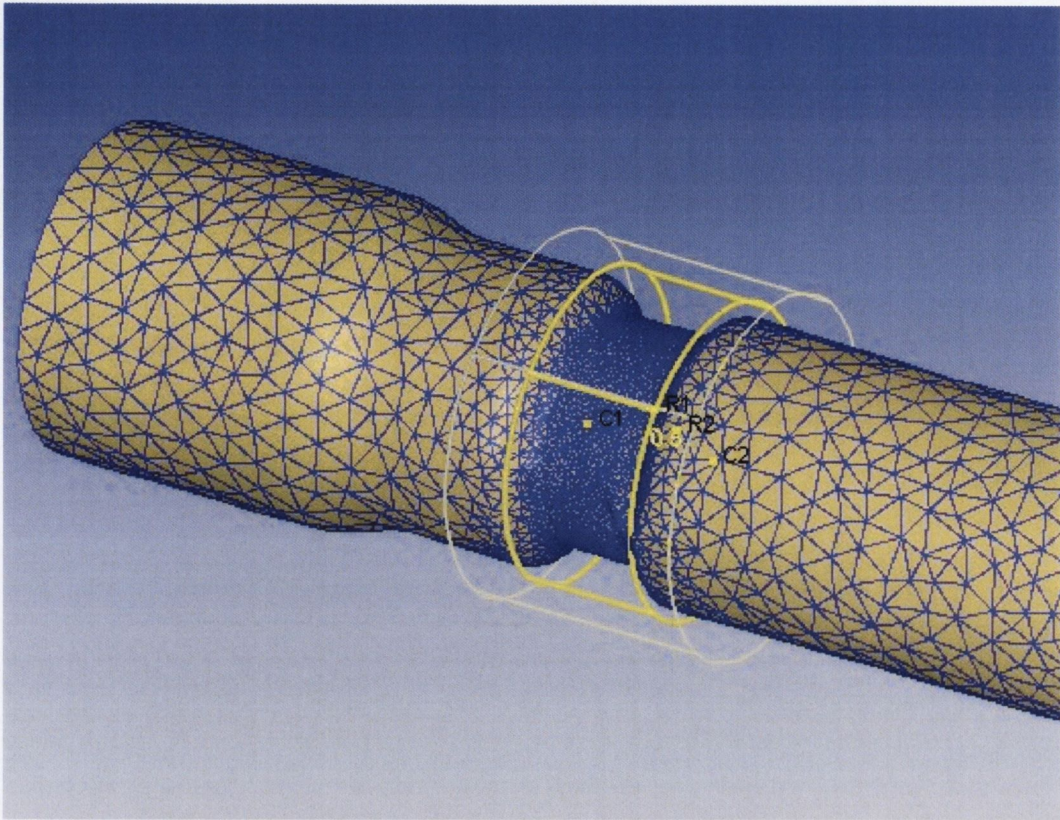


Figure 4.24 Mesh density windows.

Due to the setup employed, slipping was prevented with the computational time taking about 5 weeks to model the Double Groove Form Rolling process with rigid dies and plastic workpiece running on a 526 MB RAM processor. Unlike the previous methods this modelling approach had the added benefit of being able to run with an elastoplastic workpiece and rigid dies which to the author's knowledge was the first time this had been achieved. However, the computational time increased dramatically taking up to 10 weeks to run the model of the Double Groove Form Rolling process.

It should be noted that because the workpiece is stationary, any material displacement in the model can be directly attributed to the material movement generated by the dies. This has significant benefits as opposed to a moving workpiece, where it is very difficult to differentiate between the movement attributed to the rotation of the workpiece from the movement due to material displacement.

4.2.6 3D Die Stress Analysis

An added benefit of this process is that it was possible to obtain die stress values by a process known as *die stress analysis*. At any stage during the simulation the forces that are exerted on the workpiece can be interpolated onto the die which then allows for stress data to be calculated from the model.

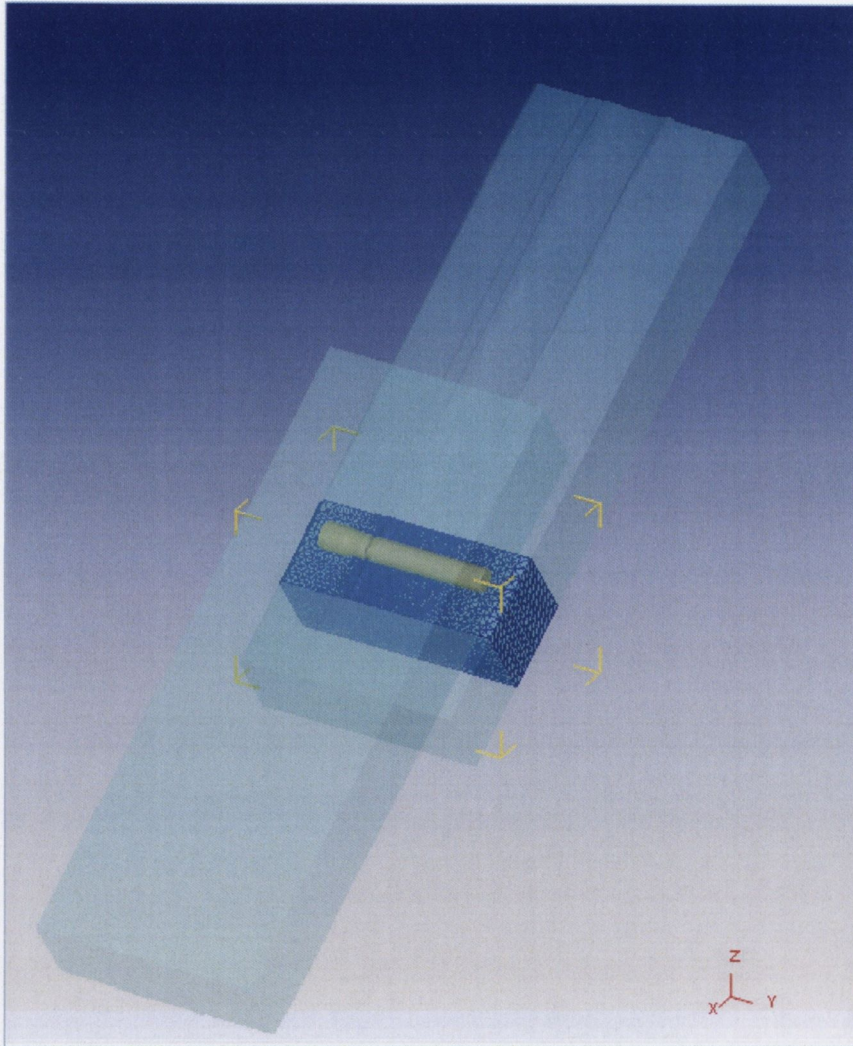


Figure 4.25 Reduced section of the die from which die stress results are obtained.

However, due to the size of the die even the maximum allowable mesh elements in DEFORM3D, which number 200,000, are insufficient to mesh the die with the required density. Insufficient mesh density will create an inaccurate geometry which will lead to the development of artificially high stresses. Having this number of elements is computationally unfeasible and can take up to 2 days to

run each a die stress analysis process for each point of contact that the user wishes to model.

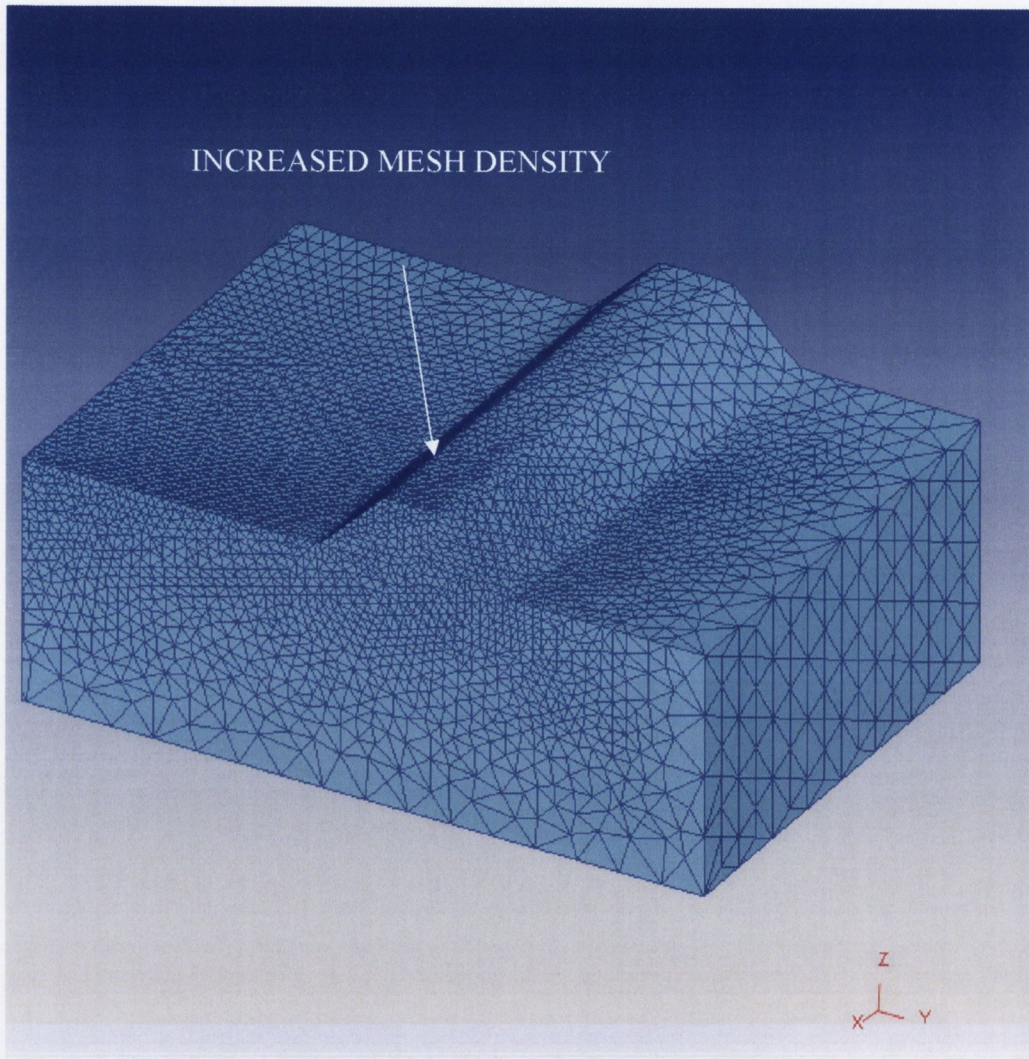


Figure 4.26 Illustration of the mesh density of the die while using die stress analysis.

Therefore, in order to obtain accurate die stress results smaller sections of the die were modelled instead. These 3D sections of the die are placed where the workpiece will be at a particular stage in the process and is meshed with the density concentrated at the predicted area of contact.

This approach allows for as few as 30,000 elements to model the relevant die geometry. Figure 4.25 shows the original setup with the extra section of the die in place from which the *die stress analysis* was run and the forces were interpolated from the workpiece to the die section. Figure 4.26 is a view of the

mesh which has increased density at the area where the workpiece would be in contact with the die especially at the groove corners.

CHAPTER 5

RESULTS & DISCUSSION

CHAPTER 5

RESULTS & DISCUSSION

The following chapter will present a description of the material behaviour during the formation of a Double Groove within a fastener while being Form Rolled. The geometry of both grooves will be used to determine the validity of the model. Once this has been achieved the experimental and FE analysis will focus on explaining how a major crack developed on the surface of the second groove of the fastener. This is of interest because the mechanism by which surface cracking occurs in Form Rolling is not fully understood. In the past, analysis consisted of using slip-line field theory. Though slip line field theory can be successfully applied to predict the central fracture in a fastener it can not predict the tri-axial stress states existing on the surface of the fastener. These stresses cycle from tension to compression at different stages of the process as will be shown.

FE results will be presented on the nature of the various stress components at the centre of the workpiece and explain why central fracture is not evident in the experimental tests.

The chapter will conclude with the FE results of the stresses within the tooling which show why the tool did not fail when in use. However, an interesting characteristic of the process is the distribution of tensile and compressive stresses which will be commented upon.

5.1 Workpiece Deformation

In order to be able to state with confidence that the 3D FE simulation of this process provided an accurate representation of the experimentally Form Rolled test pieces, it was necessary to validate the model. If this objective is achieved, the model can then be used to predict material flow within the workpiece and quantify tool and workpiece stresses in order to predict and explain certain modes of tool and workpiece failure. In order to achieve this, the dimensions of particular features from the experimental test fasteners were compared to predicted dimensions, obtained from of the FE model. The features of the fastener investigated in this section are:

- The total length of the fastener
- Geometry of the two grooves

These features were selected because they indicate whether the simulation is accurately modelling the material flow for the Form Rolling process. It will be shown that there was a good correlation between the experimental and FE dimensions for the features mention above.

5.1.1 Validation of the Finite Element Model

While Form Rolling the Double Groove fasteners, the fastener rotates 7 times before the grooves are fully formed. Therefore, experimental tests were carried out whereby 20 fasteners were Form Rolled and in each case the movement of the die was reversed and the fasteners taken out and measured for every rotation (360°) of the fastener as described in chapter 4.1.

Figure 5.1 shows the progression from left to right of the developing grooves after each rotation of the workpiece. Similar to Figure 5.1, Figure 5.2 shows the fastener geometry after each rotation, but taken from the FE model. By visually comparing these figures it can be seen that there appears to be a very good geometrical correlation between the FE and experimental fasteners after each rotation. In particular, this is evident when looking at the fastener after four rotations where the initiation of the second groove is seen to have begun on the fastener surface. However, in order to comprehensively validate the FE model, measurements of the experimental and FE fasteners were compared for every rotation of the fastener. The FE measurements were obtained by means of *data extrapolation* of the appropriate nodal coordinates from DEFORM3D which were then averaged.



Figure 5.1 Experimental Form Rolled Double Groove fasteners shown for every 360° rotation.



Figure 5.2 FEA representation of the progression of Form Rolling a Double Groove feature onto a workpiece shown for every 360° rotation.

Figure 5.3 shows the labels of all the locations at which dimensions were measured for both the experimental and FE tests. The experimental and FE dimensions compared were:

L the fastener length

N O D E F dimensions that make up the first groove

Q R H I J dimensions that make up the second groove

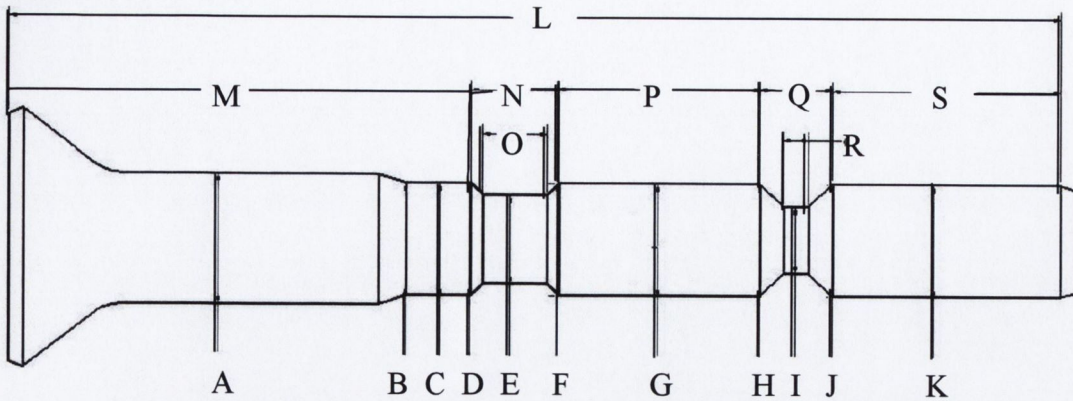


Figure 5.3 Labels for the locations at which dimensions were taken from experimental fasteners and the FE model.

As mentioned previously, the first stage of validating the FE model was to compare the lengths of the fasteners obtained from the FE and experimental tests. Table 5.1 shows that for every 360° rotation of the workpiece, there is close correlation between the experimental and FE measurements of the length of the fastener. The percentage difference is taken to be the difference between the experimental and FE result divided by the larger value and multiplied by a hundred.

Rotation Number ($\times 360^\circ$)	EXP Mean Fastener Length (L) (mm)	FEA Mean Fastener Length (L) (mm)	%DIFF
0	36.51	36.51	0.000
1	36.64	36.75	0.3
2	36.94	37.98	2.74
3	37.19	37.28	0.24
4	37.73	37.79	0.16
5	37.98	38.08	0.26
6	38.58	38.54	0.1
7	38.64	38.57	0.18

Table 5.1 Experimental and FE measurements for the length of the fastener for every 360° of rotation.

The differences in the results can be explained by experimental error whereby during the Form Rolling of the fastener it was very difficult, due to jogging of the machine, to stop the fastener at exactly 360° rotation. However, the accuracy of the FE model is demonstrated when comparing the FE and

experimental results at the end of the process where there is only 0.07mm difference in lengths of the fasteners which equates to a percentage difference of only 0.18%. Figure 5.4 is a plot of the mean experimental length and the mean FEA measured length increase due to the material displaced while forming each groove. As shown in Figure 5.1 the process consists of three separate stages which are distinguishable by the changing slopes in the respective plots. The first stage consists of forming the first groove. The slope of the lines in this stage remain approximately constant because approximately the same volume of material is displaced per rotation of the workpiece. The second stage shows a slight increase in the slope of the lines. This is because the second groove is started before the first groove is completed. Therefore, the material from both grooves is displaced simultaneously thereby increasing the average volume of displaced material which lengthens the fastener. The slopes of the lines in the third stage are attributed to the volume displaced by the second groove only. As shown, the slopes of the lines from the 6th to the 7th rotation decreases as the groove nears completion.

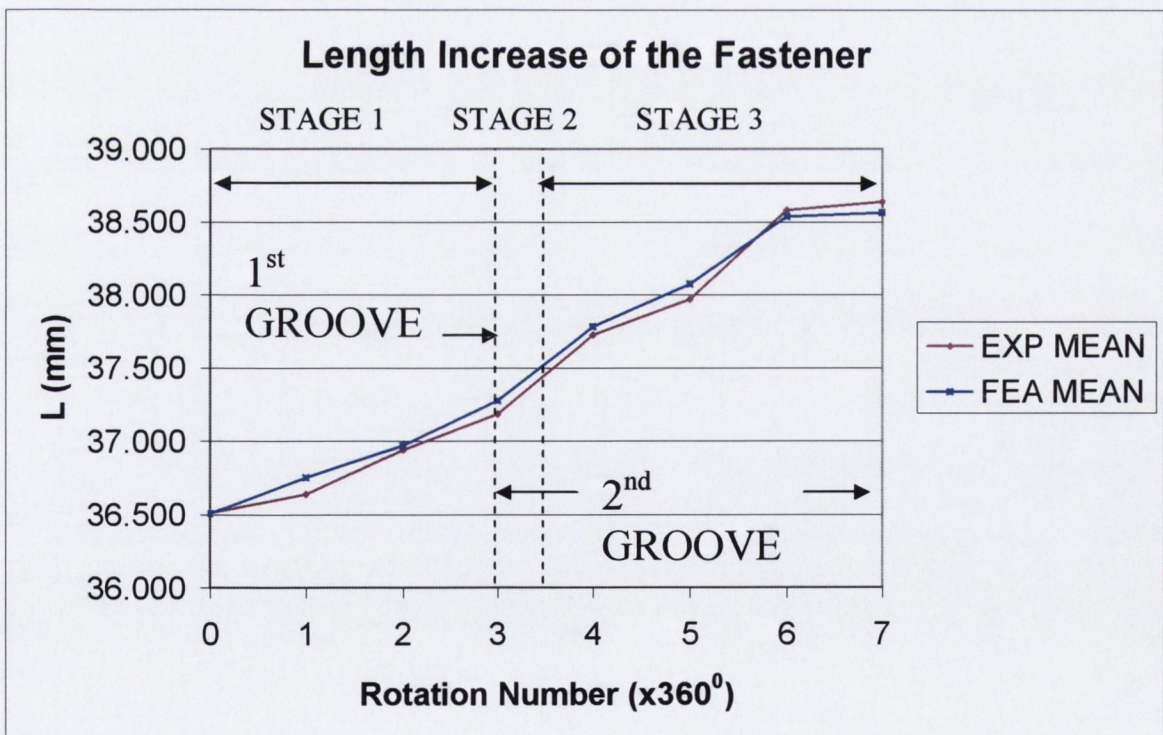


Figure 5.4 Average of the experimental and FEA measured lengths (mm), L , of the fastener taken for every 360° rotation of the workpiece.

The second stage of validating the model was to compare the final geometries of both grooves as predicted by the FE model with those from the

experimental tests. Table 5.2 below, compares the final geometries of the first groove of the experimentally rolled fasteners to those obtained from the FE model. Labels N, O, D, E and F are illustrated in Figure 5.3 where N and O indicate the separate widths of the groove, D and F are the outer edge diameters and E is the inner diameter of the groove.

	N	O	D	E	F
EXP (mm)	3.08	2.13	4.07	3.15	4.07
FEA (mm)	3.31	2.28	4.08	3.2	4.09
% DIFF	6.95	6.58	0.25	1.56	0.49

Table 5.2 Average of the first groove dimensions (mm) taken from experimental tests and the FE model with the percentage difference (%) between them.

It can be seen that the results obtained from the FE model shown in Table 5.2 are slightly greater than those obtained experimentally (for geometries N and O, which are the major and minor widths of the first groove, respectively). The discrepancy between the results can be explained by comparing the finished fastener as predicted by the FE model, shown in Figure 5.5, to a cross-section of an experimental sample, shown in Figure 5.6. It can be seen that the corners of the groove in Figure 5.5 i.e. the FE model, are slightly rounded which makes it difficult to accurately determine the groove width. However, the experimental test sample had sharp angled edges and this made it easier to measure the respective geometries accurately. This probably accounts for the percentage difference between the FE and experimental results of 6.95% and 6.58% for labels N and O respectively, shown in Table 5.2.

There appears to be a very good correlation of the measurements of D, E and F where the respective percentages differences are 0.25%, 1.56% and 0.49%. The experimental results are less than the FE results due to the pressure exerted on the dies during rolling which reduced the workpiece diameter slightly.

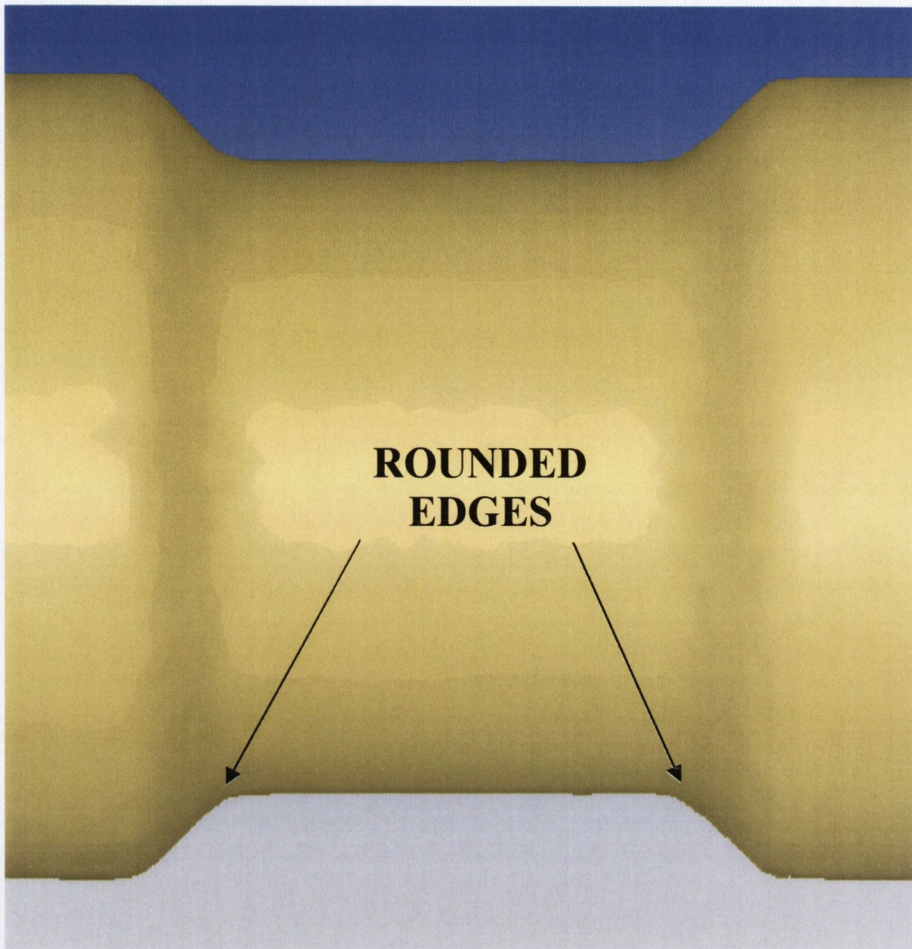


Figure 5.5 Finite element representation of the first groove Form Rolled onto a workpiece which indicates the rounded edges at the corners of the groove.

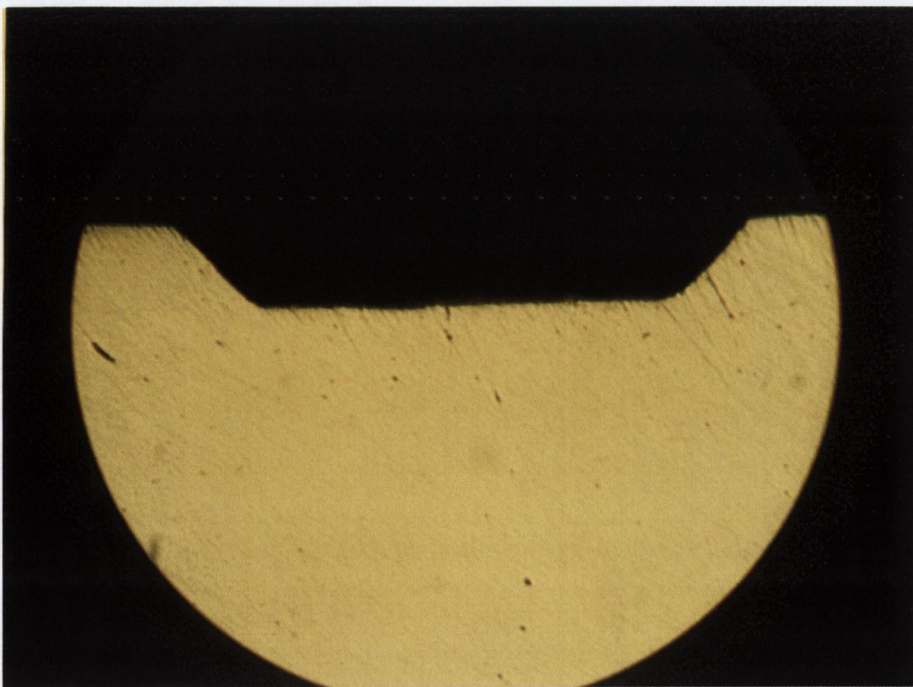


Figure 5.6 Picture of a cross-section of the first groove from a finished Form Rolled workpiece. (x50)

Table 5.3 below, compares the final geometries of the second groove of the experimentally rolled fasteners to those obtained from the FE model. Labels Q, R, H, I and J are as illustrated in Figure 5.3.

	Q	R	H	I	J
EXP (mm)	2.574	0.971	4.066	2.296	4.061
FEA (mm)	2.612	0.950	4.070	2.380	4.073
% Difference	1.455	2.163	0.098	3.529	0.295

Table 5.3 Second groove dimensions (mm) taken from experimental tests and the FE model.

Similar to the first groove, the difference between the FE and experimental measured geometries for the major and minor widths, labels **Q** and **R** respectively, of the second groove can be attributed to the rounded corners of the FE model. However, there is still good correlation between both sets of results which indicate a very small percentage difference of 1.455% and 2.163% for labels **Q** and **R** respectively. As for the first groove, the experimental and FE measurements of the side diameters of the groove i.e. labels **H** and **J**, are very similar. However, the smallest diameter of the groove, label **I**, is less than the anticipated diameter as per the die design. The diameter should have been 2.424mm, however both the experimental and FE results are below this value which indicates that necking has occurred at the base of the second groove. This will be discussed in more detail in section 5.2.2.1.

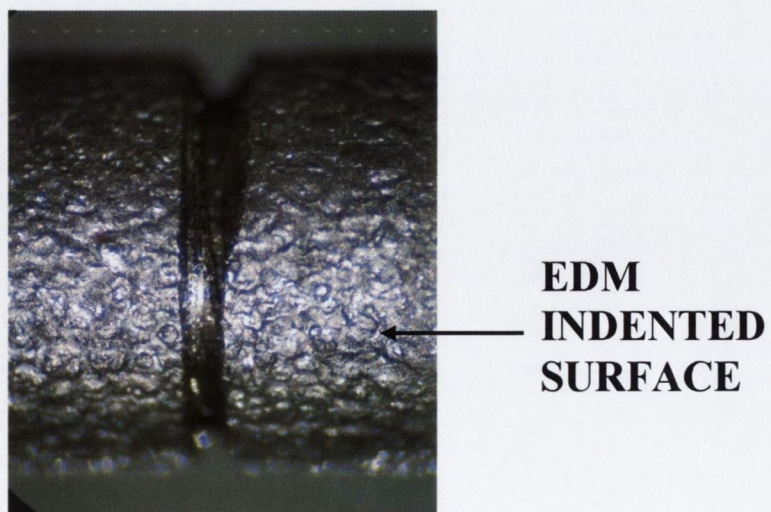


Figure 5.7 Roughened surface on the workpiece due to the EDM finish on the tooling.

It should be noted that experimental error for the measurements of the diameters at the side of the groove up as far as the dwell of the die can be attributed to the EDM surface of the die which is indented onto the workpiece, as shown in Figure 5.7. In the dwell section of the die there was no EDM surface enabling the roughened surface to be ironed from the workpiece.

5.1.2 Workpiece Material Flow

As previously stated the die features that generated the groove shapes in the workpiece were designed to cause the material to flow towards the tip of the fastener. It should be noted that for all of the figures showing axial (longitudinal) views of the fastener in this chapter, the head and tip of the fastener are towards the left and right respectively of the figures. With this in mind Figures 5.8 (a) and 5.9 (a) show the workpiece shape after the first and last 360° workpiece rotation. Figures 5.8 (b) and 5.9 (b) show the corresponding vector plots of the material flow. For the velocity vector scale the dark blue colour represents the least and red the greatest velocity magnitude. The same scale for the magnitude of the material velocity was applied to both figures.

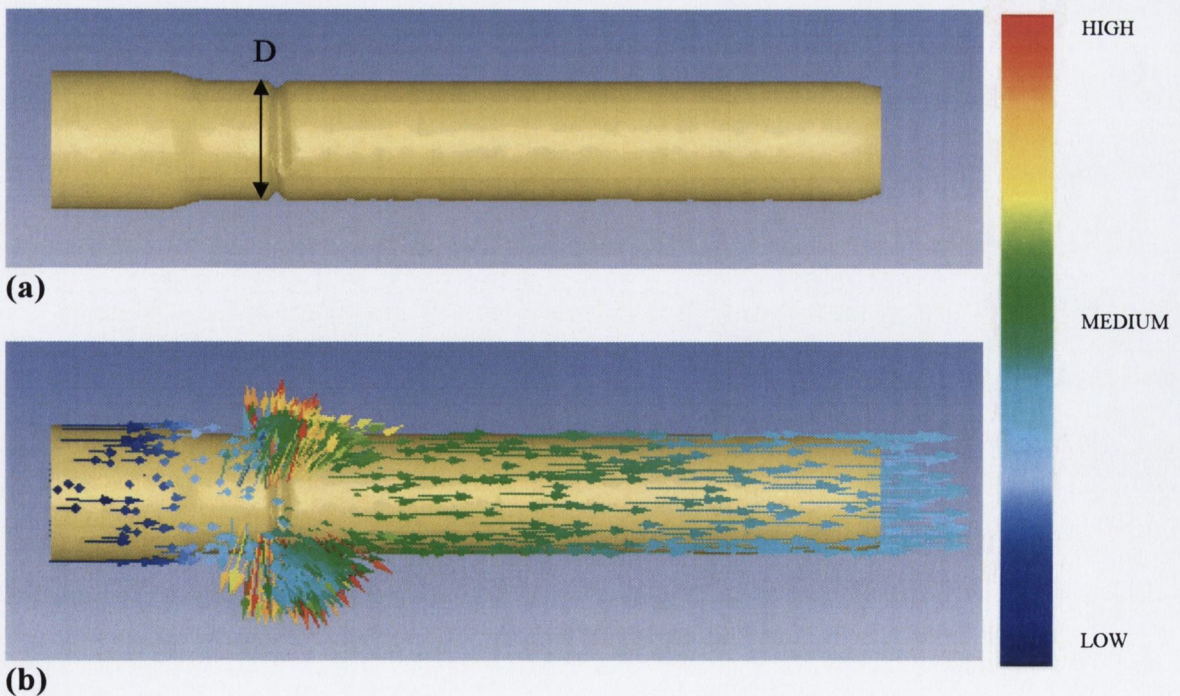


Figure 5.8 (a) Surface of the workpiece after 360° rotation and **(b)** the associated vector plot.

As intended by the die design Figures 5.8 (b) and 5.9 (b) confirm that the workpiece material flow is predominantly towards the tip of the workpiece. This is in keeping with experimental results where the distance from the diameter labelled **D** in Figures 5.8 (a) and 5.9 (a) to the fastener head i.e. labelled as **M** in Figure 5.3, did not increase during the process. **D** is similarly labelled in Figure 5.3.

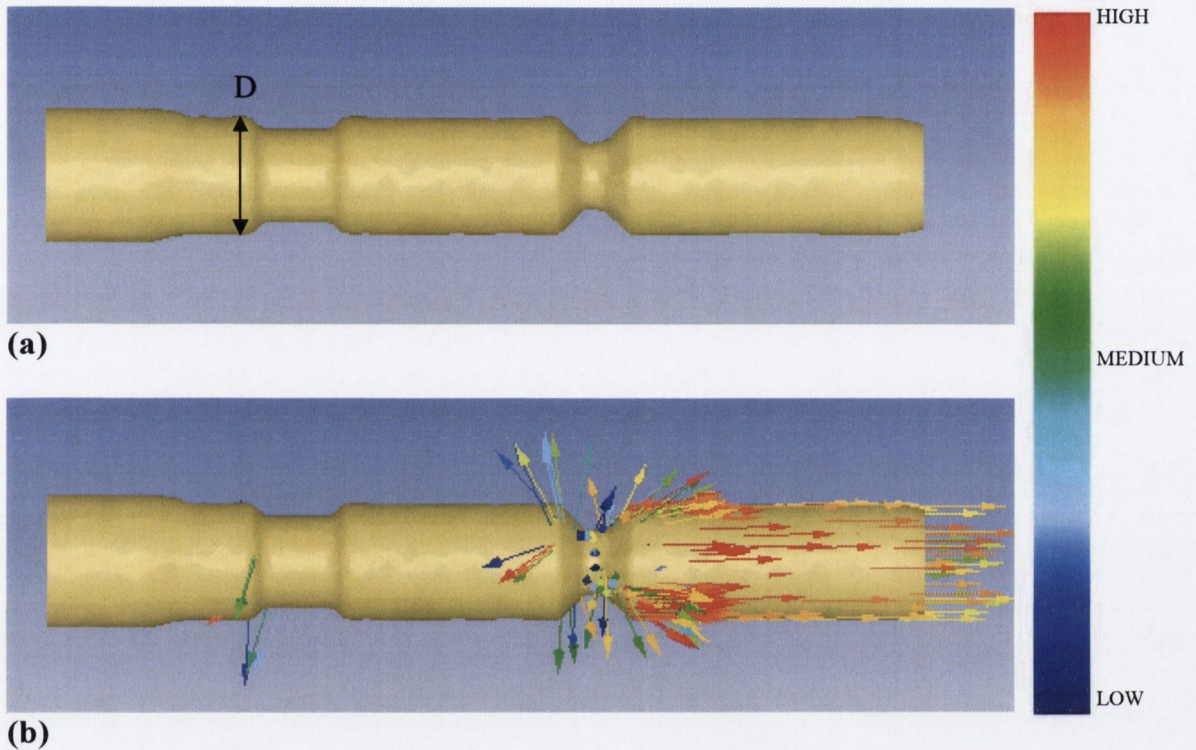


Figure 5.9 (a) Surface of the workpiece during the last 360° rotation and **(b)** the associated vector plot.

5.2 Workpiece Defect Mechanisms

Various modes of fastener surface defects have been previously discussed in Chapter 2. These included:

- Lapping
- Necking
- Cracking
- Twisting
- Squaring

Of these five modes of failure the first four can be investigated using the 3D model developed as part of this project. However, squaring cannot be investigated because the FE model setup, as described in Chapter 4.2.5, does not allow for interfacial slip to occur between the dies and the fastener because the workpiece is stationary.

In this section, the appearance of minor cracks along the base of the groove will be shown, using a two-tailed t test, to occur at regular intervals which suggest that they are generated by excess *wave form* material causing lapping. This will be followed by an investigation into the contributing factors that generated a major crack on the surface of the second groove of the workpiece.

5.2.1 Lap Generation

Lapping as described in section 2.1 is generated when material folding occurs and has been identified using both experimental and FE analysis. Material folding occurs at two locations on the groove namely:

- The angled sides of the groove
- The base of the groove

The mechanism by which material folding occurs at each location during the formation of the grooves will now be addressed.

5.2.1.1 Lapping at the Angled Sides of the Groove

As shown previously in Figures 5.8 (b) and 5.9 (b), material flows predominantly towards the tip of the fastener. However, this is not the case for the material directly beneath the die feature that forms the grooves onto the fastener.

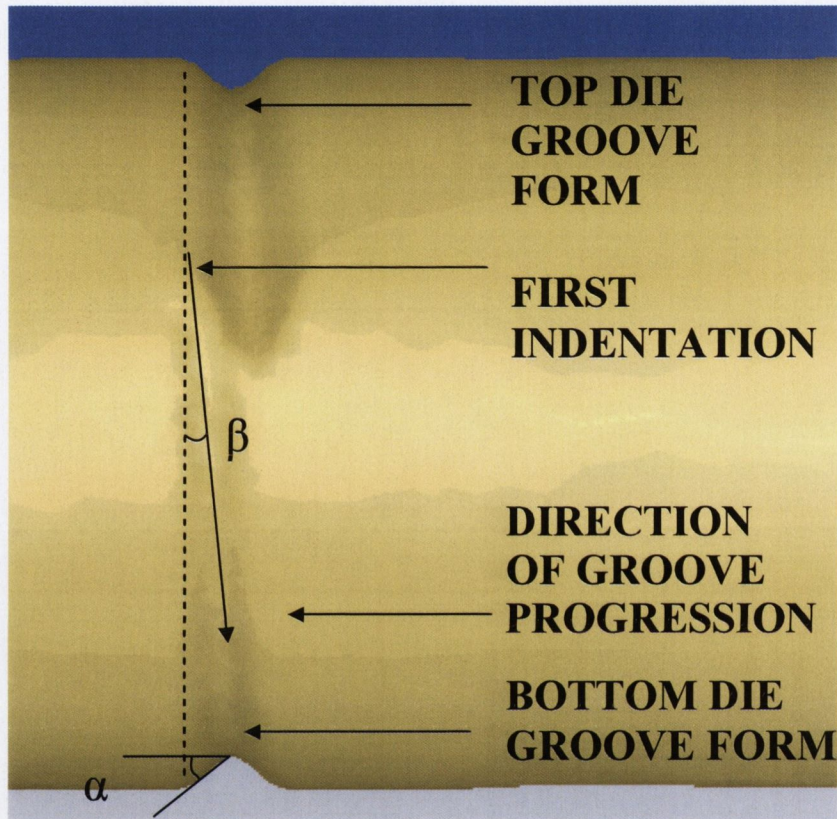


Figure 5.10 Form Rolled groove features through 180° rotation of the workpiece.

Figure 5.10 shows the indentation of the fastener generated by the dies after 180° rotation. The groove forms simultaneously at the top and base of the fastener through the actions of the top and bottom dies, respectively. In Figure 5.10, the first point of indentation of the bottom die onto the workpiece is shown. It can be seen that the dashed line in Figure 5.10 is collinear to the first point of indentation. From this line all of the material flows towards the tip of the fastener i.e. from left to right. Therefore, this dashed line indicates the outmost edge of the groove. Also labelled in this figure are α and β which are the forming and stretching angles, respectively. The geometries of these angles are transferred from the dies onto the workpiece. As the workpiece rotates, the path of the die is indented onto the workpiece, progressing in a helical fashion onto the workpiece as illustrated by the

solid arrow. The stretching angle, β , can be determined by tracing a line through the centre of the groove. This was measured from the FE model as 4° for the first groove which is equal to the stretching angle on the actual die, as shown in Appendix A.

Figures 5.11 (a), 5.12 (a) and 5.13 (a) show the development of the first groove after 180° , 270° and 360° rotation of the fastener respectively. Figures 5.11 (b), 5.12 (b) and 5.13 (b) show the nodes that are in contact with the dies, blue for the top die and red for the bottom die at 180° , 270° and 360° rotation respectively. The shaded area in these figures illustrates the contact area between the workpiece and the dies. The rate at which the full groove depth is achieved during the *knifing* stage of the die is determined by the inclined angle, γ , which was previously shown in Figure 1.6. The *knifing* stage is 12.34mm in length and equivalent to 347° workpiece rotation. On completion of the *knifing* stage, the width of the groove is gradually increased as shown in Figures 5.13 (a) and (b).

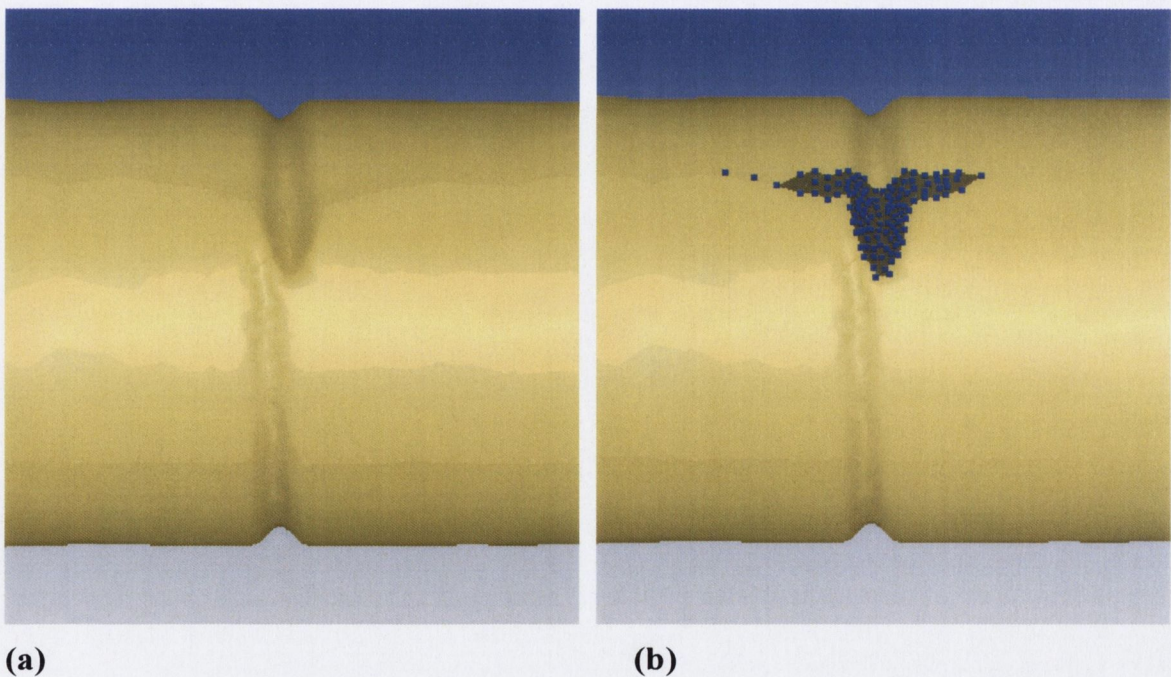


Figure 5.11 (a) Illustration of the first groove form and **(b)** area of contact between the workpiece and the bottom die, after 180° workpiece rotation.

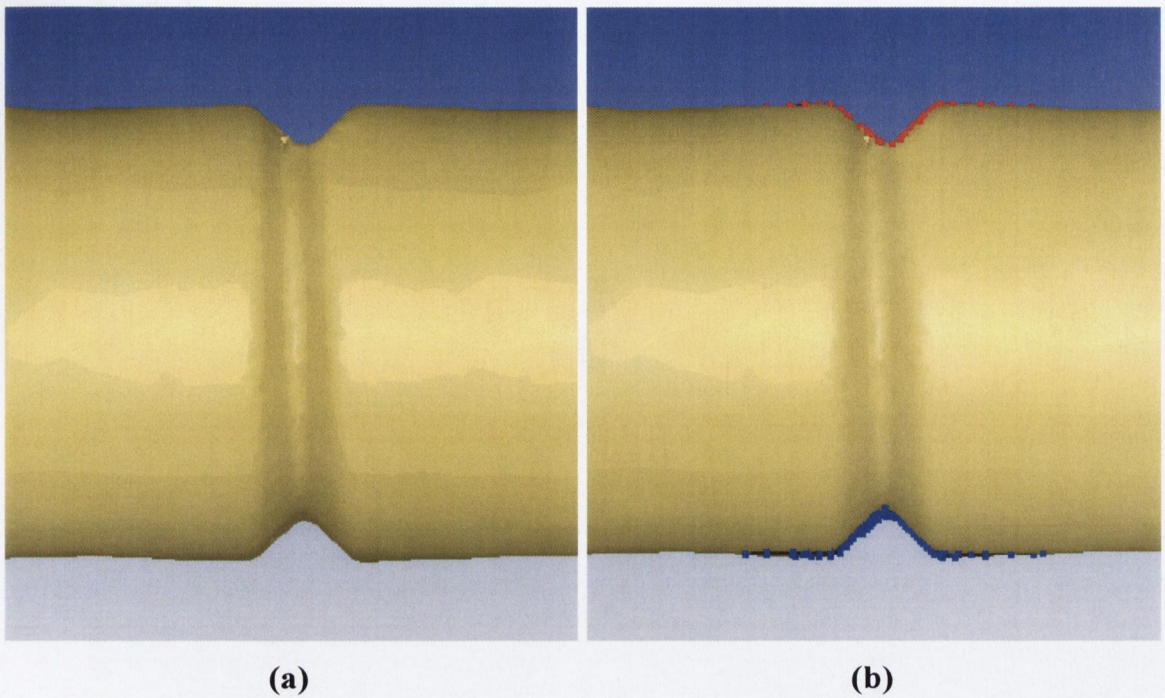


Figure 5.12 (a) Illustration of the first groove form and **(b)** area of contact between the workpiece and both dies, after 270° workpiece rotation.

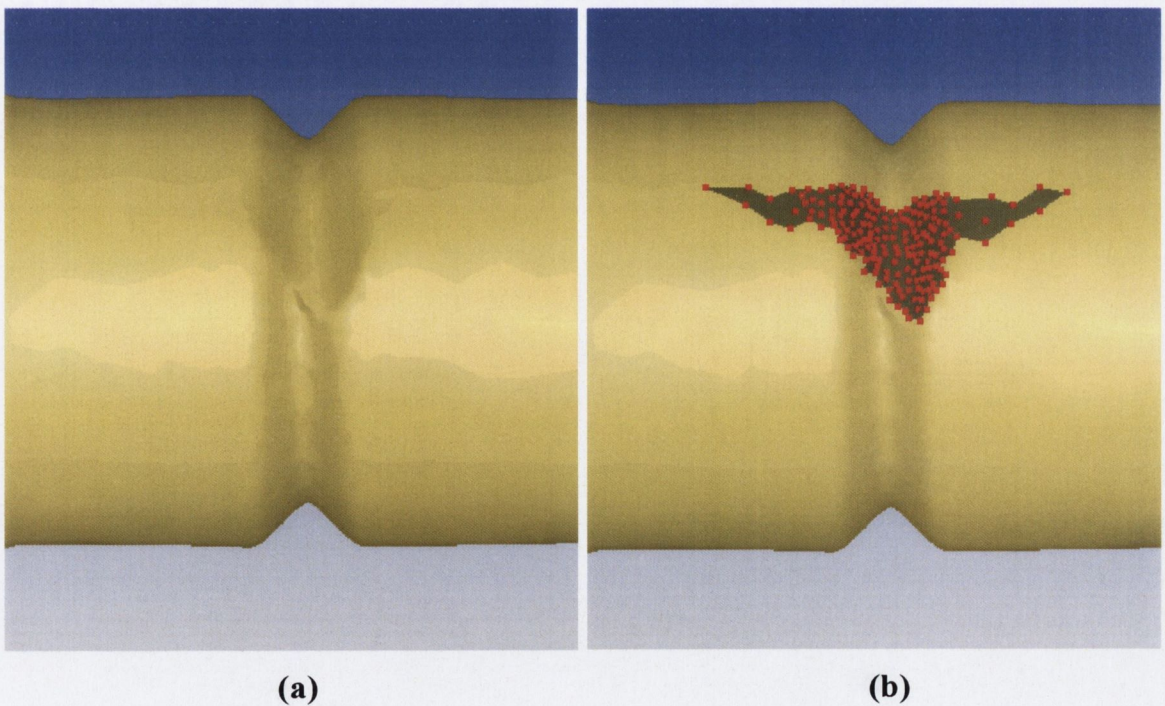


Figure 5.13 (a) Illustration of the first groove form and **(b)** area of contact between the workpiece and the top die, after 360° workpiece rotation.

Given the nature of the Form Rolling process, material folding along the side of the groove will tend to occur at intervals of 180° workpiece rotation until

the side of the groove is fully formed. Figure 5.14 is a magnified image of Figure 5.11 (a) which illustrates the shape of the groove after 180° rotation just when the top die is about to pass over the point of initial penetration made by the bottom die. As illustrated, the top die has generated a V shaped geometry as it forms the groove. As discussed previously, the left side of this V form is aligned with the outmost edge of the groove, shown by the dashed line, and the point of the V form is moving in a helical direction determined by the stretching angle, β . Because the point of the V form is not in line with the outmost edge of the groove, it forms material that was not plastically deformed by the bottom die. Therefore, a slight misalignment of the individual groove forms, generated by the top and bottom dies, occurs. Therefore, the groove is formed in a helical fashion as the workpiece rotates.

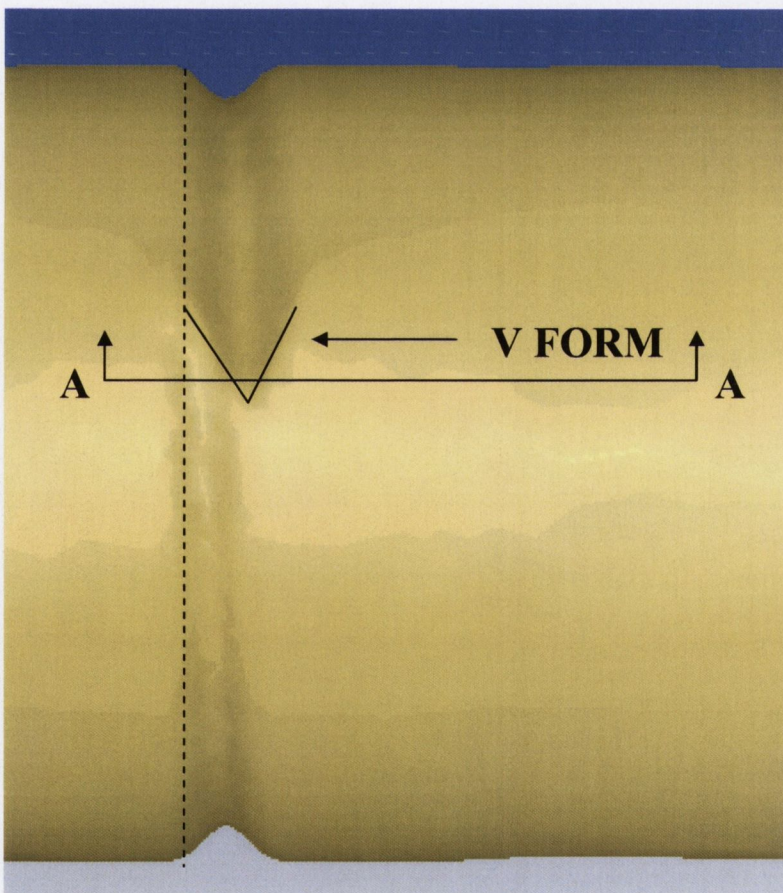


Figure 5.14 Illustration of the V form shape produced by a die after 180° workpiece rotation.

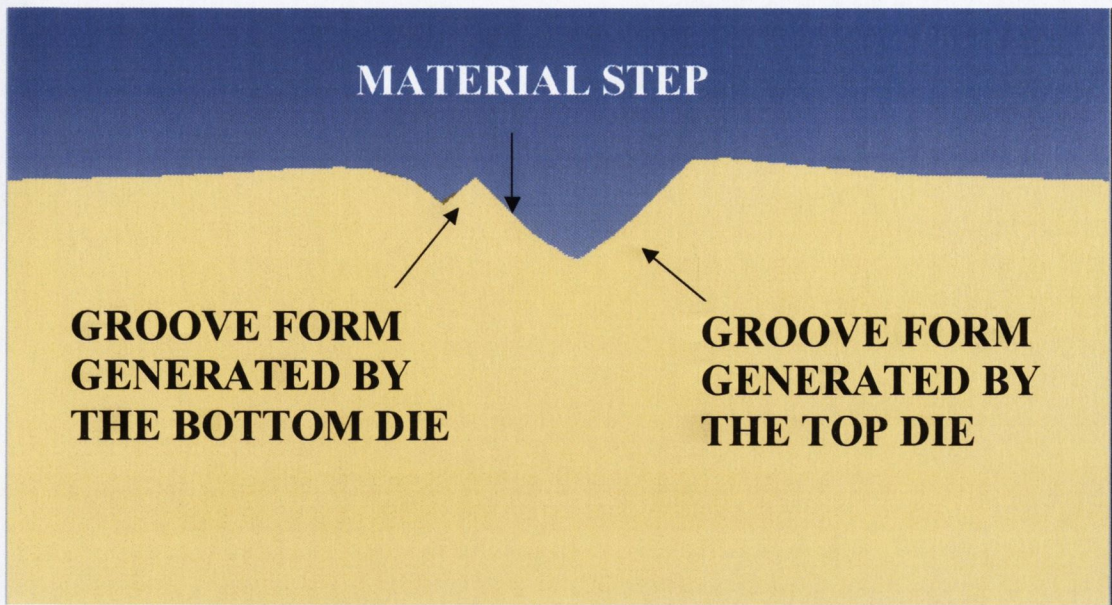


Figure 5.15 Illustration, taken through Section AA from Figure 5.14, of the generation of a material step after 180° fastener rotation.



Figure 5.16 Vector plot of material flow for a cross-section taken through the first groove after 180° fastener rotation.

Figure 5.15 is an axial cross-section, taken through the solid line AA from Figure 5.14. Figure 5.15 also shows the misalignment of the separate groove forms, generated by the top and bottom dies which results in the formation of a step of material between them. As the top die continues to form the groove, the material flows both towards the head and tip of the fastener, as illustrated in Figure 5.16. Therefore, the material step shown in Figure 5.15 “Folds” and is flattened into the side of the groove. A cross-section of the fastener taken at the same location as that shown in Figure 5.15, but after a further 20° fastener rotation is shown in Figure 5.17. From this figure it can be seen that the projecting material has “Folded” onto the groove surface. This “Folding” of the step material is known in industry as a “Lap”.

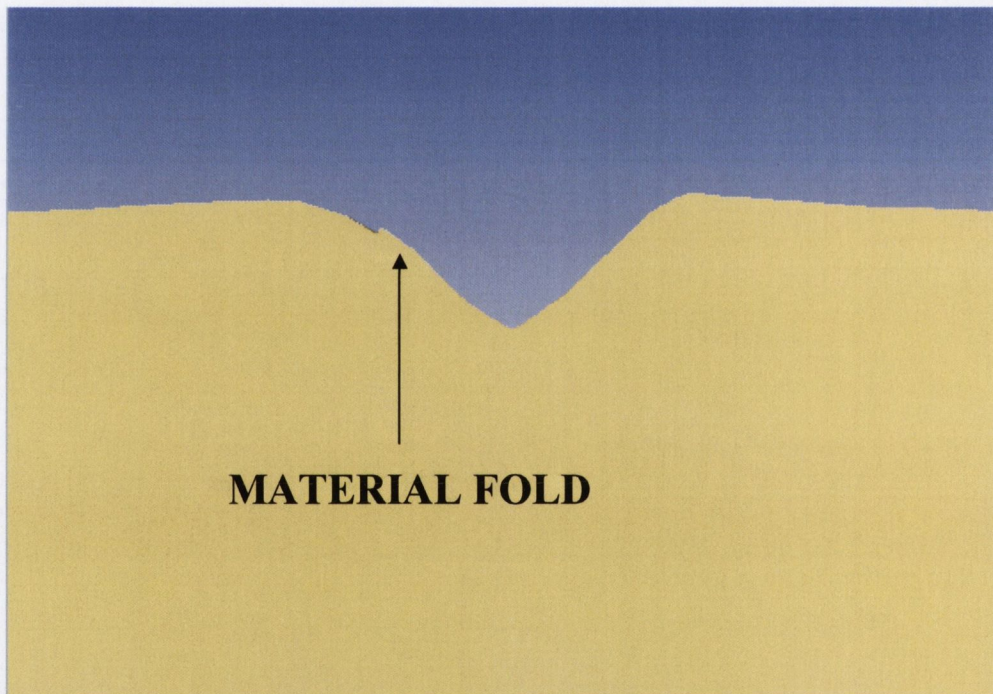


Figure 5.17 Illustration of the generation of a material fold after 200° rotation of the fastener.

The FE simulation results presented in Figures 5.11-5.17 have been validated by an examination of the cross-sections of experimental test pieces which are presented in Figures 5.18 and 5.19. Figure 5.18 shows a magnified image of a cross-section of the fastener after approximately 360° rotation. The figure confirms the FE predicted geometry illustrated in Figure 5.15, where a step of material exists between the separate groove forms. As the die continues to form

the groove, the top of the V form, as shown in Figure 5.14, is aligned with the outer edge of the groove in both the top and bottom die grooves. As the workpiece rotates, material is pushed towards the outer edge of the groove which causes the material to fold and then lap as it is compressed against the side of the groove as shown in Figure 5.19.

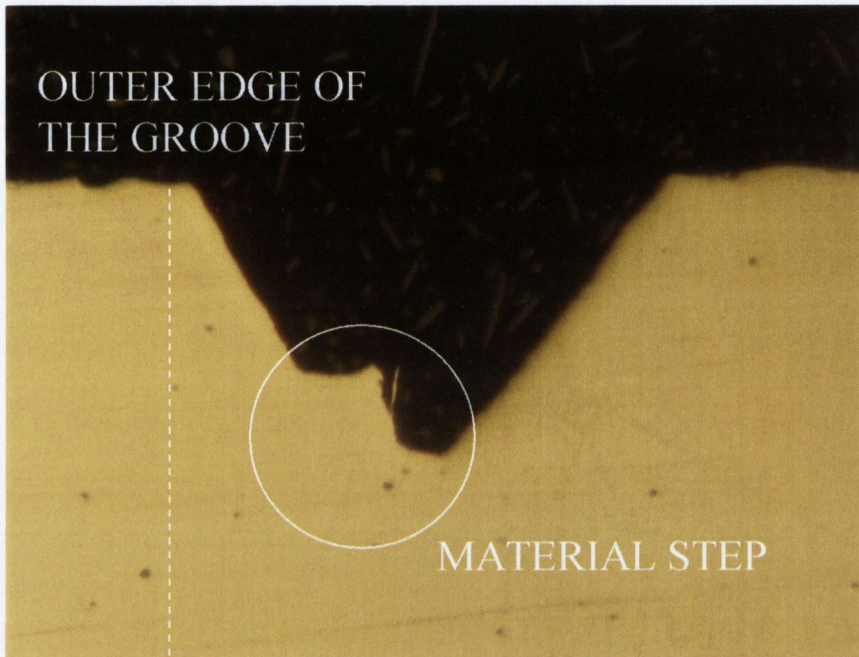


Figure 5.18 Image of cross-section of the workpiece taken after approximately 360° rotation. (x100)

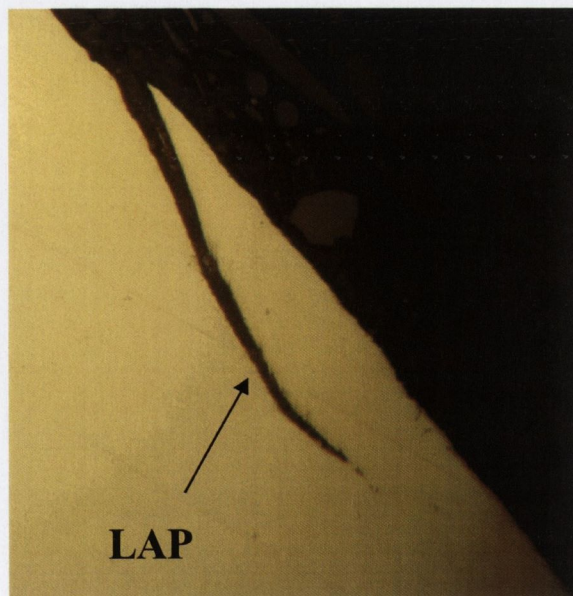


Figure 5.19 Lap located at the same position where folding material was observed during the Form Rolling of the side of the groove. (x200)

5.2.1.2 Lapping at the Base of the Groove

Having described how laps are produced at the side of the groove, a description will now be presented showing how lapping can lead to the generation of small cracks at the base of the groove.

Due to the helical path of the groove formation, the Form Rolling process generates an interesting feature, namely a “*Wave Form*”. This build up of plastically deformed material in front of the die/workpiece interface was first described as a *wave form* by Nefedov and Brezhnev [63] and has been observed in the experimental tests (Figure 5.20) undertaken for this project. The shape of this material corresponds well to that illustrated by Pater and Weronki [42] when they calculated the contact area between the die and workpiece, as shown in Figure 2.2.

The material flow resulting from the *wave form* is very complex and therefore requires further scrutiny.

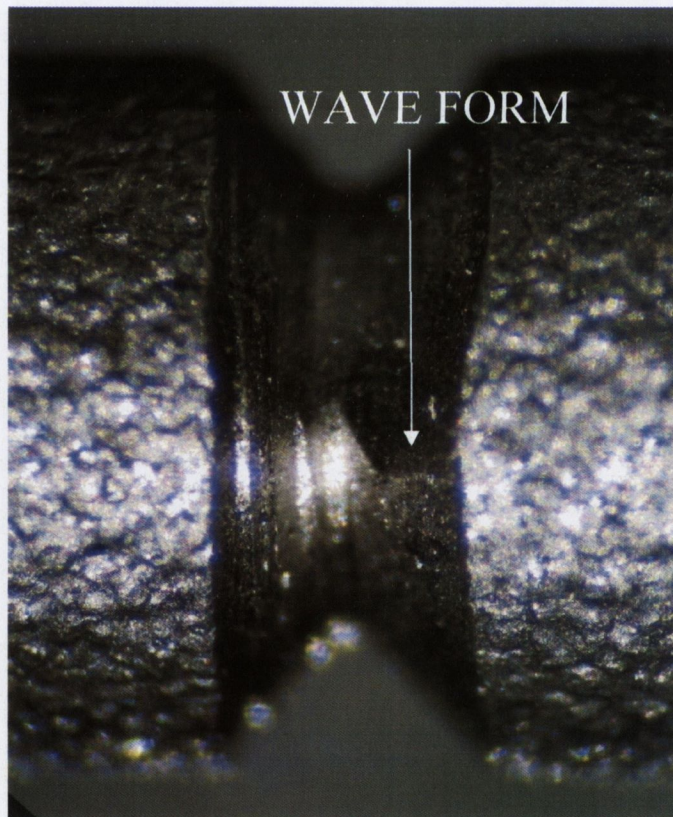


Figure 5.20 Picture of a *wave form* of deformed material on the second groove after 5 rotations of the fastener. (x4)

Figures 5.21 (a)-(d) show the gradual progression of forming the groove and the similarity between the *wave form* in the experimental tests to the FE model.

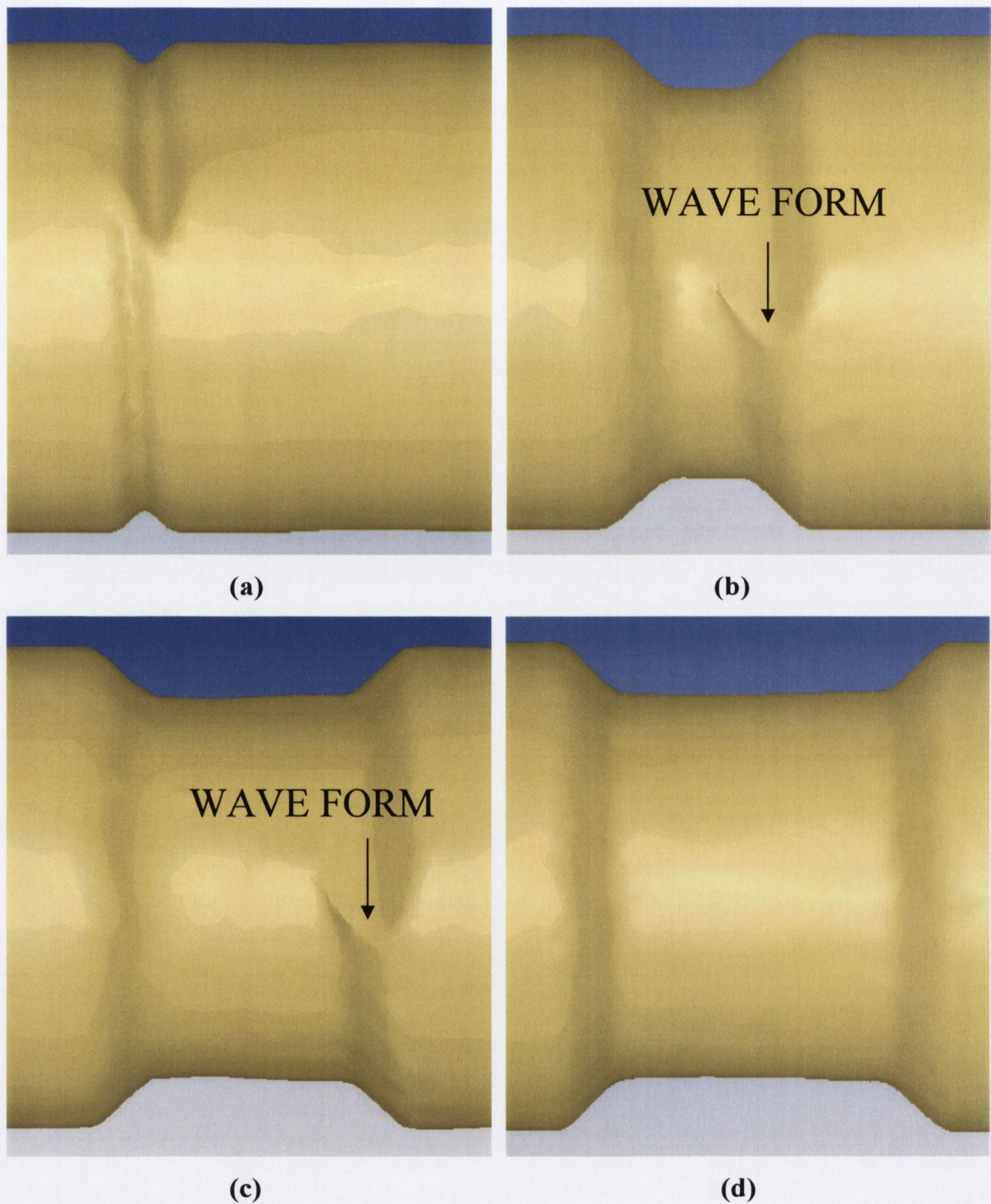


Figure 5.21 Generation of a *wave form* in the fastener material as the first groove is Form Rolled through (a) 180° (b) 720° (c) 900° and (d) 1260° rotation.

Figures 5.22 and 5.23 show vector plots of the fastener material flow after 540° workpiece rotations where the surface is translucent, as termed in DEFORM3D. Figure 5.22 (b) is the same plan view as (a) but with the addition of the shaded contact area between the top die and the fastener, with the contact nodes shown in blue.

As indicated by the red arrow originating at the *wave form* the magnitude of the velocity is greatest flowing towards the head of the fastener. This can be explained by studying Figures 5.23 (a) and (b) which show side views of the vector plots at the same stage in the process as Figures 5.22 (a) and (b). In Figure 5.23 (a) the *wave form* can be seen as having a lip shape rising from the workpiece which is circled. As the fastener rotates this material is far easier to deform than the bulk of material to the right of the groove. Consequently, the material will flow in the direction of least resistance i.e. towards the head of the fastener.

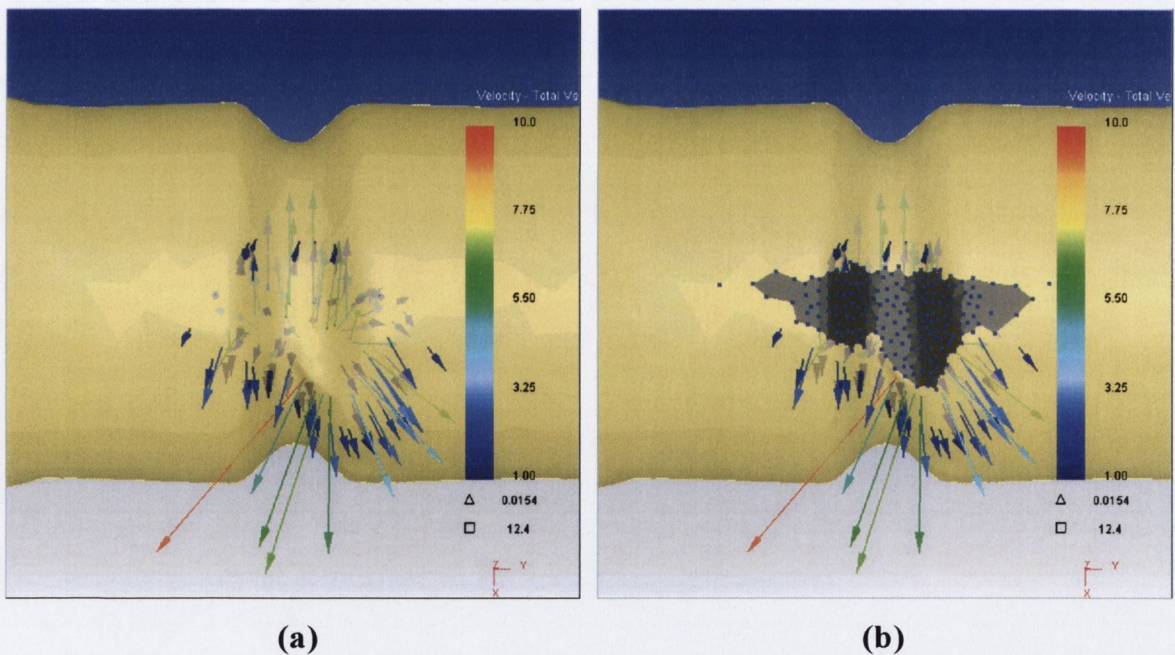


Figure 5.22 (a) Plan view of the material flow vector plot and (b) die/workpiece contact area, of the first groove after 540° rotation.

Figures 5.23 (a) and (b) also show the direction of material flow directly underneath the die/fastener interface. These material velocity vectors show that as the groove is Form Rolled the material beneath the die is compressed and flows towards the centre of the fastener, as indicated by the yellow and green arrows.

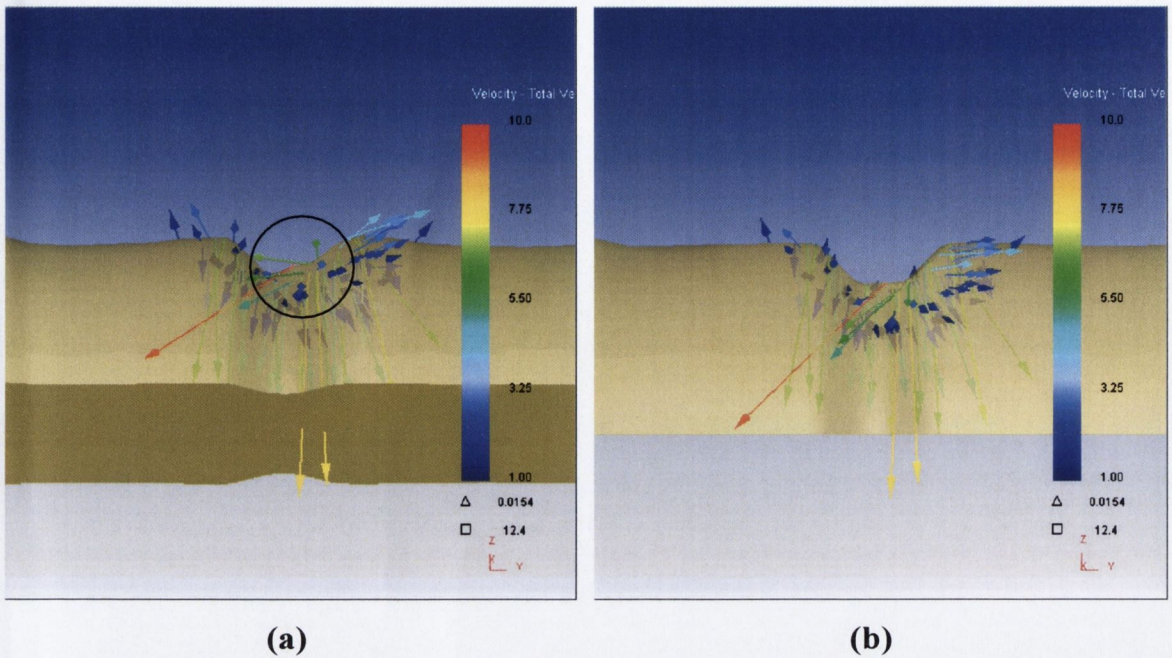


Figure 5.23 (a) Angled view and (b) side view of the velocity vectors in a cross-section of the workpiece after 540° rotation, located at the first groove.

This is perhaps better illustrated in Figure 5.24 which is a translucent radial view looking through the tip of the fastener showing the velocity vectors from the first groove. This figure is taken at the same stage of the process as the previous figures. The direction that the *wave form* material flows, which is labelled, indicates that the fastener is travelling in a clockwise direction. As described previously, the arrows beneath the die/fastener interface point in a radial plane towards the centre of the fastener. This occurs at both die/workpiece interfaces thus indicating compression. Elastic recovery, also known as *springback*, occurs when deformed material is unloaded and this region is also shown in Figure 5.24 whereby the vectors indicating elastic recovery are initiated once the fastener material is no longer in contact with the die.

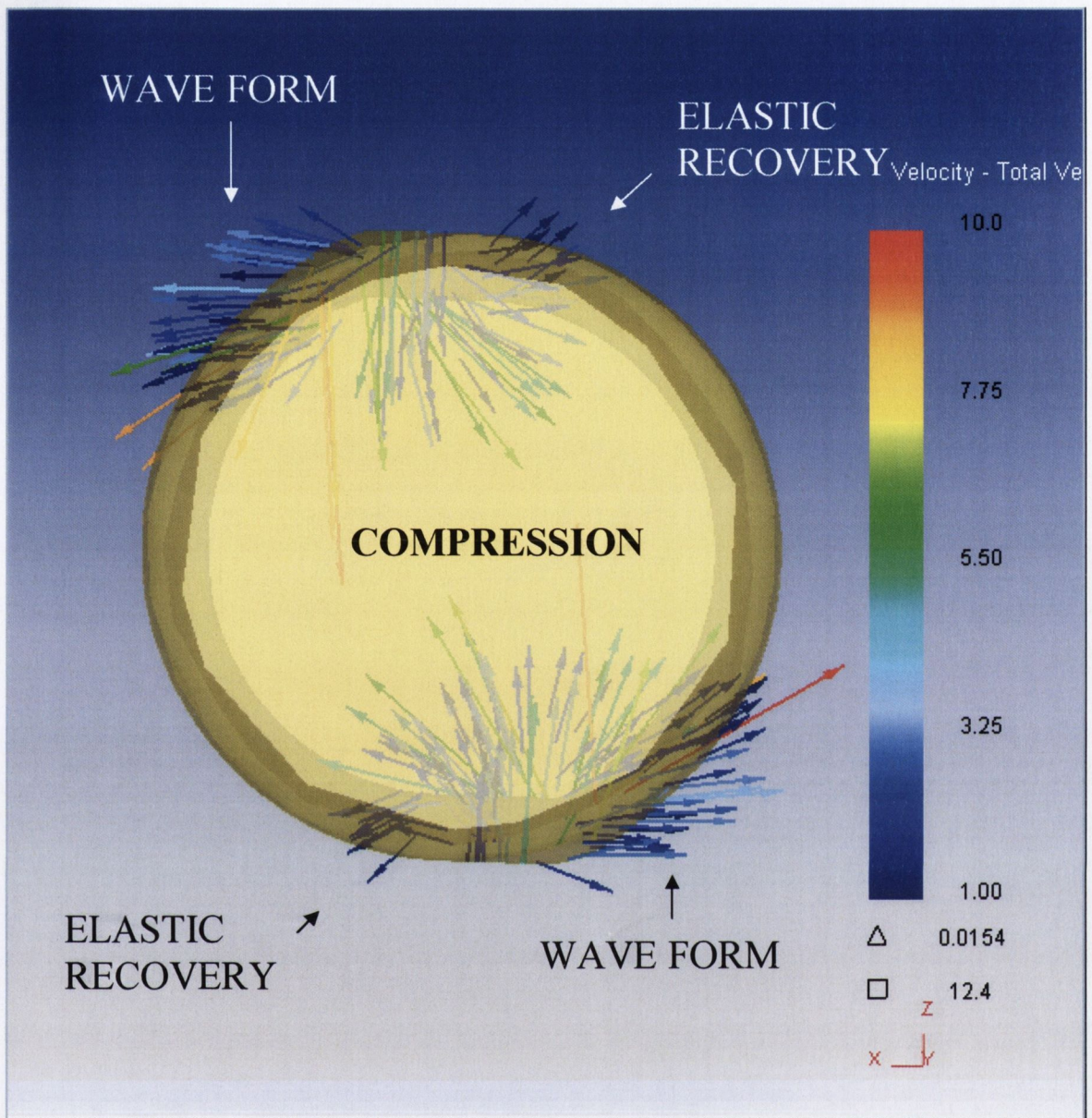


Figure 5.24 Translucent radial view through first groove after 540° rotation.

Another characteristic of the Form Rolling process is the generation of an elliptical shaped fastener as described by Tselikov [12] for a CWR process and illustrated in Figure 5.25. The elliptical form is created by the pressure and geometry of the dies which determine the level of plastic flow, as shown in Figure 5.25, due to the effect of the formation of the *wave form*.

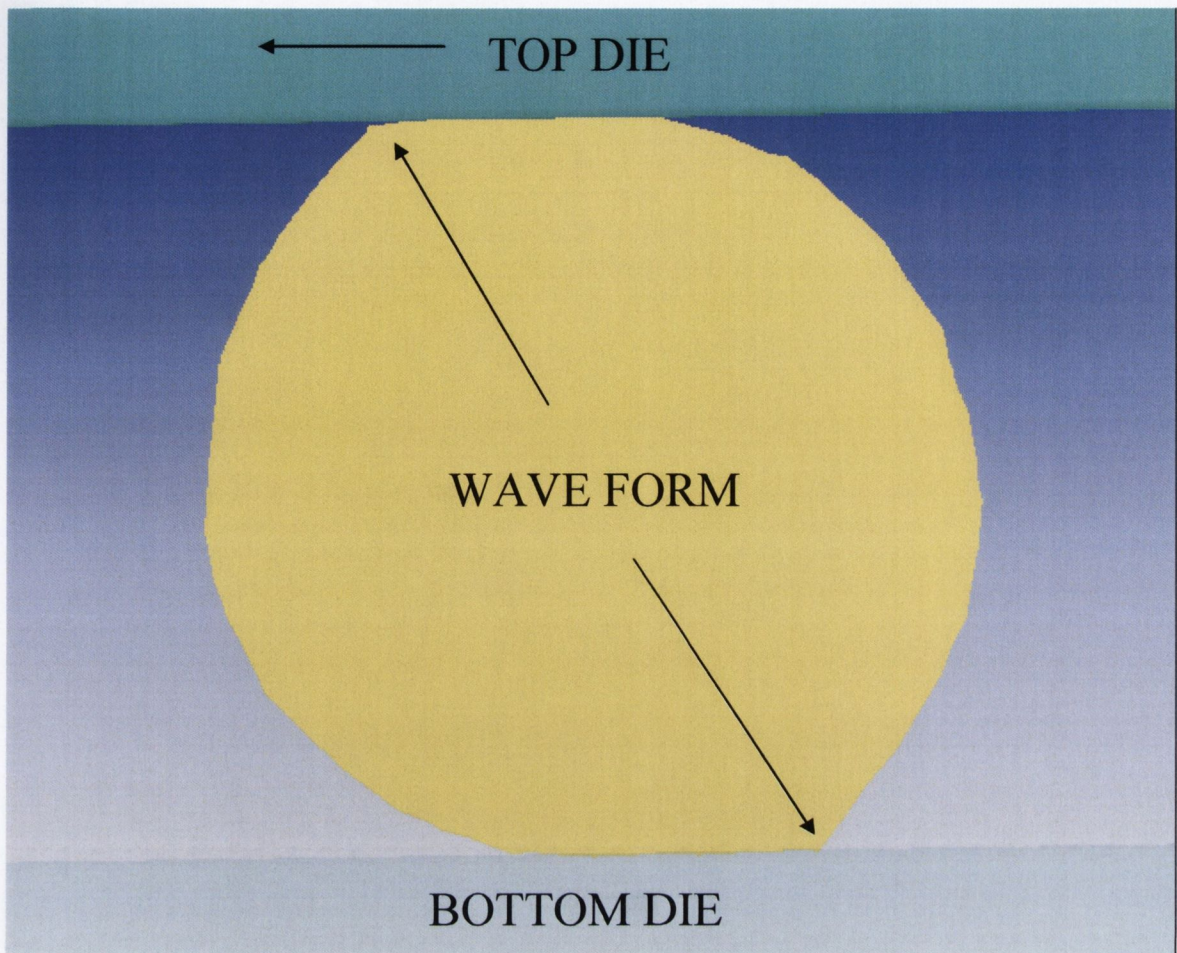


Figure 5.25 Radial cross-section through the smallest diameter of the workpiece at 540° rotation.

On initial inspection of the experimental test fasteners the laps at the base of the groove appear to be cracks, as shown in Figure 5.26. If this were the case it would pose obvious concerns about the life of the products in service. Intuitively, if cracking was caused by high stress concentration it would be likely to occur at the corner of the workpiece. However, after 2 rotations (720°), as shown in Figure 5.27, there appears to be no cracking at the corners of the groove. Therefore, it can be surmised that the small cracks which appear at regular intervals along the base of the groove are due to the effects of lapping. This will be discussed further in the next section.

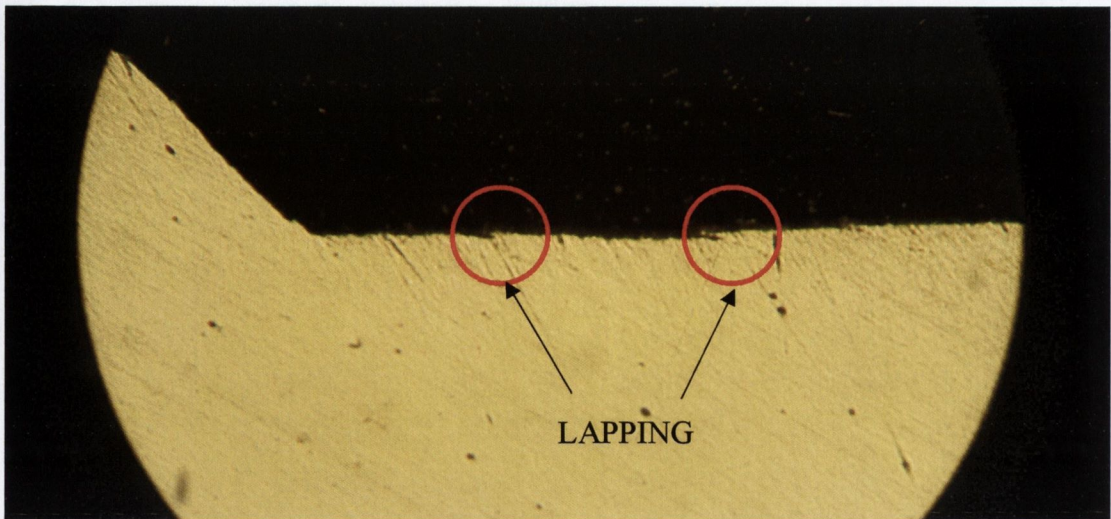


Figure 5.26 Cross-section of the first groove of a finished fastener. (x50)

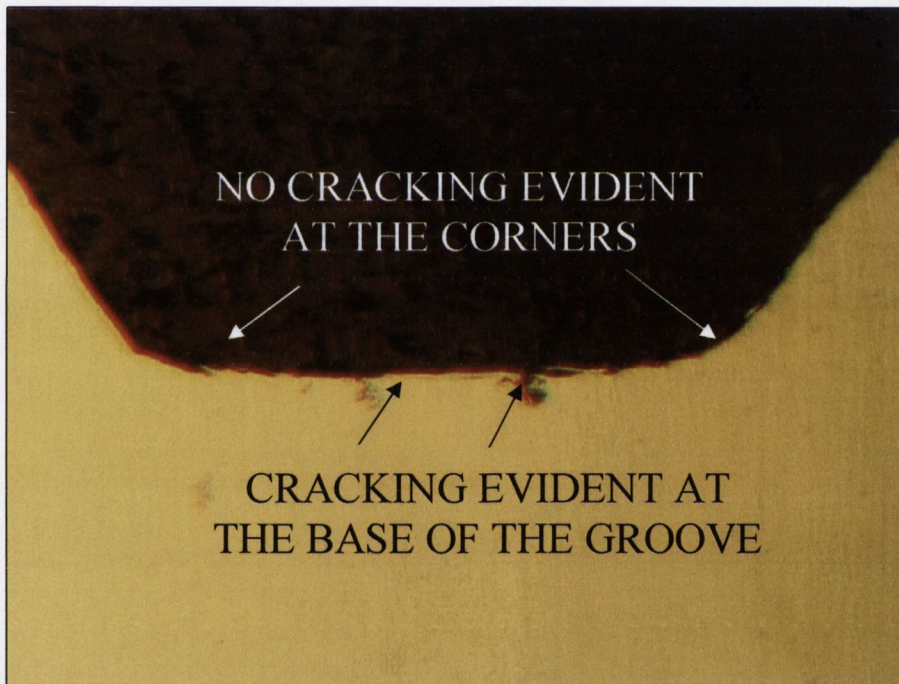


Figure 5.27 Cross-section of the fastener showing that there is no evidence of cracking at the corner of the first groove after 720° rotation. (x100)

In summary, two locations were found where laps were generated on the fastener surface due to the particular die design studied in this investigation. The first was on the left side of the groove. Laps at this location are generated during the *knifing* stage of the die. The number of laps is determined by the number of fastener half rotations required to complete the *knifing* stage which itself is determined by the inclined angle, γ . Therefore, for this particular groove design it

would be preferable to have a large inclined angle to reduce the number of rotations during the *knifing* stage thereby reducing the number of laps at the side of the groove. Alternatively, a very small inclined angle could be employed to more gradually form the material per half rotation of the fastener. This would have the effect of reducing the amount of material displaced per half rotation which would reduce the risk of inducing laps. It should be noted that laps do not occur on the right side of the groove during the *knifing* stage which also applies to the right side of the completed groove. Folding on the right side of the groove would only occur if the stretching angle, β , was very large. To prevent this occurring, the recommended stretching angle is between 3° and 5° [16, 58].

The second location where laps were found is at the base of the groove. Lapping at the base of the groove is generated due to the *wave form* material folding as the groove is widened which is determined by the stretching angle, β . Therefore, in order to prevent lapping at the base of the groove the size of the *wave form* must be decreased. To do this, the stretching angle, β , should be decreased so that the groove is Form Rolled more gradually. However, this would require machines with greater stroke lengths to fit longer dies which may not be commercially feasible.

Perhaps an alternative to the above suggestions would be to merge the *knifing* and *stretching* stages into one. Therefore, as the groove is widened its depth is also incrementally increased along the length of the ramp section of the die. This would have the effect of more gradually displacing material to form the groove.

5.2.1.3 Validation that Laps are Generated at the Base of the Groove

Having explained how lapping can be generated by material folding and being compressed by the dies, evidence is still required to support this hypothesis. Therefore, two-tailed t tests were performed using experimental data. However, first a description of the number and position of the small cracks that were found at the base of the first groove will be given. The results obtained from which will be applied to the t tests.

The locations where lapping was observed are illustrated in Figure 5.28 for the first groove. The first groove on the fastener was formed during the first 3.5 rotations, and as discussed previously the groove is formed in a helical path which was determined by the stretching angle, β . Therefore, if a point on the surface is taken at the start of the process, that point would experience 7 separate indentations from the dies as the fastener was rotated 3.5 times. As illustrated in Figure 5.28, numbers 1 to 7 show approximately where laps were found in a completely formed fastener as shown in Figure 5.29 below. If these laps were generated by the dies then they should be equally spaced along the base of the groove form.

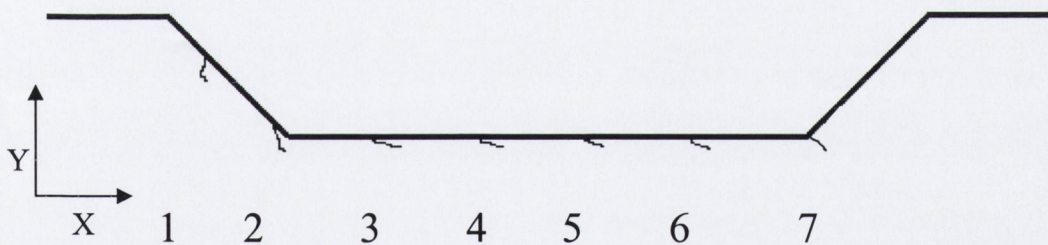


Figure 5.28 Illustration of the appearance of defects due to lapping in the first groove of the workpiece over 3.5 rotations.

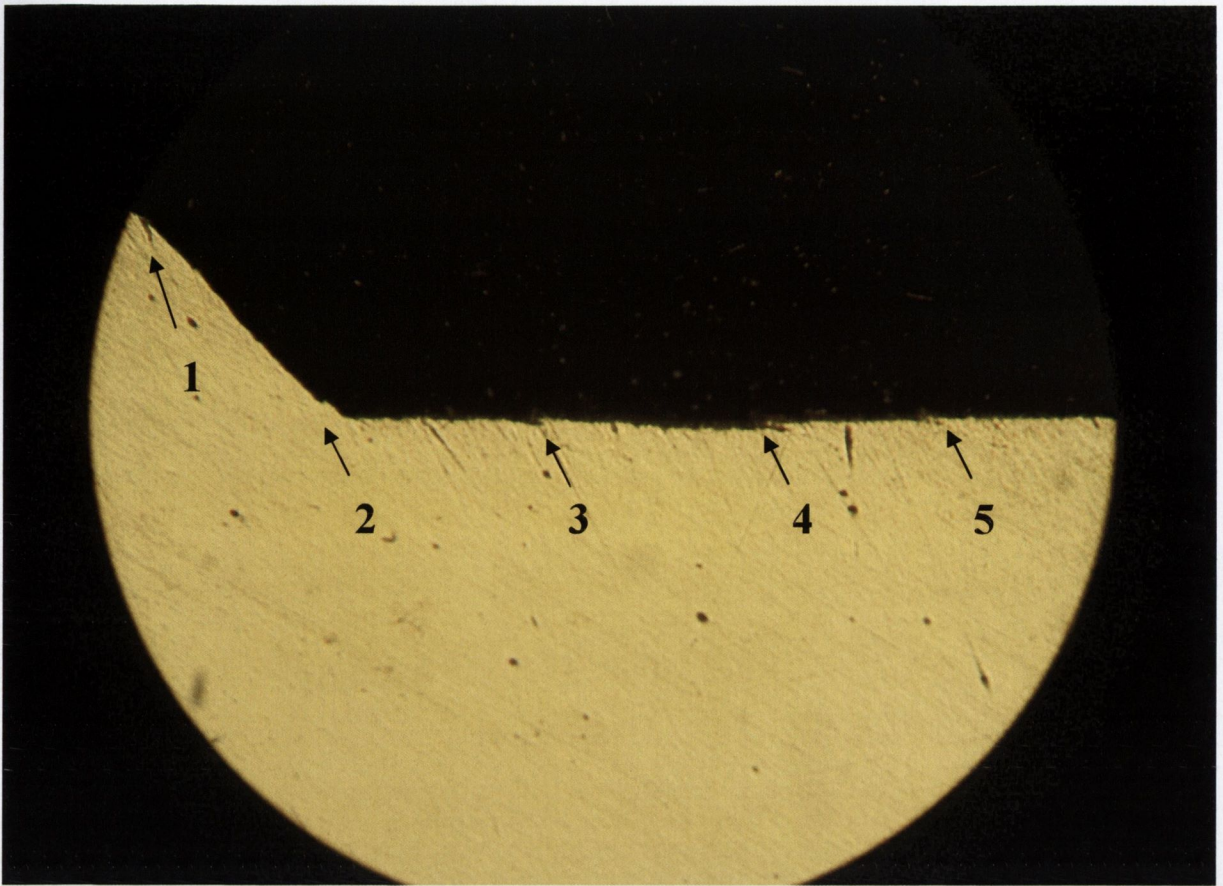


Figure 5.29 Origin of numbered cracks on the base of the groove. (x100)

In order to predict the probability that the experimentally observed laps occurred at regular intervals determined by the die geometry, two-tailed t tests were performed. Due to their position on the groove base, the distances from laps 3 to 4, 4 to 5 and 5 to 6 were averaged from a sample number of 10 fasteners and then the mean distances were separately applied to the t tests. Lap 7 was not applied to the t test because less material was displaced in the final half rotation than the other previous rotations. This had the effect of providing less material to form a lap. Consequently, a seventh lap was not always found in the cross-section of the fasteners.

The t test compares the null hypothesis, H_o , to an alternate hypothesis, H_A , for the statement that a population mean, μ_o , is equal to a specified mean value. If the geometry of the die generated the laps, a regular distance of 0.454mm should be between each lap because the same volume of material is displaced per half rotation. Therefore, the specified mean is 0.454mm which is the distance that the

groove width increased by per 180° fastener rotation in the axial direction, as shown in Figure 5.28.

The specified mean was compared to the alternate hypothesis which was whether the mean of the distances between the individual cracks, could to within a 95% confidence level, belong to the specified mean. The hypothesis and the method of calculating a t value are outlined below:

$$H_0: \mu_0 = 0.454\text{mm}$$

$$H_A: \mu_0 \neq 0.454\text{mm}$$

For a t test:

$$t = \frac{\bar{X} - \mu_0}{s_{\bar{x}}} \quad (5.1)$$

where

\bar{X} = Sample average

$s_{\bar{x}}$ = Estimate of the variance

and

$$s_{\bar{x}} = \frac{s}{\sqrt{n}} \quad (5.2)$$

where

n = Sample number

s = Standard deviation

When the t value was calculated, the critical value of t was obtained whereby

$$t_{\alpha(2),v}$$

where

$$\alpha = 0.05$$

(2) = 2 tailed t test

$$v = n-1$$

Therefore if $|t| > t_{\alpha(2),v}$, then the null hypothesis can be rejected and the sample population has a mean that is not equal to the specified mean. However, if $|t| < t_{\alpha(2),v}$, the hypothesis is true.

The t values calculated for each of the two tailed t tests were as follows:

- Crack 3 to 4: $t = -0.6060683$
- Crack 4 to 5: $t = -0.9687581$
- Crack 5 to 6: $t = 1.5356945$

The critical value of t was found to be 2.262. Therefore, as the magnitudes of all of the separate t values are less than the critical value, the hypothesis for each distance between the cracks as belonging to the specified mean of 0.454mm is true. Therefore, the probability of the magnitude of the t values lies within a 95% confidence level can be expressed as:

$$P(|t| \leq 2.262) = 0.05$$

A Z test generates a standard score for the specified mean i.e. 0.454mm, with respect to the measured distances from the respective laps and returns the two-tailed probability for the normal distribution. This function is used to assess the likelihood that a particular observation is drawn from a particular population [82] The Z value can be described as:

$$Z = \frac{\bar{X} - \mu_0}{\sigma_x} \quad (5.3)$$

where

$$\sigma_x = \sqrt{\frac{\sigma^2}{n}} = \text{Population standard error of the mean} \quad (5.4)$$

The respective P values for the three Z tests are:

- Crack 3 to 4: $P = 0.72777$
- Crack 4 to 5: $P = 0.83367$
- Crack 5 to 6: $P = 0.06231$

Therefore, as each of the P values are greater than 0.05, there is a 95% likelihood that the distances between the cracks belong to the hypothesised value of 0.454mm which was determined by the die geometry.

5.2.2 Surface Fracture

This section will present results to explain how a crack was initiated at the base of the second groove and subsequently propagated. The first groove will not be addressed because there was no evidence of necking or fracture in that groove.

5.2.2.1 Analysis of Surface Fracture

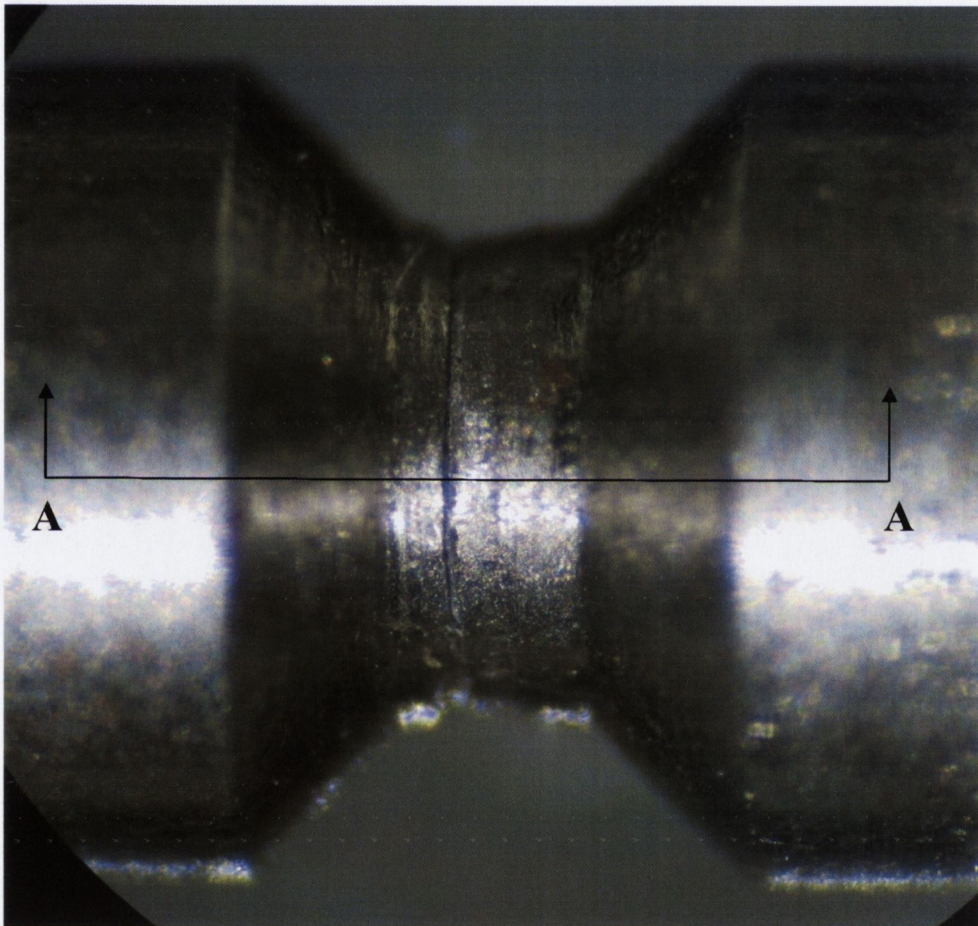


Figure 5.30 Photograph of the second groove surface of a fully Form Rolled fastener. (x4)

Figure 5.30 shows a photograph taken through an optical microscope of a finished workpiece. A crack on the surface is clearly visible around the circumference of the fastener. Figure 5.31 shows a cross-section taken through section AA in Figure 5.30, revealing that the crack is visible because as it propagated into the body of the fastener, material became detached from the surface.

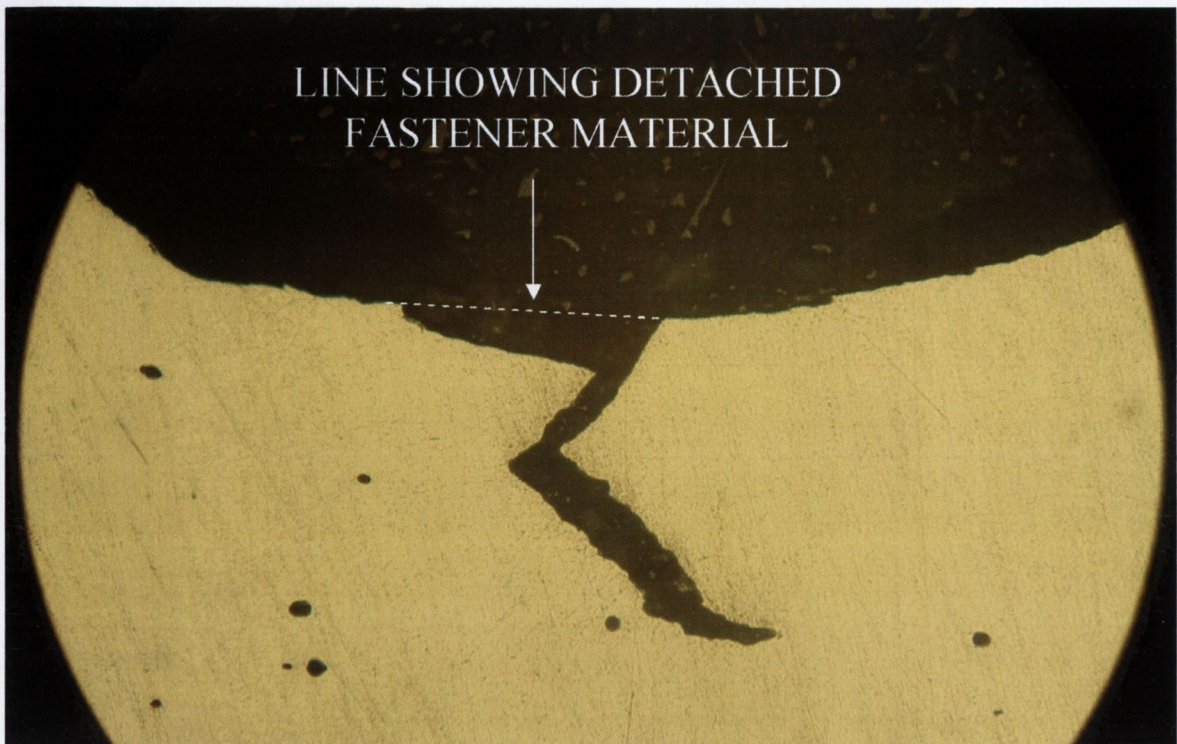


Figure 5.31 Photograph of a cross-section of the second groove showing a crack and illustrating missing fastener material. (x100)

However, the question remains as to how the crack was initially formed. The crack shown in Figures 5.30 and 5.31, developed during 5 and 6 rotations of the fastener. Figure 5.32 is a photograph of one sample taken after 5 rotations. The steps labelled 1–5 which appear at regular intervals were formed by *reverse lapping*, as the motion of the top die was reversed so that the workpiece could be extracted. The step labelled 5, as can be seen in Figure 5.32, is located at the base of the groove. This step of material is at the location where the large crack developed between the 5th and 6th rotation of the workpiece, as shown in Figure 5.33.

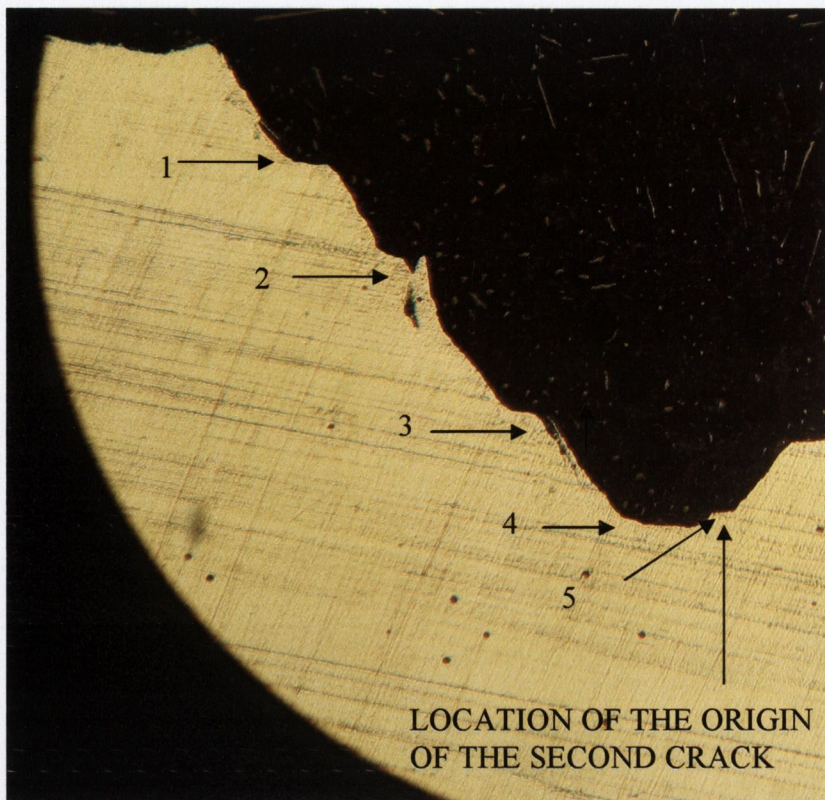


Figure 5.32 Material folds along the periphery of the second groove after 5 rotations of the fastener. (x50)

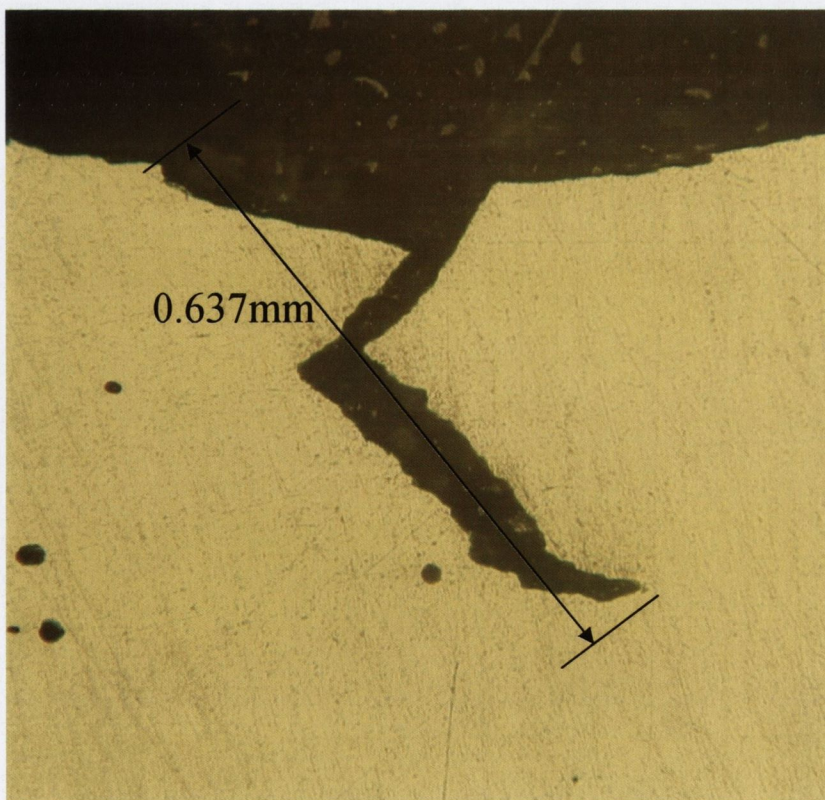


Figure 5.33 Photograph showing the length of a crack in the second groove which first appeared after 6 rotations of the fastener. (x100)

Therefore, if it is assumed that a lap containing a small crack developed at the base of the groove in the same location as where a major crack was found, the question remains as to how the crack propagated.

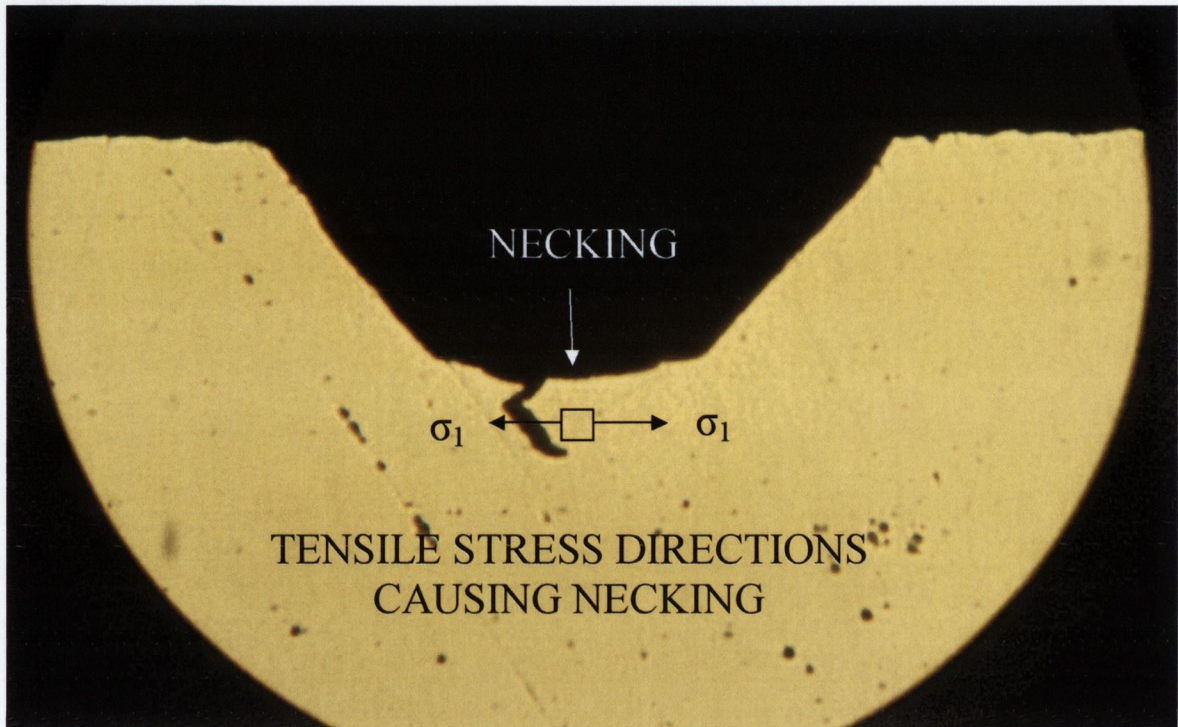


Figure 5.34 Location of necking in the second groove of the workpiece as observed in experimental testing.

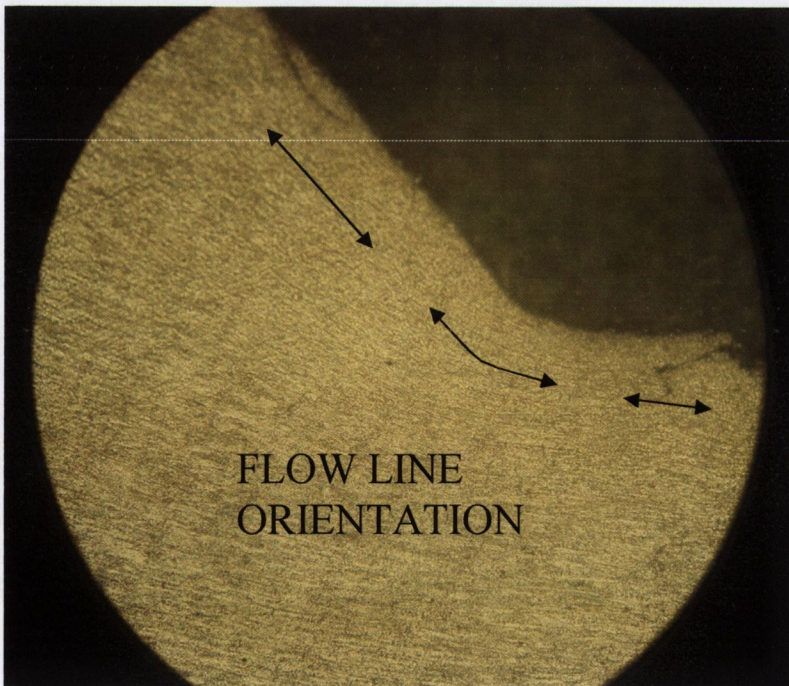
Figure 5.34 shows the cross-section of the workpiece after 6 rotations. It is apparent that necking has occurred i.e. excessive straining of the material at the centre of the groove. After the 6th and 7th rotations the mean of the experimental measured diameter, labelled I in Figure 5.3 was 2.358mm and 2.296mm respectively. This equated to a difference of the means of 0.067mm and an overall difference from the anticipated dimension (2.424mm), as per the die design, of 0.128mm. Therefore experimental results would suggest that the fastener had experienced the affects of necking.

Evidence was sought to corroborate the experimental results from the FE model of the process. However, the mean of the final diameter of the second groove was measured at 2.38mm which when compared to the expected geometry of 2.424mm there was a difference of 0.044mm. This result suggests that the fastener in the FE model also experienced necking but not to the same extent as in the actual fastener. Further investigation was undertaken using a combination of

etched macroscopic samples, to reveal the material flow lines and the crack tip, and to provide details of the stress distributions so as to determine the cause of the crack propagation.



(a)



(b)

Figure 5.35 (a) Photograph of a macroetched axial cross-section of a finished fastener using 2% Nital etchant for 30 seconds (x50). (b) Photograph of the circled section in (a) showing the direction of material flow lines. (x200)

Figure 5.35 (a) shows a macroetch of the cross-section of the finished fastener produced using a 2% Nital etchant for 30 seconds to reveal the flow lines of the fastener material. As shown, in Figure 5.35 (b) the material flow lines are particularly compressed at the corner of the groove which is an indication of the level of plastic deformation generated during this process.

Figure 5.36 shows a magnified view of the major crack in the second groove taken after 6 rotations. The circled area in Figure 5.36 is magnified further in Figure 5.37 which shows coalescing voids at the crack tip. This is further illustrated in Figure 5.38 which is a photograph of the same sample and view as in the previous figure but has been macroetched to reveal the voids in the material and a crack passing through them. From observations of the crack in Figure 5.38 the dimpled profile of the crack surface is typical of ductile fracture either brought about by excessive tensile or shear stress. Li *et al* [48] stated that large tensile stresses are responsible for initiating void opening while shear stress determines the density and the size of voids within the workpiece. Under tensile stress, slip dislocation occurs between metal crystals [59]. The optimum angle for slip dislocation corresponds to the maximum shear flow angle of 45° to the maximum principal stress direction. Hence, voids are generated in a direction 45° to the maximum principal stress direction and elongated by the shear stresses. As the slip deformation becomes more extensive, voids merge into a macroscopic crack. This is shown in Figure 5.38 where the etchant has eroded some of the material to reveal the path of the crack which is at approximately a 45° angle to the direction of the flow lines. The flow line direction will be shown in the next section to correspond to the direction of the maximum principal stress thereby validating the hypothesis stated above for crack generation and growth.

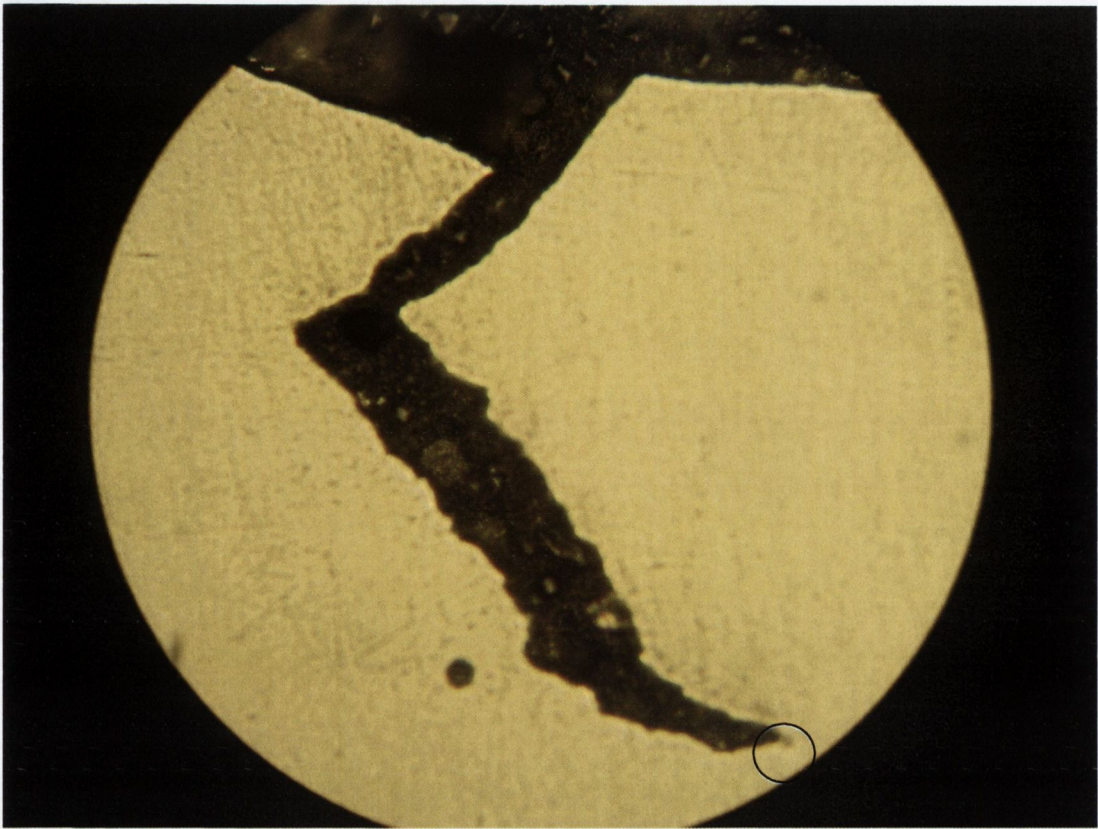


Figure 5.36 Photograph of a crack in the second groove after 6 rotations of the workpiece. (x500)

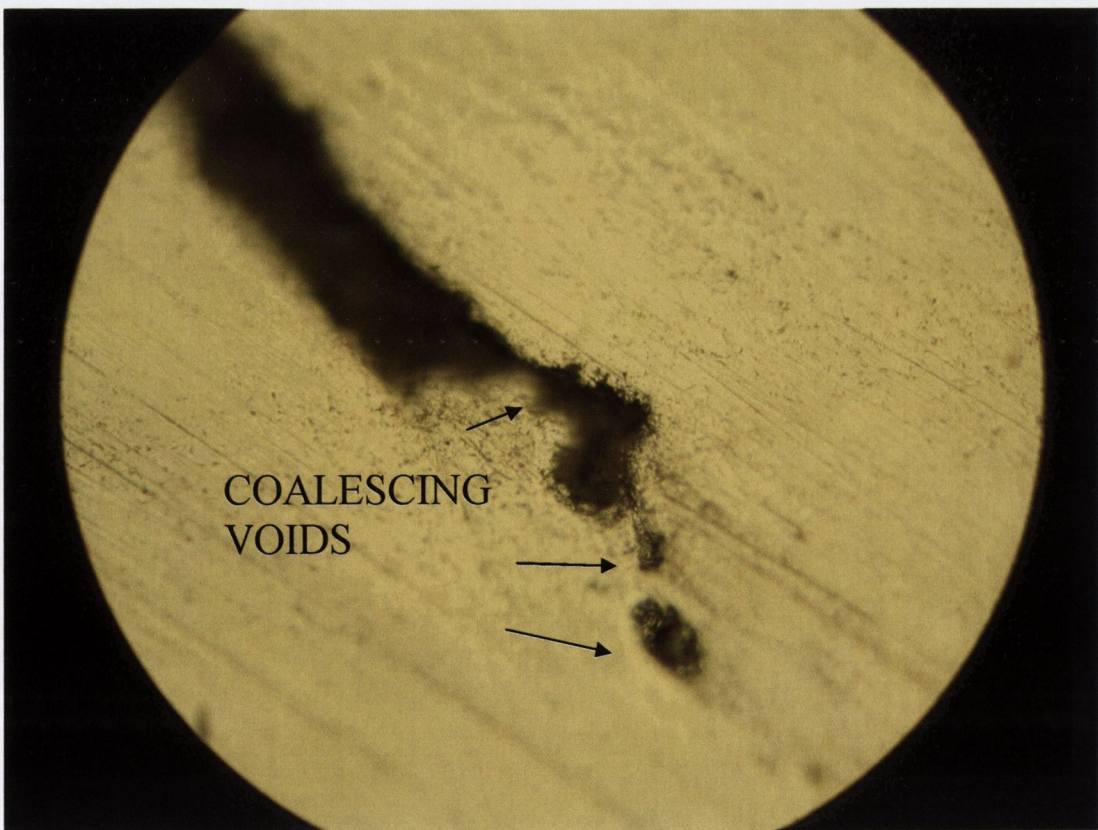


Figure 5.37 Orientation of voids at the crack tip. (x1000)

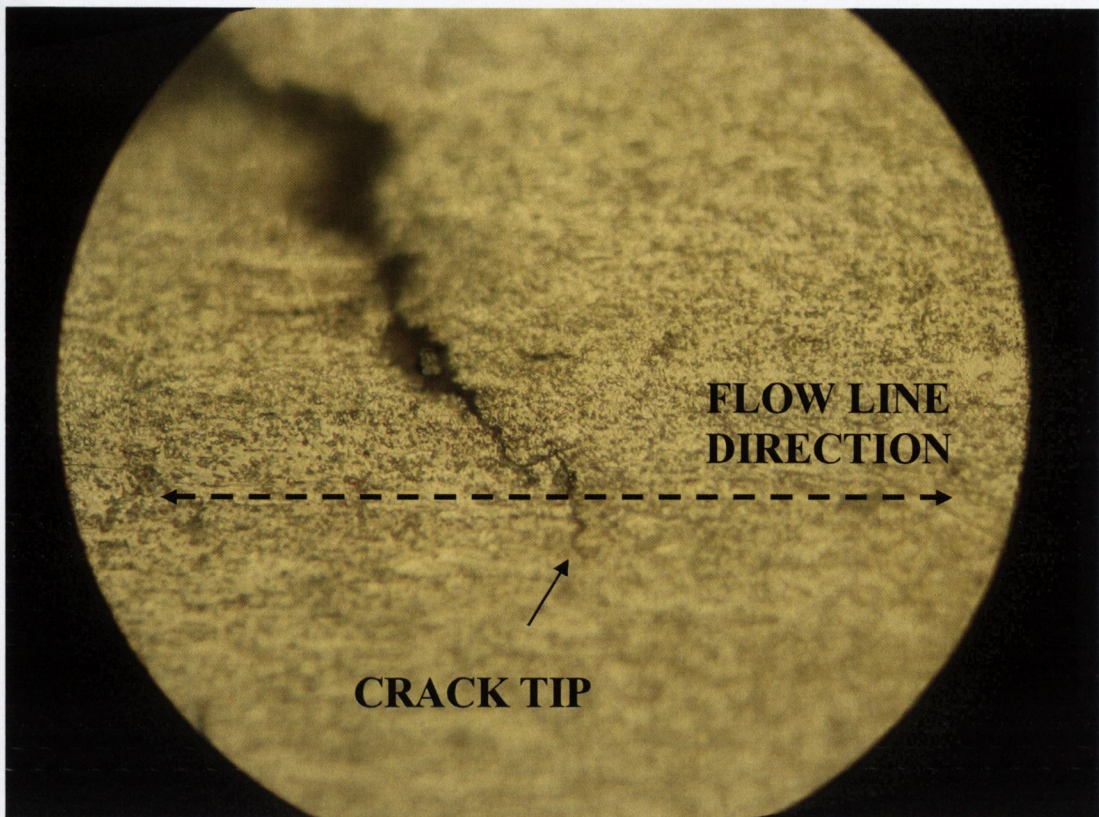


Figure 5.38 Macroetch revealing the direction of the crack tip. (x1000)

5.2.2.2 Stress State Analysis of a Fastener During Form Rolling

Li *et al* [48] stated that “void opening is due to large tensile stresses”. Therefore, the following section will comprise of an investigation using the finite element program DEFORM3D to study where tensile stresses occur on the surface of the workpiece and whether these stresses are large enough to induce ductile fracture.

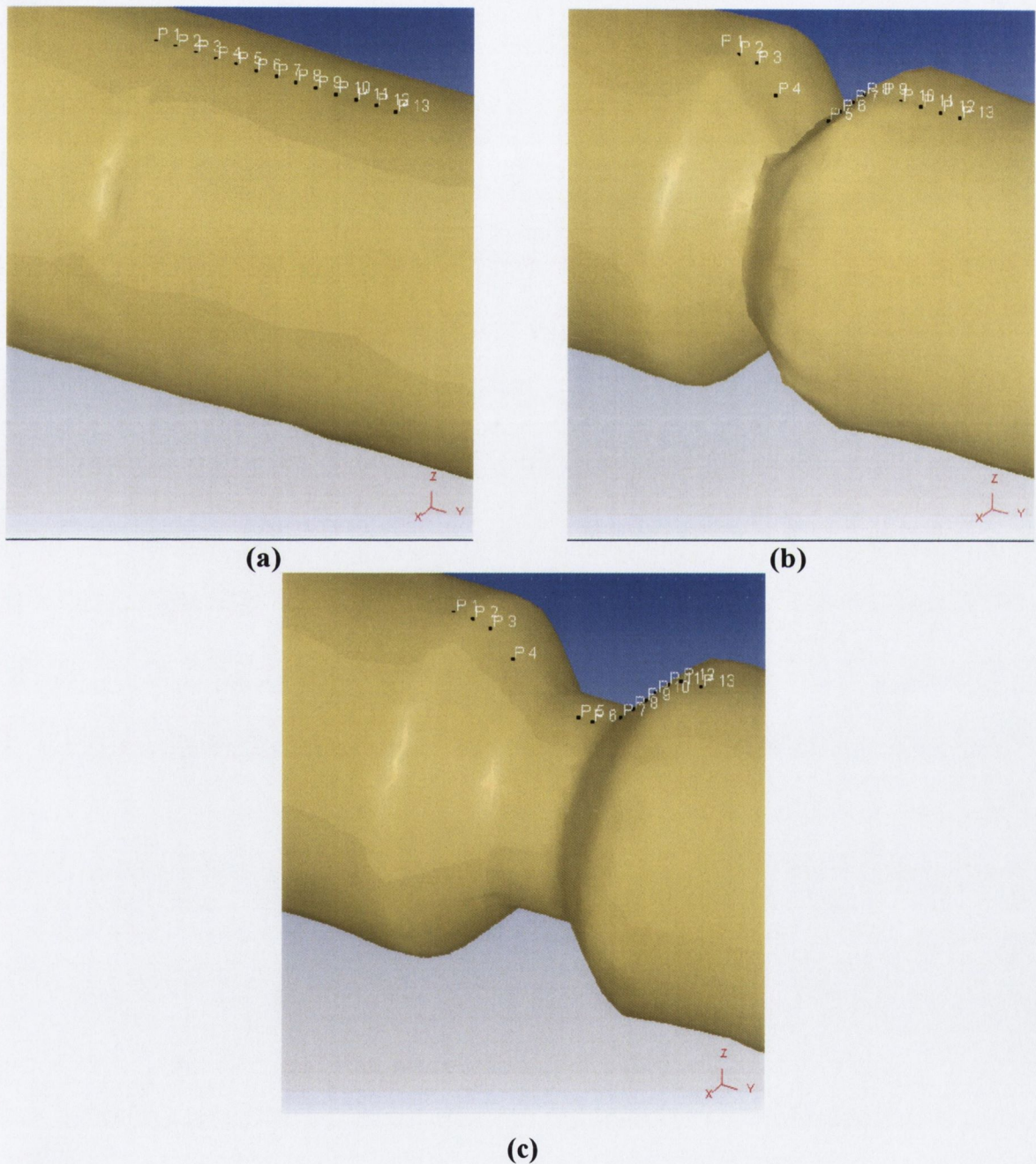


Figure 5.39 Selection of 13 selected points along the surface of the workpiece at regular intervals of 0.25mm during the Form Rolling of the second groove after (a) 3 (b) 5 and (c) 7 rotations.

Ductile fracture can only occur in the presence of plastic deformation. Therefore, the von Mises (effective) stress which indicates plastic yielding of the material is plotted across the surface of the workpiece throughout the forming of the second groove. This is achieved by a method known as *point tracking* in the DEFORM3D program. Points were selected across the surface of the workpiece, ranging from one side of the groove to the other at increments of 0.25mm, as shown in Figure 5.39 (a). As the workpiece is formed these points are displaced, as can be seen in Figures 5.39 (b) and (c), and during *point tracking* information on various material parameters including material velocity, stresses and strains are stored for each point. It should be noted that the points move triaxially and not just in a single plane. This will be addressed later in the section dealing with fastener twisting.

Figure 5.40 is a plot of the effective stress against the number of rotations of the workpiece for the 13 selected points throughout the process. It should be noted that for every half rotation either the top or bottom die is in contact with the *point tracking* points. The cyclical nature of the effective stress distribution at the surface of the workpiece can be described in conjunction with Figures 5.41 and 5.42. Figure 5.41 shows the surface effective stress distribution on the workpiece after 5.5 rotations. The *point tracking* points corresponding to this stage in the process are labelled **A** in Figure 5.40. At this stage the die and the points are in contact resulting in a peak of the effective stress values. As the workpiece continues to rotate, the points come out of contact with the die whereby the effective stress gradually decreases. The effective stress for a single cycle reaches the trough of the curves after 90° rotation where the points are at 90° to the die/workpiece interface, as shown in Figure 5.42 and labelled **B** in Figure 5.40. To complete the cycle the points come back into contact with the die resulting in a gradual increase of the effective stresses, at the workpiece surface, until they reach a peak at full contact, labelled **C** in Figure 5.40.

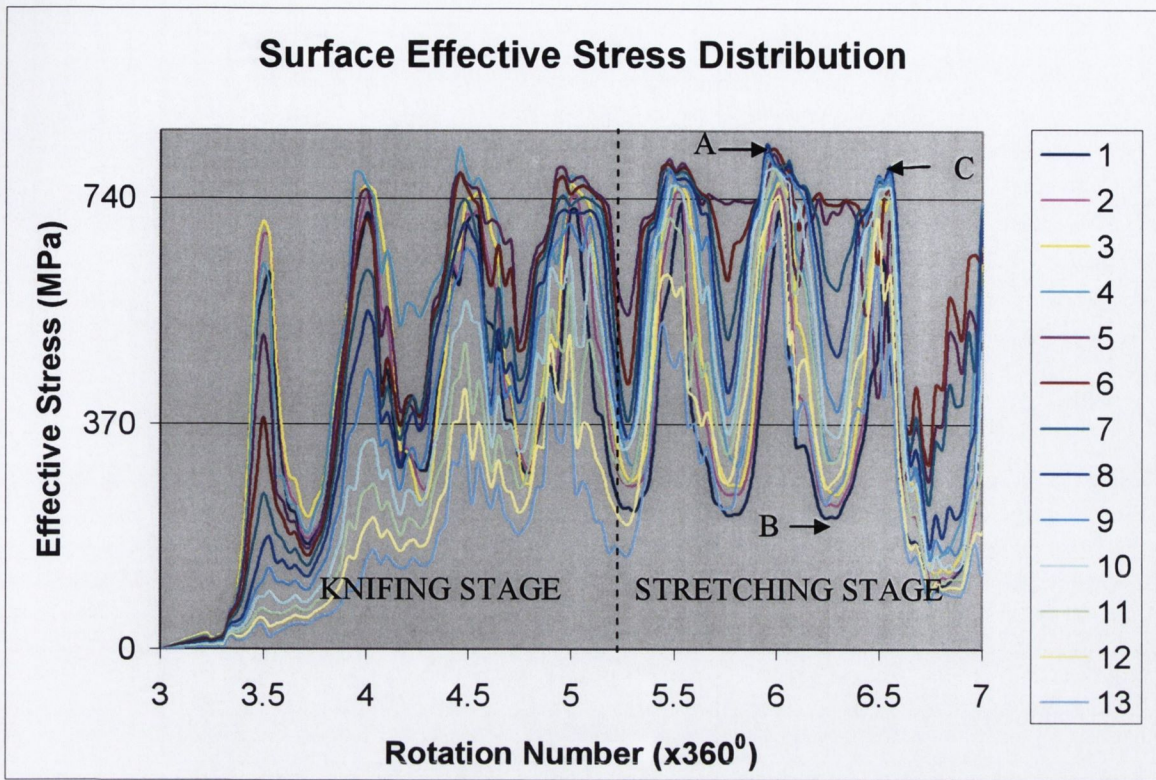


Figure 5.40 Surface effective stress distribution while forming the second groove.

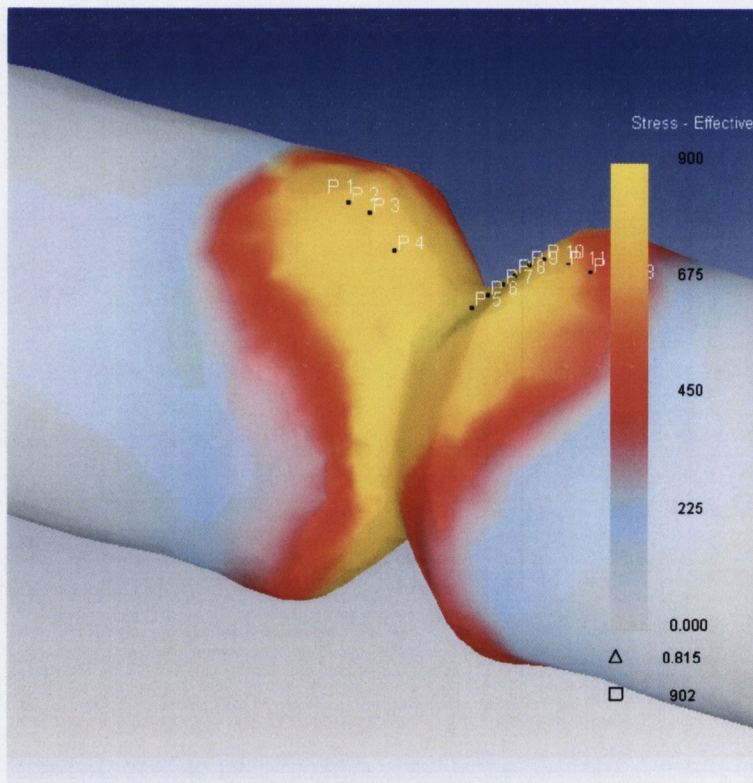


Figure 5.41 Effective stress distribution after 5.5 rotations of the workpiece where the point tracking points are in contact with the die.

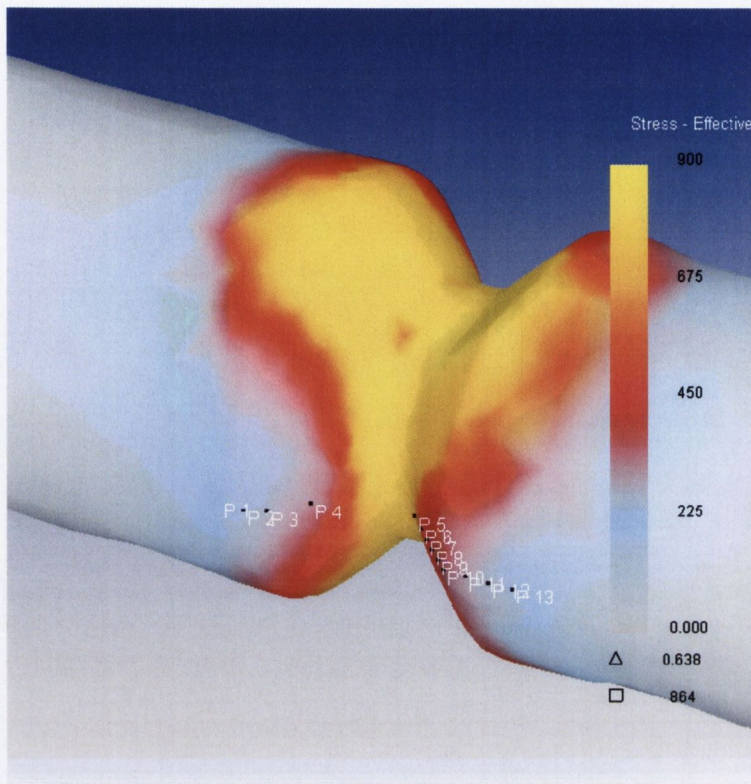


Figure 5.42 Effective stress distribution after 5.75 rotations of the workpiece where the *point tracking* points are not in contact with the die.

The graph in Figure 5.40 can be divided into two sections. The first consists of the *knifing* stage of the die and the second consists of the *stretching* stage. The transition from one stage to the other occurs after 5.2 workpiece rotations, as indicated by the dashed line. The y axis grid line at 372MPa represents the yield strength of the material; therefore any values above this line are plastically deformed. From this graph it can be determined that the points on the left of the workpiece flow plastically first and the others follow suit as the groove is formed. During the *knifing* stage, the effective stress gradually increases as the diameter of the workpiece is reduced to form the groove. As the plot transfers to the *stretching* stage the peaks of the curves continue to increase until they reach C in Figure 5.40.

To further investigate the various stress states during the process, the *knifing* and *stretching* stages will be addressed separately in the following sections.

5.2.2.2.1 Knifing Stage

As illustrated in Figure 5.43, point 4 (circled) is the point that is subjected to the greatest displacement during the *knifing* stage of the process. Therefore, point 4 will be used to plot the worst case scenario from the available points which would give an indication of the development of the stresses during this phase of the process.

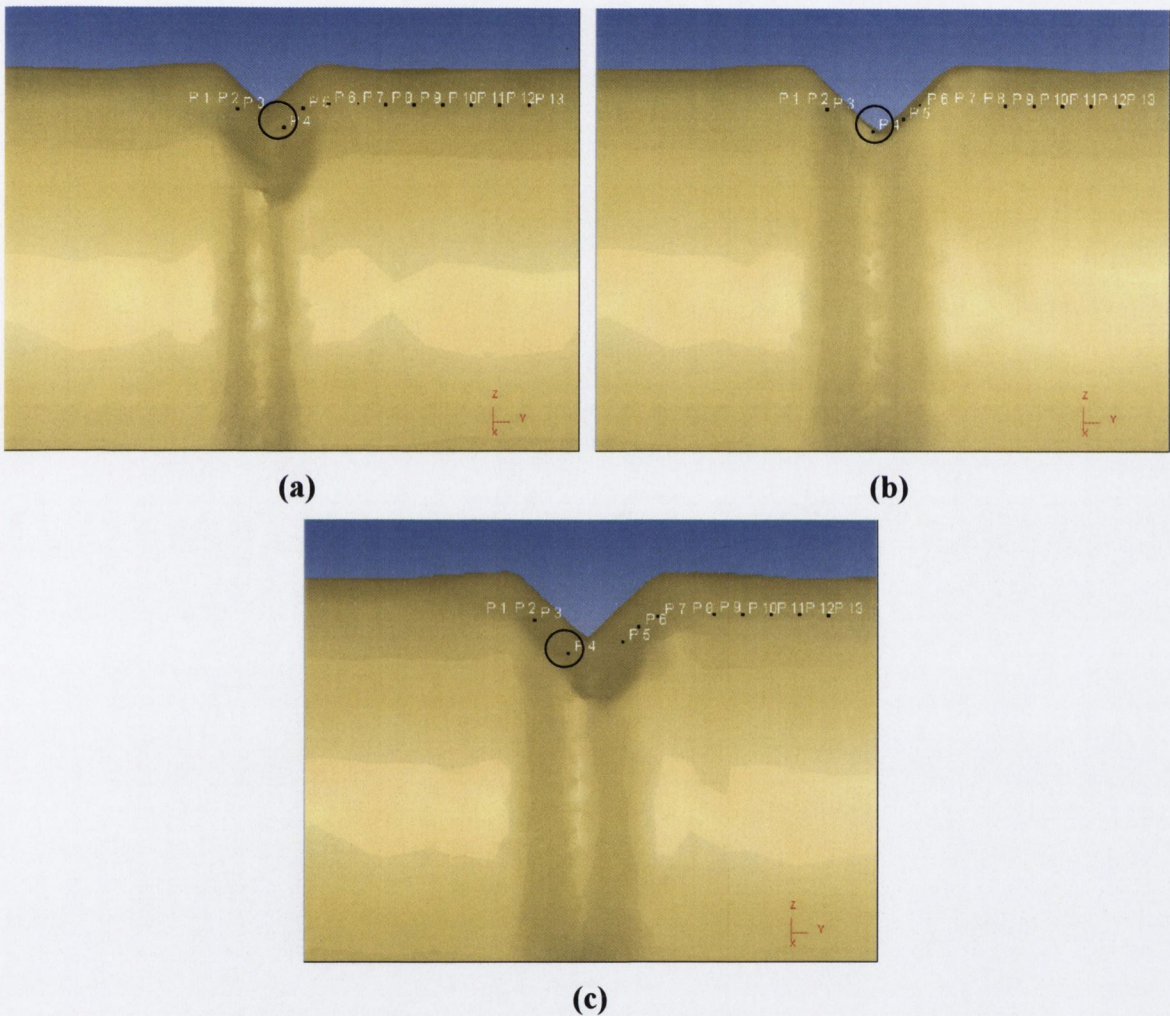


Figure 5.43 Illustration of the displacement of point 4 as it moved from one side of the groove profile after (a) 4 rotations, to other after (b) 4.4 and (c) 4.5 rotations.

As discussed previously the magnitude of effective stress depends on whether point 4 is in contact with the die or not. As can be seen in Figure 5.44, the workpiece material around point 4 is in a continuous state of plasticity from rotation 3.8 to 5.1, labelled **A** and **B** respectively. This can be explained by the changing position of point 4 from the left side of the *V* form, as shown in Figure

5.43 (b), to the right side of the V form, as shown in Figure 5.43 (c) occurs between 4.4 and 4.5 rotations. This brings about an increase of the effective stress for the same stage as can be seen in Figure 5.44. After this point however, the effective stress at point 4 begins to decrease because the maximum deformation zone is at the point of the V form and not at point 4.

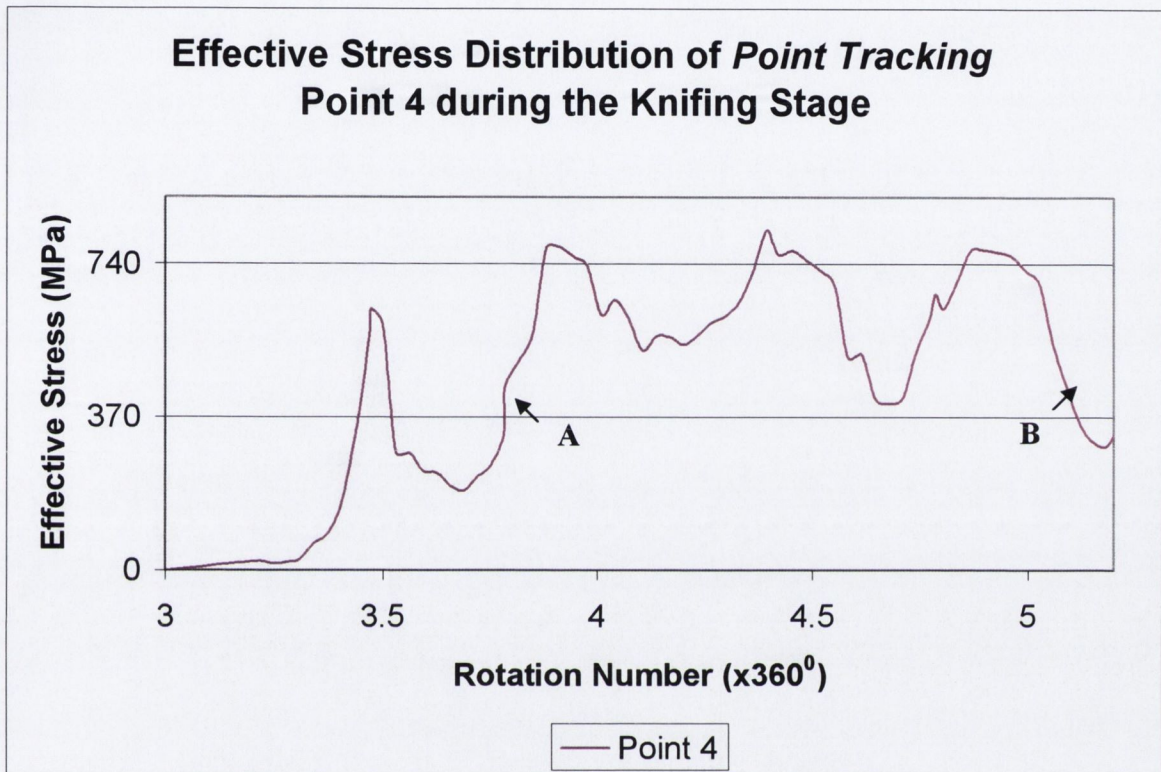


Figure 5.44 Effective stress distribution of point 4 during the *knifing* stage of the forming process.

Figure 5.45 is a plot of the axial, hoop and radial stresses associated with point 4 during the *knifing* stage of the forming process. As can be seen, the stresses tend to cycle, peaking at 90° to the die/workpiece interface as shown in Figure 5.42. Therefore, as the groove diameter is further reduced, the pressure exerted by the dies at the die/workpiece interface has the affect of compressing the workpiece similar to a compression test. As such, the induced axial, hoop and radial tensile stresses increase, at the sides of the workpiece that are not in contact with the die, for every half rotation of the fastener during the *knifing* stage. This trend is verified in Figure 5.46 which is a plot of the maximum radial, hoop and axial stresses during the process. Figures 5.45-5.46 show that at 90° to the die/workpiece

interface the surface axial stress is always the largest of the tensile stresses and the hoop stress is the smallest tensile stress.

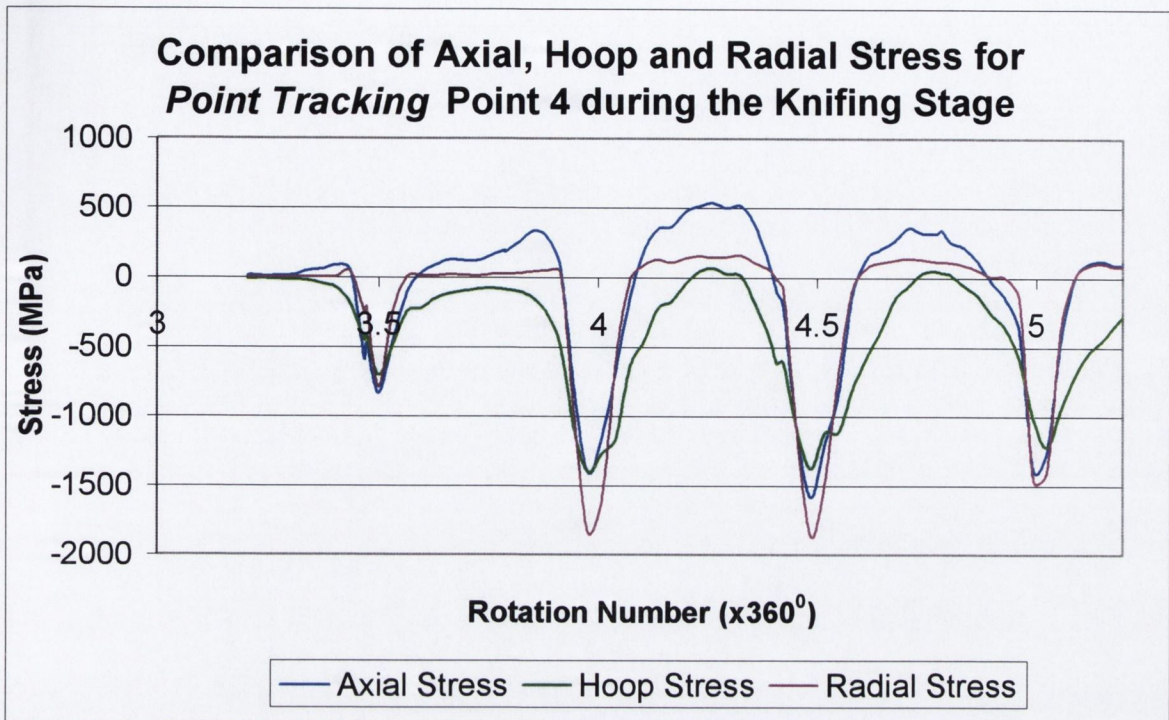


Figure 5.45 Comparison of the surface axial, hoop and radial stresses for point 4 during the *knifing* stage while forming the second groove.

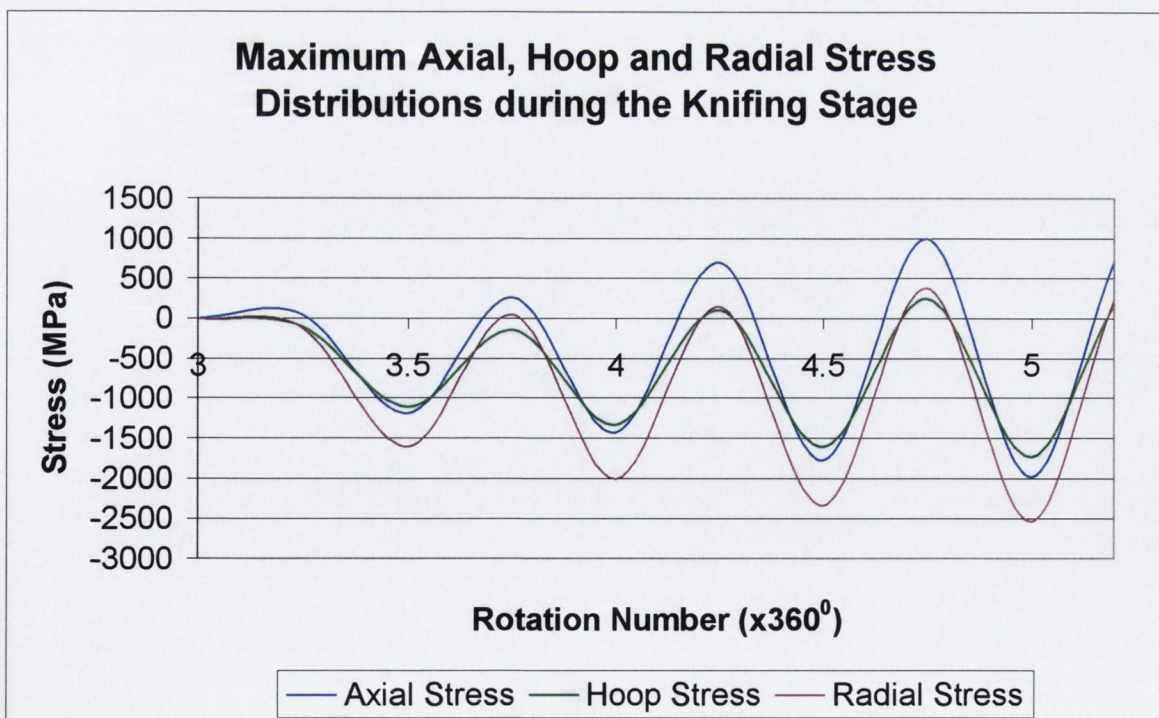


Figure 5.46 Comparison of the maximum axial, hoop and radial stresses during the *knifing* stage while forming the second groove.

Figure 5.46 shows that all of the tensile stresses increase throughout the *knifing* stage reaching a maximum after 5.2 rotations. Figure 5.47 illustrates the distribution of the axial tensile stress on the surface of the fastener after 5.2 rotations, at 90° to the die/workpiece interface.

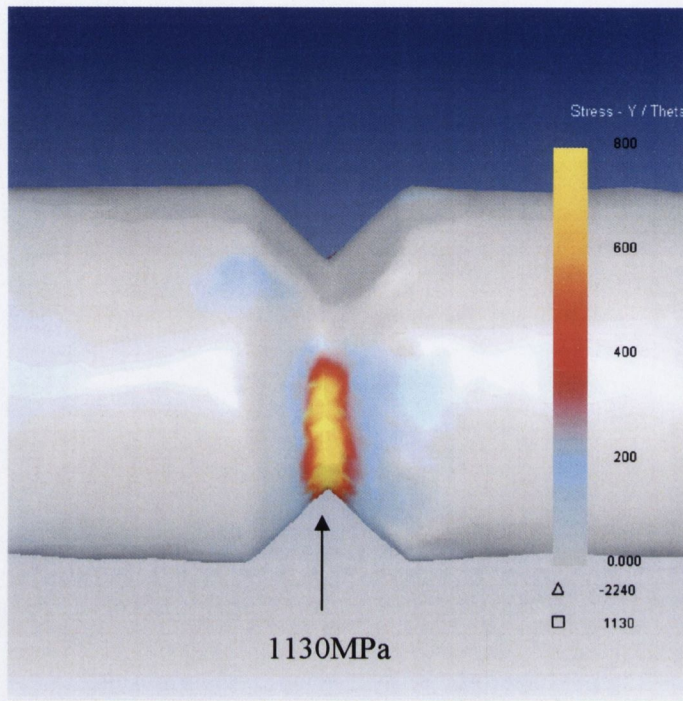


Figure 5.47 Axial tensile stress distribution after 5.2 rotations at 90° to the die/workpiece interface.

The magnitude of the maximum axial tensile stress is approximately 50% greater than the next nearest directional stress after 5.2 rotations which is the radial stress. Therefore, it is more likely that high axial tensile stress concentrations will promote void formation and that the radial and hoop tensile stresses are not as significant as the axial stress in contributing to void formation.

Compressive stresses are generated at the die/workpiece interface. Figure 5.45 shows that the compressive stresses attributed to point 4 increase with increasing diameter reduction until the point moves to the left of the groove. This is validated in Figure 5.46 showing that the maximum compressive stresses increase with increasing diameter reduction during the *knifing* stage. Figure 5.48 shows the maximum radial compressive stress distribution that was found to be 2520MPa after 5.2 rotations.

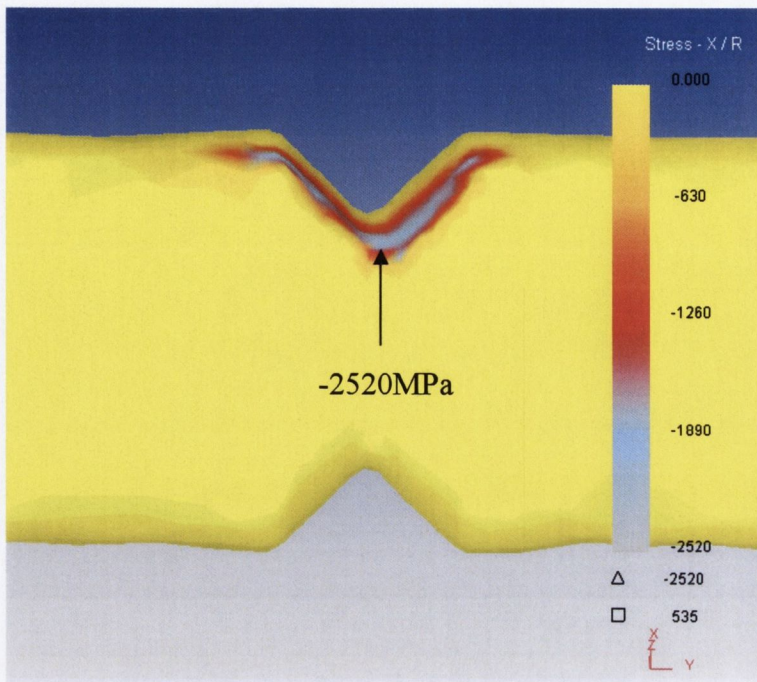


Figure 5.48 Radial compressive stress distribution after 5.2 rotations generated at the die/workpiece interface.

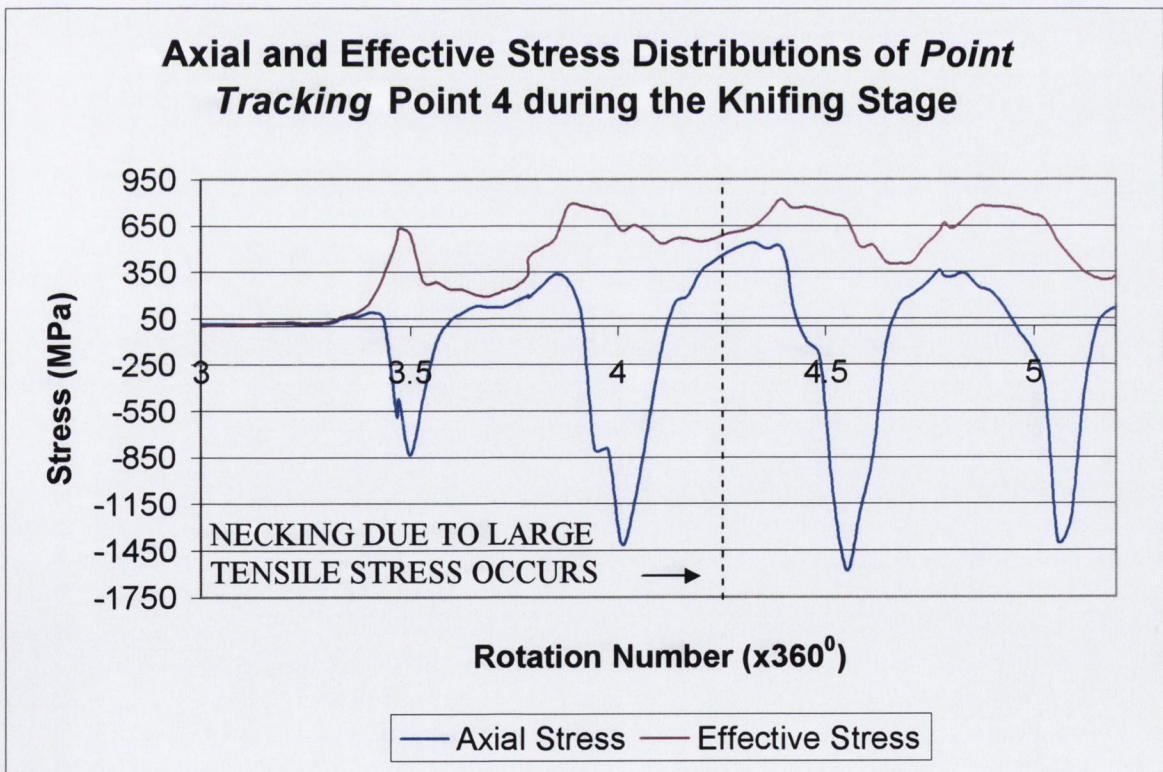


Figure 5.49 Comparison of the axial and effective stresses for point 4 during the *knifing* stage.

By comparing the axial tensile stress to the effective stress, attributed to point 4 in Figures 5.49, it can be determined that at 90° to the die/workpiece interface necking first occurred at 4.25 rotations because the material had yielded as illustrated by the effective stress of 609MPa and the axial tensile stress was 390MPa. For every half rotation after rotation 4.25 the surface material at 90° to the die/workpiece interface experienced necking.

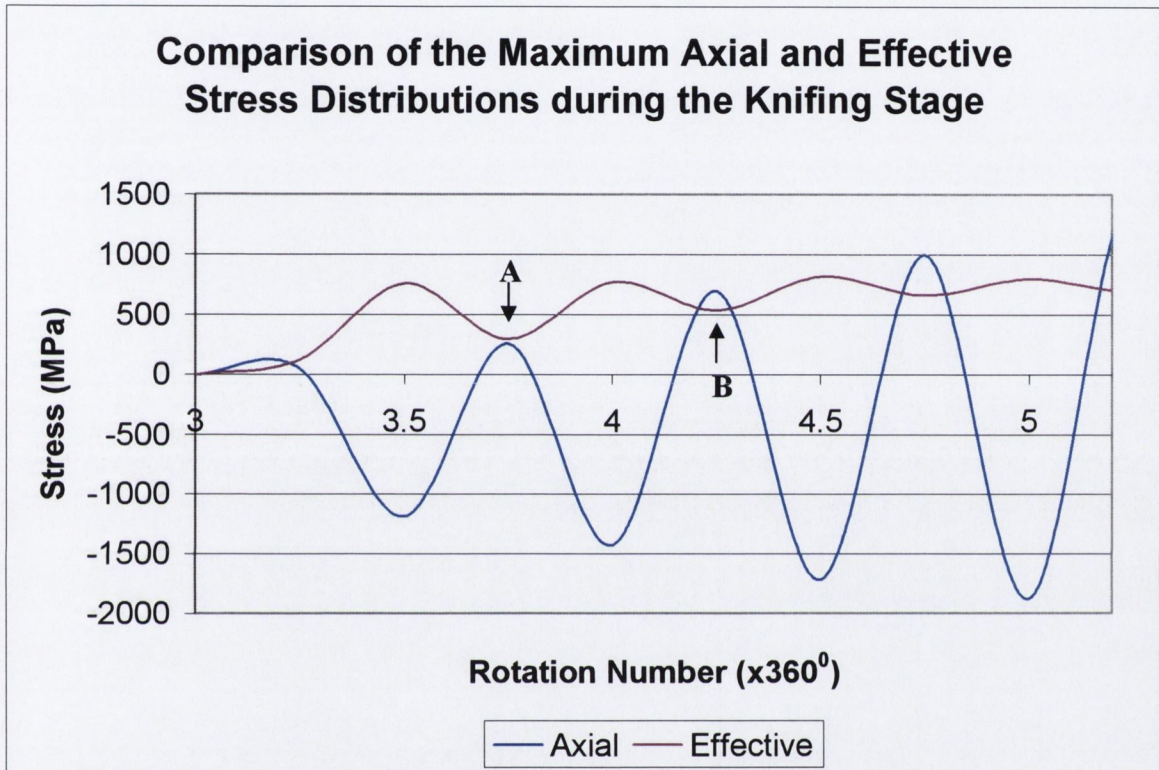


Figure 5.50 Comparison of maximum axial and effective stresses during the *knifing* stage.

This is verified in Figure 5.50, showing the maximum axial and effective stress distributions, where at label **A** the maximum effective stress measures 300MPa after 3.75 rotations. However, after 4.25 rotations, labelled **B**, the maximum effective stress is 540MPa and the maximum axial tensile stress is 779MPa which is shown in Figure 5.51.

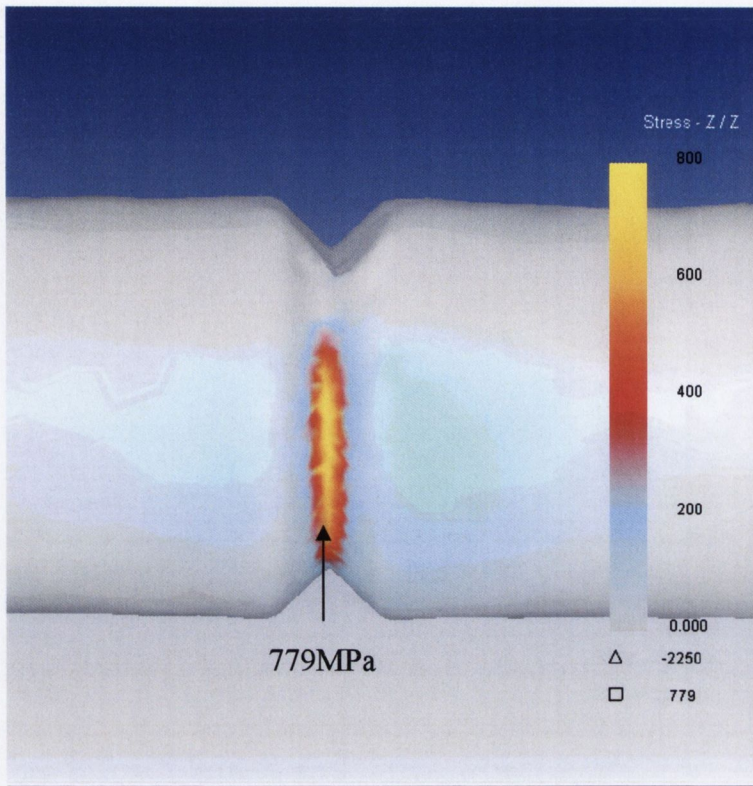


Figure 5.51 Axial tensile stress distribution taken after 4.25 rotations.

5.2.2.2.2 Stretching Stage

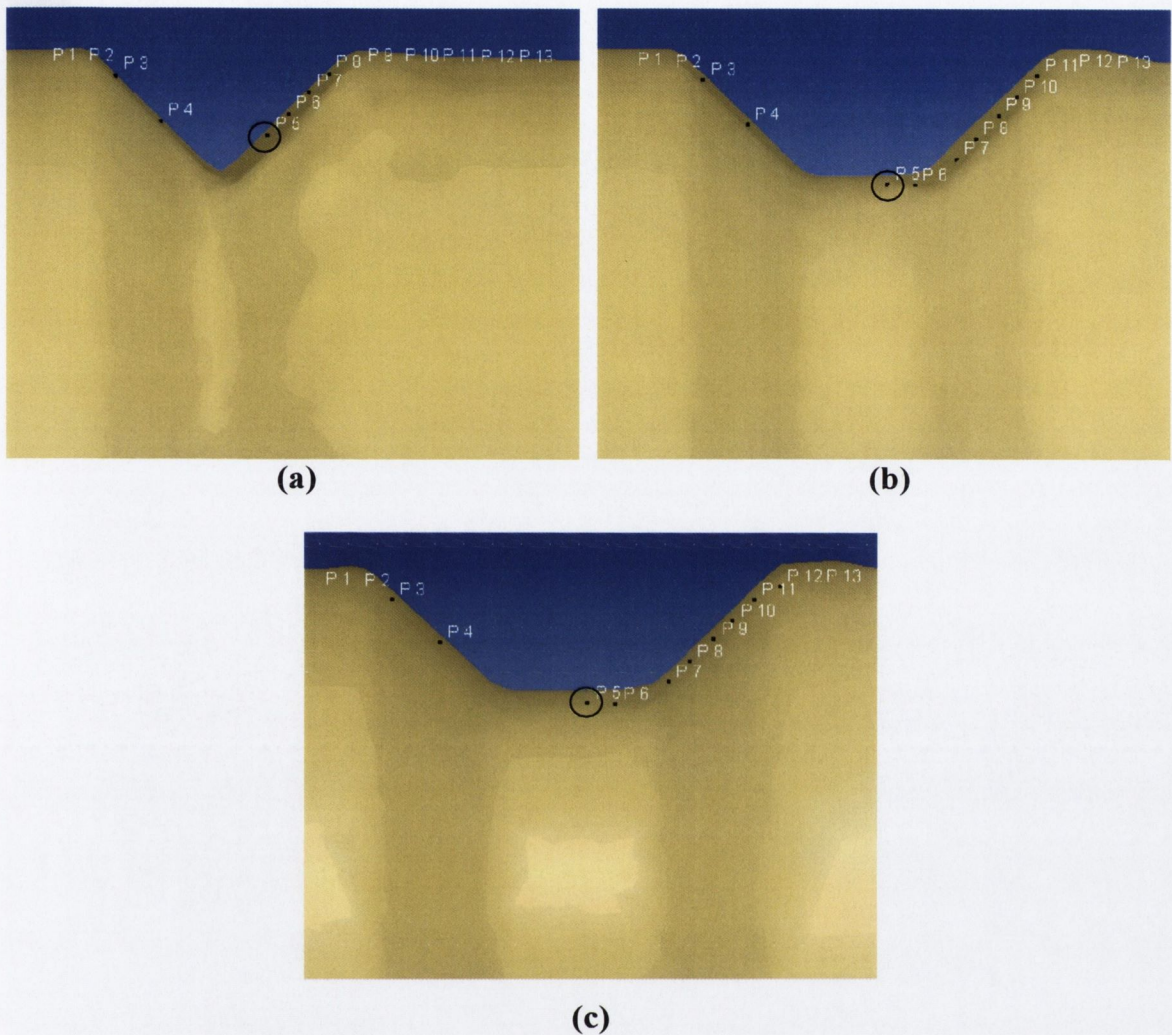


Figure 5.52 Illustration of the displacement of point 5 during the stretching stage of the die after (a) 5, (b) 6 and (c) 7 rotations, respectively.

From analysing the *point tracking* results it was found that point 5 experienced the most deformation and is positioned closest to where the crack developed at the base of the groove, as shown circled in Figure 5.52. Therefore, this point was selected to describe how the stresses develop during the stretching stage and will then be compared to the maximum stress plots for the same stresses.

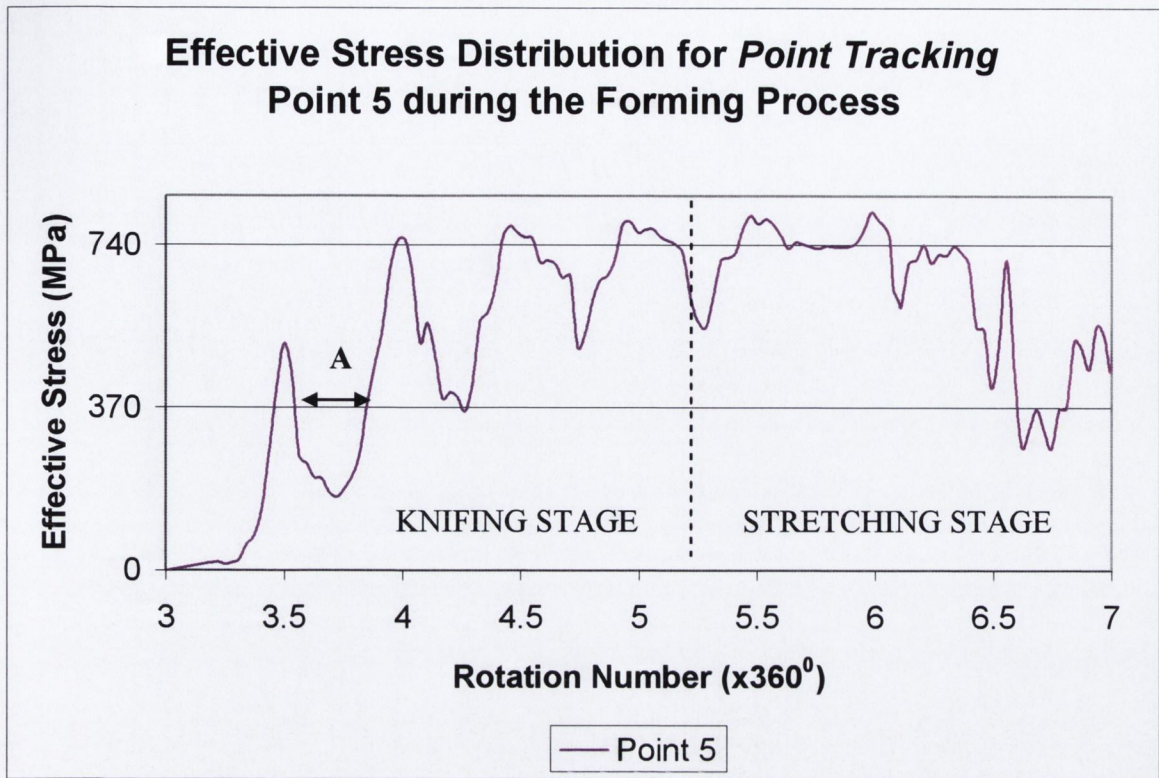


Figure 5.53 Surface effective stress distribution of point 5 while forming the second groove.

Figure 5.53 is an effective stress plot of point 5 taken from Figure 5.40 where the dashed vertical line indicates the transition from the *knifing* to the *stretching* stage of the die. It shows that the effective stress exceeds the initial yield stress for nearly the whole process, i.e. from rotation 3.5 to 6.6, except for a brief period between rotations 3.55 and 3.75 as indicated by **A** in Figure 5.53 (which incidentally was also shown for point 4 in the previous section).

Figure 5.54 is a plot of the axial, hoop and radial stress distribution associated with point 5. These were plotted to determine whether the levels of tensile stresses were large enough to initiate void formation at point 5 on the surface of the workpiece.

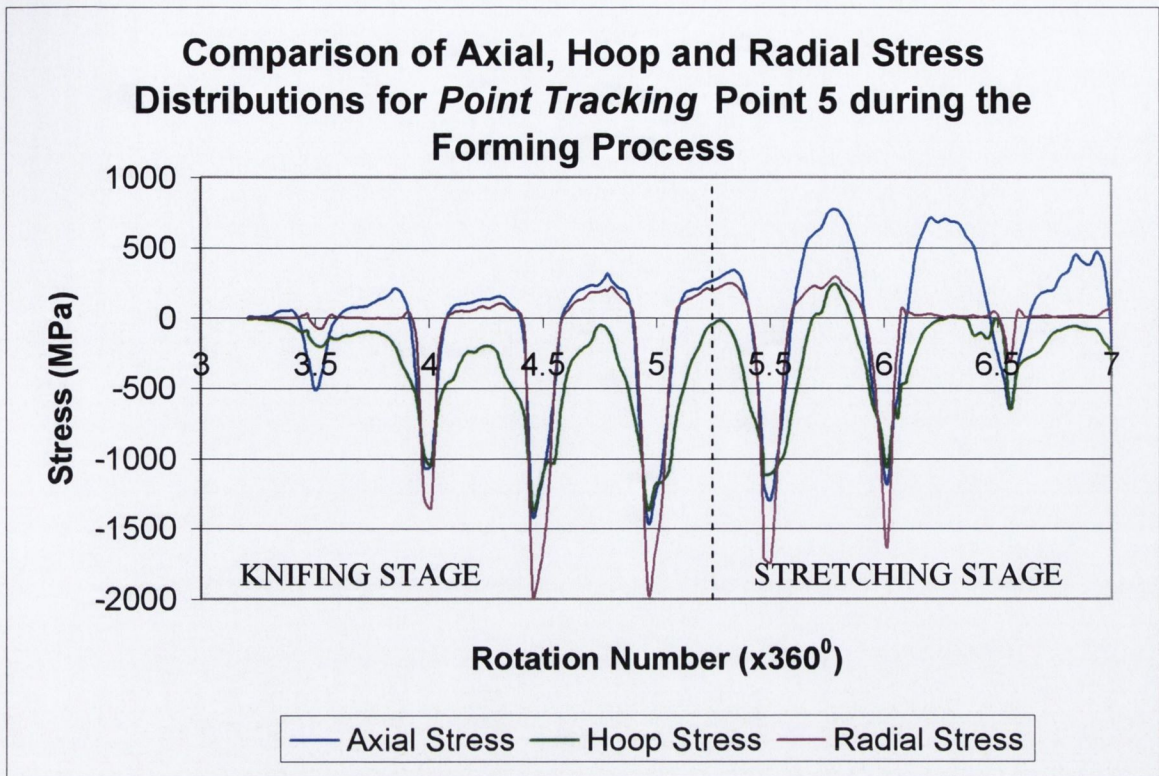


Figure 5.54 Comparison of the surface axial, hoop and radial stresses at point 5 while forming the second groove.

Again, the cyclical nature of the stress distributions is revealed in Figure 5.54. All of the stresses are compressive when in contact with the die i.e. for every half rotation starting at the 3rd rotation. During the *knifing* stage, until the required depth of the groove is achieved. The axial and radial stresses show increasing compressive values on the completion of each half rotation. However, once the *stretching* stage starts i.e. at the dashed line in Figure 5.54, these compressive stresses decrease while the tensile stresses increase as the groove widens from the 5th to the 6th rotation. The change of the position of point 5 from the 5th to the 6th rotation is illustrated in Figures 5.52 (a) and (b). The increase in the axial tensile stress is related to the *stretching* of the workpiece material where point 5 moves from the right side to the base of the groove. This results in large axial tensile stresses concentrated at 90° to the die/workpiece interface. As indicated by the graph in Figure 5.54 the maximum axial, hoop and radial tensile stresses, for point 5, are found at rotation 5.75. The radial stress is not zero because point 5 is below the surface. However from rotation 6 on point 5 approaches zero because the material about point 5 was strained consequently moving it closer to the surface.

However, on comparing Figure 5.54 to Figure 5.55, which is a plot of the maximum axial, hoop and radial stresses during the process, some differences between the respective graphs become apparent. Figure 5.55 shows that the maximum axial tensile stress decreases slightly once the *stretching* stage has started. This is because the cutting action of the *knifing* stage, which generates high stresses in the workpiece material, is now complete. On the other hand, the trend of the maximum compressive stresses is in agreement with Figure 5.54 whereby the maximum compressive stresses decrease steadily. As can be seen in Figure 5.54, the radial stress, for point 5, has a tendency to be greater in compression and less in tension than the axial stress. Also shown in Figures 5.54 and 5.55, is that the hoop stress is the smallest of the three stresses in tension and compression. This shows that ductile failure will likely occur due to excessive axial tensile stress that induces necking, at 90° to the die/workpiece interface, as the groove is widened.

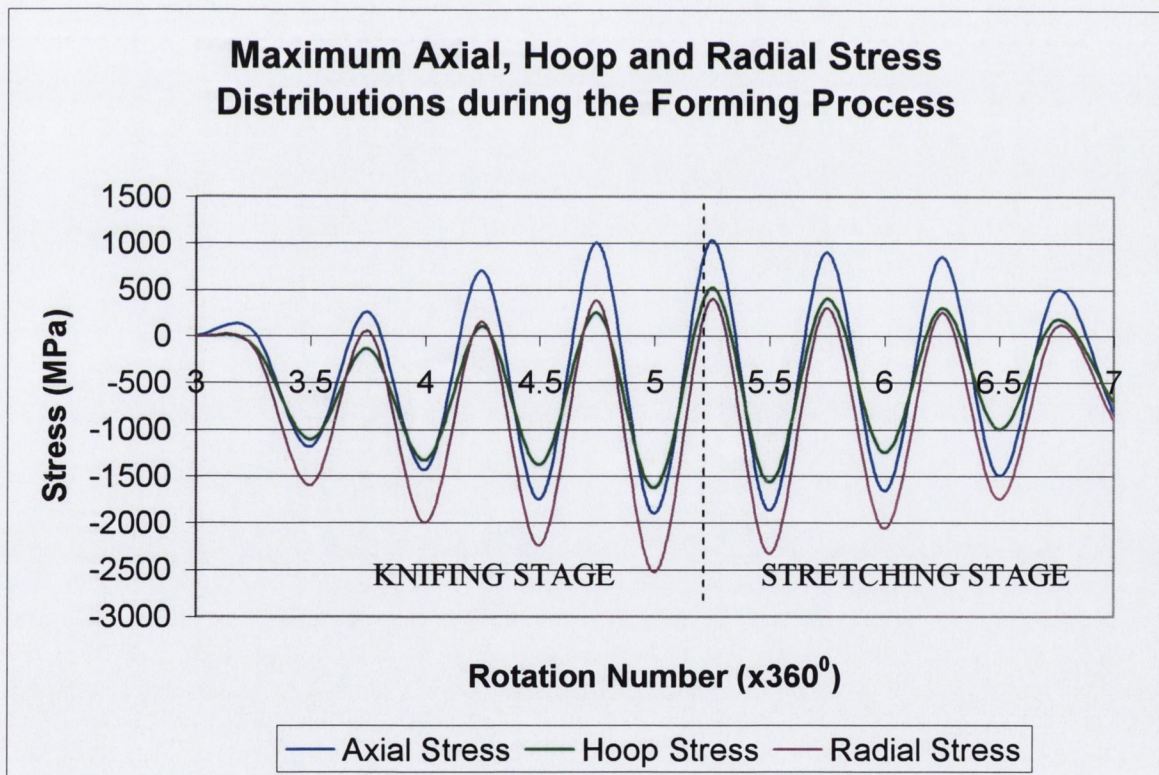


Figure 5.55 Comparison of the maximum axial and radial stresses during the forming of the second groove.

Figures 5.56 and 5.57 show, using a colour shaded plot of the same scale, the axial and radial tensile stresses on the surface of the fastener after 5.75

rotations. (Note that the compressive stresses have been omitted). These figures illustrate the difference in the magnitude and area of the tensile stress distribution for the axial and radial directions respectively, which are the largest of the three directional stresses.

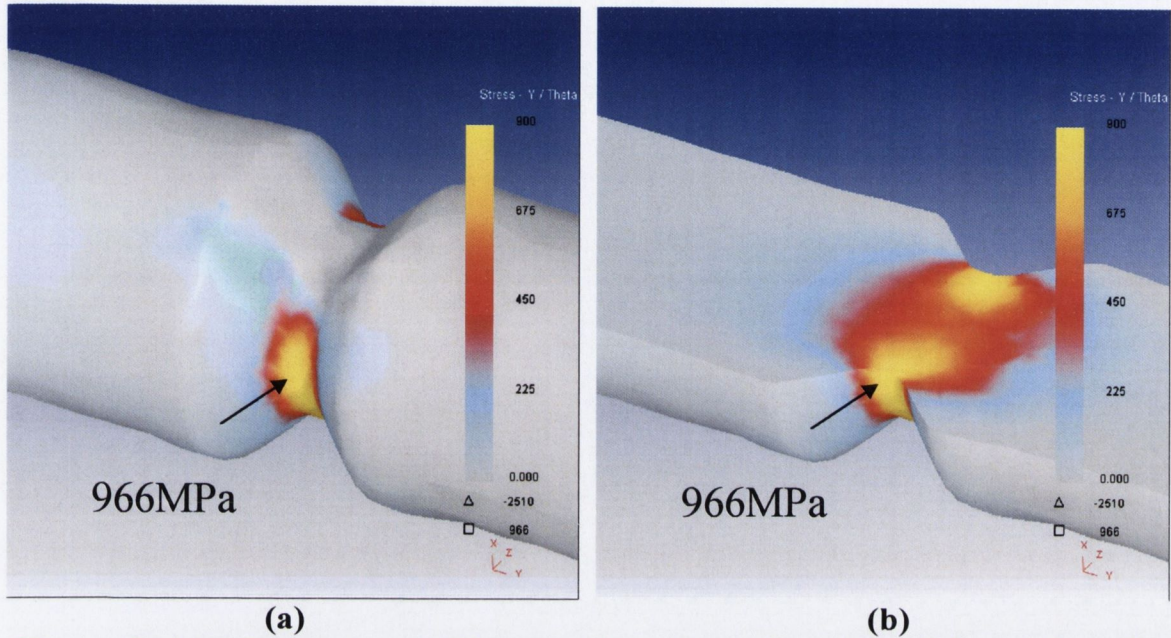


Figure 5.56 (a) Isometric and (b) isometric cross-section view of the axial tensile stress distribution on the workpiece after 5.75 rotations.

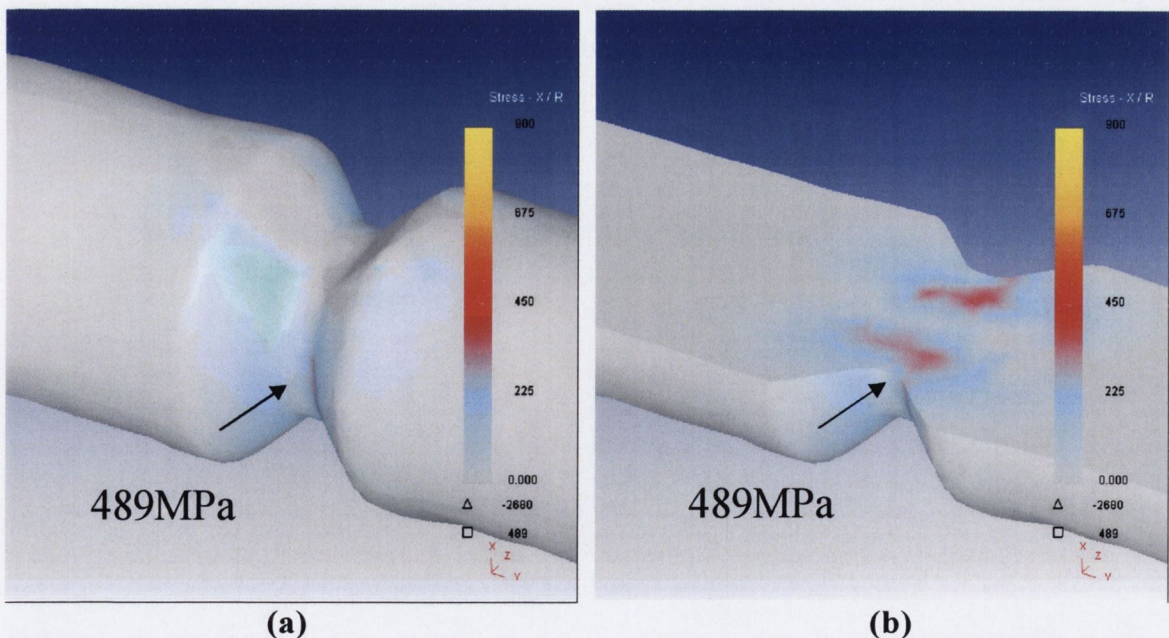


Figure 5.57 (a) Isometric and (b) isometric cross-section view of the radial tensile stress distribution on the workpiece after 5.75 rotations.

As can be seen, during the *stretching* stage the maximum tensile stress in the axial and radial directions is 966MPa and 489MPa after 5.75 rotations,

respectively. This indicates that the material in the central region at the base of the groove is being pulled apart, as shown in Figure 5.56, which causes necking continuously at intervals of 180° rotation i.e. at 90° to the die/workpiece interface, until the end of the process.

Figure 5.58 is a graph comparing the maximum axial and effective stresses. From rotation 4.25 on, there are large axial tensile stress concentrations, located at the surface of the workpiece, at 90° to the die/workpiece interface. Once the maximum depth has been reached, the maximum axial tensile stress decreases slightly during the *stretching* stage of the die.

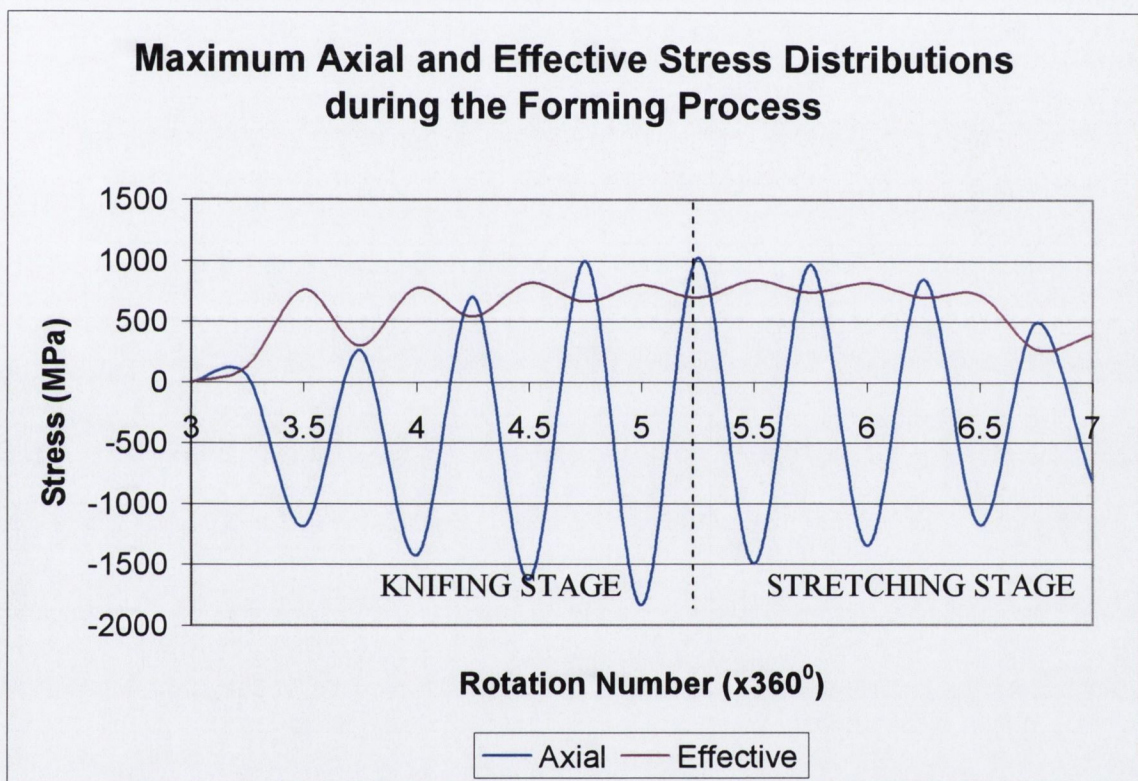


Figure 5.58 Comparison of the maximum surface axial stress to the maximum surface effective stress while forming the second groove.

Figure 5.59 shows a side view, taken after 5.75 rotations, of a vector plot of the maximum principal stresses where all but the groove section of the workpiece is removed (thus leaving the geometry of the workpiece outlined in green), it is clear that the maximum principal stress is acting in the axial direction towards the tip of the fastener. Therefore, as shown in Figure 5.60, the direction of the maximum principal stress acts in the same direction as the axial tensile stress.

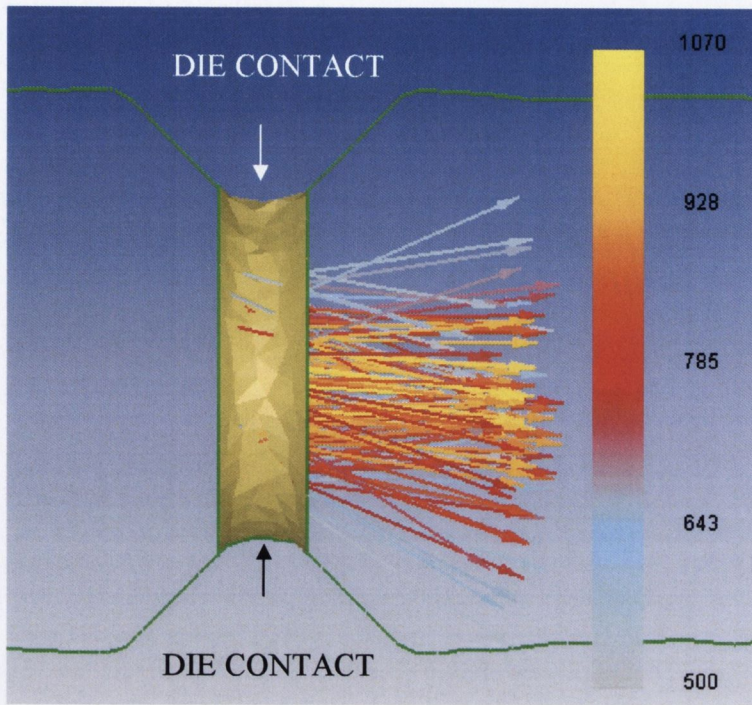


Figure 5.59 Vector plot of the maximum principal stress where the profile of the workpiece is highlighted in green.

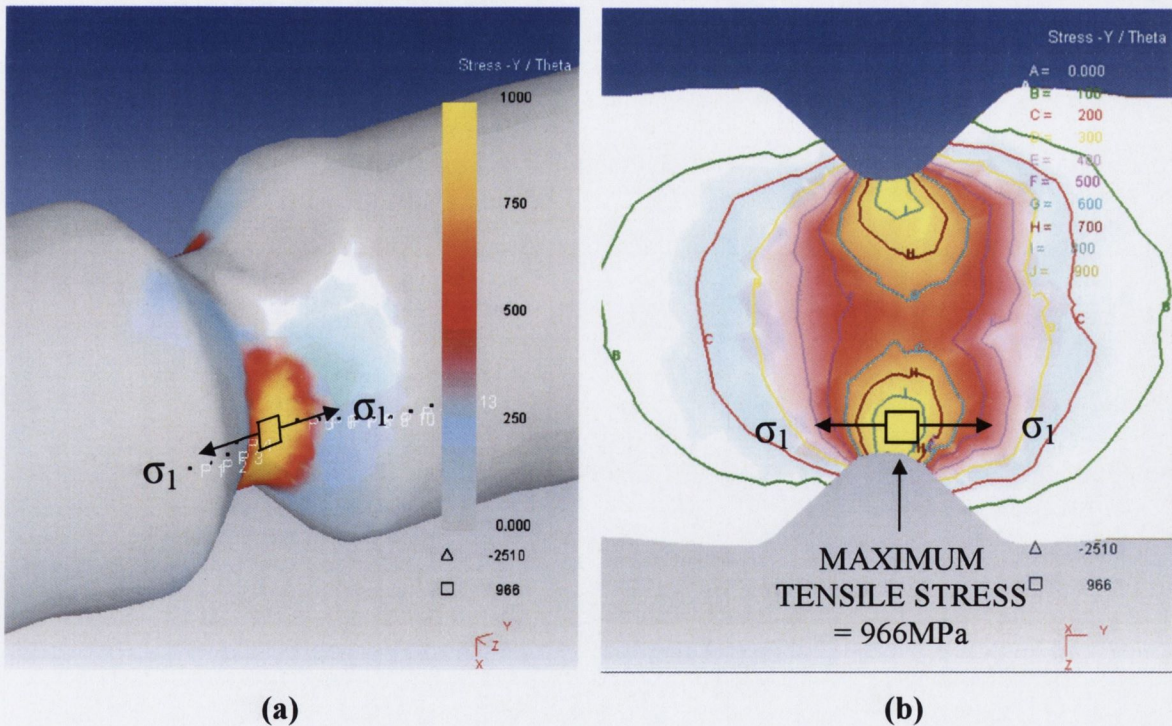


Figure 5.60 Illustration of the positions of the point tracking point after 5.75 rotations with an (a) isometric and (b) axial cross-section view of the tensile stress distribution.

Therefore, any cracks would be elongated in a direction normal to the maximum principal stress due to tensile force in the principal direction which is in

agreement with Li *et al* [48] who stated that “*if the tensile stresses are large enough in magnitude, they can accelerate void growth by opening matrix material in the direction of the highest principal stress*”. This would explain why the crack moved radially into the workpiece and not longitudinally. However, as already discussed, void formation can be promoted by both tensile and shear stresses where the shear stresses generate the expansion and density of the voids. The shear stresses will be investigated in the following section.

5.2.2.3 Combination of Tensile and Shear Stress in Crack Formation and Propagation

As stated in the previous section, workpiece fracture occurred between 5 and 6 rotations. Therefore, the axial tensile stresses and shear stresses developed in the fastener will be analysed at intervals of quarter rotations (90°) starting at the 5th and finishing at the 6th rotation. Figures 5.61–5.65 show side views of the axial tensile stress and the corresponding shear stress after 5, 5.25, 5.5, 5.75 and 6 rotations, respectively. As can be seen in these figures the axial tensile stresses and shear stresses are found in the same region of the workpiece i.e. at 90° to the die/workpiece interface at the base of the groove. For both the tensile and shear stresses, the areas that they affect increase as the groove is widened. The regions of shear stress at the base of the groove are generated at each corner of the groove and act in opposite directions to each other. As can be seen from the figures below, the negative (blue) and positive (yellow) shear stresses are pointing in and out of the page respectively. The magnitude of the shear stresses ranges from 395MPa to 423MPa. It should be noted that this region corresponds to the position where a lap was shown to occur on the surface of the workpiece.

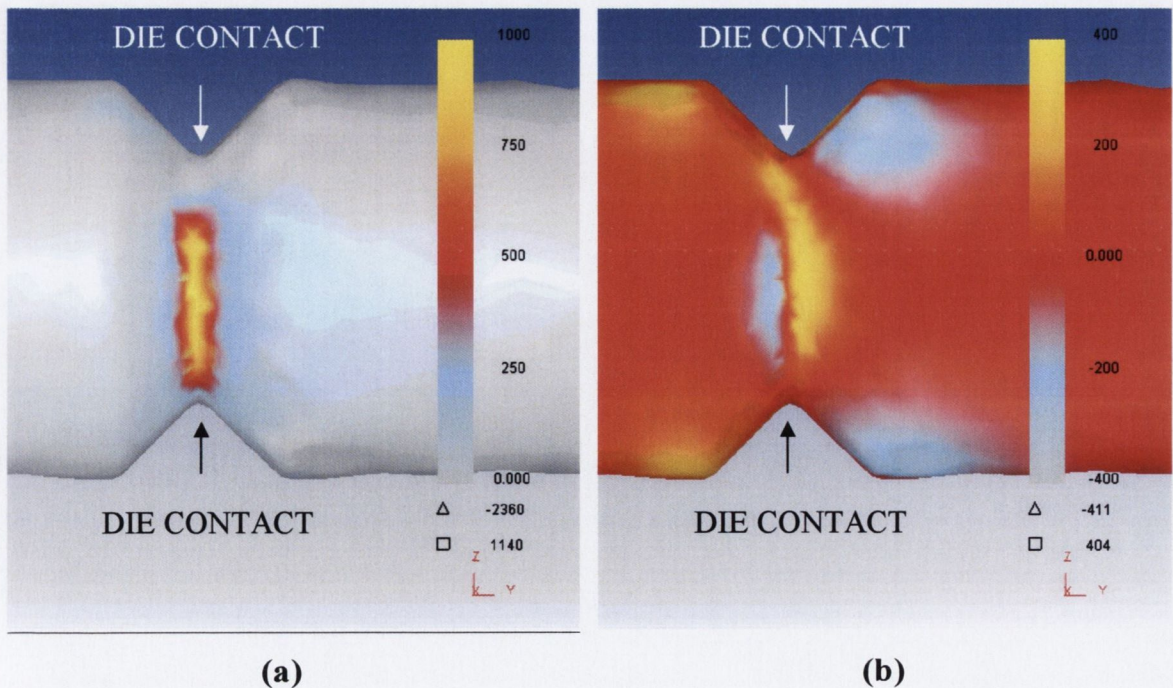


Figure 5.61 Side view of the (a) axial tensile stress and (b) shear stress, τ_{zr} , surface distribution on a fastener after 5 rotations.

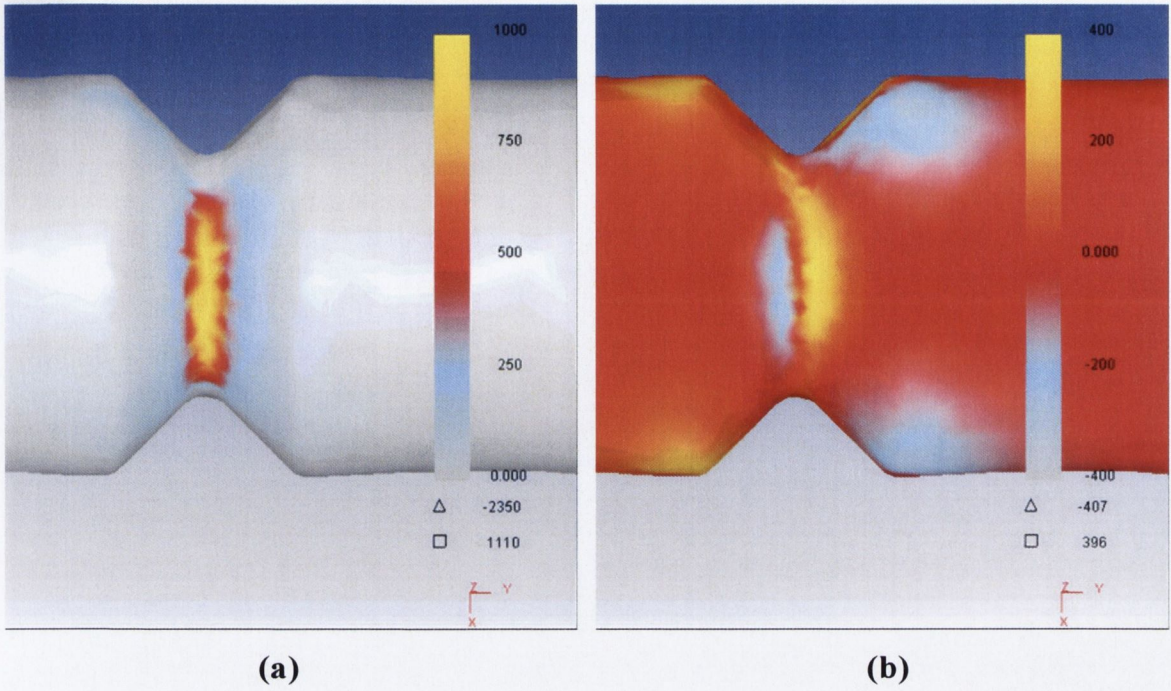


Figure 5.62 Side view of the (a) axial tensile stress and (b) shear stress, τ_{zr} , surface distribution on a fastener after 5.25 rotations.

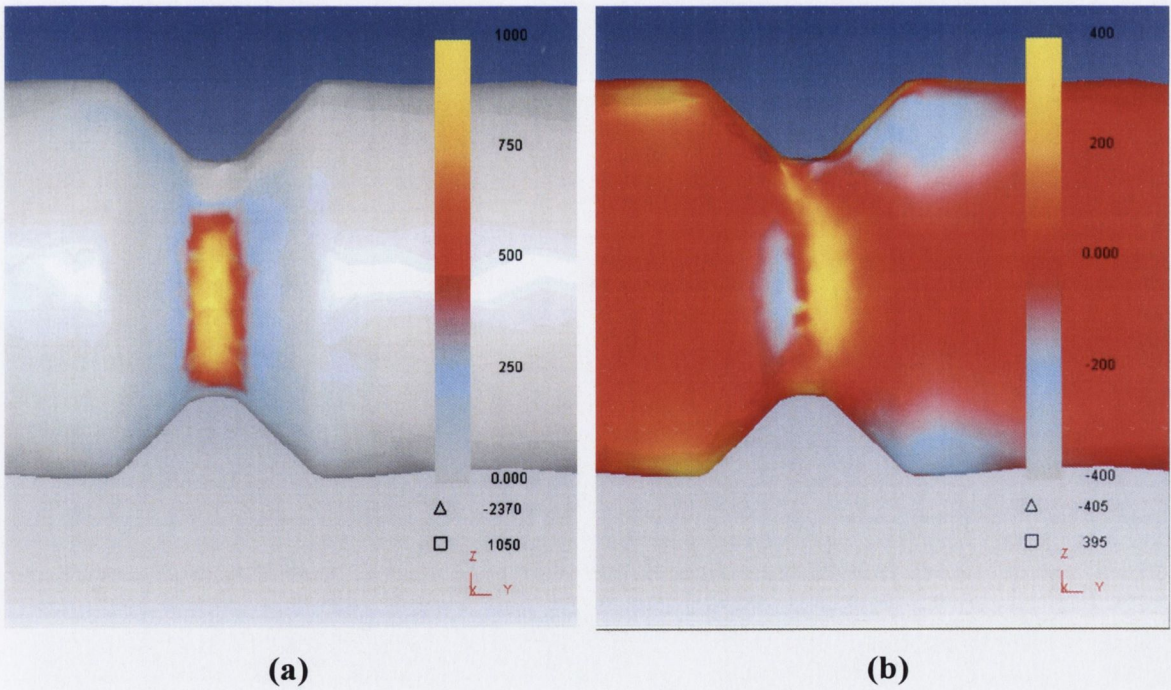


Figure 5.63 Side view of the (a) axial tensile stress and (b) shear stress, τ_{zr} , surface distribution on a fastener after 5.5 rotations.

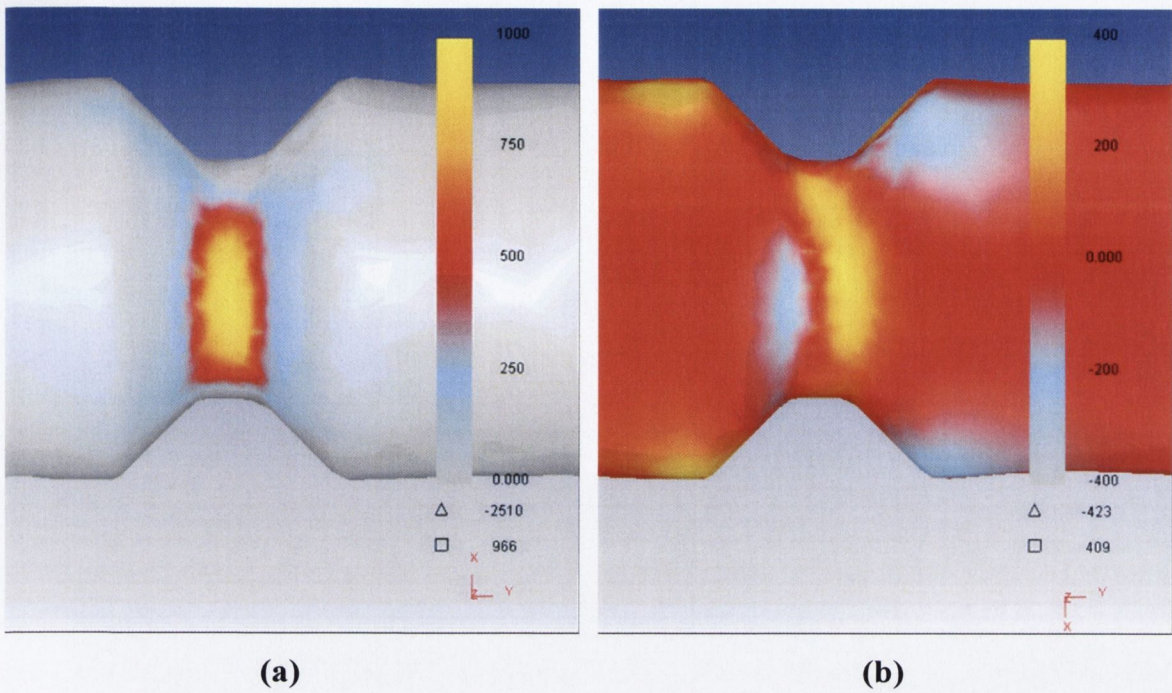


Figure 5.64 Side view of the (a) axial tensile stress and (b) shear stress, τ_{xz} , surface distribution in a fastener after 5.75 rotations.

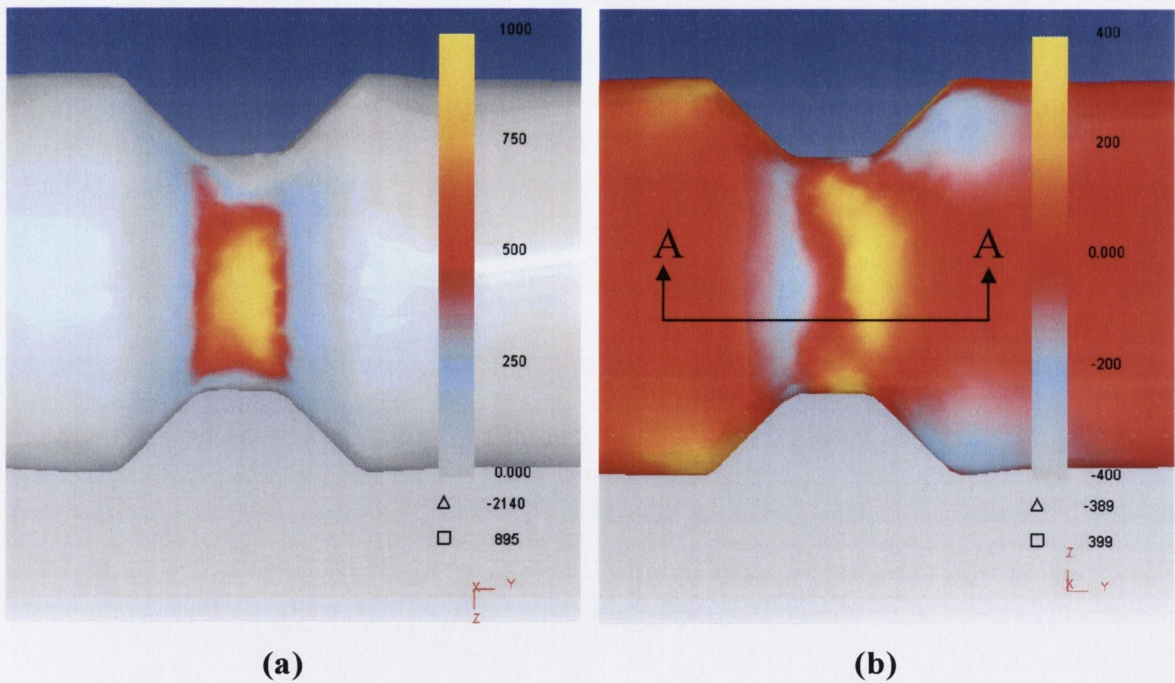


Figure 5.65 Side view of the (a) axial tensile stress and (b) shear stress, τ_{xz} , surface distribution on a fastener after 6 rotations.

In order to better comprehend how the induced shear stresses helped to propagate the small crack that was generated due to lapping, axial (longitudinal)

cross-sections were taken from Figures 5.61 (b)–5.65 (b) at 90° to the die/workpiece interface through line AA in Figure 5.65 (b).

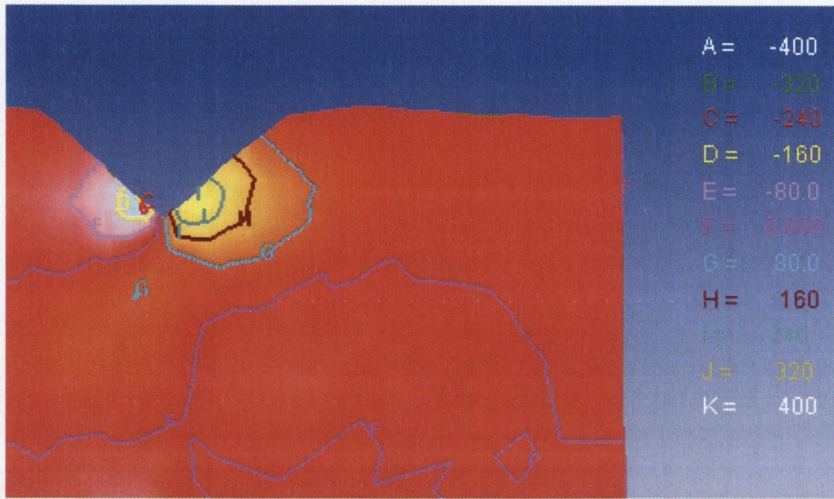


Figure 5.66 Axial cross-section of the shear stress, τ_{zt} , distribution after 5 rotations.

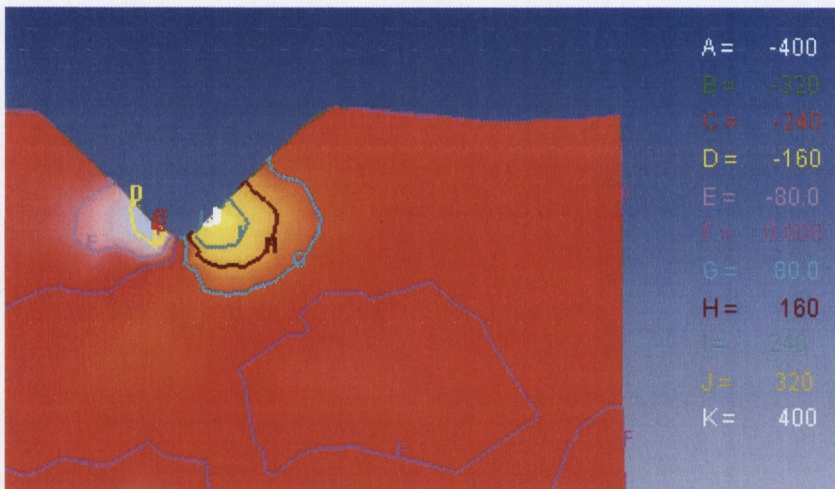


Figure 5.67 Axial cross-section of the shear stress, τ_{zt} , distribution after 5.25 rotations.

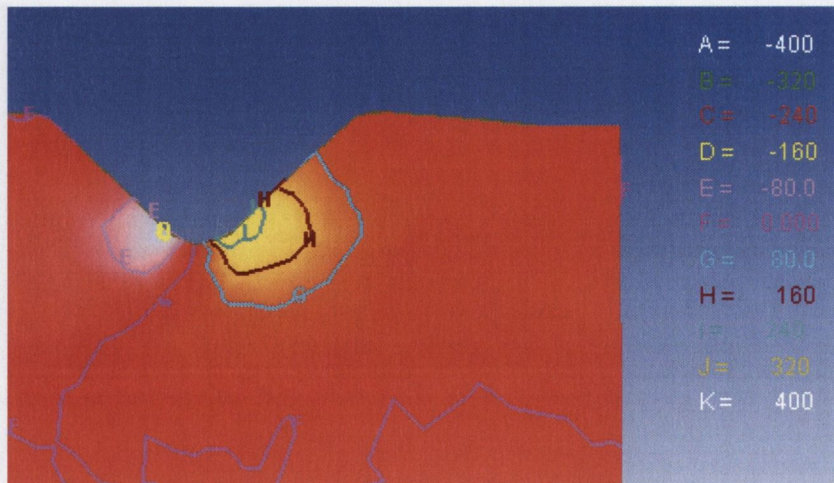


Figure 5.68 Axial cross-section of the shear stress, τ_{zt} , distribution after 5.5 rotations.

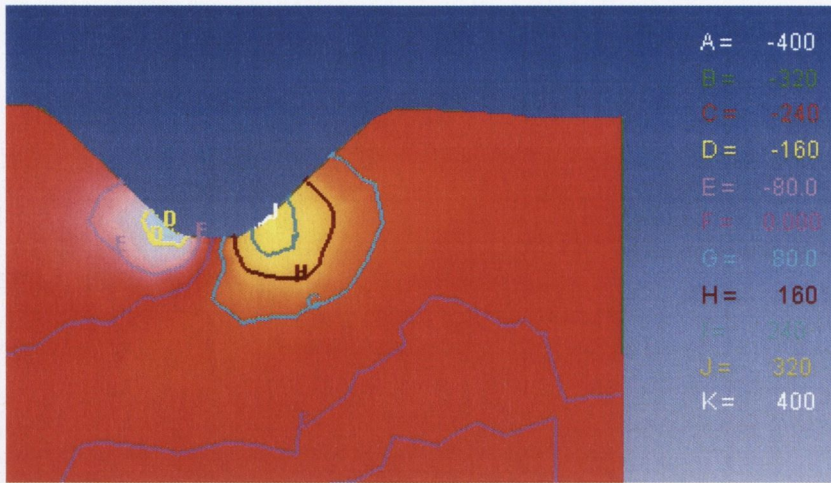


Figure 5.69 Axial cross-section of the shear stress, τ_{zr} , distribution after 5.75 rotations.

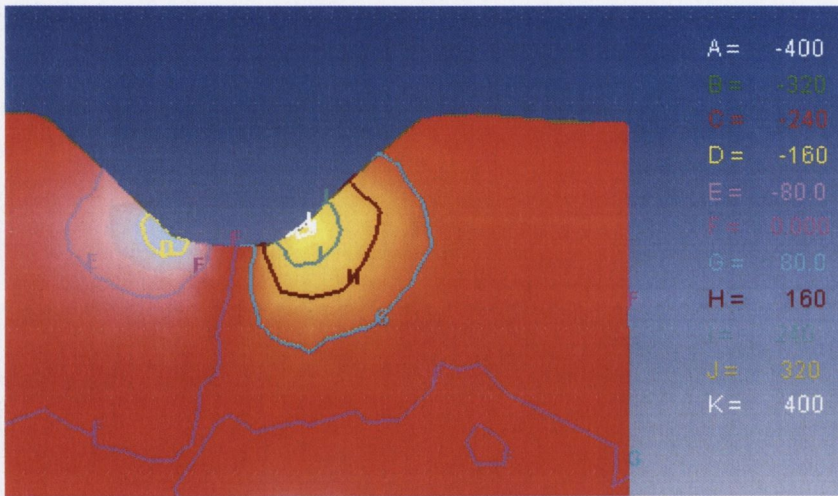


Figure 5.70 Axial cross-section of the shear stress, τ_{zr} , distribution after 6 rotations.

As can be seen from Figures 5.66–5.70, at the corners of the groove the shear stresses are pointing in opposing directions. The material on the right corner is subjected to greater shear than that on the left and is distributed around the corner radius. Therefore, as the groove was incrementally widened, the level of the shear stresses at the right corner of the groove increased which caused the crack to propagate due to shear in the deformation zone at 90° to the die/workpiece interface.

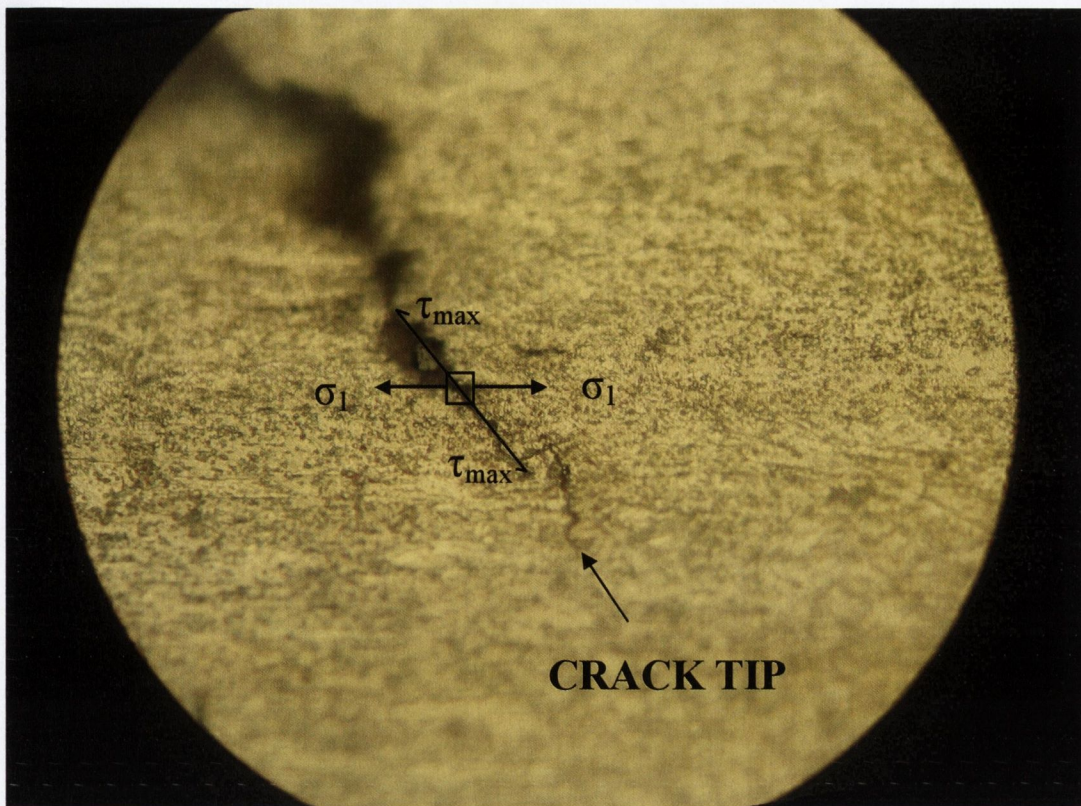


Figure 5.71 Macroetch revealing the direction of the crack tip with an illustration of the maximum principal stress direction. (x1000)

Consequently, the conditions for crack propagation have been generated whereby large tensile stresses were found in conjunction with large shear stresses on the surface of the workpiece in the region where the crack appeared at the base of the groove. These tensile stresses initiated void growth and subsequently the large shear stresses propagated the crack at a 45° angle to the maximum principal stress direction to generate a ductile shear failure mechanism, as shown in Figure 5.71.

5.2.2.4 The Normalised Cockcroft-Latham Fracture Law Applied to Predict the Location of Surface Fracture

In order to predict the location of fracture on the surface of the workpiece the Normalised Cockcroft-Latham fracture law was applied to the simulation results. This fracture law is suitable for upsetting simulations that generate high tensile stresses [71, 72] and is used to determine the likelihood of premature failure due to tensile stresses that cause void evolution. As previously mentioned in section 2.2.1, the maximum damage value, C , indicates the probable position where ductile shear fracture is most likely to occur.

Figure 5.72 is a plot of the distribution of the damage attributed to point 5 of the *point tracking* points which indicates that the damage increases dramatically during the *stretching* stage as the groove is widened. As can be seen, the maximum damage value for point 5 occurred between 5.85 and 6 rotations.

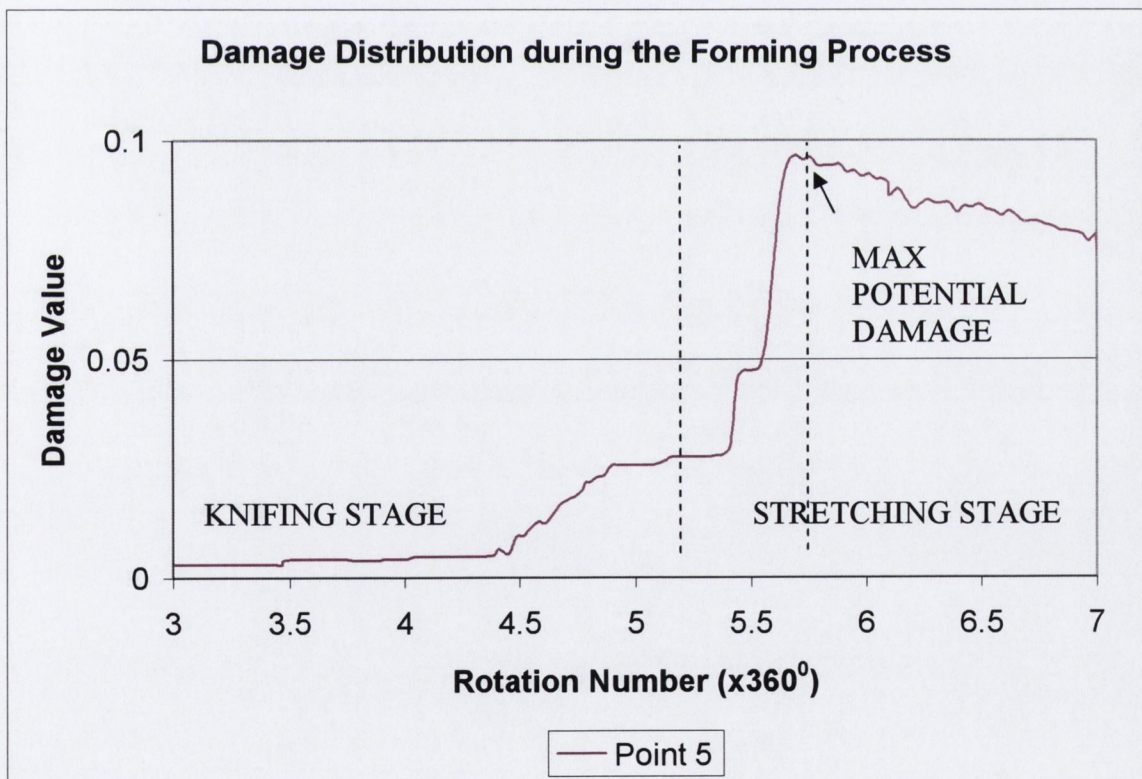


Figure 5.72 Damage distribution of point 5 while forming the second groove.

However, as shown in Figure 5.73 the maximum C value during the simulation occurred after 5.75 rotations and was measured as 0.106. This value

can then be considered to be the critical damage value for the particular material used and considered as a material property. This conforms to experimental results where cracking was found to occur between the 5th and 6th workpiece rotations. Another interesting result is that this critical damage value was found at the base of the groove at 90° to the die/workpiece interface which is the same region where the large tensile and shear stresses were found as discussed in the previous section.

This indicates that the damage model has successfully determined the likely pattern for the onset of fracture in the workpiece.

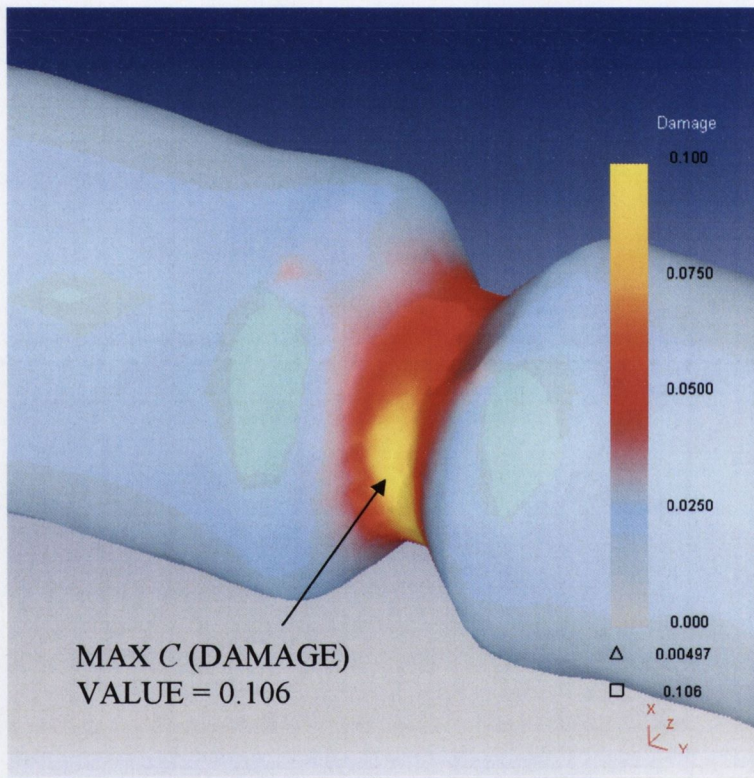


Figure 5.73 Surface damage distribution in the workpiece after 5.75 rotations.

5.2.3 Development of Shear Induced Twist

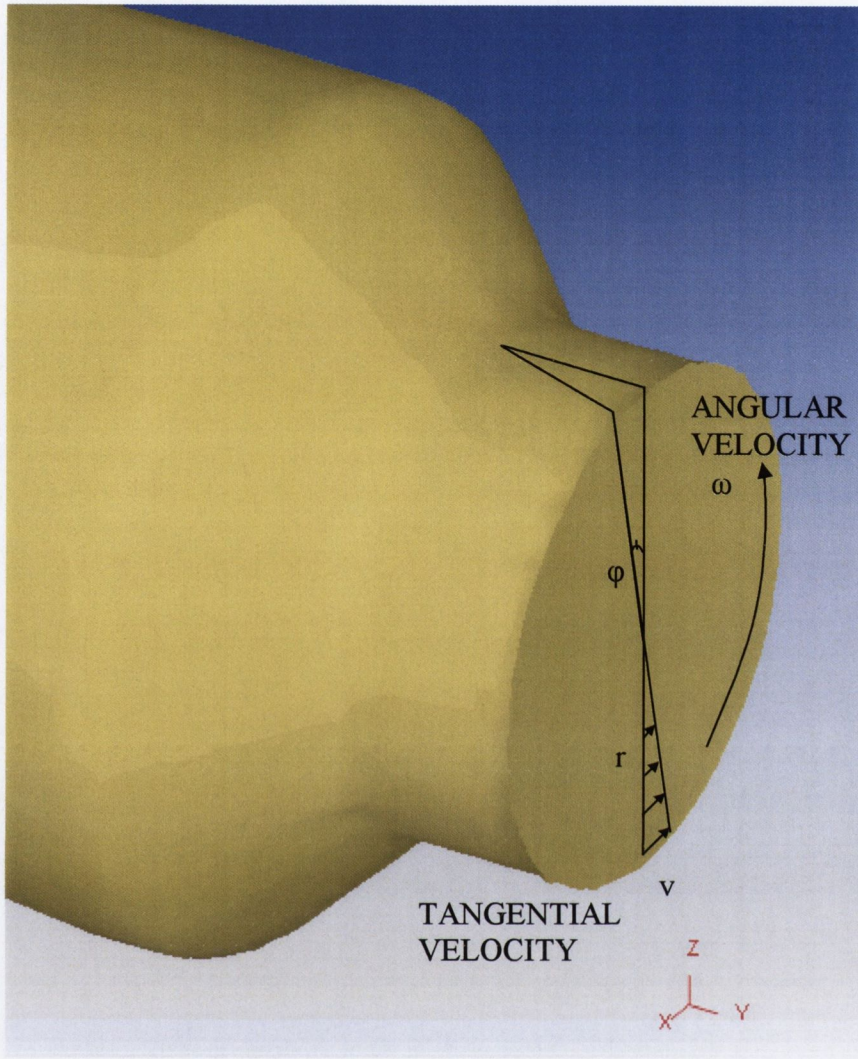


Figure 5.74 Schematic of the angle of twist, ϕ .

In the previous section it was established that surface cracking was due to a combination of axial tensile stresses and shear stresses. However, a feature of the Form Rolling process that has not been investigated very extensively is the *Twisting Effect* [49, 56]. During Form Rolling of the second groove as shown in Figure 5.74, relative torsion exists due to tangential velocity differences in the deformed zone that increase as the depth of the groove increases. Therefore, the effects of twisting are increased the greater the depth of the deformation zone.

The analysis presented will be divided into two sections. The first concerns the *knifing* and the second the *stretching* stage of the die. The *knifing* stage ranges from the 3rd to the 5th rotations, and the *stretching* stage ranges from the 5th to the

7th workpiece rotations. *Point tracking* was used to map and quantify the material displacement as the groove was formed so that the angle of twist could be obtained. It should be noted that the starting distance between each point is 0.25mm in the y direction, as shown in Figure 5.75 (a) and that the points were placed 0.01mm below the surface.

5.2.3.1 Twist During the Knifing Stage

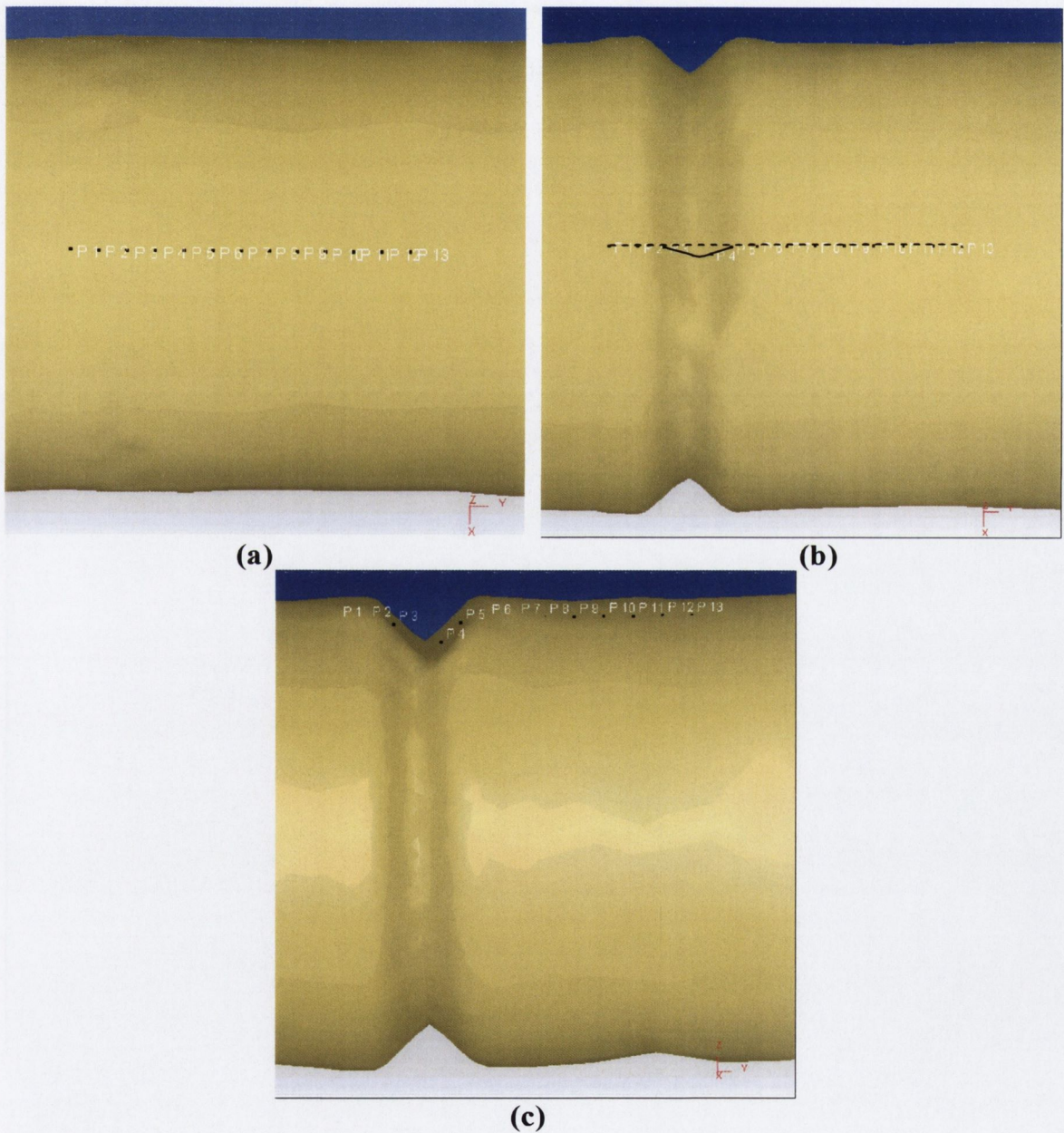


Figure 5.75 Plan view of the point tracking points plotted (a) before indentation of the second groove occurred i.e. after 3 rotations, (b) after 4 rotations and (c) a side view taken after 4 rotations.

During the formation of the groove the workpiece material is first displaced, due to a *knifing* action, by the dies until the full groove depth is reached. Figures 5.75 (a) and (b) show a plan view of the *point tracking* points after 3 (starting) and 4 rotations of forming the second groove. The workpiece is in the *knifing* stage of the die, as can be seen by the right angle groove form in Figure 5.75 (c). Figure 5.75 (c) is a side view of the workpiece after 4 rotations that shows the displacement of the z coordinates of the points.

Table 5.4 shows the change in the (x, y, z) coordinates of the 13 selected *point tracking* points along the second groove from the 3rd to the 4th rotation of the workpiece. From the perspective of Figure 5.75 (a), the x direction is up and down, the y direction is from left to right and the z direction is in and out of the page. This table shows the three points that have moved the most are points 3, 4 and 5 as can be seen in Figure 5.75 (b) and (c). The dashed line in Figure 5.75 (b) shows the line on which points 1-13 were originally positioned. The solid line indicates the displacement of the points due to torsional forces acting on the material which induces tangential shear stress thus causing material displacement and twisting within the deformation zone.

Point Number	x (mm)	y (mm)	z (mm)
1	0.0000	0.0090	0.0010
2	0.0018	0.0060	-0.0010
3	0.0112	0.0020	-0.0550
4	0.0318	0.1350	-0.2010
5	0.0040	0.0530	-0.0340
6	0.0000	0.0260	0.0070
7	0.0030	0.0200	0.0050
8	0.0020	0.0170	0.0030
9	0.0030	0.0150	0.0010
10	0.0030	0.0150	0.0010
11	0.0020	0.0150	0.0010
12	0.0020	0.0140	0.0010
13	0.0010	0.0140	0.0000

Table 5.4 Change of the x, y and z coordinates (mm) of the 13 selected *point tracking* points from 3 to 4 workpiece rotations.

Figures 5.76 (a), (b) and (c) show the radial, axial and hoop strain distributions, respectively. As can be seen most of the material during the *knifing*

stage moves in the axial direction. This is because the material is pushed to either side of the V form towards the head and tip of the fastener. Movement in the radial direction occurs to a lesser extent whereby point 4 has advanced the greatest by 0.0418mm. The change in position of point 4 can also be attributed to the generation of tangential shear stresses due to the differing tangential velocities at different depths in the deformation zone. The shear stresses pointing towards and away from the workpiece are shown in Figure 5.76 (d) where the contact area between the die and the workpiece is shaded.

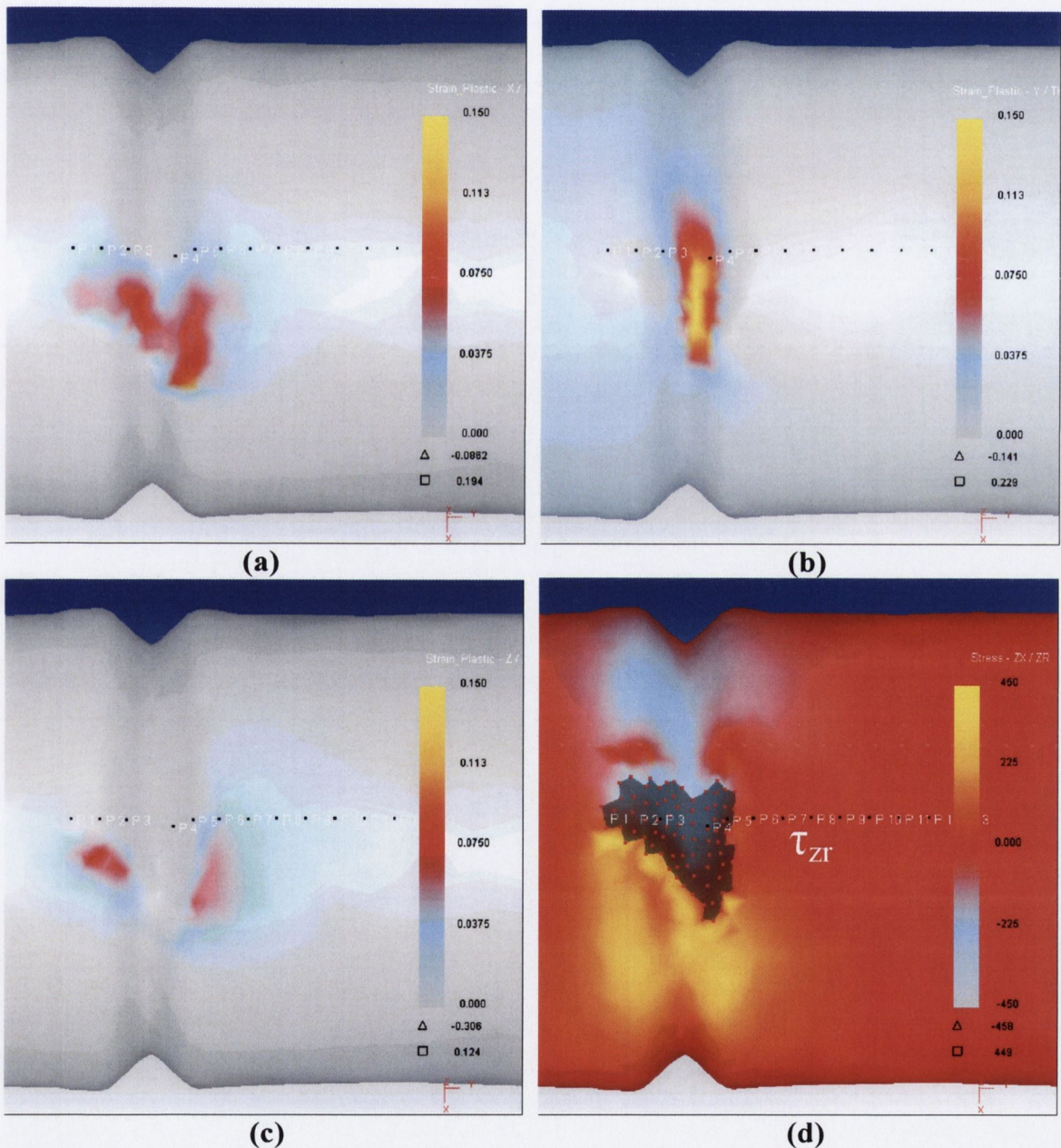


Figure 5.76 Plan view of the surface strains in the (a) radial, (b) axial, (c) hoop directions and the (d) corresponding shear stress τ_{ZR} with the contact area shaded, taken after 4 rotations.

Table 5.5 shows the change in the (x, y, z) coordinates of the *point tracking* points from the 3rd to the 5th workpiece rotation. Figures 5.77 (a) and (b) show a plan and side view, respectively, of the *point tracking* points after 5 rotations of the workpiece. The strain distributions in the radial, axial and hoop directions for the same stage in the process are shown in Figures 5.78 (a), (b) and (c) respectively.

Point Number	x (mm)	y (mm)	z (mm)
1	0.0050	0.0080	0.0020
2	0.0030	0.0060	0.0040
3	0.0180	0.0210	-0.0611
4	0.0380	0.0160	-0.4380
5	0.1190	0.4600	-0.4520
6	0.0890	0.3470	-0.2850
7	0.0496	0.2320	-0.1490
8	0.0234	0.1100	-0.0320
9	0.0074	0.0620	0.0040
10	0.0050	0.0550	0.0090
11	0.0030	0.0500	0.0080
12	0.0023	0.0490	0.0020
13	0.0020	0.0460	0.0014

Table 5.5 Change of the (x, y, z) coordinates (mm) of the 13 selected *point tracking* points from 3rd to the 5th workpiece rotation.

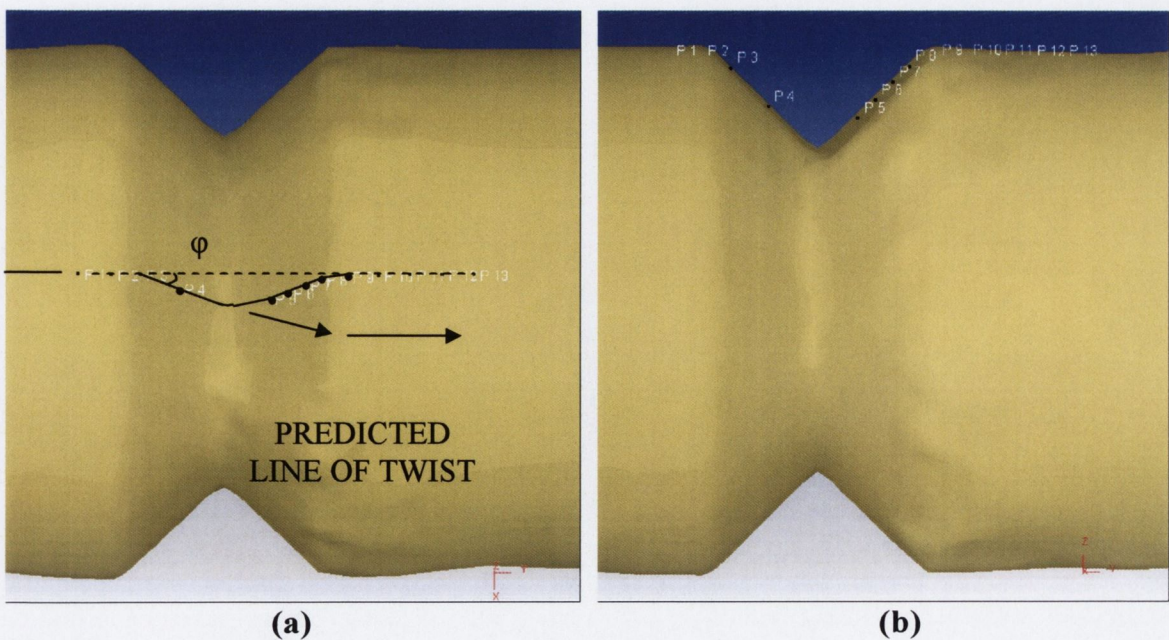


Figure 5.77 (a) Plan and (b) side view of the fastener after 5 rotations.

As can be seen in the Figure 5.77, point 4 is now to the left of the V form in the groove and the distance in the y direction between points 4 and 5 has increased from 0.168mm after the 4th rotation to 0.694mm after the 5th rotation. This shows that the material was subjected to large plastic strain in the axial direction as shown in Figure 5.78 (b), especially in the region between points 4 and 5.

From Table 5.5 points 4 to 8 have all moved in the x direction since the previous rotation. Of these, point 5 has moved the most and point 8 the least in the x direction since the groove was first initiated and measured at 0.119mm and 0.0234mm respectively, as shown in Table 5.5. Points 4 to 8 have been displaced the most because they are in the deformation zone. However, due to the model setup the die is not fully in contact with the workpiece. This is illustrated in Figure 5.78 (d). Contact is only shown in the deformed region; therefore, a torque is not applied at the maximum diameter of the fastener. Consequently, torsional forces are not exerted along the whole groove, especially on the right side resulting in a less than anticipated displacement of points 6 to 13. These points should incrementally increase in line with the arrows in Figure 5.77 (a) as described by Danno and Tanaka [56]. This line determines the angle of twist ϕ .

However, because the necessary torsional forces are not applied at the outer diameter, the shear stresses diminish on the right side with the result that the points are not displaced to the anticipated extent. In order to rectify this, models should be run with differing die/workpiece interferences to ensure die/workpiece contact along the entire length of the workpiece. Having stated this however, points in the deformation zone at the base of the groove experience the *twisting effect* because of the tangential differences of the shear stresses at different depths in the deformation zone.

This is shown in Figure 5.78 (d) where the largest shear stresses are found at the central region of the groove surface and not at the right side, as has been reported by Danno and Tanaka [56].

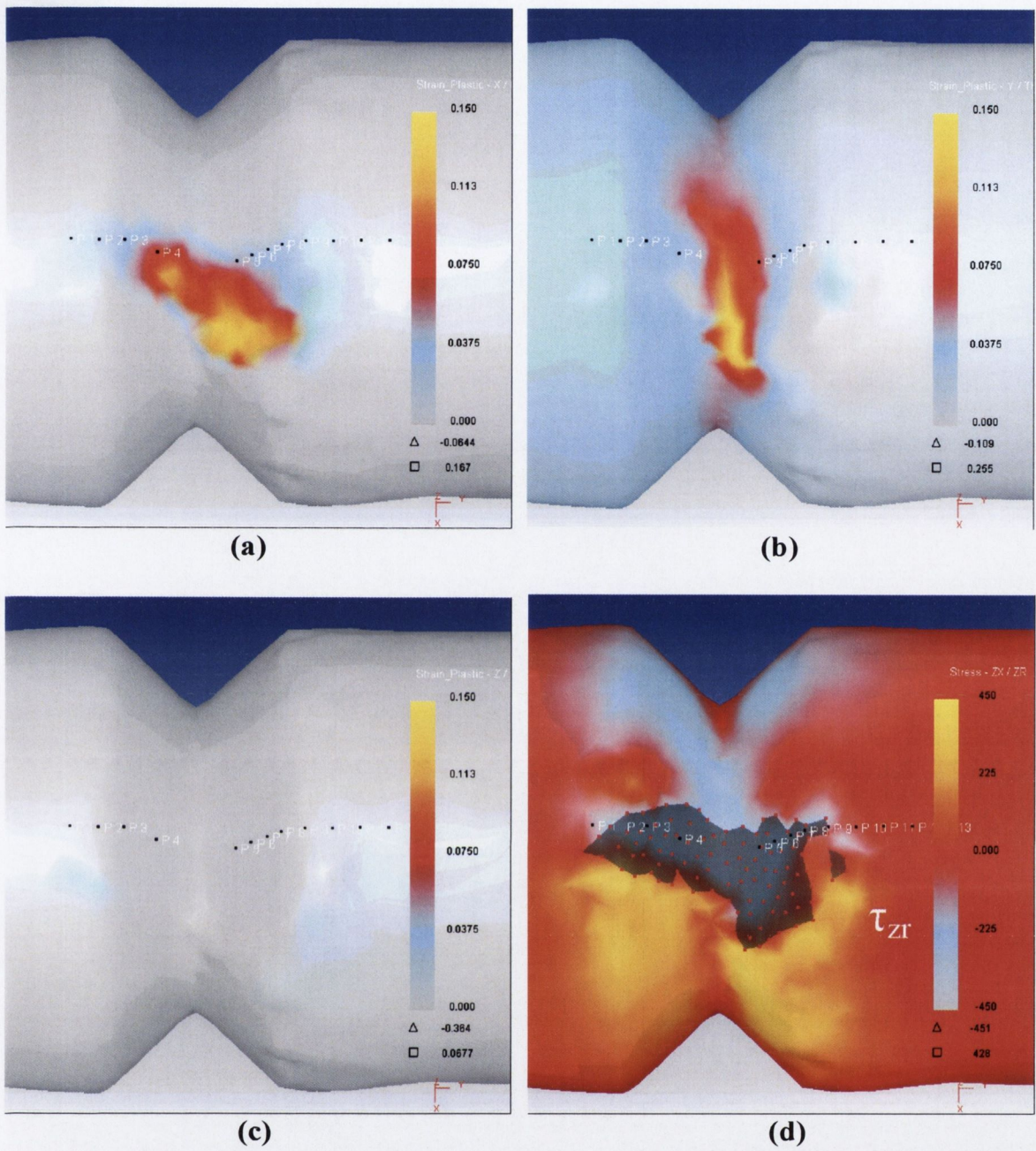


Figure 5.78 Plan view of the (a) radial, (b) axial, (c) hoop strains and the (d) corresponding shear stress τ_{zr} with the contact area shaded, after 5 rotations.

5.2.3.2 Twist During the Stretching Stage

After 5.2 rotations of the workpiece, the *stretching* stage on the die starts i.e. the groove reaches its maximum depth whereby the width is then gradually increased. The changing coordinates from the start of the process to the 6th rotation are shown in Table 5.6.

Point Number	x (mm)	y (mm)	z (mm)
1	0.0050	0.0140	0.0040
2	0.0060	0.0110	0.0035
3	0.0190	0.0140	-0.0600
4	0.0370	0.0270	-0.4440
5	0.1030	0.6870	-0.8340
6	0.1330	0.6150	-0.8010
7	0.0835	0.6360	-0.5490
8	0.0631	0.5100	-0.4190
9	0.0422	0.4090	-0.2690
10	0.0212	0.2790	-0.1470
11	0.0190	0.1620	-0.0140
12	0.0020	0.1380	0.0060
13	0.0010	0.1320	0.0020

Table 5.6 Change of the (x, y, z) coordinates (mm) of the 13 selected point tracking points from the 3rd to the 6th workpiece rotation.

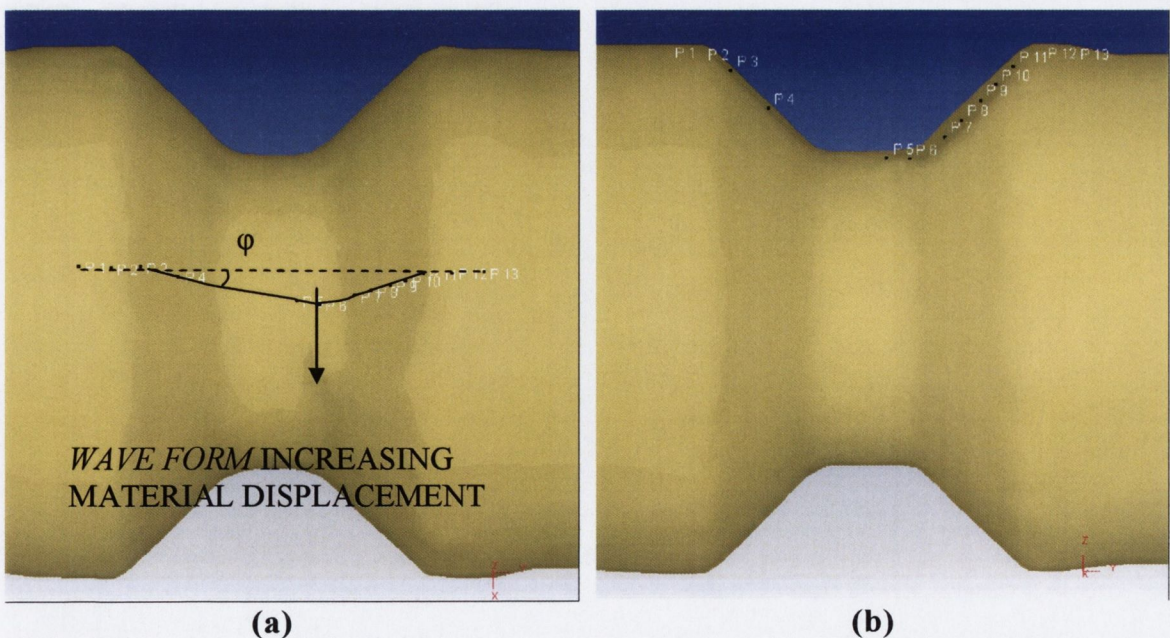


Figure 5.79 (a) Plan and (b) side view of the fastener after 6 rotations.

Figures 5.79 (a) and (b) show a plan and side view, respectively, of the *point tracking* points after 6 rotations. Similar to the previous examples, the twist in the groove is approximated by the solid line which is generated by tangential shear stresses.

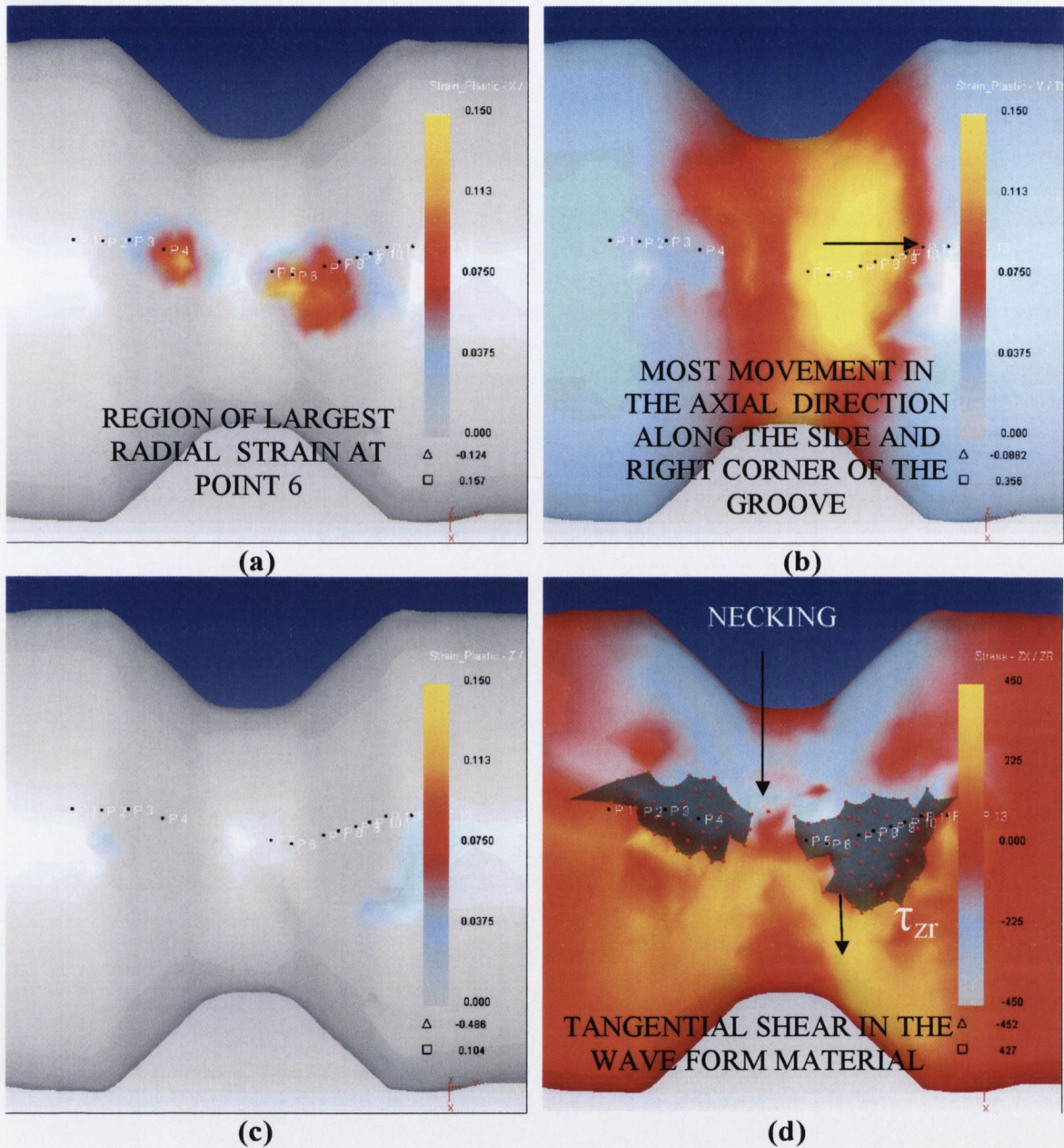


Figure 5.80 Plan view of the (a) radial, (b) axial, (c) hoop strains and the (d) corresponding shear stress τ_{zr} with the contact area shaded, after 6 rotations.

At this stage the material in the centre of the groove is subjected to large amounts of strain in particular on the right side of the groove in the y (axial) direction, as shown in Figure 5.80 (b). This happens because the material flows

predominantly towards the tip of the fastener, the rate of which is determined by the stretching angle β , on the die.

The difference between points 4 and 5, as can be seen in the Figure 5.80, has decreased slightly in the y direction from the previous rotation, to 0.66mm. This is because point 4 has not changed position since the previous rotation, however, point 5 has moved towards point 4 due to the *wave form* material moving and folding towards the head of the fastener which was discussed in section 5.2.1.2. Point 5, which in the previous rotation had moved the furthest in the x direction, is now the second furthest because the tangential shear stress at point 6 is greater than at point 5. This is illustrated in Figure 5.80 (a) where the area of greatest strain in the x direction coincides with point 6. Point 6 has moved 0.133mm in the x direction since the second groove was first started.

The tangential shear stress in the workpiece after 6 rotations is shown in Figure 5.80 (d). The shaded area showing the die/workpiece contact area indicates that at the centre of the groove surface there is no die/workpiece contact. This is because the axial force acting in the deformed region is greater than the yield strength which induces necking. Also note that the largest tangential shear indicated by the arrow in Figure 5.80 (d) coincides with point 6 in the deformation zone.

Point Number	x (mm)	y (mm)	z (mm)
1	0.0050	0.0100	0.0040
2	0.0080	0.0070	0.0050
3	0.0200	0.0260	-0.0580
4	0.0380	0.0200	-0.4470
5	0.1390	0.6920	-0.8370
6	0.1470	0.6180	-0.8410
7	0.0889	0.7030	-0.5890
8	0.0633	0.5890	-0.4610
9	0.0431	0.4890	-0.3120
10	0.0250	0.6580	-0.1960
11	0.0190	0.2450	-0.0660
12	0.0080	0.1590	0.0050
13	0.0030	0.1650	0.0020

Table 5.7 Change of the (x, y, z) coordinates (mm) of the 13 selected point tracking points from 3 to 7 workpiece rotations.

Table 5.7 shows the change in the coordinates of the points from the 3rd to the 7th workpiece rotation. As shown in Figure 5.81 (a), the *twisting effect* on the groove can be divided into two sections. The first ranges from point 3 to point 6 where an approximately linear line can be drawn. The second section ranges from point 6 to point 11 where an approximately linear line can also be drawn however it changes direction. Therefore, as previously discussed the *twisting effect* is evident in the first section because of the relative difference of the torsional forces at different depths of the groove which create differing tangential shear stresses in the deformation zone. However, at the extreme right side of the groove twisting is not shown to have occurred. This is because torsion was not applied to the maximum diameter of the workpiece as there was no die contact, as shown previously in Figure 5.80 (d). Therefore, there would have been a reduction in the pressure on the right side of the groove which would have reduced the torque and as such the *twisting effect* in the deformation zone.

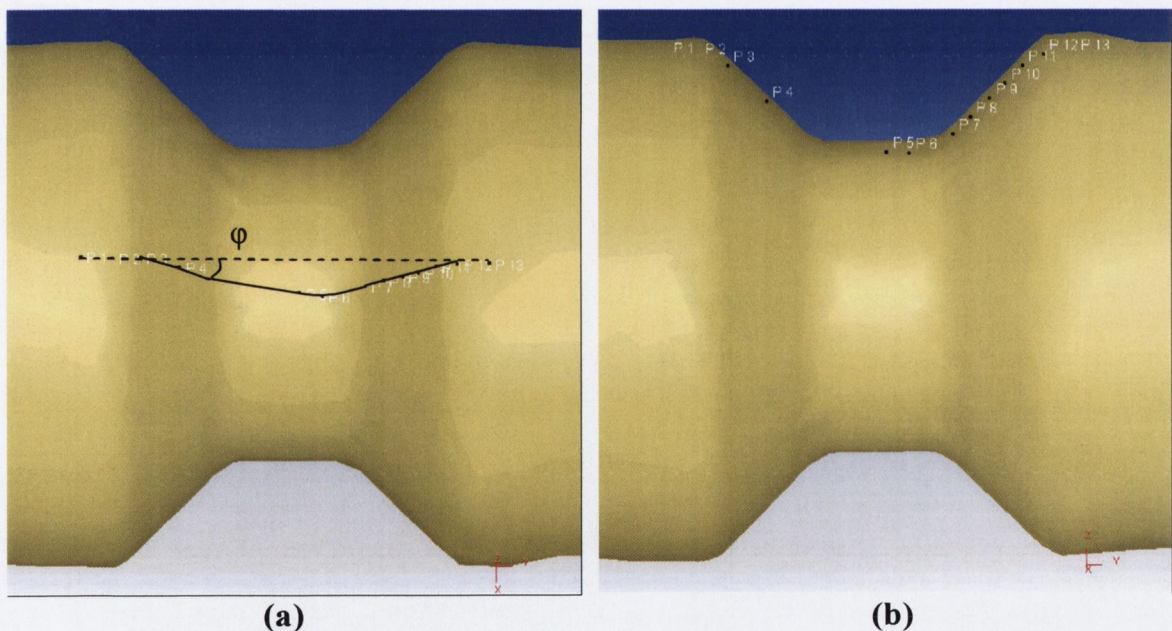


Figure 5.81 (a) Plan and (b) side view of the workpiece surface after 7 rotations.

If it was assumed that twisting did not have an effect on the point coordinates then points 5 and 6 should have displaced the same distance in the x direction because the same volume of material was formed per rotation of the workpiece in the *stretching* stage of the die. However, this clearly is not the case which would indicate that twisting has occurred. Therefore, it has been

successfully shown that a *Twisting Effect* is induced within the groove. This can be attributed to material displacement which is affected by the differing angular velocities at different groove depths. The angle of twist from point 3 to 6 was measured as 2.295° . However, a more complete analysis would consist of running models which slightly compress the entire length of the fastener during the forming process. This would provide enough pressure for twisting to be realized across the entire groove and not just at the base, as is shown in the analysis just described.

5.3 Internal Workpiece Defects

A potentially destructive characteristic of the Form Rolling process is the generation of cracks and voids at the centre of the workpiece. As discussed in section 2.1.2, the shape of the central voids depended on the configuration of the tooling where flat and two-roll machines were found to produce cruciform shaped cracks [48, 56] in the workpiece and three-roll machines generated annular cracking along the central axis of workpiece [12]. All of the tests in those studies were carried out using either cold Aluminium or hot/warm steel alloys. In the investigation carried out by the present author, cold low alloy steel was Form Rolled. However, there were no signs of central cracking as described by the authors above. In order to understand why this was the case, results from the FE model will be discussed in terms of the level of the internal tensile and shear stresses developed during the *knifing* and *stretching* stages of the die feature that formed the second groove. The Normalised Cockcroft-Latham fracture law and the hydrostatic stress will also be discussed as to the likelihood of predicting cracking in the centre of the workpiece.

As described in section 2.1.2 the formation of internal voids and cracks has been attributed to a combination of radial tensile stresses and shear stresses in the centre of the workpiece. This is similar to the stress state induced on a billet during Mannesmann seamless pipe forming and has therefore been termed the *Mannesmann Effect* [16, 48, 49, 57]. Therefore, these stresses will be investigated along with the axial stress because Teterin and Luzin [50] suggested that axial tensile stresses limit the radial tensile stresses which contribute to internal failure.

As before, *point tracking* was performed to obtain stress/strain values at the centre of the workpiece. The same number of points are selected, with equal spacing of 0.25mm as shown in Figure 5.82.

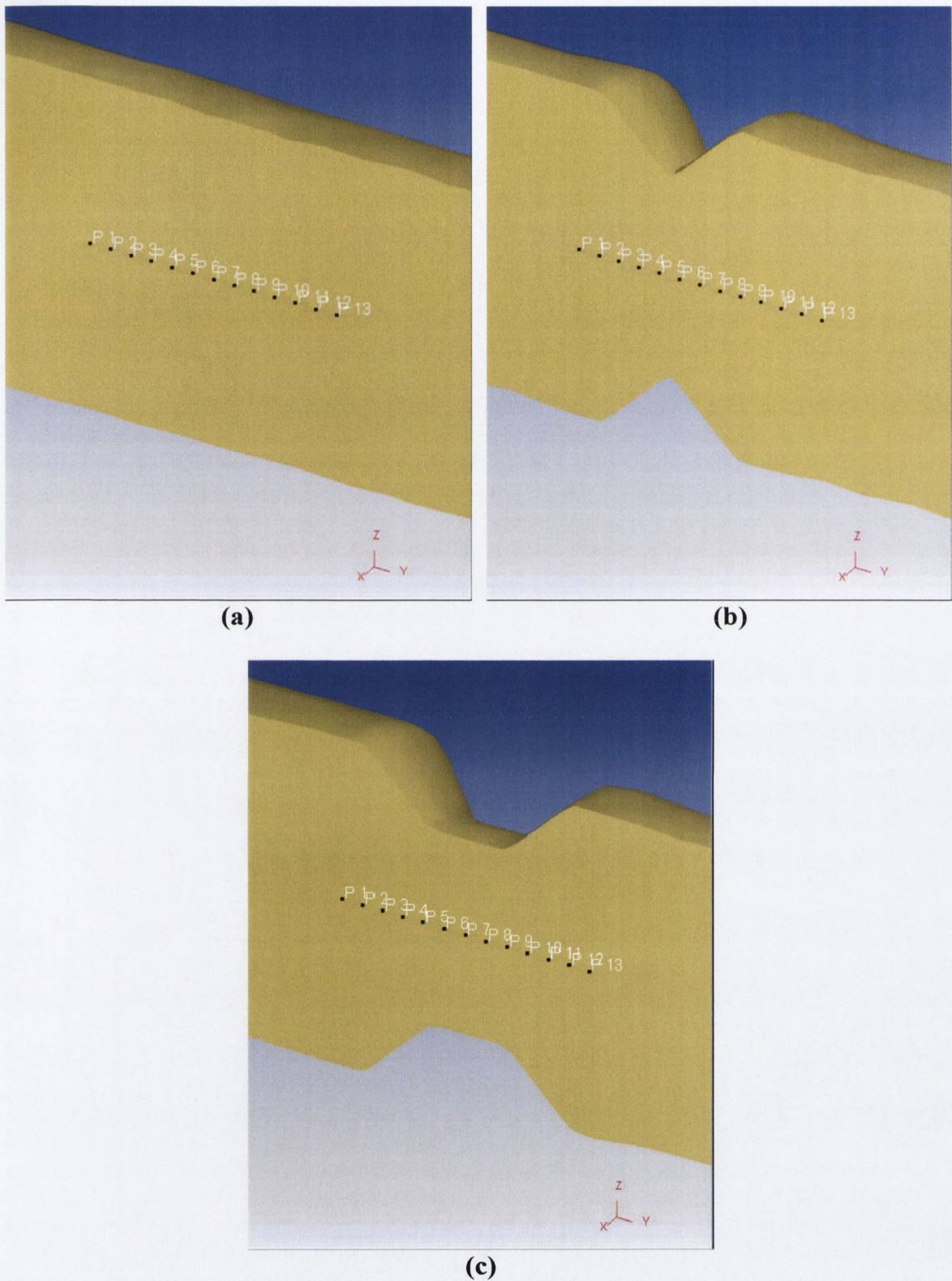


Figure 5.82 Selection of 13 selected points at the centre of the workpiece, at regular intervals of 0.25mm, during the Form Rolling the second groove after (a) 3 (b) 5 and (c) 7 rotations.

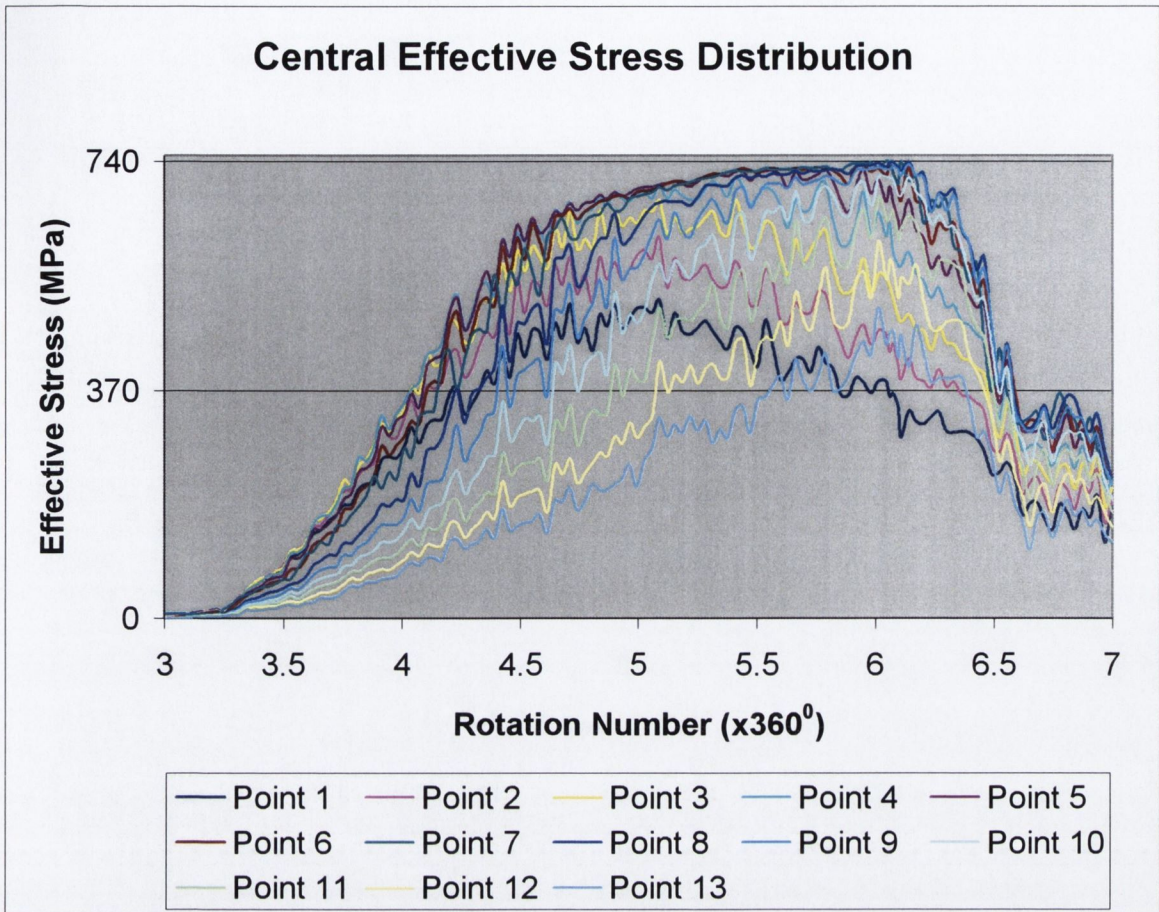


Figure 5.83 Effective stress distribution at the centre of the workpiece at the selected point tracking points while forming the second groove.

As can be seen in Figure 5.82 the *point tracking* points moved very slightly. This is reflected in the graph above, in Figure 5.83, where the points furthest from the first indentation i.e. points 8 to 13 are affected by the effective stress later than the preceding points. Consequently, point 6 will be used in the analysis of the stress/strain distributions because it experiences the greatest level of effective stress during the *knifing* and *stretching* stages by virtue of its position at the centre beneath the groove form. Therefore, this discussion will simultaneously describe both the *knifing* and *stretching* stages by referring to plots of point 6.

It should be noted that unlike the surface stress plots, the central stress plots do not cycle or experience large material displacement. Therefore, point 6 which as shown experiences the largest effective stress was found to be almost identical to the maximum stress values. Consequently, the maximum values are assumed in the following graphs to be represented by point 6.

5.3.1 Central Stresses Developed During the Knifing and Stretching Stages

Figure 5.84 is a plot of the effective stress change in the centre of the workpiece at point 6 while forming the second groove. The dashed line indicates the transition from the *knifing* to the *stretching* stage.

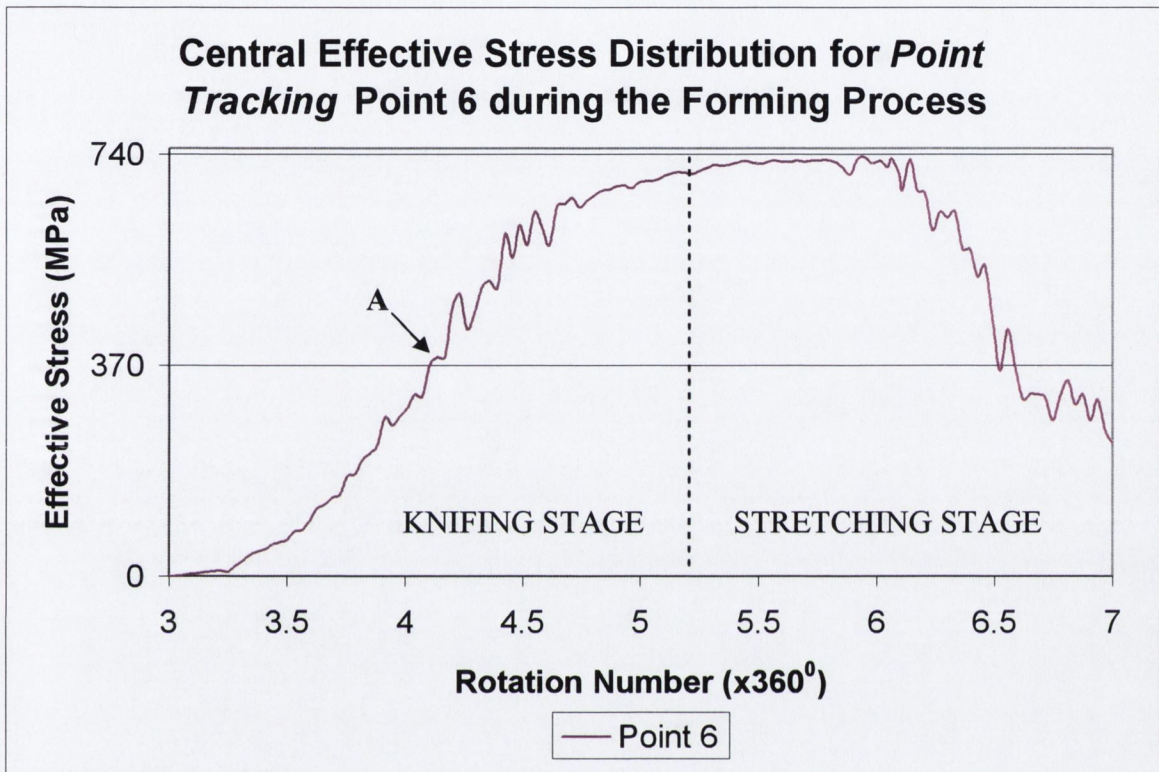


Figure 5.84 Effective stress distribution at the centre of the groove at point 6 while forming the second groove.

The curve shows that from the start of the *knifing* stage the effective stress level increases rapidly and after 4.1 rotations, labelled **A** in Figure 5.84, the effective stress is greater than the yield strength of the material. From this point on the material at the centre of the workpiece at point 6 has yielded. Figure 5.85 shows an axial (longitudinal) cross-section of the workpiece corresponding to 4.1 rotations.

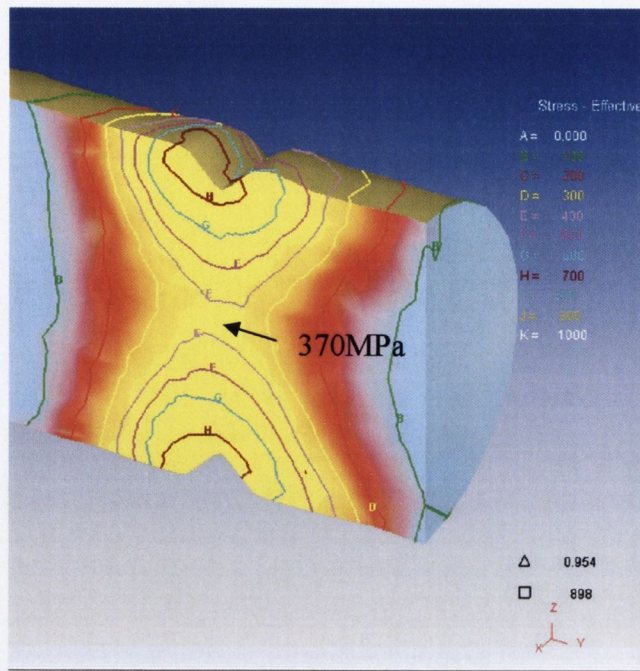


Figure 5.85 Effective stress distribution after 4.1 rotations of the workpiece.

As can be seen the effective stress emanates from the V shapes at the top and bottom of the workpiece at the die/workpiece interface.

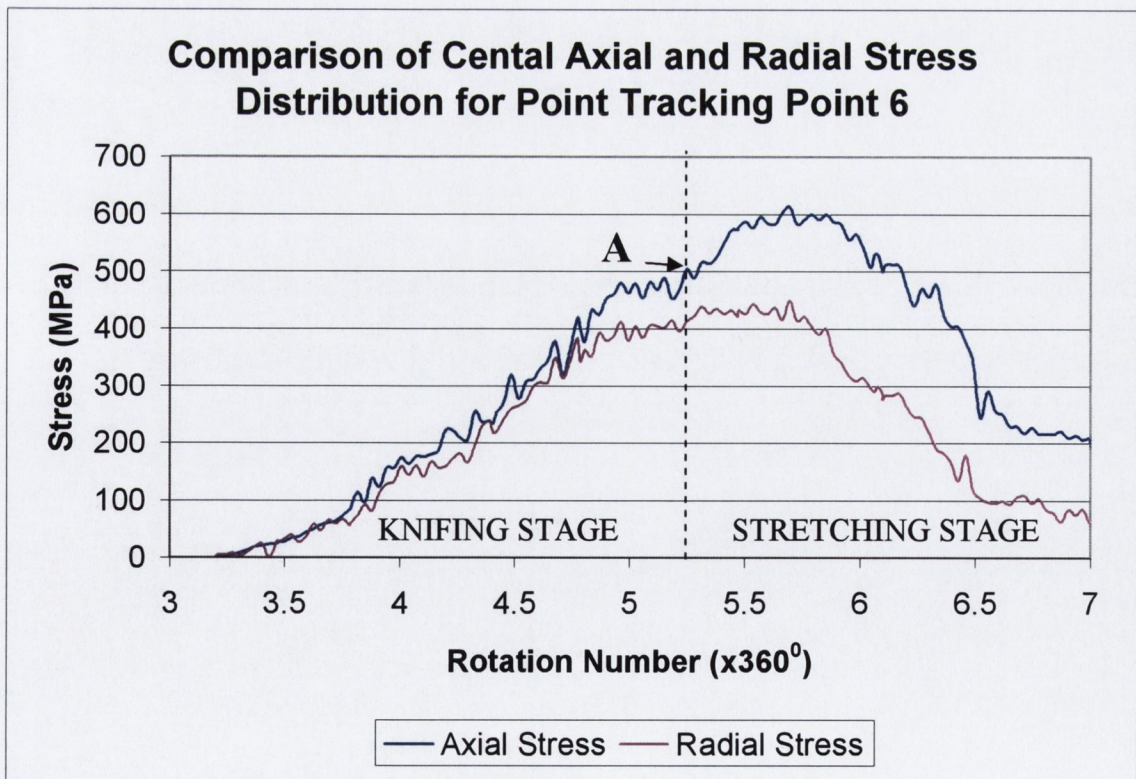


Figure 5.86 Comparison of central axial and radial stress distribution for point 6 while forming the second groove.

Teterin and Luzin [50] found that the axial tensile stresses limit the radial tensile stresses in a CWR process when discussing internal failure mechanisms. This was verified by in Figure 5.86 which is a plot of the axial and radial stress distributions at the centre of the fastener. As can be seen, at no stage does the radial stress exceed the axial stress. Both directional stresses are tensile for the whole process and increase quickly from the start to the end of the *knifing* stage which is indicated by the dashed vertical line in Figure 5.88. Once the *knifing* stage is completed and the groove has started to widen, the axial and radial tensile stresses starts to diminish, the point of which is labelled A.

Figures 5.87–5.90 show radial cross-sections of the workpiece illustrating the distributions of the radial and axial tensile stresses after 4, 5, 6 and 7 rotations which can be compared to the graph in Figure 5.86 for a visual representation of the stress distributions.

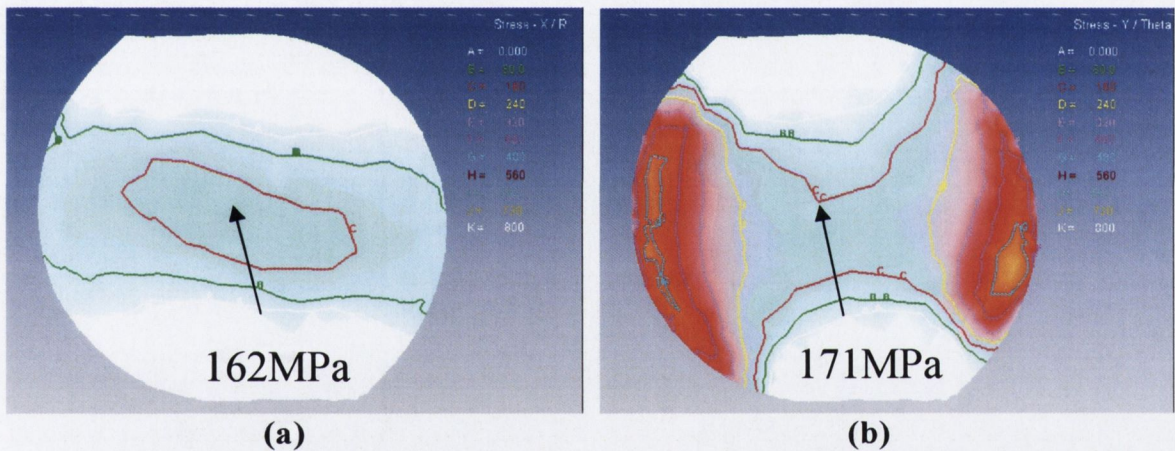


Figure 5.87 (a) Radial and (b) axial tensile stress distribution after 4 rotations.

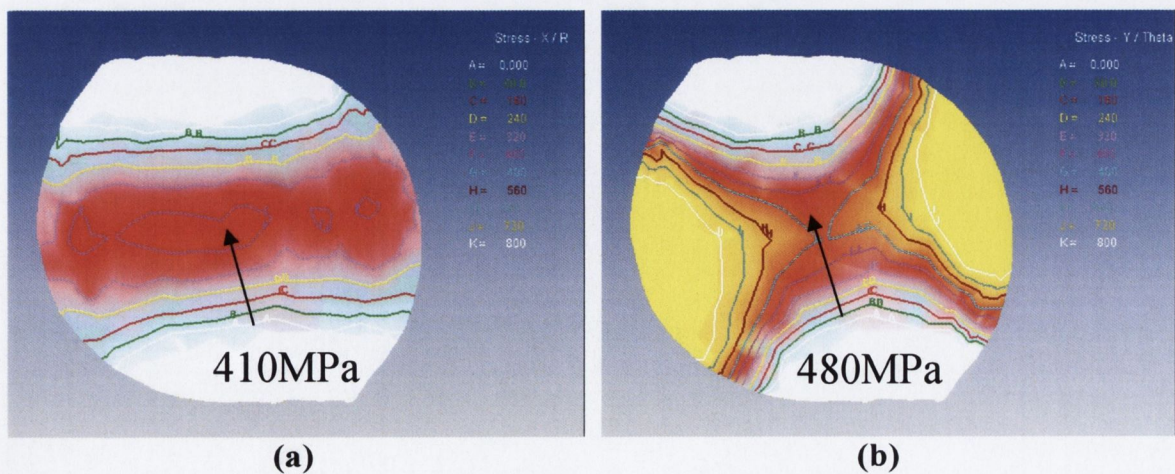


Figure 5.88 (a) Radial and (b) axial tensile stress distribution after 5 rotations.

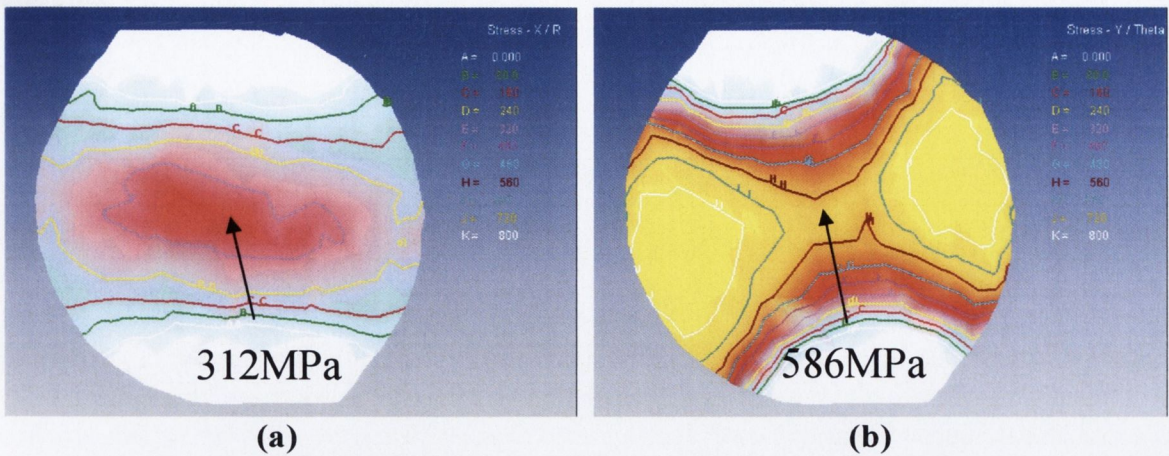


Figure 5.89 (a) Radial and (b) axial tensile stress distribution after 6 rotations.

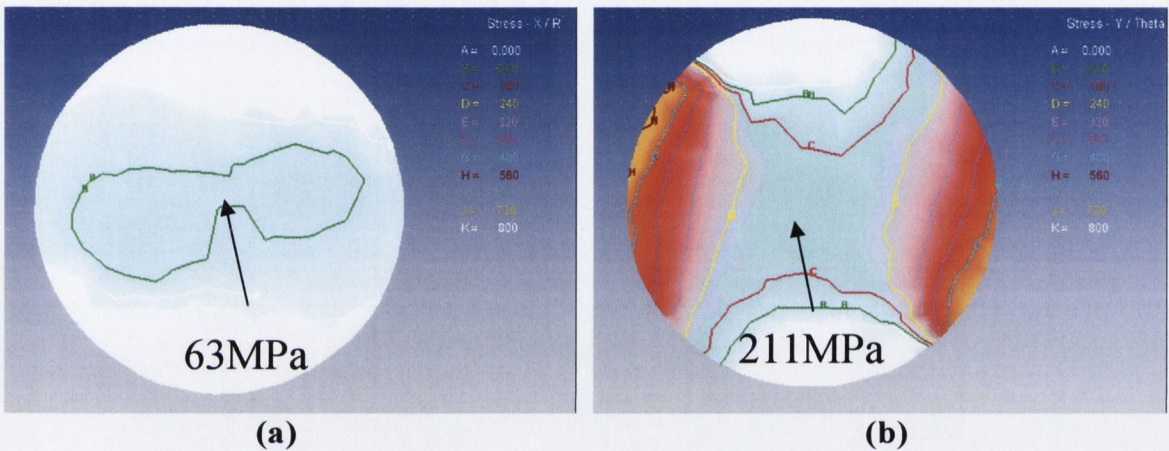


Figure 5.90 (a) Radial and (b) axial tensile stress distribution after 7 rotations.

Li *et al* [48] stated that central void formation is generated by radial tensile stress and shear stress which increases the size and density of the voids. Therefore, from Figure 5.86 it can be deduced that the radial tensile stress level is dependent on the amount of diameter reduction of the workpiece material. However, there was no evidence of void formation during the *knifing* stage in experimental analysis. Therefore the level of the radial tensile stress was not sufficient to generate void formation.

At the start of the *stretching* stage of the die the radial tensile stress levels off until the 6th rotation and then gradually decreases. The reason why the radial stress levels off is because the die is lengthening the fastener at a constant rate while forming the base of the groove.

Excessive radial stress in conjunction with large shear stresses opens up small voids in the matrix material. However, there was no evidence of internal

fracture in the experimental billets and this can be explained by referring to the illustrations in Figures 5.91 and 5.92 which show cross-sections of the workpiece of the shear stress in the fastener after 5 and 6 rotations respectively. As previously stated, the shear yield strength of the workpiece material is 214MPa. And as can be seen from the figures below, the maximum shear value at the centre of each cross-section is less than the shear yield strength. Therefore, if voids were present their size would not be increased because the shear stress is not of a sufficient magnitude at the centre of the workpiece.

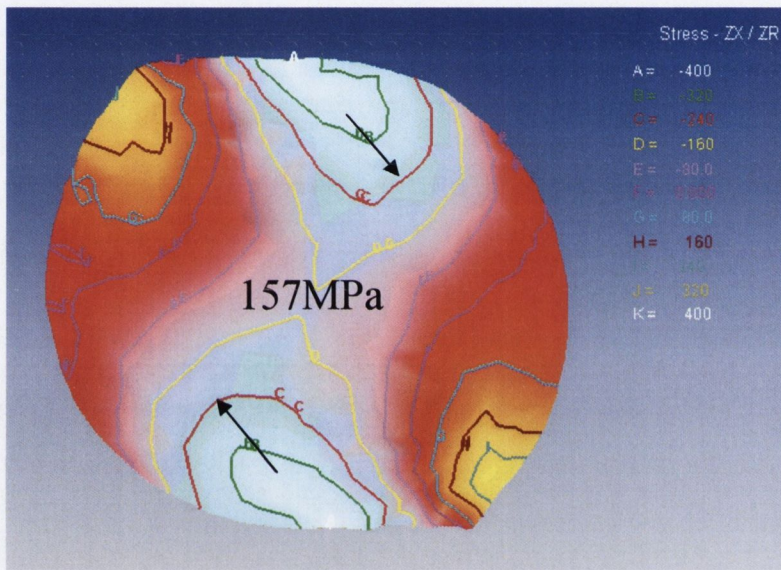


Figure 5.91 Shear stress distribution in a radial cross-section after 5 rotations.

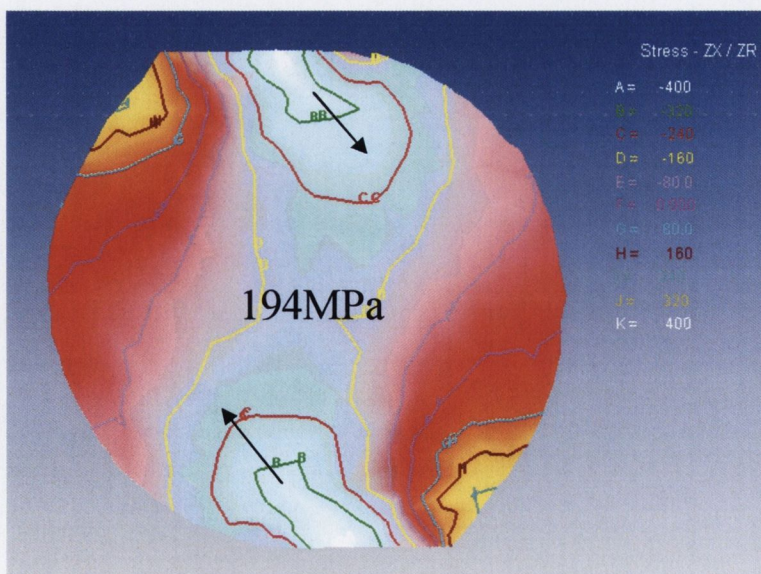


Figure 5.92 Shear stress distribution in a radial cross-section after 6 rotations.

Figure 5.93 shows the distribution of the magnitude of the shear stress at the centre of the workpiece. As shown the shear stress gradually increases at the start of forming the groove until it reaches a maximum at the 6th rotation which was measured as 205MPa. Then the shear stress decreases as the groove is widened. This indicates that void evolution is more likely to occur during the knifing stage of the die than the stretching stage. Therefore, with greater diameter reduction the shear stress would reach a value which would then cause central fracture.

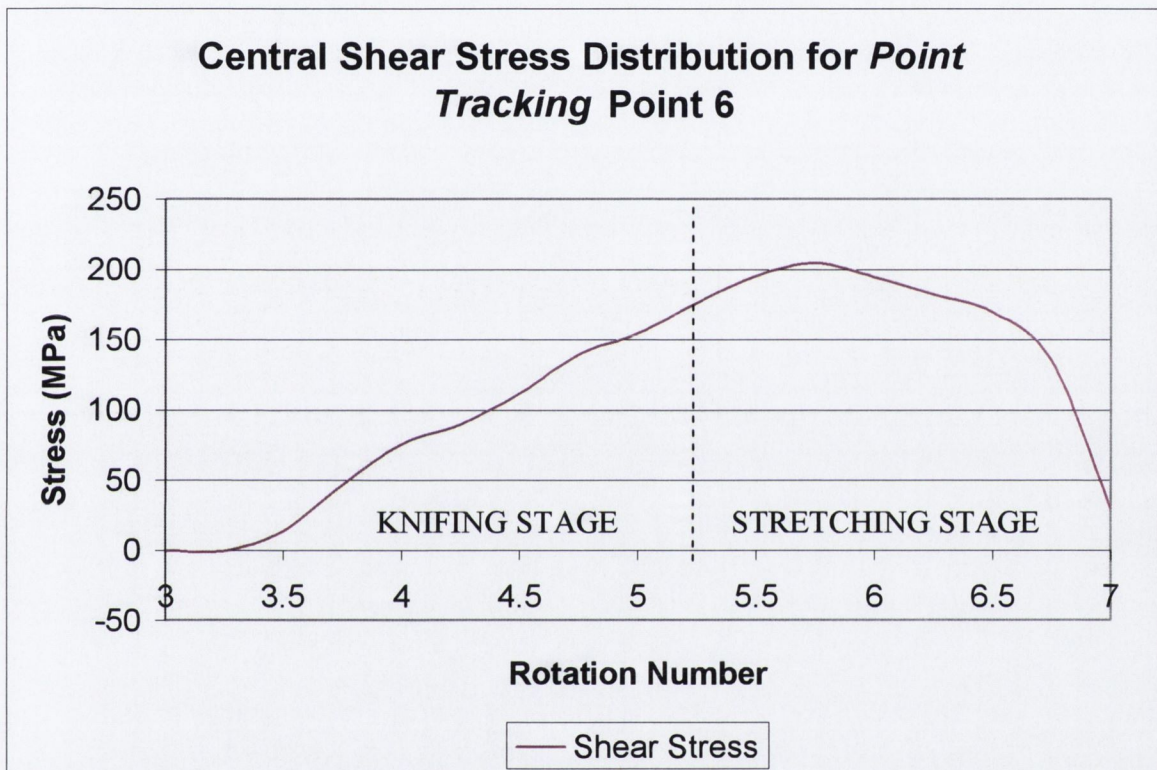


Figure 5.93 Magnitude of the shear stress distribution at the centre of the workpiece.

5.3.2 The Normalised Cockcroft-Latham Fracture Law Applied to Predict the Location of Central Fracture

Having shown the stress states within the workpiece throughout the modelling of the second groove, the Normalised Cockcroft-Latham fracture law was used to determine the likelihood of ductile failure in the interior of the workpiece. The critical damage value, C , was determined as 0.106 at the location where surface cracking occurred. Therefore, if fracture is to occur at the centre of the workpiece the critical value should be reached.

Figure 5.94 shows the distribution of the Normalised C-L damage values for point 6 from the *point tracking* points. This shows that according to the Normalised C-L law the risk of central fracture increases with increasing diameter reduction during the *knifing* stage. However, ductile fracture at the centre of the workpiece is most likely to occur during the *stretching* stage of the die. As the maximum damage value in Figure 5.94 is less than the critical damage C value of 0.106, obtained from the prediction of cracking on the surface of the workpiece, fracture is not predicted to occur at the centre.

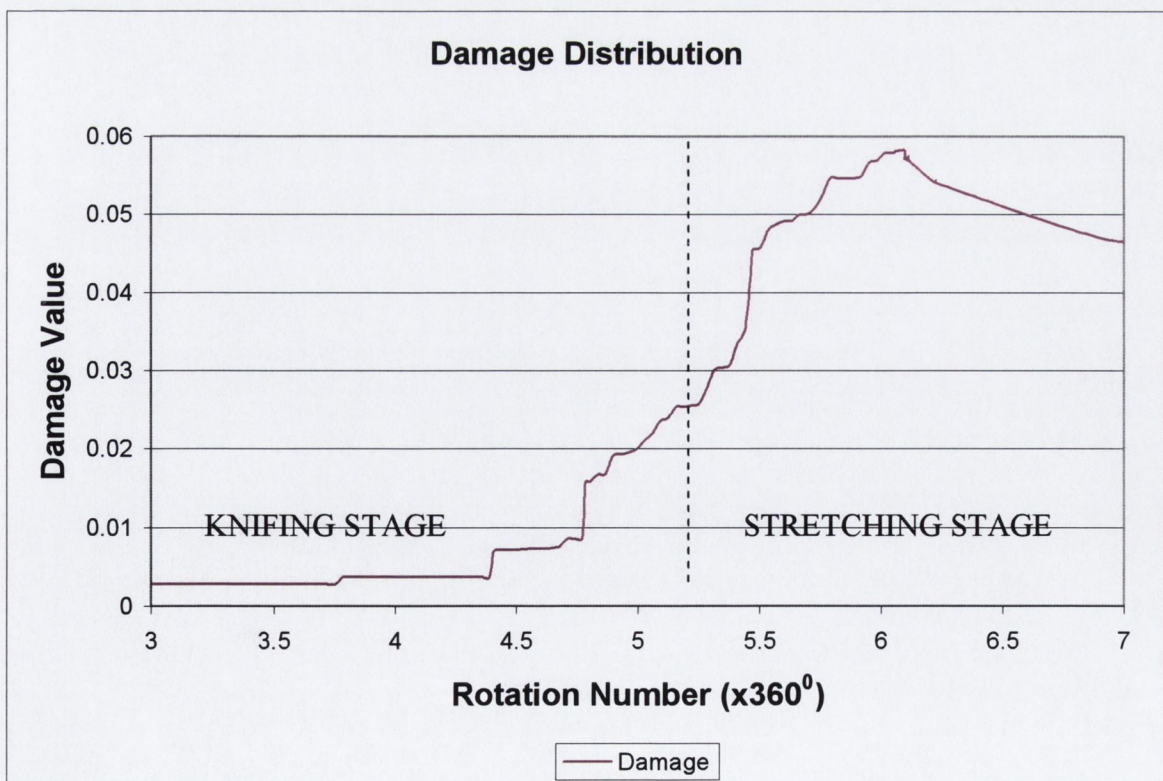


Figure 5.94 Damage distribution for point 6 while forming the second groove.

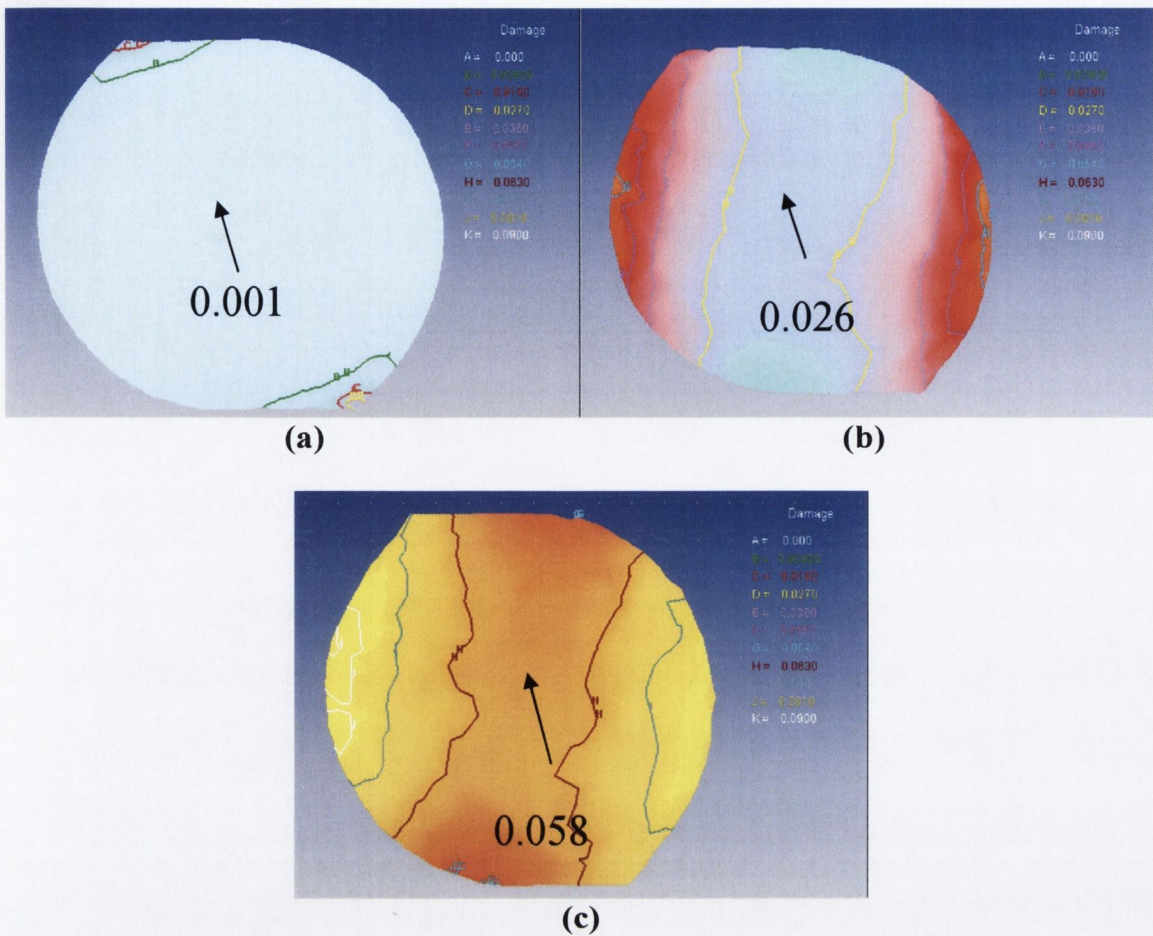


Figure 5.95 Damage distribution related to the Normalised Cockcroft-Latham fracture law after (a) 4, (b) 5 and (c) 6 rotations.

Figures 5.95 (a)-(c) show the Normalised Cockcroft-Latham fracture distribution in radial cross-sections of the workpiece; taken through the region of greatest damage after 4, 5 and 6 rotations, respectively. As can be seen, the likelihood of damage at the centre increases with increasing diameter reduction, as discussed previously in relation to the surface damage fracture results. However, assuming that the critical damage value is 0.106, fracture is not predicted in the centre of the workpiece where the maximum C value is 0.058. This is in agreement with the tensile and shear stress analysis of the process in the previous section and also with experimental observations.

5.3.3 Prediction of Internal Fracture Location using Hydrostatic Stress

An indicator that can be used to predict internal workpiece failure is the level of the hydrostatic stress, σ_h . Fang *et al* [57] stated that “*high compressive hydrostatic stress can prevent material from fracture*”. Therefore, regions of tensile hydrostatic stress fracture more easily than compressive hydrostatic stress. Figure 5.96 below is a plot of the hydrostatic stress attributed to point 6 taken from the *point tracking* data. This graph shows that the hydrostatic stress at the centre of the workpiece is tensile which makes the central region susceptible to fracture.

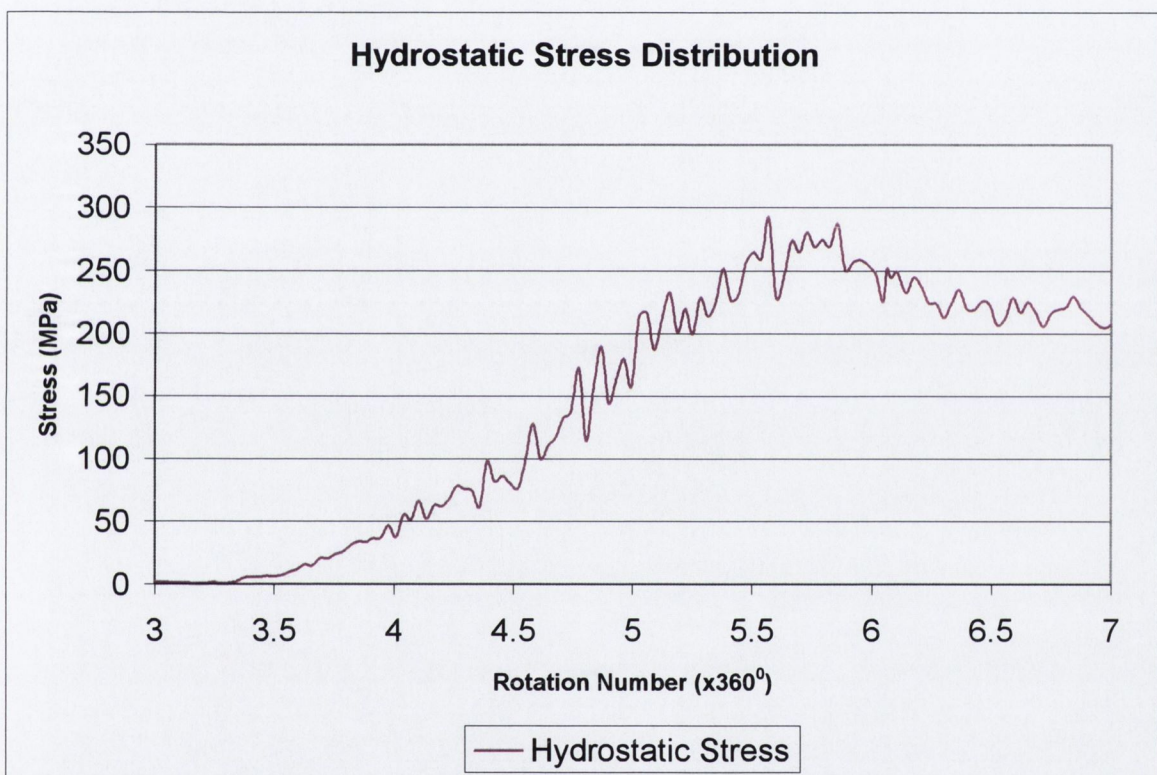


Figure 5.96 Hydrostatic stress distribution attributed to point 6 while forming the second groove.

Figures 5.97 (a), (b), and (c) show radial cross-sections of the workpiece through the second groove after 4, 5 and 6 rotations respectively. Similar to the analysis of the Normalised Cockcroft-Latham fracture law. As can be seen, these figures support Fang *et al* [57] insofar as tensile hydrostatic stress is found at the centre of the workpiece. However, contrary to the findings of Fang *et al* the maximum hydrostatic stress is located in a region at a 90° angle to the

die/workpiece interface away from the centre. In the sequence shown below, the maximum tensile hydrostatic stress of 550MPa occurred after 5 rotations of the workpiece i.e. just before the groove has reached its full depth, as can be seen in Figure 5.97 (b). The tensile hydrostatic stress in the centre of the workpiece was measured at 297MPa at the same stage of the process.

Therefore, in terms of the hydrostatic stress the fastener is more likely to fracture at the sides that are not in contact with the die, than at the centre of the workpiece. This result agrees with previous experimental and FE analysis where fracture occurred on the surface of the workpiece and there was no indication of internal rupture.

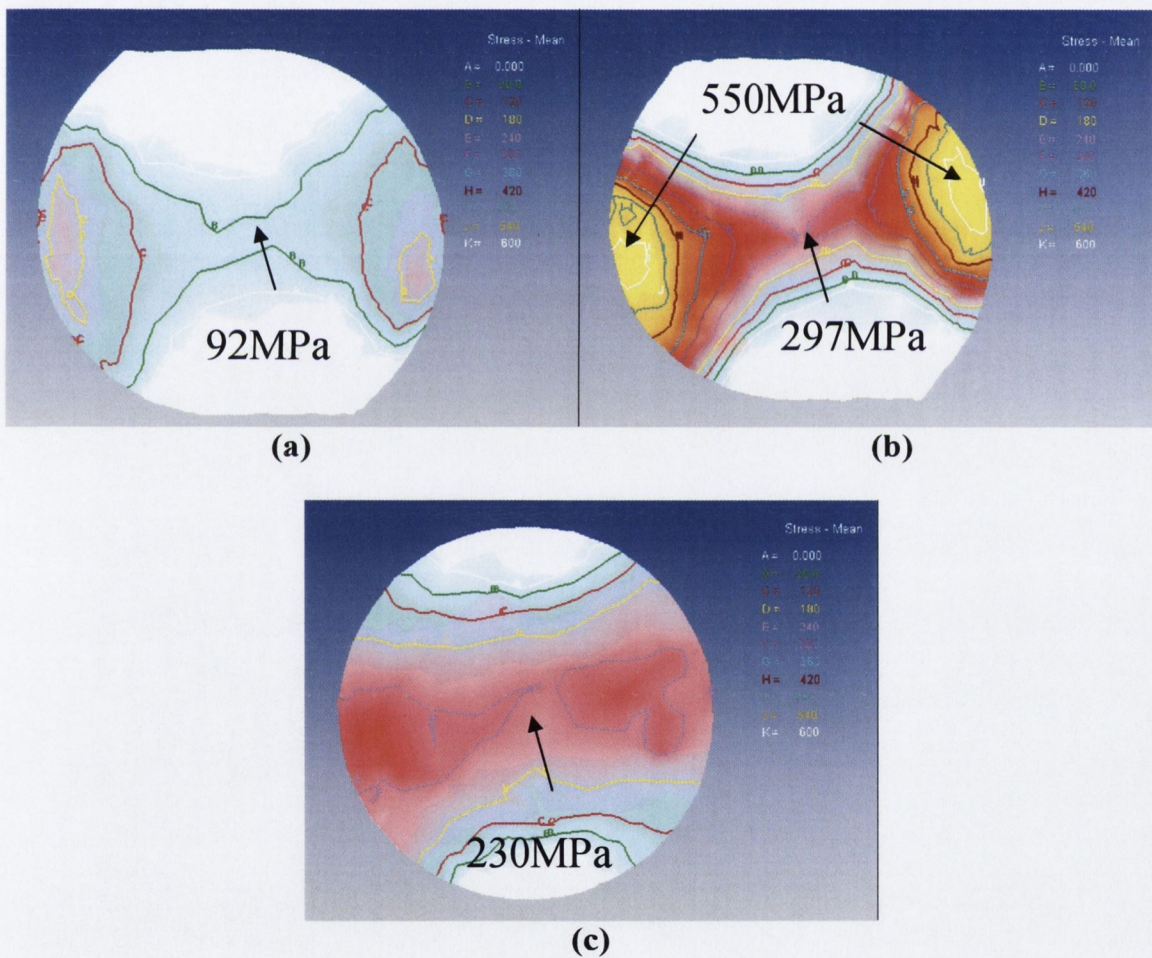


Figure 5.97 Tensile hydrostatic stress distribution in radial cross-sections of the workpiece taken after (a) 4, (b) 5 and (c) 6 rotations.

5.4 Die Stress Analysis

This investigation was not only concerned with the workpiece and its associated modes of failure, but was also concerned with the stresses within the tooling which have an effect on the life of the tool. During testing no cases of rapid tool fracture were recorded and since only approximately 200 pieces were rolled using the tooling there were no signs of fatigue. However, finite element analysis is a useful tool which can be used to predict tool stresses, as described earlier in chapter 4.2, which can then be applied to predict likely causes of tool failure. The tool material used in this analysis is M2 tool steel which has a yield strength of 2500MPa. In the following section the tool stresses associated with the die feature that formed the second groove are examined.

5.4.1 Stress Analysis of the Die Feature that Formed the Second Groove

Figures 5.98–5.101 are illustrations obtained from DEFORM3D of the die surface effective stress values after 4, 5, 6 and 7 rotations of the workpiece, respectively. The forces that were generated during the forming process were interpolated from the workpiece onto the surface of a small section of die which was positioned in contact with the workpiece.

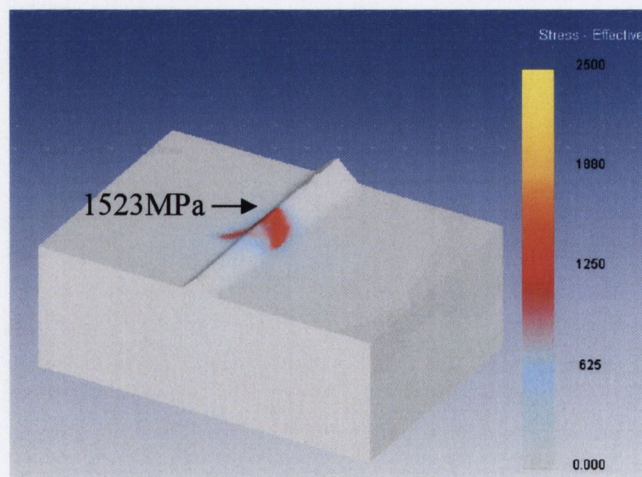


Figure 5.98 Die effective stress of the feature that formed the second groove taken after 4 rotations of the workpiece.

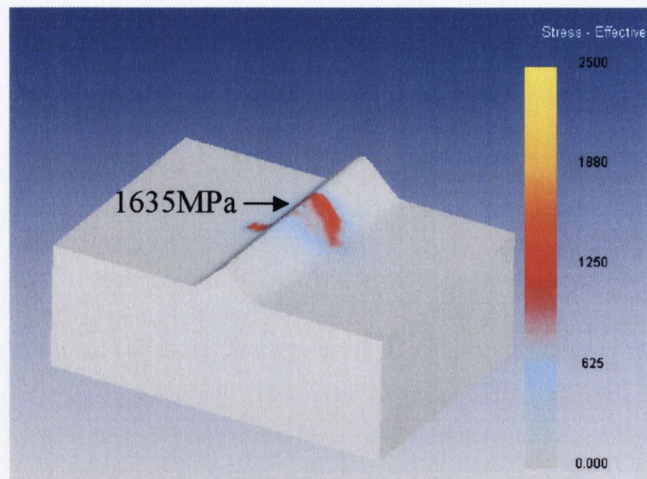


Figure 5.99 Die effective stress of the feature that formed the second groove taken after 5 rotations of the workpiece.

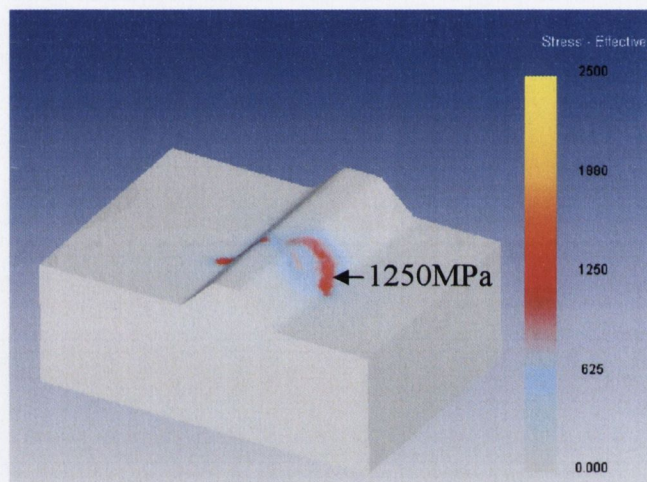


Figure 5.100 Die effective stress of the feature that formed the second groove taken after 6 rotations of the workpiece.

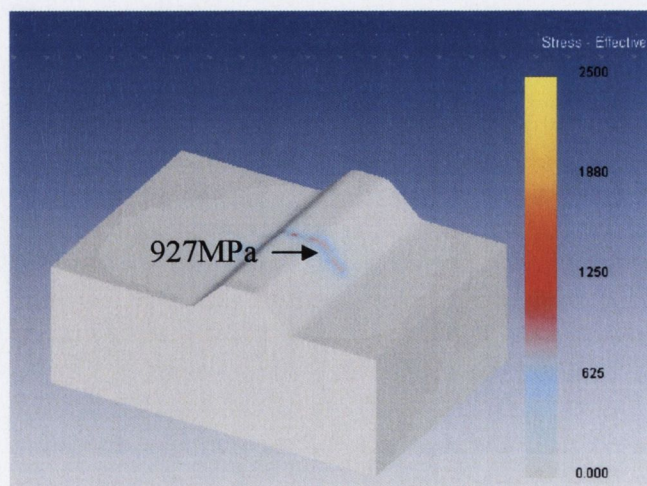


Figure 5.101 Die effective stress of the feature that formed the second groove taken after 7 rotations of the workpiece.

The effective or von Mises stress was obtained because it is the level of stress that predicts yielding when the shear strain energy reaches a critical value [80]. Therefore, if the von Mises stress is less than the yield strength of the M2 tool steel, the tooling will not fail from the point of view of just one cycle. Of course, over a number of cycles fatigue will determine the tool life.

As shown in Figure 5.98-101, the effective stress never exceeds the yield strength of the tool steel. The maximum effective stress was recorded after each quarter rotation and is plotted in Figure 5.102.

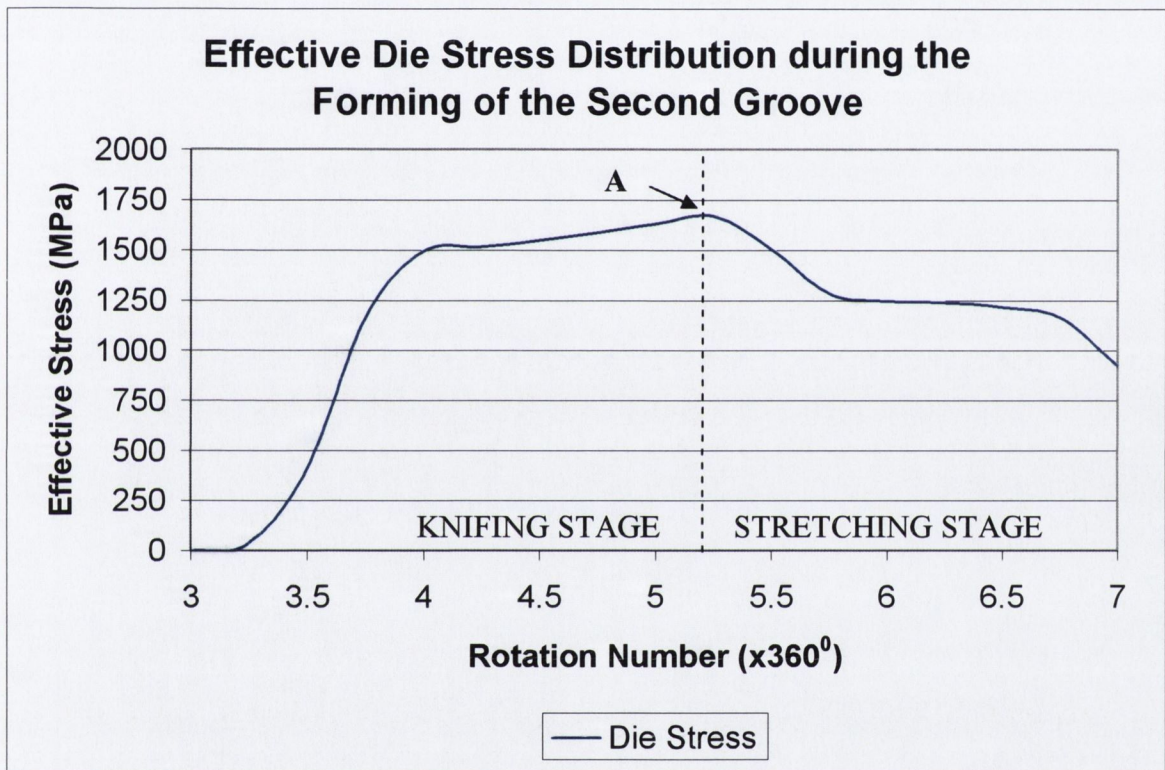


Figure 5.102 Maximum die effective stress distribution while forming the workpiece.

The die effective stress gradually increases to reach a maximum of 1672MPa at the end of the *knifing* stage, labelled A. Then once the required depth of the groove has been reached, the effective stress decreases during the *stretching* stage. This is because the load on the die is no longer concentrated on the *V* form of the *knifing* edge of the die. Therefore, during Form Rolling the most critical stage of stress concentration exists during the *knifing* stage where the sharp edge created by the included forming angle, 2α , acts as a stress concentration. This is shown in Figure 5.103, which is a cross-section through the second form from the

die after 4 rotations of the workpiece. From this figure it can be seen that the stresses are mainly concentrated within the included angle of the die.

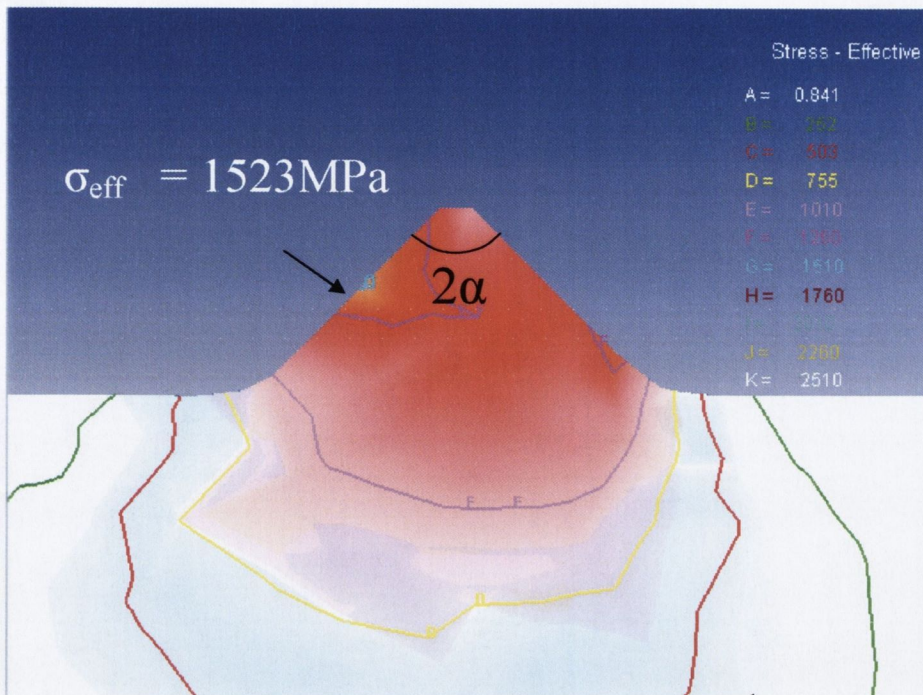


Figure 5.103 Effective stress distribution in the die form that Form Rolled the second groove taken after 4 rotations of the workpiece.

The effective stress during the *stretching* stage decreases to about 1250MPa after 5.75 rotations and remains at a constant level until 6.5 rotations because the same volume of material is displaced per half rotation of the fastener during the *stretching* stage. The final stage of the die, the *dwell*, corresponds to the 7th rotation. During this stage the stresses in the die decrease because the groove forms are complete.

The effective stress distribution is determined by the contact area between the die and the workpiece. This is illustrated in Figure 5.104 on the right side of the form where the groove in the workpiece is Form Rolled from left to right towards the tip of the workpiece. Therefore, the contact area on the right side of the form is greater than on the left or the centre because it is in contact with the *wave form* material on the surface of the workpiece.

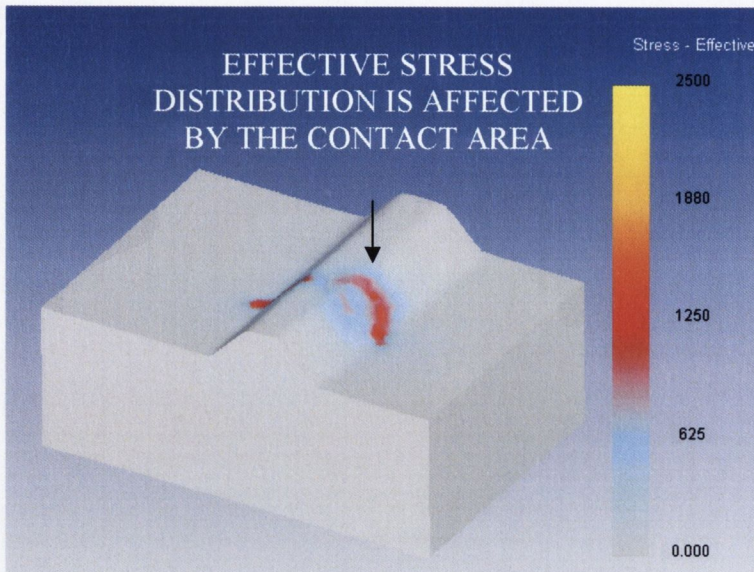


Figure 5.104 Die effective stress distribution in the die form that Form Rolled the second groove after 6 rotations of the workpiece.

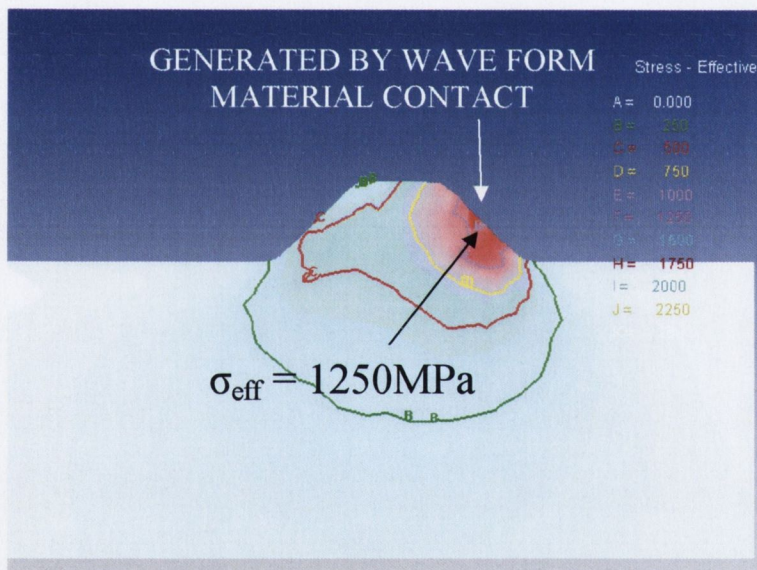


Figure 5.105 Cross-section view of the die effective stress distribution in the die form that Form Rolled the second groove after 6 rotations of the workpiece.

This is further illustrated in Figure 5.105 which is a cross-section taken through the maximum effective stress found during the 6th rotation. The extent of the stress distribution shows that the force exerted onto the workpiece emanates from where the workpiece material resists deformation. Therefore, as the side of the groove in the workpiece is formed the material of the *wave form* is generated because it flows in the direction of least resistance. However, the material on the side of the groove is deformed towards the tip of the workpiece due to a

combination of high compressive and shear stresses thereby generating larger forces which induce a higher stress concentration at the side of the die rather than where the wave form material is in contact. As shown in Figure 5.105, the maximum effective stress is 1250MPa on the right of the second form that generates the second groove in the workpiece. Notice also that the stress is concentrated at the side of the form and extends into the die material from the right side. At no stage in the process does the maximum effective stress exceed the yield strength of 2500MPa of the M2 tool steel. Therefore, rapid fracture of the die is not anticipated. This result is supported by experimental testing where at least 200 pieces were Form Rolled without any evidence of tool failure.

Figure 5.106 shows the distribution of the maximum principal stress in the die after 5 rotations of the workpiece. As can be seen coloured blue, the maximum principal compressive stresses are concentrated at the die/workpiece contact area. The region of maximum principal tensile stress which is not in contact with the workpiece is coloured yellow. Note that as the workpiece rotates down the length of the die, compressive stresses are first generated just ahead of and at the die/workpiece contact zone. Tensile stresses are generated behind the die/workpiece contact area as the workpiece continues to rotate. Therefore, the die is subjected to changing stress states from compression to tension as the workpiece is formed.

Typically these tools would produce 50,000 parts [1] which would mean that the surface of the tooling would experience alternating stress states from compressive to tensile for every part produced. In fatigue analysis the cyclical range from the compressive to the tensile stresses greatly affects the fatigue life of the tool. As shown in Figure 5.106 the stresses range from -1780MPa to +988MPa giving a total range of 2768MPa. The large range of principal stress cycles in the tooling would indicate that there may be fatigue issues which could arise through repeated use. However, fatigue analysis is not within the scope of this research project.

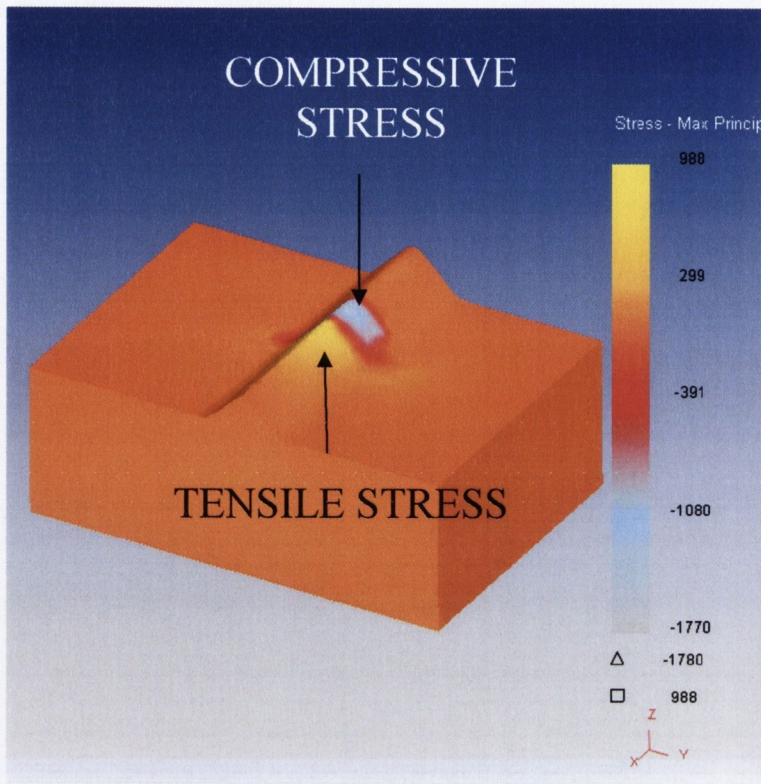


Figure 5.106 Maximum principal stress distribution in the die form that Form Rolled the second groove after 5 rotations of the workpiece.

In summary, die stress analysis was performed in order to determine whether the die would fail due to rapid fracture. The maximum die von Mises stress of 1672MPa was encountered after 5.25 rotations of the workpiece and was found to be 67% that of the yield strength of the M2 tool steel, which is 2500MPa. Therefore, rapid fracture is not predicted. This is in keeping with experimental results which showed no signs of chipping or fracture. However, due to the large range from the maximum compressive to tensile principal stress, low cycle fatigue fracture may ensue.

CHAPTER 6
CONCLUSIONS

CHAPTER 6

CONCLUSIONS

To the author's knowledge, finite element analysis has not been used to determine the mechanisms by which lapping and twisting surface failures occur. Therefore, the aim of this thesis was to analyse how these surface defects were generated by using finite element analysis to predict the material flow behaviour during the Form Rolling process. Another aim was to predict the stress distributions that are generated during the process and then apply them to describe how a crack developed on the surface of the workpiece. The general conclusions are detailed under two headings, these being "material flow behaviour" and "stress distributions".

6.1 Material Flow Behaviour

The accuracy of the model was shown by comparing selected geometries from the model to the geometries of the test fasteners. Once this had been established the finite element model was used to predict the material flow behaviour.

6.1.1 Lapping

To the knowledge of the author, this is the first 3D finite element analysis of the generation of the lapping defect on the surface of a fastener. It was shown that, during the *knifing* stage of the die, material folds were generated due to the helical path of the groove as it was formed on the workpiece. These folds were then compressed to form laps at the side of the groove.

During the *stretching* stage, lapping occurred at the base of the groove due to excess *wave form* material. *Wave form* material is generated due to plastic deformation generated ahead of the die/workpiece interface as the workpiece rotates. It was found that the *wave form* predominantly flowed in the direction of least resistance i.e. opposite that of the helical groove path progression. Therefore, this material has a tendency to fold while forming the groove which was compressed as the workpiece rolled, to form a lap at the base of the groove.

The appearance at regular intervals of small cracks at the base of the groove were statistically attributed to the geometry of the die and were therefore attributed to lapping.

6.1.2 Twisting Effect

The *twisting effect* was shown to have occurred in the deformation zone at the base of the groove. The angle of twist ϕ was found to be 2.295° . Twisting was also shown at the sides, close to the base of the groove. However, twisting was not evident along the entire sides of the groove because there was not enough die pressure to generate sufficient torque on the outer diameter of the workpiece.

6.2 Stress Distributions

6.2.1 Surface Stress Distributions

To the author's knowledge, this is the first occasion that the cyclical workpiece stresses generated during a Form Rolling process have been plotted. The cyclical nature of the alternating stresses at the surface of the fastener was investigated using the FE model. This revealed that during the Form Rolling process:

- The axial, hoop and radial stresses were shown to cycle, reaching a trough and peak while in and out of die/workpiece contact, respectively
- Predominantly, the stresses were in tension at 90° to the die/workpiece interface, the largest being the axial stress measured at 1130MPa at the end of the *knifing* stage
- The stresses were all compressive at the die/workpiece interface, the largest being the radial stress measured at 2520MPa at the end of the *knifing* stage
- The stresses gradually increased with increasing diameter reduction during the *knifing* stage of the die
- The stresses gradually decreased as the groove was widened during the *stretching* stage of the die

6.2.1.1 Surface Fracture

It was determined that a lap at the base of the second groove was the origin of a surface crack that developed between the 5th and 6th rotations of the workpiece. Experimental analysis revealed that the crack evolved due to a ductile failure mechanism whereby dimpled voids were shown with a crack linking them. The FEM showed that in the region where the crack occurred experimentally, there was a high concentration of axial tensile stresses at 90° to the die/workpiece interface. During the 5th and 6th rotations it was shown that these axial tensile stresses in conjunction with large shear stresses at the base of the groove were responsible for void formation and coalescence. This was confirmed in the FEM where large shear stresses at the base of the groove propagated the crack at a 45° angle to the maximum principal stress direction. The maximum axial tensile stress during this stage was 1130MPa after 5.2 rotations i.e. at the end of the *knifing* stage. The maximum shear stress of 423MPa occurred after 5.75 rotations at 90° to the die/workpiece interface whilst forming the second groove.

The Normalised Cockcroft-Latham fracture law was applied to the FEM and successfully predicted the location and stage of the process that the surface fracture was found in the experimental fastener. The damage values increased rapidly during the *stretching* stage of the die. The critical damage value, C , was 0.106 which was found at the base of the second groove after 5.75 rotations.

6.2.2 Internal Stresses

The internal stress states were investigated using the FE model which showed that:

- The axial and radial stress are completely tensile at the centre of the workpiece throughout the process
- The axial stress limits the radial stress
- The axial and radial stresses increase with increasing diameter reduction of the workpiece during the *knifing* stage

- During the *stretching* stage the axial and radial stresses remain at a constant level and then decrease as the groove nears completion
- The shear stresses in the workpiece increase with increasing diameter reduction at the centre of the workpiece during the *knifing* stage
- During the *stretching* stage the shear stresses level off and then decrease as the groove nears completion

The shear stresses were found not to be of a magnitude large enough to induce void evolution at the centre of the workpiece. However, if the workpiece diameter was further reduced the shear stresses emanating from the die/workpiece interfaces would cause void evolution.

The Normalised Cockcroft-Latham fracture law determined that fracture was more likely to occur at the surface of the workpiece than at the centre. The maximum damage value was 0.058 which occurred after 6.2 rotations.

High tensile hydrostatic stresses were found at the central portion of the workpiece, however, in terms of hydrostatic stress, it was found that fracture was more likely to occur nearer the surface than at the centre of the workpiece. The maximum tensile hydrostatic stress was 550MPa found near the periphery of the workpiece and the maximum tensile hydrostatic stress at the centre of the workpiece was 297MPa.

6.2.3 Die Stress Analysis

To the author's knowledge there is no available literature pertaining to the tool stresses developed during Form Rolling. Using die stress analysis it was found that:

- The maximum effective stress in the die was 1635MPa which is 67% that of the yield strength of the M2 tool steel which is 2500MPa; therefore, rapid fracture is not predicted which concurs with experimental observations

- The effective tool stress is at a maximum at the end of the *knifing* stage and then levels off in the *stretching* stage of the die because the same volume of material is displaced per half rotation of the die
- The workpiece, as it is rolled, generates compressive stress in the die in front of and in contact with the die/workpiece interface
- Tensile stress is generated behind the die/workpiece interface as the workpiece advances along the die
- This alternating stress state, which has a large range from compression to tension, would suggest that in service this die is most likely to fail due to fatigue

CHAPTER 7
FUTURE WORK

CHAPTER 7

FUTURE WORK

There exists a wide scope for further development of the Form Rolling process. Firstly, the correct interference between the die and workpiece could be determined so that adequate pressure is distributed across the entire length of the fastener and not just in the deformation zones as in the presented model. To do this, would require a modern Form Rolling machine which is rigid enough to prevent the dies from moving apart while forming the workpiece. The machine should also be equipped with process control capabilities so that the die alignment and the interference between the dies and the workpiece, which are critical to a good Form Rolling process, can be recorded. The recorded interference could then be applied to a FE model which could then be used to more accurately model the twisting effect across the entire deformation zone. Experimental fasteners with a line marked along their lengths could be rolled and then compared to the FE model to determine the accuracy of the twisting effect predicted by the model.

Currently, 3D FE packages to the knowledge of the author, cannot model the workpiece rotating between the dies where an elastoplastic workpiece is used. Issues concerning contact are the primary reason for this. However, in the latest release of DEFORM3D it is possible to model a rotating plastic workpiece which suggests it is only a matter of time when an elastoplastic workpiece with elastic dies can be modelled. This would increase the accuracy of any further simulations and provide the ability to determine the influence of friction on the process. To date studies have been conducted to determine the influence of contact, however only the *guiding* stage which in some CWR processes is a lead in to the *knifing* stage have been modelled. In future work there is the scope to investigate the contact between the dies and the workpiece taking into account the changing roughness of the die surface which consists of an EDM surface on the flat of the die and a smooth surface on the features that form the desired geometries.

When in time the simulation run time is sufficiently decreased to make it feasible, models should be run using a range of differing parameters to determine the influence of the ramp length, the diameter reduction and the forming, stretching and inclined angles. These models should be compared to experimental

analysis in order to try quantifying and eliminating various associated modes of failure.

Models could also be simulated to determine the affects of introducing corner radii on the die to reduce die stresses and also make it easier for material to flow around the die corners as it plastically deforms. This could have a diverse affect on the occurrence of lapping and cracking in the finished fasteners.

Different die designs could also be performed where the *knifing* and *stretching* stages are merged whereby the depth and width of the grooves are achieved simultaneously along the ramp of the die. This would have the affect of distributing the deformation more gradually which would lead to lesser workpiece and tool stresses.

As described in this thesis, the Normalised Cockcroft-Latham fracture law successfully predicted the location of the surface fracture. Experimental tests could be performed focusing between the 5th and 6th rotation of the workpiece in order to determine the exact moment the surface crack started to propagate. This could then be compared to the model in order to accurately determine the critical damage value, C , for the particular material used. Providing that the same material is used in further tests, this critical damage value can be treated as a material parameter and be applied to other Form Rolling models. In these models, elemental kill, which deletes any elements that match the critical damage value, could be applied to predict the shape and location of any fractures in the actual workpiece.

REFERENCES

- [1] R.W. Orlomoski, "*Form rolling for increase profits*", Wire Ind., 12, pp 734-738, 1989.
- [2] J. Holub, "*Transverse hot rolling*", Machinery 102(3), 129-134, 1969.
"*Wedge-roll forming makes UK debut*", Metalworking Prod. Issue 1, 43-45, 1969.
- [3] W. Kaul and L. Mockel, "*Shaft forging, the East German way*", Metalworking Prod. Issue 8, 49-50, 1969.
- [4] S.E. Rogers, "*The impact of drop forging research*", Metal Forming 37(12), 356-361, 1970.
- [5] A.C. Hobdell and A. Thomas, "*Approaches to cheaper forgings*", Metal Forming, 36 (1) 17-25, 1969.
- [6] F. Neuberger, L. Mockel, I. Rotz, "*Transverse rolling*", Metal Forming 35(10), 279-284, 1969.
- [7] "*Flashless forging of long-shaped components*", Metal Forming 35(2), 50-51, 57, 1968.
- [8] N.A. Grechkin, A.P. Sichennoi et al., "*Three high 120 mill at Dzerzhinskii works for rolling circular periodic sections*", Stal (in English), Vol. 5, 369-371, 1964.
- [9] "*Transverse forging-the Erfurt UWQ80 machine*", Metal Forming 37(2), 51-52, 1970.
- [10] "*Flashless forging*", Metal Forming 37(5), 133, 1970.
- [11] Zb Pater, "*Theoretical method for estimation of mean pressure on contact area between rolling tools and workpiece in cross wedge rolling processes*", Int. J. Mech. Sci. Vol. 39, No. 2, pp. 233-243, 1997.
- [12] A.I. Tselikov, "*Stress and strain in metal rolling*", Mir Publishers, Moscow, 1967.
- [13] Joseph P. Domblesky and Feng Feng, "*A parametric study of process parameters in external thread rolling*", Journal of Materials Processing Technology 121, 341-349, 2002.
- [14] G.V. Andreyev, "*Transverse-Wedge Rolling*", Russian Engineering Journal, 54, 8, pp. 73-76, 1974.
- [15] A. Lebek, "*Rollmaschine zur Herstellung von Rotationssymmetrischen Korpern*" Deutsches Patent, 10089V, 1879.

- [16] X. Fu and T.A. Dean, "Past developments, current applications and trends in the cross wedge rolling process", *Int. J. Machine Tools Manufacture*, Vol. 33, Part 3, pp 367-400, 1993.
- [17] G. Simonds, "Maschine zur Herstellung von Wagenachsen. Werkstücken für Gewenrlanfe und anderen unregelmäßig Geformeten Schiedestücken", Deutsches Patent, 36494Y, 1885.
- [18] G. Erkenzweig, "Walzbacken zum Walzen von Rotationskörpern", Deutsches Patent, 78382V, 1893.
- [19] J. Holub, Czechoslovakia Patent, No. 100161, 1961.
- [20] A.F. Balin, "Forgings of cross wedge rolling", Mashgiz, Moscow, 1969.
- [21] A.I. Tselikov, M.V. Garbarich and M.V. Vasilichikov, "Special Rolling Machine", Metallurgiya, Moscow, 1971.
- [22] A.I. Tselikov, E.A. Stosha, N.I. Kralov, "The rolling machine to produce shaft with small multiple diameters", Soviet Patent A.S. 418260, 1974.
- [23] G.A. Dulov and J.E. Astafiev, "Roll of cross wedge rolling", Soviet Patent A.S. 325076, 1972.
- [24] N.T. Deordiev, L.N. Nikolisku, N.T. Udovin *et al.*, "The machine of metal forming", Soviet Patent A.S. 387773, 1973.
- [25] G.V. Andreev, E.M. Makushok, V.M. Segal, "Equipment of cross rolling", Soviet Patent A.S. 460925, 1975.
- [26] G.V. Andreev, E.M. Makushok, V.M. Segal, "Cross wedge rolling machine", Soviet Patent A.S. 478661, 1975.
- [27] V.M. Prokolov, L.N. Nikoliskij, V.S. Perevozchikov, "Flat rolling", Soviet Patent A.S. 462646, 1975.
- [28] V.B. Urazov, "Design development of rolling machine", *Kuznech. Shtamplb. Proiz.* 2, 26, 1984.
- [29] Z. Marciniak, "The tool of making stepped shaft", Soviet Patent A.S. 357700, 1972.
- [30] K. Belmont, "Wedge rolling for preforms and as a substitute for machining", SME Technical Paper MF74-606, 1974.
- [31] M. Motomura, Japanese Patent, No. 215224, 1955.
- [32] S. Shirai, Japanese Patent, No. 272130, 1960.
- [33] Z.H. Hu, X.H. Xiu and D.Y. Sa, "The utilization of one-roll cross rolling process for spanner preform", *Forging and Stamping Technology* 2(5), 33-35, 1977.

- [34] Z.H. Hu, X.H. Xiu and D.Y. Sa, "*The principles, processes and machines of helical rolling and cross wedge rolling*", Metallurgical Industrial Press, Beijing, 1985.
- [35] "*The design and manufacturing of two-roll cross wedge rolling machine*", Summary Report of University of Beijing Science and Technology and Hua Shan Machine Tool Factory, 1976.
- [36] D.S. Li, X.P. Fu and Z.M. Ni, "*The instruction of H680 two-roll cross wedge rolling machine*", NORINCO-MFTI Technical Report, No. 88-07, 1988.
- [37] D.S. Li, X.P. Fu, Z.M. Ni and W. Zhang, "The manual of H800 two-roll cross wedge rolling machine", NORINCO-MFTI Technical Report, No. 88-12, 1988.
- [38] Q.T. Dong, "*Key problems in the design of type D46 wedge cross rolling machine*", Proceedings of the 4th International Conference on Rotary Metalworking Process, 251-257, Beijing, China, 1989.
- [39] G.F. Luan, C.W. Guo, Y.C. Yu and L. Liang, "Research on 3-roll cross wedge rolling of stepped shafts and its application in industry", Proceedings of the 4th International Conference on Rotary Metalworking Process, 251-257, Beijing, China, 1989.
- [40] http://www.ewmenn.de/english/programm/indexprogramm_e.html
- [41] V.S. Smirnov, "*Cross rolling*", (Poperechnaya prokatka), Mashgiz, 1948.
- [42] Z. Pater and W. Weronki, "*Determination of the contact area between the rolling tools and the workpiece in cross rolling process*", Journal of Materials Processing Technology, 45, 105-110, 1994
- [43] G.W. Andreev, W.A. Kluszin, E.M. Makuszok, W.M. Segal, V.Y. Shukin, "*Cross wedge rolling*", Science and Technology, Minsk, 1974.
- [44] H. Tsukamoto, K. Morimoto, T. Juge, K. Takahashi, "*Advance technology of plasticity*", Vol. 2, 936-941, 1984.
- [45] A.I. Celikov (ed.), "*Cross wedge rolling at the mechanical engineering*", Mashinostroenie, Moscow, 1982.
- [46] Z. Pater, "*Theoretical method for estimation of mean pressure on contact area between rolling tools and workpiece in CWR processes*", International Journal of Mechanical Science, Vol. 39, No. 2, 233-243, 1997.
- [47] Y. Dong, K.A. Tagavi, M.R. Lovell, Z. Deng, "*Analysis of stress in cross wedge rolling with application to failure*", International Journal of Mechanical Sciences 42, 1233-1253, 2000.

- [48] Q. Li, M.R. Lovell, W. Slaughter and K.A. Tagavi, "*Investigation of the morphology of internal defects in cross wedge rolling*", Journal of Materials Processing Technology 125-126, 248-257, 2002.
- [49] G. Thompson and J.B. Hawkyard, "*Crack formation in transverse rolling – A review*", Proc. 1st Int. Conf on Rotary Metalworking Processes, pp 171-184, 1979.
- [50] P.K. Teterin and Yu.F. Luzin, "*On the mechanism of metal rupture during cross rolling*", Stal (in English), 10, pp. 758-760, October 1960
- [51] A.I. Tselikov, V.M. Lugovski and E.M. Tret'yakov, "*The theory of transverse cold rolling in three-roll machine*", Russian engineering Journal, 7, pp. 44-48, 1961.
- [52] W.E. Johnson and A.G. Mamalis, "*Survey of some physical defects*", Proc 17th Int. MTDR Conf, pp 607-621, 1977.
- [53] I.I. Kazanskaya, M.G. Paninov, V.I. Ippolitov, "*Reason for the development of defects in transverse helical rolling of round periodic sections*", Stal (in English), 9, pp 709-711, 1962.
- [54] V.S. Smirnov, "*Cross rolling in machinery construction*", (Poperechnaya prokatka v mashinostroenii), Mashgiz, 1957.
- [55] A. Danno and T. Tanaka, "*Characteristics of billet deformation in 3-roll wedge rolling of axisymmetric stepped shafts*", Toyota Central Research and Development laboratories, Inc. Japan, Proc. 3rd Int. Conf. on Rotary Metalworking Processes, pp. 333-343, Kyoto, Japan, 1984.
- [56] A. Danno and T. Tanaka, "*Hot forming of stepped shafts by wedge rolling with three rolls*", Journal of Materials Processing Technology, 9, 21-35, 1984.
- [57] G. Fang, L.P. Lei, P. Zeng, "*Three-dimensional rigid-plastic finite element simulation for the two-roll cross-wedge rolling process*", Journal of Materials Processing Technology, 129, 245-249, 2002.
- [58] Z. Pater, W. Weronki, J. Kazanecki, A. Gontarz, "*Study of the process stability of cross wedge rolling*", Journal of Materials Processing Technology, 92-93, 458-462, 1999.
- [59] W.O. Alexander, G.J. Davies, K.A. Reynolds, E.J. Bradbury, "*Essential metallurgy for engineers*", Van Nostrand Reinhold.
- [60] A. Danno and T. Awano, "*Effect of rolling conditions on formation of central cavity in 2-roll cross rolling*", Journal of the Japan Society for Technology of Plasticity, 17, 181, 117-124, 1976.

- [61] G.V. Andreev, "Transverse-wedge rolling", Russian Engineering Journal, Vol. 54, Issue 8, 1974.
- [62] L.V. Guzavichus, A.S. Dubeni, S.M. Krasnevskij, "Cylindrical pattern to define plastic features of material in rolling process", Soviet Patent A. S. 538272, 1976.
- [63] A. A. Nefedov and L. A. Brezhnev, "A study of metal deformation under transverse helical rolling", Stal (in English), 5, 371-374, 1964.
- [64] M. Hayama, Journal of Mechanical Working Technology, 3, 31, 1979.
- [65] H. Tsukamoto, K. Morimoto, J. Juge, K. Takahashi, Advance Technology Plasticity, 2, 936, 1984.
- [66] Y. Dong, M. Lovell, K. Tagavi, "Analysis of interfacial slip in cross-wedge rolling: an experimentally verified finite-element model", Journal of Materials Processing Technology, 80-81, 273-281, 1998.
- [67] Y. Dong, M. Lovell, K. Tagavi, "Analysis of interfacial slip in cross-wedge rolling: a numerical and phenomenological investigation", Journal of Materials Processing Technology 97, 44-53, 2000.
- [68] M. Ashby and D. Jones, "Engineering Materials 1", 2nd Ed., Butterworth Heinemann.
- [69] R. Tornqvist, "Design of Crashworthy Ship Structure", PhD Thesis, Technical University of Denmark, Department of Mechanical Engineering, June 2003.
- [70] ASM Handbook, "Forming and Forging", ASM International, Metals Park, OH, Vol. 14, 1988.
- [71] T. Altan, H. Kim and M. Yamanaka, "Prediction and elimination of ductile fracture in cold forgings using FEM simulations", Transactions of the NAMRI/SME, Vol. 23, Pg 63-69, 1995.
- [72] S. Ghosh, M. Li and D. Gardiner, "A Computational and Experimental Study of Cold Rolling of Aluminum Alloys with Edge Cracking", Journal of Manufacturing Science and Engineering, Pg 74-82, Vol. 126, February 2004
- [73] Y. Boa and T. Wierzbicki, "A Comparative Study on Various Ductile Crack Formation Criteria", Transactions of the ASME, Vol. 126, Pages 314-324, July 2004
- [74] http://www.ncat.edu/~ccmradm/Dr%20homepage/meen_860/Chapter2.pdf
- [75] http://www.saarstahl.com/english/produkte/waermebehandlung_eigenschaften/ph/grafiken/bild_24a.jpg

- [76] Y. Dong, M. Lovell and K. Tagavi, "*Analysis of interfacial slip in cross-wedge rolling: and experimentally verified finite-element model*", Journal of Materials Processing Technology 80-81, 273-281, 1998.
- [77] Y. Dong, M. Lovell and K. Tagavi, "*Analysis of interfacial slip in cross-wedge rolling: a numerical and phenomenological investigation*", Journal of Materials Processing Technology 97, 44-53, 2000.
- [78] M. Lovell, "*Evaluation of Critical Interfacial Friction in Cross Wedge Rolling*", American Society of Mechanical Engineers, Vol. 123 April 2001.
- [79] Y. Dong, M. Lovell and K. Tagavi, "*Influence of Material Properties and Forming Velocity on the Interfacial Slip Characteristics of Cross Wedge Rolling*", Journal of Manufacturing Science and Engineering, Vol. 123 Nov.2001.
- [80] W. Johnson and P.B. Mellor, "*Engineering plasticity*", Van Nostrand Reinhold, London, 1973.
- [81] R. H. Wagoner, J.-L. Chenot, "*Metal forming analysis*", Cambridge University Press (2001).
- [82] J. H. Zar, "*Biostatistical Analysis*", Fourth Ed, Prentice.

